Geochemical study of Archean gabbro-anorthositic rocks and magnetitite bodies of the Mayurbhanj Mafic Igneous Complex, Singhbhum Craton, India: Implications for origin of base metal sulfide mineralization

Thesis submitted for the Degree of Doctor of Philosophy (Science) in Geology of Jadavpur University

2022

Chirasree Bhattacharjee

DST-INSPIRE Senior Research Fellow

Ph.D. INDEX No: 177/16/Geol.Sc./25

Registration No: SOGEO1117716

Department of Geological Sciences

Jadavpur University

Kolkata 700032

India

যাদবপুর বিশ্ববিদ্যালয়
কলকাতা-৭০০০৩২, ভারত

JADAVPUR UNIVERSITY
KOLKATA-700032, INDIA

FACULTY OF SCIENCE : DEPARTMENT OF GEOLOGICAL SCIENCES

Dr. Sisir K. Mondal
Professor of Geology, Jadavpur University (India)
Research Associate of American Museum of Natural History (NYC, USA)

Ph.D: Jadavpur University (2000)
Postdoc (2002-2003): Indiana University (Bloomington, USA)
Postdoc (2004-2006): American Museum of Natural History (NYC, USA)
Senior Researcher (2008-2010): NordCEE-Copenhagen University (Denmark)
JSPS short-term Invitation fellow (2013): Kanazawa University (Japan)

CERTIFICATE FROM THE SUPERVISOR

This is to certify that the thesis entitled 'GEOCHEMICAL STUDY OF ARCHEAN GABBRO-ANORTHOSITIC ROCKS AND MAGNETITITE BODIES OF THE MAYURBHANJ MAFIC IGNEOUS COMPLEX, SINGBHUM CRATON, INDIA: IMPLICATIONS FOR ORIGIN OF BASE METAL SULFIDE MINERALIZATION' submitted by CHIRASREE BHATTACHARJEE who got her name registered on 04.11.2016 (Ph.D. Index No: 177/16/Geol. Sc./25 and Ph.D. Registration No: SOGEO1117716) for the award of Ph.D. (Science) degree of Jadavpur University, is absolutely based upon her own work under the supervision of Professor Sisir Kanti Mondal and that neither this thesis nor any part of it has been submitted for either any degree/diploma or any other academic award anywhere before.

Sisir Kanti Mondal 28/07/2022

Signature of the supervisor, date with official seal

Sisir Kanti Mondal
Professor of Geology
Jadavpur University

Contact address: Department of Geological Sciences, Jadavpur University, 188 Raja S. C. Mallick Road, Kolkata-700032, India
Telephone : 0091-33-24572730 (office); 0091-9748078079 (mobile)
E-mail : sisir@geology.jdvu.ac.in; sisir.mondal@gmail.com & smondal@amnh.org
Website : https://sites.google.com/site/sisirgeology/ & http://www.iptri.in

Contents

Acknowledgements

I take this opportunity to express my profound gratitude and deep regards to my supervisor Prof. Sisir Kanti Mondal for his exemplary guidance, monitoring and constant encouragement throughout my thesis work. I am thankful to Prof. Sanjoy Sanyal, Prof. Sisir Kanti Mondal, former HODs, and Prof. Dipak C. Pal, present HOD of the Department of Geological Sciences, Jadavpur University for giving the access to the laboratory facilities to conduct the research work. I sincerely acknowledge the Government of India Department of Science and Technology for the DST-INSPIRE-fellowship, the UGC-CAS of Department of Geological Sciences, Jadavpur University for partial financial support, Government of India DST-PURSE-II to the University, and CEFIPRA-Indo-French International Collaborative Project-6007-1 of Prof. Sisir Kanti Mondal and Prof. Laurie Reisberg (CNRS-CRPG, Nancy, France) for partial financial support for analytical works. I am thankful to my junior Ratul Banerjee, Senior Research Fellow of my lab for his support. I am grateful to my parents and family for their continuous encouragement and support during the entire period of my thesis work.

Abstract

The Mesoarchean Mayurbhanj Complex of the Singhbhum Craton contains magmatic Fe-Ti-V rich oxide ore deposits within a gabbro-norite-anorthosite suite of rocks. The immediate country rocks of the mafic complex belong to the Early Archean Iron Ore Group supracrustal rocks of the Gorumahishani - Badampahar greenstone belt and ~3.1Ga granite plutons. The gabbro-noritic rocks of the Mayurbhanj Complex (Betjharan section) consist of plagioclase (An_{26-69}), clinopyroxene ($En_{42-54}Fs_{4-36}Wo_{22-42}$), and orthopyroxene ($En_{67-81}Fs_{15-28}Wo_{4-5}$) as cumulus phases with intercumulus Fe-Ti-oxides (magnetite and ilmenite) and sulfides (pyrite, pyrrhotite, chalcopyrite) as disseminated phases whereas, the gabbro-anorthositic rocks (Hatichhad section) contain cumulus plagioclase (An_{1-49}) and clinopyroxene ($En_{24-38}Fs_{31-49}Wo_{14-44}$) with magnetite and ilmenite in the intercumulus phases. The magnetitite ores consist of magnetite and titanomagnetite as cumulus phases with ilmenite as exsolved phases. Disseminated sulfides are mainly present along the grain boundaries of accessory Fe-Ti oxide grains, within interstitial spaces of silicate minerals, as inclusions within the silicate minerals and along altered fracture zones of the silicate host within the gabbro-norite. The mineral chemical study suggests the gabbroic rocks of the Mayurbhanj Complex are the products of fractionation of a Fe-Ti rich basaltic magma. Two pyroxene thermometry yields temperature of 1199°C - 956°C for the gabbro-norites and 1096° - 839°C for the gabbro-anorthosites which are close to the primary liquidus temperature of pyroxene from a fractionated basaltic magma. The intercumulus magnetite of the gabbro-norite and gabbro-anorthosite have high concentration of Cr (22301 - 67433 ppm), Ni (896 - 3880 ppm) and Cr_2O_3 (0.03 - 0.21 wt. %), V_2O_3 (0.73 - 1.19 wt. %) indicating early fractionation of the accessory magnetite in the gabbro-norite and gabbro-anorthsosite than the cumulus magnetite of the magnetitite layers. The lower concentration of V (30211 - 34608 ppm) in

the accessory magnetite of the gabbro-noritic rocks than in the magnetitite (48534 - 64855 ppm) suggests partitioning of vanadium into clinopyroxene within these rocks. The co-existing magnetite and ilmenite pairs in gabbro-norite, gabbro-anorthosite and magnetitites have yielded a temperature range of 798°C - 330°C with fO_2 11.38 – 38.35 reflecting various stages of cooling and sub-solidus re-equilibration of the mineral phases under QFM±2 condition. The continuous fractionation of the parental basaltic magma leads to Fe and Ti enrichment in the magma, and separation of a Fe-Ti rich liquid from the basaltic magma. The residual silicate melt became Si-rich. The magnetitite layers were formed from the Fe-rich liquid. The *in-situ* trace element analyses of the oxide minerals indicate higher chalcophile element (Pb = 2 - 11 ppm, Zn = 6773 - 8139 ppm, Mo = 25 - 68 ppm) concentrations in accessory magnetites of the gabbro-noritic rocks implying equilibration with co-magmatic sulfide mineral assemblages. The partitioning behavior of HFSE (Zr, Hf, Ta, Nb) in the magnetite and ilmenite is mainly dependent on the Ti^{4+} content of the minerals. Pyrite is the most abundant sulfide minerals present within the gabbro-norites. The probable mechanism for the formation of the sulfide assemblage was decrease of FeO activity of the parental basaltic magma due to crystallization of magnetite that triggered the sulfide saturation and formation of an immiscible sulfide liquid. The *in-situ* major and trace element analysis suggest two varieties of sulfides - (i) pyrite grains surrounded by rim of Fe-oxide minerals, and show negative Ni anomaly in trace element pattern. These pyrite grains were formed after pyrrhotites which are magmatic in origin, and (ii) pyrite grains which have enrichment of Pb (27 - 3120 ppm), Ag (8 - 15 ppm), Bi (0.2 - 9 ppm), As (48 - 6561 ppm), and Sb (0.4 - 18 ppm) indicate hydrothermal alteration of primary magmatic pyrite grains.

The bulk-rock major and trace element data of the gabbro-norite-anorthosite rocks of the Mayurbhanj Complex supports more primitive geochemical character of the gabbro-norites from the Betjharan section than the gabbro-anorthosites of the Hatichhad section. The plots of CaO, Al_2O_3, (Na_2O+K_2O) vs. MgO suggest both pyroxene and plagioclase were controlling the formation of gabbro-norite, and plagioclase was the early crystallizing phase for the gabbro-anorthosite rocks. In the chondrite normalized REE plot depletion of HREE in the gabbro-anorthosites than the gabbro-norites is due to lower modes of clinopyroxene grains in the former. The bulk rock Sm-Nd isotope analysis yields an isochron age of 3022 ± 180 Ma for the gabbro-anorthositic rocks of the Mayurbhanj Complex. Enrichment in LILE, negative Nb, Ta and Ti anomalies with weak positive Zr and Hf anomalies indicate small degree of crustal contamination which is also indicated by the plots of various incompatible elements (Zr vs. TiO_2, La vs. Sm, Th vs. Yb and Zr/Sm vs. Nb/Ta) where the samples of the Mayurbhanj Complex show minor affinity towards the older crustal materials of the Singhbhum Craton. The parental Fe-Ti-rich basaltic magma of the gabbro-norite-anorthositic rocks were originated by partial melting of a metasomatized continental lithospheric mantle wedge in an active continental margin setting. The parental magma emplaced in the shallow crustal magma chamber where the gabbro-norite-anorthositic rocks and magnetitite layers were formed by fractional crystallization process. The parental Fe-Ti-rich basaltic magma was emplaced within the Early Archean TTG dominated continental crust (OMTG, SBG I, II). The contemporaneous granitic plutons were formed due to crustal reworking of these older TTG [SBG I, II, OMTG] rocks. The negative ε_{Nd} of the gabbroic rocks (-4.4±3.3) suggests overprinting of post-magmatic hydrothermal alteration upon the crustal contamination. Comparison with time-equivalent ultramafic-mafic magmatic events suggests that the ~3.1 Ga Mayurbhanj Complex represents an amalgamation phase of the supercontinent 'Ur'. The Mayurbhanj Complex together with the time equivalent Dhanjori Complex, Jagannathpur-Malangtoli ultramafic-mafic volcanics, Keshargaria mafic dyke swarm, Nuasahi-Sukinda ultramafic-mafic Complex of the Singhbhum Craton and the Sargur-Nuggihalli-Holenarsipur greenstone belt of the western Dharwar Craton represents a major component of the Ghatgaon Large Igneous Province which is part of a large scale global ultramafic-mafic event of that time forming the supercontinent ‘Ur’.

CHAPTER 1

INTRODUCTION

1. Introduction

Magnetitite bodies of mafic igneous complexes are one of the main sources of titanium and vanadium ore deposits. Titanium and vanadium bearing magnetites commonly occur in the gabbroic unit with magnetitite bands at the upper part of the ultramafic-mafic igneous complexes (Haggerty, 1976; Cameron, 1979; Reynolds, 1985a, 1985b; Zhou et al., 2005; Charlier et al., 2006; Pang et al., 2008; 2009; Wang et al., 2008; Hou et al., 2012, Liu et al., 2015; She et al., 2015; Gao et al., 2017; Pang and Shellnutt, 2018; Wang et al., 2018; Zhang et al., 2018; Bai et al., 2019; Bhattacharjee and Mondal, 2021). Whereas, some of the significant deposits of the world occur as stratiform bodies within the layered mafic igneous complexes (e.g., Bushveld Complex, South Africa and Skaergaard intrusion, Greenland), while another type of deposits occurs within non-layered massif type mafic intrusions, mostly as irregular veins, lenses, stringers and inconsistent layers (e.g., Adirondack and the Duluth complex, USA). Mafic intrusions of overall gabbroic composition host magmatic Cu-Ni-PGE sulfide deposits e.g., the plutonic suite of the Siberian Continental Flood Basalt Province at Limahe and the Emeishan Flood Basalt Province at Baimajhai (SW China) and several world-class V-Ti magnetite deposits e.g., Panzhihua and Hongge of the Emeishan Continental Flood Basalt Province (SW China) that occur at the upper level of the layered sequences (Wager and Brown, 1968; Irvine, 1975; Cawthorn, 1996; Zhong et al., 2009; Wang and Zhou, 2013; Zhou et al., 2013; Liu et al., 2015; Ripley and Li, 2018). The largest layered mafic intrusion Bushveld Complex of South Africa hosts the world's richest chromite and magmatic Ni-Cu (PGE) sulfide deposits (e.g., Cawthorn, 2005; Tegner et al., 2006). Other than the Bushveld Complex, the Skaergaard intrusion of east Greenland is an example of a magmatic sulfide deposit that occurs in the upper part of the layered complex (e.g., McBirney, 1996; Holwell et al., 2015). The magnetitite ore bodies from the layered mafic intrusions are also reported to host Pd-dominated PGE (Platinum-Group Elements) that are associated with minor occurrences of primary magmatic sulfide minerals (e.g., Bai et al., 2012; Howarth et al., 2013; Prichard et al., 2018). To understand the genesis and geochemical evolution of ultramafic-mafic magmas and the processes associated with the formation of Ti-V-bearing magnetite deposits, the layered intrusions are the main interest of study for the last few decades (e.g., Wager and Brown, 1968; Irvine, 1975; Cawthorn, 1996; Keays et al., 1999; Charlier et al., 2015).

The different types of Fe-Ti oxide ore deposits are characterized by different mineralization styles (e.g., Charlier et al., 2015). According to Rose (1969) and Charlier et al. (2015) these deposits could occur within tabular intrusives, stocks, sills or dykes in massive anorthosites, stratified accumulations in layered segments of anorthosite massifs or in layered intrusions. The massive type deposits contain hemo-ilmenite (±Ti-magnetite in some deposits) and constitutes >90% of the mineral assemblage. These ores are coarse grained with polygonal tabular crystal of hemo-ilmenite with plagioclase, orthopyroxene and spinel (e.g., Rose, 1969; Charlier et al., 2015). The stratiform deposits are found in layered intrusions and is made up of anorthosite cumulates, troctolite, leuconorite, norite, gabbro-norite with Fe-Ti-P rich rocks at the top of the layered series (e.g., Duchesne and Charlier, 2005; Charlier et al., 2015). The massive to layered tabular bodies form sills (~10 m thick) in anorthosite plutons and extend for several kilometers which are parallel to the foliation of anorthosite. These rocks are modally layered and massive ilmenite occurs at the footwall contact. In these structure oxide minerals are accumulated in the lower part and the upper eroded parts contain co-crystallizing plagioclase, ± orthopyroxene and olivine (e.g., Charlier et al., 2007; Morisset et al., 2010; Charlier et al., 2015). The Lenticular ore bodies are intimately associated with the host rock and observed locally in anorthosite plutons. The ore bodies display gradation into the host rocks with individual orebody morphologies are like lenses, veins or layers (e.g., Charlier et al., 2009; Chen et al., 2013; Charlier et al., 2015). The igneous origin of these Fe-Ti oxide deposits is accepted worldwide (e.g., Charlier et al., 2015) and the proposed mechanisms for the oxide minerals accumulation are: (a) segregation of an immiscible Fe-Ti-P rich fluid) (e.g., Philpotts, 1982; Lindsley, 2003; Charlier et al., 2008; 2013; Charlier and Grove, 2012); (b) fractional crystallization with gravitational settling of oxide minerals accompanied with plagioclase flotation (e.g., Toplis and Carroll, 1995; Charlier et al., 2006; 2007; 2008; 2009; 2010b); (c) magma mixing (e.g., Irvine, 1977; Charlier et al., 2006; 2010b); (d) polybaric crystallization (e.g., Charlier et al., 2015); (e) solid state remobilization (e.g., Duchesne, 1996; 1999; Charlier et al., 2015); (f) hydrothermal remobilization (e.g., Li et al., 2014)

In the Singhbhum Craton of eastern India, Fe-Ti-oxide ore deposits are present in the Mayurbhanj Complex and in the Nuasahi ultramafic-mafic complex (Roy, 1956; Chakraborty, 1959; Banerji, 1984; Mohanty et al., 1999; Das and Mukherji, 2001; Mohanty et al., 2008; Das, 2014; Prichard et al., 2018). The present work is based on the gabbro-anorthositic rocks and magnetite ores of the Mayurbhanj Complex. Previous research works on the Mayurbhanj Complex were focused on the mineralogy and various textures of the vanadium bearing titaniferous magnetitite ores (Roy, 1955, 1956; Das and Mukherji, 2001; Das, 2014). Mainly mineralogy, textural study, ore petrography and origin of the ore bodies were described by the previous researchers. Roy (1955) described various textural relationships and different exsolution intergrowths between magnetite, ulvöspinel, ilmenite, hematite and made an attempt to find out temperature and the mode of formation of the intergrowths. Roy (1956) described field realtionships, petrography of the ore minerals, and suggested the origin of the magnetitite layers by late-magmatic ‘residual liquid injection’ process. Das (2014) described various micro-intergrowths of the oxide minerals within the titaniferous magnetitite ores of the Mayurbhanj Complex and the genesis of the ore layers by a late-stage Fe-Ti rich residual liquid injection.

There has not been any attempt to characterize the Mayurbhanj Complex using detailed major and trace element geochemistry of different rock-forming minerals and Fe-Ti-oxide minerals from the gabbro-anorthositic rocks and the magnetitite ores. Systematic mineral chemical data for the Mayurbhanj Complex not only can constrain its magmatic history, but also allow refinement of previously-proposed ore-forming conditions and comparison with other layered intrusions. One of the relevant questions is, for instance, whether the intrusion formed from a single differentiating magma like the Skaergaard and Kiglapait intrusions or multiple pulses of magma like the Freetown Layered Complex (Chalokwu et al., 1995) and the Kap Edvard Holm Complex. The scenario of Skaergaard intrusion showed a moderately evolved tholeiitic magma (rich in P and Ti) followed a trend of differentiation characterized by exceptionally strong iron enrichment and relatively little increase of silica until the very latest stages of differentiation when the magma split into two liquids (one very rich in iron and the other in silica) (e.g., McBirney, 1996). In the Kiglapait intrusions the modal variation of cumulus minerals (olivine and plagioclase) confirm the fractionation history of a single magma (Morse, 1980). In contrast in the other two complexes magma emplacement have taken place by separate tranquil influxes which flowed along with the interface between a largely consolidated cumulus pile and a residual magma (Tegner et al., 1993).

The study of bulk rock major and trace element geochemistry of the mafic intrusion is important for constraining the tectono-magmatic affiliations of the plutonic complex. The petrogenesis and associated tectonic settings of the Mayurbhanj Complex were not constrained by the previous researchers. The petrogenesis and geodynamics of the Archean gabbro-anorthosite complex have important implications on recognizing the magmatism and crustal evolution because the gabbro-anorthositic rocks are an essential component in the Earth's crust, and globally these complexes constitute important components of Archean-Proterozoic crustal growth (e.g., Ashwal, 1993; Ashwal and Bybee, 2017). Gabbroic anorthosites of the Archean age are sparsely distributed and least preserved due to multiple phases of deformation, metamorphism and intrusion of several granitoid bodies. The Mayurbhanj Complex is comprised of gabbro-norite to gabbroic rocks at the lower part, whereas, the upper part is comprised of gabbroic-anorthosite to anorthositic rocks and associated with Fe-Ti oxide ores.

In my thesis work, I have conducted systematic petrographic and mineralogical studies of the common rock-forming silicate minerals, Fe-Ti oxides, and sulfide minerals in the gabbroic rocks and magnetitite ores of the Mayurbhanj Complex. These data have been used to understand the compositional variations in silicate (clinopyroxene, orthopyroxene, plagioclase) and Fe-Ti oxide minerals in the intrusion and their relevance with respect to the petrological evolution of the entire mafic igneous complex. In addition, I have addressed the issue of primary magmatic versus secondary processes of sulfide mineralization within the gabbroic rocks. *In-situ* trace element analysis of magnetite is a useful tool in geochemical exploration for Ni-Cu-PGE sulfides (e.g., Boutroy et al., 2014; Ward et al., 2018). The trace element data of Fe-Ti oxides have been used to explore the Ni-Cu-PGE sulfide potentiality of the Mayurbhanj Complex. I have calculated temperature and oxygen fugacity using co-existing Fe-Ti oxide phases to understand the extend of re-equilibration of the assemblages in the gabbroic rocks as well as within the magnetitite ores. The bulk-rock major and trace element geochemical study of the gabbro-anorthositic rocks has been conducted to understand the magma evolution and origin of the igneous complex.

The Sm-Nd method is most frequently used to date cogenetic mafic igneous rocks by the isochron method (e.g., Faure and Mensing, 2005). The Sm-Nd method is well suited for the dating of mafic volcanic and plutonic rocks of the Precambrian age because these rocks have higher Sm/Nd ratios and this isotopic systamatic is more robust than the Rb-Sr and K-Ar system because the trivalent Sm^{3+} and Nd^{3+} form stronger bonds with anions than Sr^{2+}, Rb^{+}, and K^{+} (e.g., Faure and Mensing, 2005). Hence the Sm-Nd isochron dates are older than Rb-Sr isochron dates derived from the same rocks and give a more precise crystallization age of those rocks (e.g., Faure and Mensing, 2005). The Sm-Nd isochron age has been determined for the gabbro-norite-anorthositic suite of rocks from the Mayurbhanj Complex. The crystallization age of the mafic igneous complex was hitherto unknown to the geological community. The whole rock Sm-Nd isotope studies yielded the the crystallization age as well as the emplacement age of the mafic complex. This isochron age has been correlated with earlier reported geochronological information of the other lithological units of the Singhbhum Craton and a petrogenetic model has been proposed for the Mayurbhanj igneous complex.

CHAPTER 2

GEOLOGICAL BACKGROUND

2.1. Geology of the Singhbhum Craton

The Peninsular Indian Shield is comprising of four major composites, consolidated and rigid blocks: (1) the Dharwar Craton in southern India (2) the Bastar Craton in central India (3) the Singhbhum Craton in eastern India and (4) the Bundelkhand Craton in northern India (Valdiya, 2015) (**Fig. 1a**). The Singhbhum Craton of the eastern India is bordered by the Singhbhum Mobile Belt to the north, the Eastern Ghat Mobile Belt to the southwest and the Bastar Craton to the west (Saha, 1994). The Singhbhum Craton consists of (a) an amphibolite facies supracrustal unit known as the Older Metamorphic Group (OMG), (b) tonalite-trondhjemite-granodiorite of the Older Metamorphic Tonalite Gneisses (OMTG), (c) granite-tonalite of the Singhbhum Granite Batholithic Complex (SGBC) and (d) greenschist to greenschist-amphibolite transitional facies volcanics (komatiites to komatiitic basalts) and sediments including banded iron formations of the Iron Ore Group (IOG) supracrustal unit (e.g., Saha, 1994; Mondal, 2009).

The central part of the Singhbhum Craton is occupied by the Singhbhum Granite Batholithic Complex (SBG) whereas other rocks occur mostly at the peripheral part of the craton (**Fig. 1a**). The large oval shaped body of the SGBC constitutes more than one third of the craton. This is a suit of granitoid rocks ranges from tonalite to granite and emplaced in different pulses. The earliest phase of the SBG (Phase l) is K-poor granodiorite-trondjhemite in composition and the later phases (Phase ll and lll) are granodiorite-granite in composition (Mukhopadhyay, 2001; Upadhyay et al., 2014). The different pulses of the granitic intrusions were reported from 3.52 – 3.28 Ga by different workers (Sengupta et al., 1991; Saha, 1994; Ghosh et al., 1996; Mishra et al., 1999; Upadhyay et al., 2014). The available geochronological data indicate no systematic age difference between different phases of the granitic intrusions in the craton (**Table. 1**). The distinct pulses were dated at 3.43 – 3.47

Ga (OMTG and SBG Phase-lll), 3.32 – 3.35 Ga (OMTG, SBG Phase-l, SBG Phase-ll and SBG Phase-lll) and 3.30 – 3.28 Ga (OMTG, SGBC Phase-ll and SGBC Phase-lll) (Upadhyay et al., 2014) (**Table. 1**). The SBG is intruded by a number of younger granite plutons that are known as Kuilapal granite, Mayrbhanj granite, Nilgiri granite, Bonai granite, Soda granite, Arkasani granite, Chakradharpur granite and Tamperkola granite. The radiometric age of the Chakradharpur granite is not known. The second and third phases of the Mayurbhanj granite pluton have yielded in situ Pb-Pb zircon ages of 3080±8 Ma and 3092±5 Ma, respectively (Mishra et al., 1999) (**Table. 1**). Geochemically the Mayurbhanj granite was considered as an A-type anorogenic granite (Misra et al., 2002). The most recent age information from zircon grains suggests an age of ~3.1 Ga (Chakraborti et al., 2019). The in-situ Pb-Pb zircon dating of the Tamperkola granite has yielded a crystallization age of 2809±12 Ma and 2822±67 Ma. The precise Pb-Pb whole-rock isochron age of the Soda granite pluton is 2220±54 Ma (Sarkar et al.,1985). The Kuilapal granite gneiss has yielded a whole rock Rb-Sr isochron age of 1638±38 Ma and the Arkasani granite the whole rock Rb-Sr isochron age of 1052±84 Ma (Sengupta et al., 1994). The bonai granite is separated from the Singhbhum granite by the supracrustal rocks of the Jamda-Koira basin (Sengupta et al., 1991; Mukhopadhyay, 2001) and the granitic body is compositionally high Al_2O_3 trondhjemites-tonalite-granodiorite to calc-alkaline trondhjemite. This granitic pluton yielded a whole rock Pb-Pb age of 3163±126 Ma (Sengupta et al., 1991). The Nilgiri granite also known as Kaptipada granite forms a pluton in the southern part of the Singhbhum granite and it is compositionally K_2O rich granitoids. The whole rock Pb-Pb and Sm-Nd ages mostly suggest ~3.29 Ga (Saha, 1994).

The rocks of the OMG and OMTG occur as enclaves within the SGBC (**Fig. 1a**). Based on ^{207}Pb-^{206}Pb ages of zircon grains from quartzite Goswami et al. (1995) reported 3.5 Ga

Table. 1. Chrono-stratigraphy of the Singhbhum Craton.

Stratigraphic unit		**Generalized sequence**	**Age**	**References**
	Kolhan Group	KG (Time equivalent to SMB)	2100-2200 Ma	Saha et al., 1988
Dolerite dyke swarms	Barigaon dyke swarms Pipilia dyke swarms Bhagamunda dyke swarms Kaptipada dyke swarms Keonjhar dyke swarms Ghatgoan dyke swarms Keshargaria dyke swarms	Newer Dolerite Suite	1766±1 Ma 2800.2±0.7 Ma	Shankar et al., 2014 (Pb-Pb baddeleyite age) Kumar et al., 2017 (Pb-Pb baddeleyite age)
Singhbhum Mobile Belt			2256±6 Ma	Srivastava et al., 2019
	Dhanjori-Simlipal-Dalma-Jagannathpur- Malangtoli and Singhbhum Group: Igneous and Sedimentary Sequences	Late Archaean to Proterozoic Mobile Belts (SMB)	2787±270 Ma 2799±67 Ma	Misra and Johnson, 2005 Adhikari et al., 2021 (Sm-Nd isochron age)
Archean Granite-Greenstone terrain	Mayurbhanj Granite		3080±8 Ma 3092±5 Ma 3089±6 Ma	Misra et al., 1999 (Pb-Pb date of zircon) Chakraborti et al., 2019 (LA_ICPMS zircon in geissic granite)
	Mayurbhanj Gabbro-anorthosite-ultramafics		3022±180 Ma	Mondal et al., 2021
	Singhbhum Granite Type B (Phase III)	SBG-B	3377±11 Ma 3367±7 Ma 3470±10 Ma 3292±19 Ma 3351±8 Ma	Chaudhuri et al., 2018 (SHRIMP U-Pb date of zircon) Pandey et al., 2019 (LA-ICPMS U-Pb date of Zircon)
	Iron Ore Group Igneous and Sedimentary	Iron Ore Group (IOG)	3506.8±2.3	Mukhopadhyay et al., 2008

	Sequences: Gorumahishani-Badampahar basin; Jamda-Koira basin; Tomka–Daitari basin			(Sm-Nd whole rock isochron age)
	Singhbhum Granite Type A (Phase I and II)	SBG-A (Phase I)	3350±20 Ma 3262±12 Ma	Upadhyay et al., 2014 (LA-ICPMS U-Pb date of zircon)
			3397±9 Ma 3267±6 Ma 3289±10 Ma	Chaudhuri et al., 2018 (SHRIMP U-Pb date of zircon)
		(Phase II)	3336±4 Ma 3463±8 Ma	Upadhyay et al., 2014 (U-Pb date of zircon)
			3334±15 Ma 3330±9 Ma	Pandey et al., 2019 (LA-ICPMS U-Pb date of zircon)
	Older Metamorphic Tonalite Gneiss	OMTG	4.2-4.0 Ga 3.9-3.8 Ga 3.67-3.59 Ga	Chaudhuri et al., 2018 (U-Pb date of zircon)
			3352±13 Ma 3363±12 Ma 3286±11 Ma	Pandey et al., 2019 (LA-ICPMS U-Pb date of zircon)
	Older Metamorphic Group	OMG	3317±8 Ma	Upadhyay et al., 2014 (LA-ICPMS)
			3375±3 Ma	Nelson et al., 2014 (SHRIMP)

depositional age for the sediments belonging to the OMG. A Sm-Nd whole rock isochron for the amphibolites of the OMG yielded an age of 3.3 Ga (Sharma et al., 1994) which is considered to be the crystallization age of the igneous protoliths. The metamorphic monazites overgrowing tectonic fabrics cluster in two groups (3377±45 Ma, 3256±46 Ma) suggesting two episodes of metamorphism affecting the OMG (Prabhakar and Bhattacharya, 2013). The U-Pb concordia age from rutile in mica schist of the OMG gave the metamorphic age as 3317±8 Ma (Upadhyay et al., 2014) (**Table. 1**).

The geochronological data obtained for the OMTG by different workers has a wide range. Chaudhuri et al. (2018) reported the age of inherited zircon from the OMTG rocks range from 4.2 - 3.6 Ga and also interpreted the Hadean enriched reservoir from which felsic melts were derived and persisted till Palaeoarchean. The first phase of the OMTG was emplaced around 3.45-3.44 Ga (U-Pb zircon dates; Mishra et al., 1999; Acharyya et al., 2010; Upadhyay et al., 2014) and the younger phase of the OMTG was emplaced around 3.35-3.32 Ga (Upadhyay et al., 2014). The U-Pb data from xenocrystals zircon from the OMTG yielded 4.24-4.03 Ga ages suggesting that the OMTG records oldest precursor of Hadean age in the Indian cratons (Chaudhuri et al., 2018) (**Table. 1**). Recently Pandey et al (2019) yielded U-Pb zircon ages of 3363 ± 12 Ma and 3352 ± 13 Ma from trondhjhemite samples of the OMTG. The granite samples from OMTG have concordant U-Pb age of 3286 ± 11 Ma (Pandey et al., 2019) (**Table. 1**).

The Iron Ore Group metavolcanic and metasedimentary rocks are constituting the three major greenstone belts namely (i) the Gorumahisani-Badampahar belt, (ii) Noamundi-Jamda-Koira belt, and (iii) Tomka-Daitari belt (**Fig. 1a**; Mondal et al., 2006; Mondal, 2009). The age of the IOG supracrustal sequences is considered to range between those of the evolutionary stages of the SGBC (Saha, 1994). Mukhopadhyay et al. (2008) obtained 3.5 Ga

U-Pb date of zircon from dacitic lava of the Tomka-Daitari greenstone belt (**Table. 1**). Iron Ore Group supracrustal sequence includes komatiitic dunite-peridotite rocks at the lower part and metavolcanic schist rocks (komatiitic basalt) at the upper part which are intercalated with metasedimentary rocks along with quartzite and banded iron formation (Mondal, 2009; Mondal et al., 2019). Adhikari et al. (2021) have obtained two age information of the metavolcanic rocks of the IOG– (i) ~3.57 Ga for the southern IOG and (ii) ~3.31 Ga for the eastern IOG using whole rock Sm-Nd methodology (**Table. 1**). There are ultramafic-mafic plutonic bodies (e.g., Nuasahi-Sukinda Complex, Mayurbhanj Mafic Complex) which are closely associated with the IOG supracrustal rocks and mostly occur along the southern and eastern parts of the Singhbhum Craton (**Fig. 1a**) (Mondal et al., 2001; Mondal, 2009). U-Pb zircon age obtained from the gabbroic matrix of the PGE mineralized breccia zone in the Nuasahi complex is 3.12 Ga (Augé et al., 2003). Insert the Sm-Nd isochron age by this group for the Nuasahi gabbro.

Younger volcano-sedimentary belts such as the Dhanjori-Simlipal-Malangtoli-Jagannathpur and Dalma surrounds the older rocks of the Singhbhum Craton (**Fig. 1a**). The Dhanjori basin resting unconformably over the Iron Ore Group in the NE part of the craton and consists dominantly of volcanics and volcanoclastic sediments (Roy et al., 2002). The sequence consists of a lower unit of metapelites, psammites with ultramafics mafics and an upper volcanic unit of mafic/ultramafic tuffs, intrusives and metabasalts (Roy et al., 2002). Misra and Johnson (2005) obtained the whole-rock Pb-Pb age of 2858 ± 17 Ma for the Dhanjori volcanic rocks. The Sm-Nd isochron age obtained for the Dhanjori formation was 2787 ± 270 Ma (Misra and Johnson, 2005) (**Table. 1**). The Dalma belt consists of ultramafic-mafic volcanic rocks intercalated with sedimentary sequences. The whole-rock Rb-Sr age obtained for the Dalma felsic volcanics is 2487 ± 270 Ma whereas the Jagannathpur basalts is 2250 ± 81 Ma (Mishra and Johnson 2005). The Simlipal complex is situated at the south-eastern margin of the Singhbhum craton and mainly consists of basal quartz-pebble conglomerate, quartz rich sandstone which are overlain by the alternate successions of mafic lavas, tuffs and sandstones (Bhattacharjee et al., 2021). According to Bhattacharjee et al (2021) the maximum depositional age of Simlipal complex is ~3.08 Ga (**Table. 1**) whereas Arif et al (2021) suggested U-Pb ages from detrital zircons of the Simlipal complex ranging from 3.63 – 3.17 Ga.

Several sets of mafic dykes of Neoarchean to Palaeoproterozic age are popularly known as the 'Newer Dolerite' dyke swarm are present within the Singhbhum granitic basement rocks (Saha, 1994; Shankar et al., 2014; Srivastava et al., 2019). Shankar et al. (2014) provided 1.76 Ga Pb-Pb baddeleyite age of the dyke swarm that is trending WNW-ESE, whereas Kumar et al. (2017) provided 2.8, 2.76 and 2.75 Ga Pb-Pb baddeleyite TE-TIMS dates of the NNE-SSW to NE-SW trending dyke swarms from the Singhbhum Craton. The Neoarchean dyke swarms and the volcanic successions were dated by Adhikari et al. (2021). The yielded Sm-Nd isochron age of the Jagannathpur volcanics was 2799±67 Ma and the Keshargaria mafic dyke swarms was 2800.2 ± 0.7 Ma. All the reported geochronological information of all the lithological units from the Singhbhum Craton are tabulated in the chart below (**Table. 1**).

2.2. Geology of the Mayurbhanj Mafic Complex

The Mayurbhanj gabbro-anorthositic suite of rocks mostly occur at the south-eastern part of the Gorumahisani hill, in the Mayurbhanj district of Orissa state (insert Lat & Long) and are surrounded by the granitic rocks of the Mayurbhanj felsic suite (**Fig. 1b**). The gabbro-anorthositic suite of rocks intruded into the metavolcanic and metasedimentary rocks of the IOG supracrustal unit belonging to the Gorumahishani-Badampahar greenstone

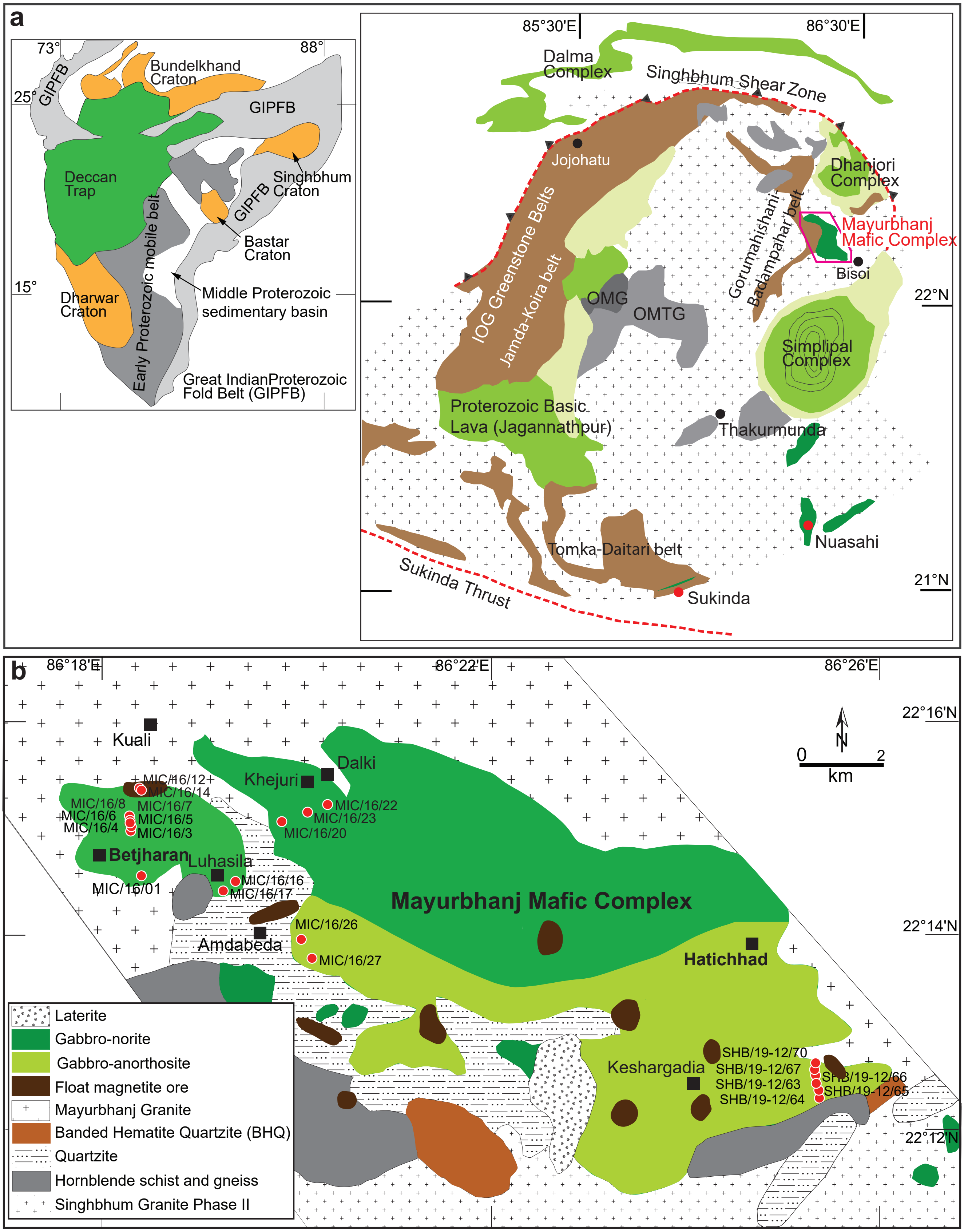

Fig. 1. (a) Geological map of the Singhbhum Craton (Compiled by Mondal et al., 2006 after Saha, 1994); Granitic Batholitic Complex; Iron Ore Group (IOG); Older Metamorphic Tonalitic Gneiss (OMTG); Older Metamorphic Group (OMG); Ultramafic-Mafic plutonic Suite; Neoarchean-Palaeoproterozoic Volcanic Sequence; Neoarchean-Palaeoproterozoic Sedimentary Sequence; **(b)** Geological map of the Mayurbhanj Complex showing the locations of samples of this study (after Das, 2014).

belt (**Fig. 1a**). The gabbro-anorthositic rocks are co-genetic to the ~3.1 Ga granitic rocks of the Mayurbhanj felsic suite (Saha, 1994). The earlier researchers (e.g., Dunn and Dey, 1942) categorized the gabbro-anorthositic suite of rocks as coeval with the mafic volcanic rocks of the IOG belonging to the Gorumahishani-Badampahar greenstone belt (**Fig. 1a**). Based on the field geology of different areas Sarkar and Saha (1962, 1963) interpreted a younger age of the mafic plutonic rocks than the granitic rocks. Saha (1994) compiled the geochronological information and classified this mafic plutonic suite of rocks from the Mayurbhanj mafic complex and the Nuasahi ultramafic-mafic complex as 'early Proterozoic gabbro-anorthositic suite' with associated V-Ti bearing ore bodies. Recently, Mondal et al. (2021) have dated the gabbro-anorthositic suite of rocks from the Mayurbhanj mafic complex by whole rock Sm-Nd methodology that yielded an Sm-Nd isoochron age of 3022 ± 180 Ma. Augé et al. (2003) obtained ~3.1 Ga U-Pb zircon age from the gabbroic matrix of the breccia zone in the Nuasahi ultramafic-mafic complex where ultramafic and chromitite fragments of the lower ultramafic unit are mantled by the pegmatitic gabbroic rocks (e.g., Mondal and Baidya, 1997; Mondal et al., 2001; Mondal and Zhou, 2010).

The mafic plutonic suite of the Mayurbhanj complex is mainly composed of gabbro-noritic rocks at the lower part followed by gabbroic-anorthosite and anorthosite, and the magnetitite bodies at the upper part of the igneous complex. The gabbro-noritic rocks are mostly present as isolated hillocks in and around Betjharan, Luhasila, Khejuri and Amdabera areas (Betjharan section) and the gabbro-anorthosites are present in and around Hatichhad area (Hatichhad section) (**Fig. 1b**). The magnetitite ore bodies occur at the upper part of the gabbro-norite-anorthositic suite of rocks. The magnetitite bodies occur as lodes, massive lenses, pockets, bands and isolated boulders and mainly concentrated in Betjharan and Hatichhad section (**Fig. 1b**). In Betjharan area the magnetitites occur as 10-320 m long massive lenses and pods within the gabbro-anorthositic rocks at the upper part of the hillock whereas in Hatichhad area the ore layer is mainly present at the top of the hillock which is 15 m wide and 350 m long with a NE-SW trend. Some field photographs are shown in **Fig. 2**.

Fig. 2. (a) Field photograph of gabbro-norite from the Betjharan section; **(b)** Field photograph of gabbro-anorthosite from the Hatichhad section; **(c)** Gabbro-norite of the Betjharan section showing modal layering (plagioclase rich and pyroxene rich modal layers); **(d)** Gabbro-anorthosite sample of the Hatichhad section; **(e)** Coarse-grained magnetitite ore from the Mayurbhanj Mafic Complex.

CHAPTER 3

METHOLOGY

3.1. Sampling and microscopic study

The samples were collected systematically from different sections of the Mayurbhanj Complex to study the variability of the gabbro-anorthositic rocks throughout the area (**Fig. 1b**). Two main sections were sampled (Betjharan and Hatichhad sections) across the overall trend of the igneous complex to identify the differentiation trend of the parental magma. In the Betjharan section (includes Betjharan-Luhasila-Khejuri-Amdabeda area) at north-western part of the complex we have collected samples from lower part of the hill to top where the magnetitite lodes are distributed (**Fig. 2a, c, e**). In the Hatichhad section (includes Keshargadia-Hatichhad area) at north-eastern part sampling has been done along a road-cutting section, running through the gabbro-anorthosite-magnetitite bodies (**Fig. 2b, d**). A total of 29 number of samples have been collected to study common rock-forming silicate, Fe-Ti oxide, and sulfide minerals to identify the spatial, as well as lithological control on their composition. All samples collected from the field were studied in hand specimen and in thin-polished sections using both transmitted and reflected light microscopes.

3.2. Analytical techniques

3.2.1. *In-situ* major and trace element analysis of minerals

Common rock-forming silicate minerals (plagioclase, pyroxene), Fe-Ti oxide grains along with sulfide minerals were analyzed using an Electron Probe Micro Analyzer (EPMA) CAMECA SXFive instrument at the Department of Geology, Banaras Hindu University (India). The CAMECA SXFive instrument was operated by SXFive Software at a voltage of 15 kV, beam size of 10 µm, and a probe current of 10 nA. Natural mineral standards fluorite, apatite, albite, halite, periclase, peridot, corundum, wollastonite, orthoclase, rutile, chromite, rhodonite, celestite, barite, hematite, crocoite, pyrite, and synthetic Ag_2Te, InAs, InSb, Ni, Co, Cu, Zn metal supplied by CAMECA-AMETEK were used for routine calibration and quantification. All the data are tabulated in **Table. 2-6.**

In-situ LA-ICPMS trace element analysis was conducted on representative magnetite and sulfide minerals using a Thermo Scientific iCAP-Q ICPMS coupled with 193 ESI Ar-F MIX Excimer laser at the LA-ICPMS laboratory of Geology and Geophysics, Indian Institute of Technology, Kharagpur (India). The samples were ablated in He atmosphere and the sample carrier gas (flow rate 0.9586 L/min) was He mixed with Ar using (Y) junction. Depending on grain size, beam diameter was varied between 30 µm and 40 µm and frequency was kept at 5 Hz. All grains were analyzed with laser energy at 4.4 J/cm^2. Analyses were performed in peak hopping mode with each analysis consisting of a 20-s background measurement with the laser turned off and a 40-s peak signal measurement with the laser turned on. Every nine point-analyses were bracketed by standard analysis. Calibration was performed using NIST610 and NIST612 glass standard and data were reduced by the Glitter© software (Griffin et al., 2008), using Fe as an internal standard. The trace element data are tabulated in **Table. 7, 8.**

3.2.2. Bulk-rock major and trace elements analysis

The whole rock analysis was done on representative n number (how many?) samples of both sections of the Mayurbhanj complex. All the samples were cleaned, crushed and pulverized to a 200-mesh size in the PGE-GEOCHEM-LAB of the Department of Geological Sciences, at Jadavpur University for bulk rock major and trace element analysis. The crushing and pulverization of the samples were carried out by single bowl RO milling systems (Model MBM 07, Insmart systems). The grinding was performed by high energy frequent collision of agate balls (99.9% SiO_2, 7.0 Mohs hardness, and 2.65 g/cc density). A quantity of 25 g sample was crushed by the machine at 600 rpm in 15 mins. The major and trace elements were analysed at the Intertek Genalysis, Maddington, Western Australia. The major element analysis was done by complete dissolution of the rock sample into a lithium borate glass. The glass melt was cast into a platinum mould which, on cooling, produced a fusion disk or glass bead. Approximately 0.7g was weighed into a platinum crucible and this was mixed with a pre-weighed amount of flux which was comprised of a mixture of lithium tetraborate and lithium metaborate. The fusion disk was analysed on a Panalytical Axios Sequential Wavelength-Dispersive X-ray Fluorescence (WD-XRF) Spectrometer. The calibration was done by standard glass beads of known composition and the corrections were made for the catch weights, instrumental drift, line overlaps and inter element enhancement / absorption matrix effects as well as moisture (done by TGA method). LOI or loss on ignition which is a part of the XRF analysis was done by using a TGA or Thermo Gravimetric Analyzer. An analysis of hygroscopic water or H_2O^- is normally not considered part of the analysis as this can vary with the atmospheric humidity therefore all XRF results are reported moisture free. LOI involves the mass loss or gain (negative LOI) on heating a sample to 1000°C. LOI is a complex oxidation/ de volatilization reaction where reduces species are oxidized and volatile components expelled. At first the instrument weighed the inert crucible and after that approximately 1gm of sample was added to the crucible and weighed the crucible and sample. The mass of the sample taken was determined by the difference. The sample was then heated to constant mass at 105°C and weighed. The mass lost as a fraction of the mass taken was the moisture. The sample was then heated to constant mass at 1000°C and weighed and the mass lost as a fraction of the dry mass was the loss on ignition or LOI.

The whole rock trace element including the REE analysis were performed by using Agilent 7700 ICPMS. Since acid digestions cannot guarantee the digestion of an entire sample as certain refractory minerals may remain undissolved. Therefore, the fusion digestions have been conducted to ensure the complete dissolution of the sample including the refractory mineral component. Rare earth elements, Ta, Nb, Zr, Hf, U and Th are commonly hosted in refractory minerals. The sample was weighed at 0.20gm and mixed with a borate flux which was a mixture of lithium tetra and meta borates, and placed in a platinum crucible. The mixture was fused in a muffle at 1000°C and the fusion product was dissolved in acid and accurately volumed in the instrument.

The base metals and some trace elements were analysed by Four Acid Digestion method in a 7900 ICPMS. This procedure involves the use of a mixture of acids ($HClO_4$, HNO_3, HF and HCl) to dissolve most oxide, sulphide, carbonate and silicate mineral species. After digestion those samples formed soluble perchlorates which easily dissolved in HCl. Some refractory minerals partially dissolve in this method and some volatile elements may be partially lost in the process e.g., Cr and Ge. The pulped samples were weighed at 0.20g ± 0.02gm into a Teflon tube. The tube was placed in a rack and the digesting acids were added sequentially with nitric acid pre-oxidation of sulphides. The rack was placed on a “hot block” which provided even heat to decompose the sample and ensured maximum dissolution. The perchloric ($HClO_4$) acid was evaporated and the residue was leached by boiling in HCl. The solution was transferred to a polystyrene tube where it was volumed and mixed. A further dilution of the digest solution was required before reading on the Agilent 7900 ICPMS with collision cell technology. Calibration was done by using solution standards of known concertation. The major and trace element data are tabulated in **Table. 9**.

3.2.3. Whole rock Sm-Nd isotope analysis

Bulk rock Sm-Nd isotopic analysis was performed at the Centre de Recherches Pétrographiques et Géochimiques in Nancy, France. Before digestion, a mixed $^{147}Sm/^{150}Nd$

isotopic tracer was added to each powdered sample and each analytical blank to allow Sm and Nd concentrations to be determined by isotope dilution. The mass of samples varied between ~30 and 100 mg depending on the Nd concentration previously determined by ICPMS. The bulk powders were dissolved by adding 1.5 mL of concentrated HF and 1.5 mL of concentrated HNO_3, and heating for 3 days at 120°C. After that, the samples were dried down and heated again for 2 days after the addition of 3 ml 6N HCl. To verify the digestion efficiency, duplicates of four samples with high Zr contents were dissolved in PTFE/TFM BOLA bombs and in these cases, 1 ml each of concentrated HF and HNO_3 were added and samples were heated for 8 days at 150°C in an oven, followed by drying and reheating in 5ml 6N HCl. Nd and Sm were separated using procedures adapted from Pin and Zalduegui (1997) including two chromatographic column steps, the first using Eichrom TRU Spec resin to extract the REE from the matrix and the second using Eichrom LN Spec to isolate Nd and Sm. The resulted solutions were analyzed using the Thermo-Scientific Neptune MC-ICPMS instrument at the CRPG laboratory. Instrumental mass fractionation was corrected using an exponential law and assuming $^{146}Nd/^{144}Nd = 0.7219$. Liquid standard JNdi (Tanaka et al., 2000) was analyzed after every third sample, yielding a mean value for $^{143}Nd/^{144}Nd$ of 0.512097 ± 0.000010 (2σ, n=16). As this value is slightly lower than the nominal value of 0.512115 proposed by Tanaka et al. (2000) for this standard, a correction of +0.000018 is included in each value to facilitate comparison with literature data. Two total chemistry blanks analyzed with the samples yielded 23 and 38 pg for Nd, and 28 and 36 pg for Sm. These values are negligible relative to the quantities of Nd (>120 ng) and Sm (>40 ng) measured in the samples.

CHAPTER 4

RESULTS

4.1. Petrography

The mafic plutonic rocks are gabbro-noritic in the Betjharan section (**Fig. 2a, c**) and gabbroic anorthosite in the Hatichhad section (**Fig. 2b, d**). The gabbro-norites are coarse-grained mesocratic rocks where pyroxene and feldspar are the main minerals and Fe-oxide and sulfide minerals are present as disseminated phases. The gabbro-noritic rocks show modal layering in terms of variation of modal abundances of plagioclase and pyroxene minerals (**Fig.2a, c**). The gabbro-noritic suite of rocks are predominantly composed of plagioclase (~50 modal %), clinopyroxene (~25 modal %), and orthopyroxene (~15 modal %) as major cumulus phases with Fe-Ti-oxide minerals as accessory phase (< 2 modal %), and sulfide minerals as disseminated phases (**Fig. 3a**). Gabbro-noritic rocks are mostly showing cumulate textures however ophitic and subophitic textures are also present (**Fig. 3b**). Plagioclase grains show sericitization and at a few places show lamellar twinning. Among pyroxenes, hypersthene is the main orthopyroxene whereas brownish augite and diopside are the major clinopyroxene grains. Augites are mostly prismatic in shape whereas diopsides are present as anhedral grains. Many clinopyroxenes are commonly altered to actinolite along the cleavage and boundary of the grains. Biotite and chlorite are present in small amounts in the altered parts of the rocks. Apatite is present in a very small amount along with plagioclase and orthopyroxene grains.

In the gabbro-noritic suite of rocks magnetite, titanomagnetite and ilmenite constitute the oxide phases (~8 modal %), and sulfide phases (<2 modal %) include pyrite, chalcopyrite and pyrrhotite. The accessory Fe-Ti oxide phases show variable sizes (50-700 µm) in the gabbroic rocks. Relatively larger grains of primary oxide minerals are commonly present in the interstitial spaces of pyroxene and plagioclase grains (**Fig. 3c, d**). The secondary oxide minerals of relatively smaller sizes are poikilitically included within

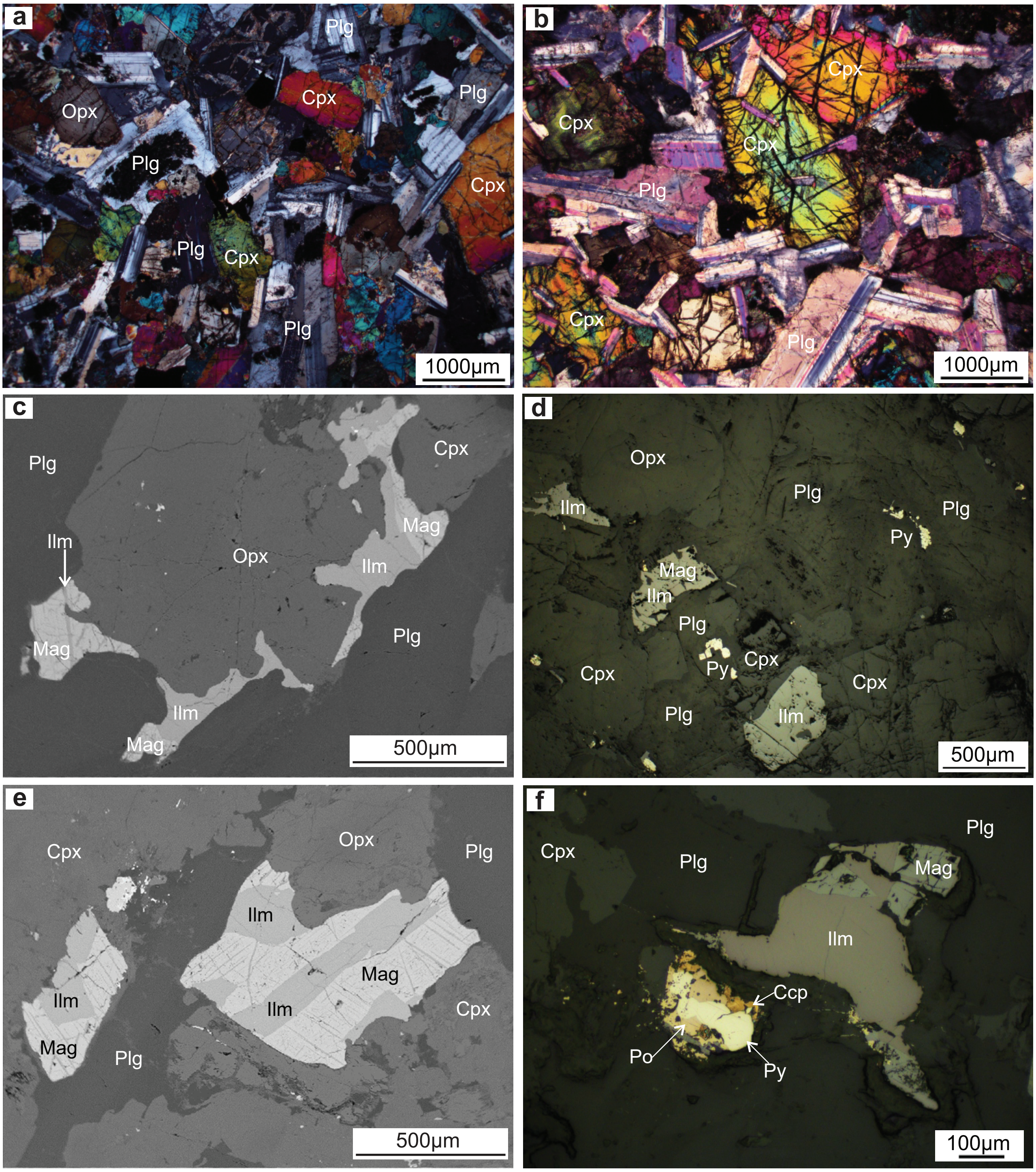

Fig. 3. Photomicrographs of the gabbro-norite from the Betjharan section: **(a)** cumulate texture (crossed polars); **(b)** ophitic, subophitic texture (crossed polars); **(c)** Back Scattered Electron (BSE) image showing Fe-Ti oxide grains occupying the interstitial spaces between pyroxene and plagioclase; **(d)** Fe-Ti oxides and base metal sulfides are present as disseminated phases in gabbro (reflected light, air); **(e)** Back Scattered Electron (BSE) image of magnetite with sandwich laths and thin lamellae of ilmenite within gabbro; **(f)** Photomicrograph showing granular exsolution of ilmenite within magnetite grain and pyrite-chalcopyrite-pyrrhotite assemblage near the grain boundary of oxide (reflected light, air); **(g)** Back Scattered Electron (BSE) image of magnetite and ilmenite where ilmenite is present as isolated grains; **(h)** Large distinct crystal of pyrite showing prominent two sets cleavages. Fe-oxide grains are present along the grain boundary of pyrite (reflected light, air); **(i)** Polycrystalline aggregates of pyrite showing ribbon-texture within plagioclase host (reflected light, air); **(j)** Pyrite grains showing spongy texture (reflected light, air); **(k)** Pyrite along with pyrrhotite and chalcopyrite are included within silicate minerals (reflected light, air); **(l)** Pyrite grains are present in the interstitial spaces of silicate minerals (reflected light, air); **(m)** Back Scattered Electron (BSE) image showing magnetite present as a rim around sulfide assemblages (pyrite-pyrrhotite-chalcopyrite); **(n)** Back Scattered Electron (BSE) image of sulfide minerals (mainly pyrite) present along the fractures of pyroxene. [Py = pyrite; Po = pyrrhotite; Ccp = chalcopyrite; Mag = magnetite; Ilm = ilmenite; Plg = plagioclase; Cpx = clinopyroxene; Opx = orthopyroxene]. Mineral name abbreviation after Whitney and Evans (2010).

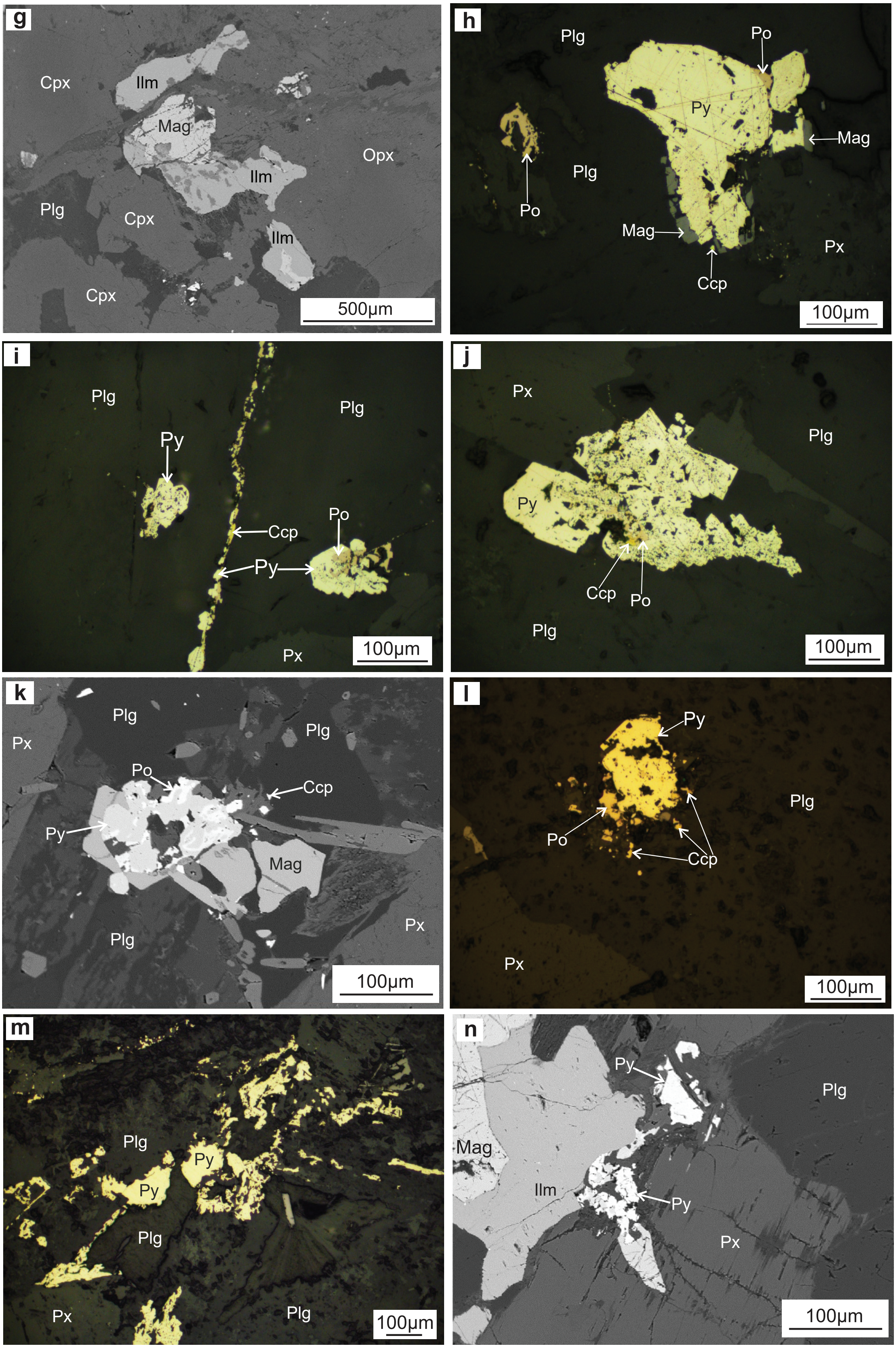

Fig. 3. continued.

pyroxene and plagioclase grains (**Fig. 3e**). In major areas within magnetite-titanomagnetite grains ilmenites are present as thick elongated lath-shaped exsolution lamellae (**Fig. 3e**), and at places, ilmenite occurs as thin lamellae within the host magnetite-titanomagnetites (**Fig. 3c, e**). The thick exsolution of ilmenites occur in small numbers, and an independent elongated grain is the most common form having sharply defined contacts with the associated titanomagnetite grains. At places, ilmenite is present as granule-exsolution defined by euhedral to anhedral exsolution of ilmenite within magnetite-titanomagnetite (**Fig. 3f, g**) and also as single isolated grains (**Fig. 3g**).

Among the sulfide minerals, pyrite is the most abundant phase in the gabbro-noritic rocks. Pyrrhotite and chalcopyrite minerals are associated with pyrite grains. The modal proportion of sulfide minerals vary widely from one sample to another (<1 to 1 modal %). Some pyrite grains are showing prominent two sets of cleavages (**Fig. 3h**). In most cases, pyrite forms small (a few microns) to large (several millimeters) anhedral grains and is associated with pyrrhotite and chalcopyrite (**Fig. 3i**). At places, smaller grains of sulfide minerals are present as inclusions within the altered zones of the primary silicate minerals. Euhedral pyrite grains of variable sizes are present as clusters at the interstitial spaces of primary silicate minerals (**Fig. 3d**). Pyrite grains at some places form polycrystalline aggregates having ribbon-like textures (**Fig. 3i**). At places pyrites occur as irregular grains with spongy texture within a silicate host (**Fig. 3j**). Sulfide minerals are commonly associated with Fe-Ti oxide grains, mostly along the boundary zones of the latter (**Fig. 3k**). A few pyrite grains are included within the silicate minerals (**Fig. 3l**), and at places are present along the fracture zones of the rocks (**Fig. 3m, n**). Pyrrhotite grains are commonly present along the grain boundaries as well as within the pyrite grains (**Fig. 3h, i, j, k, l**). Chalcopyrite is present in a few samples, randomly dispersed between pyrrhotite and pyrite grains, and occurs as a minor phase (**Fig. 3h, I, j, k, l**). There are very smaller grains of chalcopyrite that commonly occur within altered parts of silicate minerals (amphibole).

The Hatichhad section of the Mayurbhanj Complex is mainly comprised of gabbroic anorthosite, anorthosite and magnetitite (**Fig. 1b, 2d, e**). The anorthosites from the Hatichhad section is medium grained and composed of plagioclase (~90 modal %) as cumulus grains, clinopyroxene (~5 modal %), and Fe-Ti oxides (~2 modal %) as intercumulus phases (**Fig. 4a, b**). The rocks are extensively altered; Plagioclase grains are altered to saussurite as well as sericite in major areas (**Fig. 4a**). Chlorite is present as secondary silicate mineral after primary plagioclase in most of the places (**Fig. 4b**). The gabbroic-anorthosite of the Hatichhad section shows cumulate texture with plagioclase and pyroxene as cumulus phases (**Fig. 4c**). The large Fe-Ti oxide minerals are present within the interstitial spaces of pyroxene and plagioclase grains (**Fig. 4c, d**) and the smaller oxide grains are present as inclusion within clinopyroxene grains (**Fig. 4c**). In a few samples clinopyroxene grains are altered to chlorite and amphibole along grain boundaries due to alteration effect (**Fig. 4e**). Within few orthopyroxene grains exsolved clinopyroxene lamellae are present (**Fig. 4c**). Magnetite and ilmenite are the main constituent mineral phases in the Fe-Ti oxides. Ilmenite is present as exsolved lamellae within the host magnetite grains in the gabbroic anorthosites (**Fig. 4d**). In a few places ilmenite is present as exsolved phase along the inner grain boundary of host magnetite grains (**Fig. 4f**). The proportion of oxide minerals is low in the gabbroic-anorthosites of the Hathichad section than the Betjharan section. Sulfide minerals are negligible within the gabbro-anorthositic suites of the Hatichhad section.

Magnetite-titanomagnetites are the major phases in the magnetitite ores showing cumulate texture. The cumulus magnetite-titanomagnetite grains are almost euhedral in shape with polygonal outlines (**Fig. 5a**). Fine lamellae of ilmenite radiating from cracks and

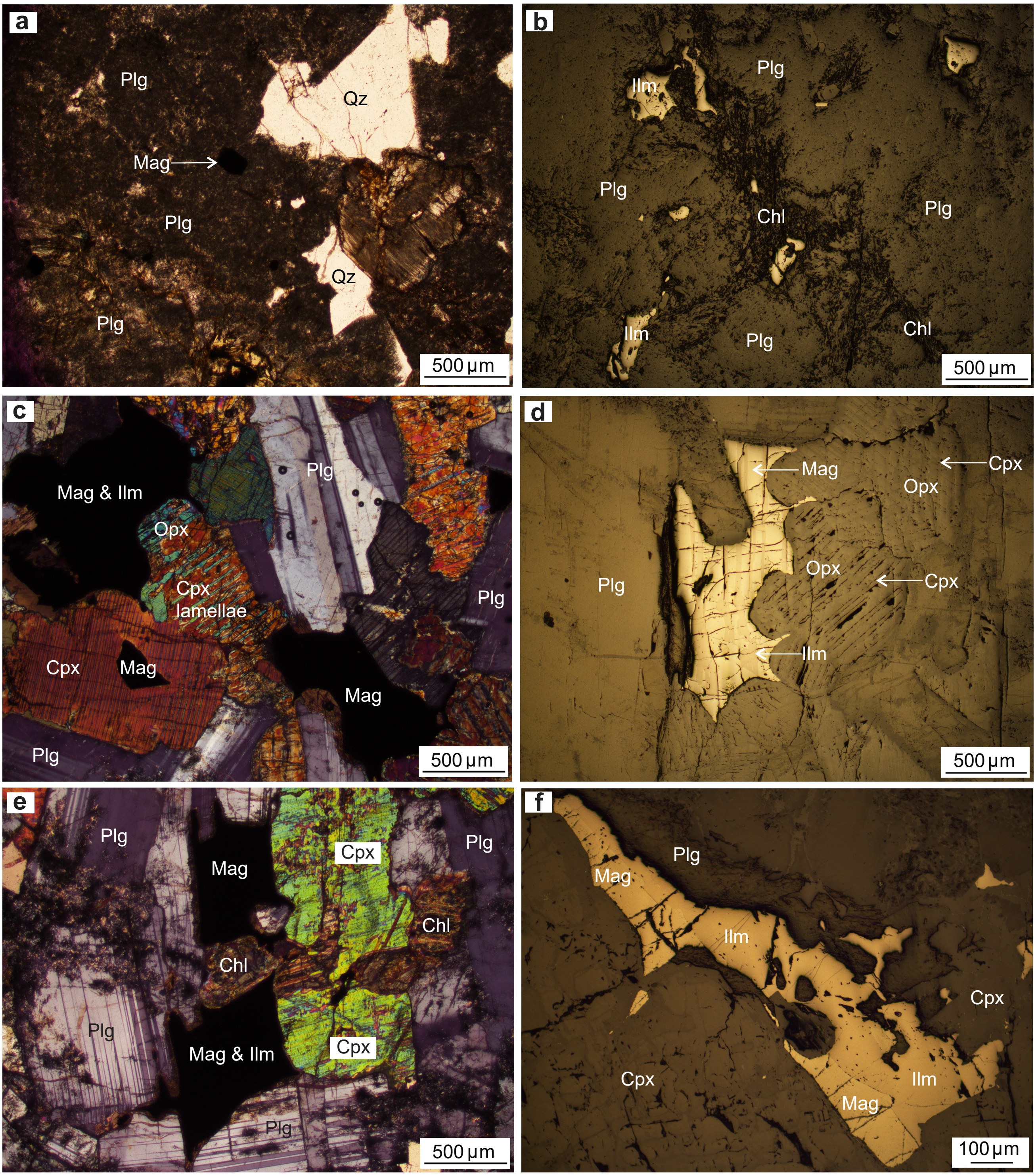

Fig. 4. Photomicrographs of the gabbro-anorthosite from the Hatichhad section: **(a)** Anorthosite showing cumulus plagioclase and pyroxene grains with quartz grains (plain polars); **(b)** Fe-Ti oxide minerals (ilmenite) present within interstitial spaces between plagioclase (reflected light, air); **(c)** Gabbro showing cumulate texture (crossed polars). Large Fe-Ti oxide grains present within interstitial spaces between plagioclase and pyroxene and small Fe-Ti oxide grains present as inclusion within pyroxene; **(d)** Interstitial magnetite grains having exsolution of ilmenite (reflected light, air); **(e)** Plagioclase and pyroxene grains altered to chlorite along fractures (crossed polars); **(f)** Exsolution of ilmenite along grain boundary of host magnetite grain. [Mag = magnetite; Ilm = ilmenite; Plg = plagioclase; Cpx = clinopyroxene; Opx = orthopyroxene].

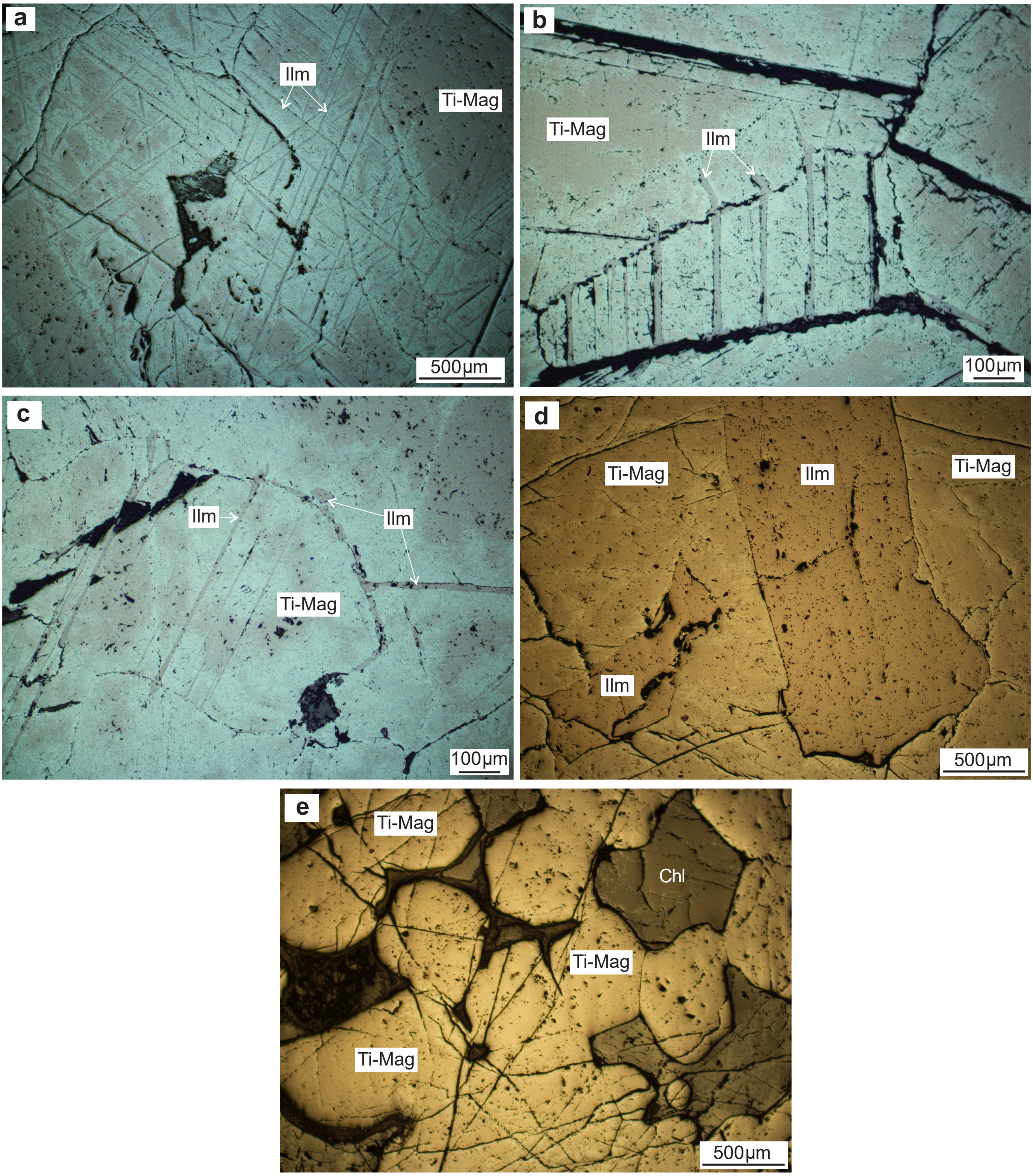

Fig. 5. Photomicrographs of magnetitite ore under reflected light (air): **(a)** Trellis intergrowth of ilmenite within titanomagnetite host (Betjharan section); **(b)** Thick ilmenite lamellae within titanomagnetite: thickness increases towards grain boundary of host titanomagnetite grain (Betjharan section); **(c)** External granules of ilmenite present as a chain-like body along the grain boundaries of titano-magnetites (Betjharan section); **(d)** Single ilmenite grain showing equilibrium assemblage with the surrounding magnetite grains (Hatichhad section); **(e)** Secondary silicate minerals (chlorite) present within interstitial spaces of titanomagnetite grains (Hatichhad section). [Mag = magnetite; Ilm = ilmenite; Ti-Mag = titanomagnetite; Chl = chlorite].

boundaries in titanomagnetite crystals form the trellis intergrowth (**Fig. 5a**) which was developed due to oxidation (Widmanstatten texture; e.g., Haggerty, 1991). The size and abundance of ilmenite exsolution lamellae increase towards the grain boundaries (**Fig. 5b**). Ilmenite lamellae that project into the titanomagnetite grains are sharply tapered and gradually disappear, on a microscopic scale, as the unoxidized areas are approached (**Fig. 5c**). There are significant changes in color, reflectivity and in the composition of the oxidized titanomagnetite: the mineral becomes whiter with an increase in reflectivity (**Fig. 5b, c**). This is due to oxidation of iron in titanomagnetite while diffusion of Ti from the host to form the exsolution of ilmenite. As a consequence, the ratios of Fe:Ti and Fe^{3}:Fe^{2+} should increase in the oxidized areas (e.g., Haggerty, 1991). The external granular ilmenites occur as small chain-like, elongated optically continuous grains along the grain boundaries of the magnetite-titanomagnetite (**Fig. 5c**). The coarse lamellae become broader at the meeting point with external granular ilmenite (**Fig. 5c**). At few places ilmenite is present as single grain in equilibrium assemblage with titanomagnetite grains (**Fig. 5d**). Within the magnetitite secondary silicate minerals (e.g., chlorite, epidote) are present in the intercumulus spaces of the magnetite grains (**Fig. 5e**). Sulfide minerals are absent in the magnetitite ores either in the hand specimens or under the microscope (reflected light), and it appears that these are devoid of any sulfide mineralization.

4.2. Chemical composition of silicate, Fe-Ti oxide and sulfide minerals

The composition of plagioclase in gabbro-noritic rocks from the Betjharan section ranges from andesine (An_{32-50}) to labradorite (An_{50-69}) with occasional oligoclase (An_{25-29}) variety (**Fig. 6a**) (**Table. 2**). The large compositional variation of plagioclase probably linked to the post-magmatic hydrothermal alteration of the assemblage. Both clinopyroxene and orthopyroxene are present in the gabbro-norite of the lower part. Compositionally

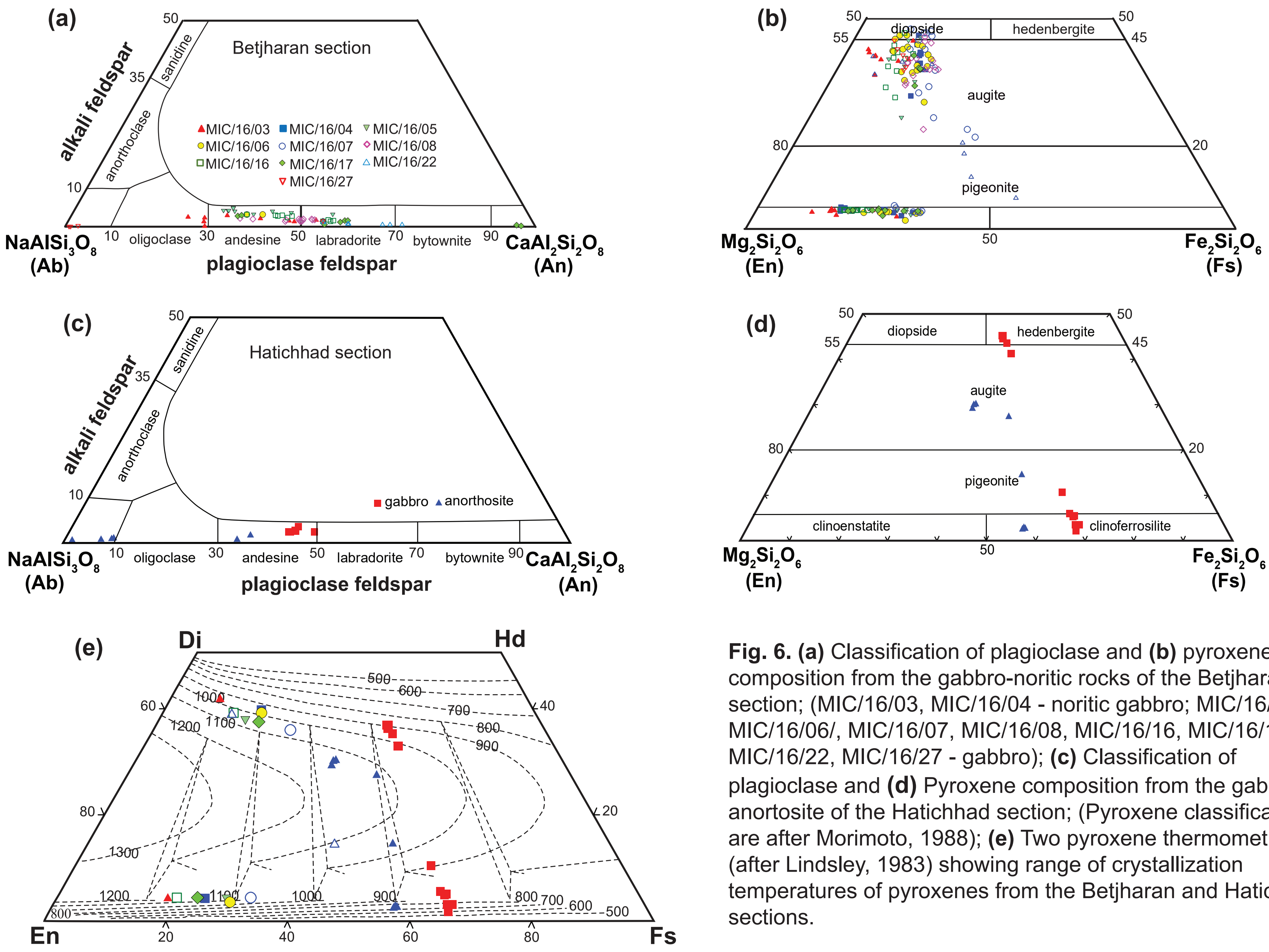

Fig. 6. (a) Classification of plagioclase and **(b)** pyroxene composition from the gabbro-noritic rocks of the Betjharan section; (MIC/16/03, MIC/16/04 - noritic gabbro; MIC/16/05, MIC/16/06/, MIC/16/07, MIC/16/08, MIC/16/16, MIC/16/17, MIC/16/22, MIC/16/27 - gabbro); **(c)** Classification of plagioclase and **(d)** Pyroxene composition from the gabbro-anortosite of the Hatichhad section; (Pyroxene classifications are after Morimoto, 1988); **(e)** Two pyroxene thermometry (after Lindsley, 1983) showing range of crystallization temperatures of pyroxenes from the Betjharan and Hatichhad sections.

clinopyroxene grains are mainly diopside and augite with minor pigeonite variety ($En_{42}Fs_{36}Wo_{22}$ to $En_{54}Fs_{4}Wo_{42}$) (**Fig. 6b**). Orthopyroxenes have compositions between bronzite and hypersthene. The compositions of orthopyroxenes range from $En_{67}Fs_{28}Wo_{5}$ to $En_{81}Fs_{15}Wo_{4}$ (**Fig. 6b**). The Mg-number [100*Mg/(Mg+Fe^{2+})] of clinopyroxene varies between 64.1 and 90.4 (**Table. 3**). The Al_2O_3 content of pyroxenes ranges between 0.40 and 3.31 wt. %, whereas TiO_2 content reaches up to 0.73 wt. %. The Cr_2O_3 concentration in clinopyroxene is reported up to 0.55 wt. %, which is higher than the orthopyroxene. The Cr_2O_3, Al_2O_3, K_2O, and CaO concentrations in clinopyroxene define an overall positive trend with Mg# (**Fig. 7a, b, e, f**) whereas TiO_2 and Na_2O show a weak negative trend (**Fig. 7c, d**). The correlation of Cr_2O_3 contents in clinopyroxene with Mg# is due to the strong preference of Cr towards pyroxene over melt with the onset of pyroxene crystallization (Dick et al., 2002; 2010). The steep negative correlation of TiO_2 content of clinopyroxene with Mg# reflects the preference of Ti for the melt phase during crystallization of pyroxene along with plagioclase (Dick et al., 2002; 2010).

The plagioclase composition of the gabbro-anorthositic to anorthositic rocks of the Hatichhad section is dominantly andesine (An_{34-49}) with few albite (An_{1-9}) variety (**Fig. 6c**) (**Table. 2**). Presence of minor albitic plagioclase probably linked to the post-magmatic hydrothermal alteration of the assemblage. Among pyroxene minerals clinopyroxene is the main phase and orthopyroxene is present in very minor quantity. The composition of clinopyroxene ranges from hedenbergite to augite ($En_{24-38}Fs_{31-49}Wo_{14-44}$) and the orthopyroxene grains are mainly clinoferrosilite in composition ($En_{24-38}Fs_{31-49}Wo_{14-44}$) (**Fig. 6d**). The Mg-number [100*Mg/(Mg+Fe^{2+})] of clinopyroxene varies from 39.8 to 53.5 (**Table. 3**). The TiO_2 content of pyroxene ranges from 0.02 - 0.3 wt. %, whereas Al_2O_3 content varies between 0.2 - 3.0 wt. %. The V_2O_3 and Cr_2O_3 content reach up to 0.06 wt. % and 0.1 wt. %.

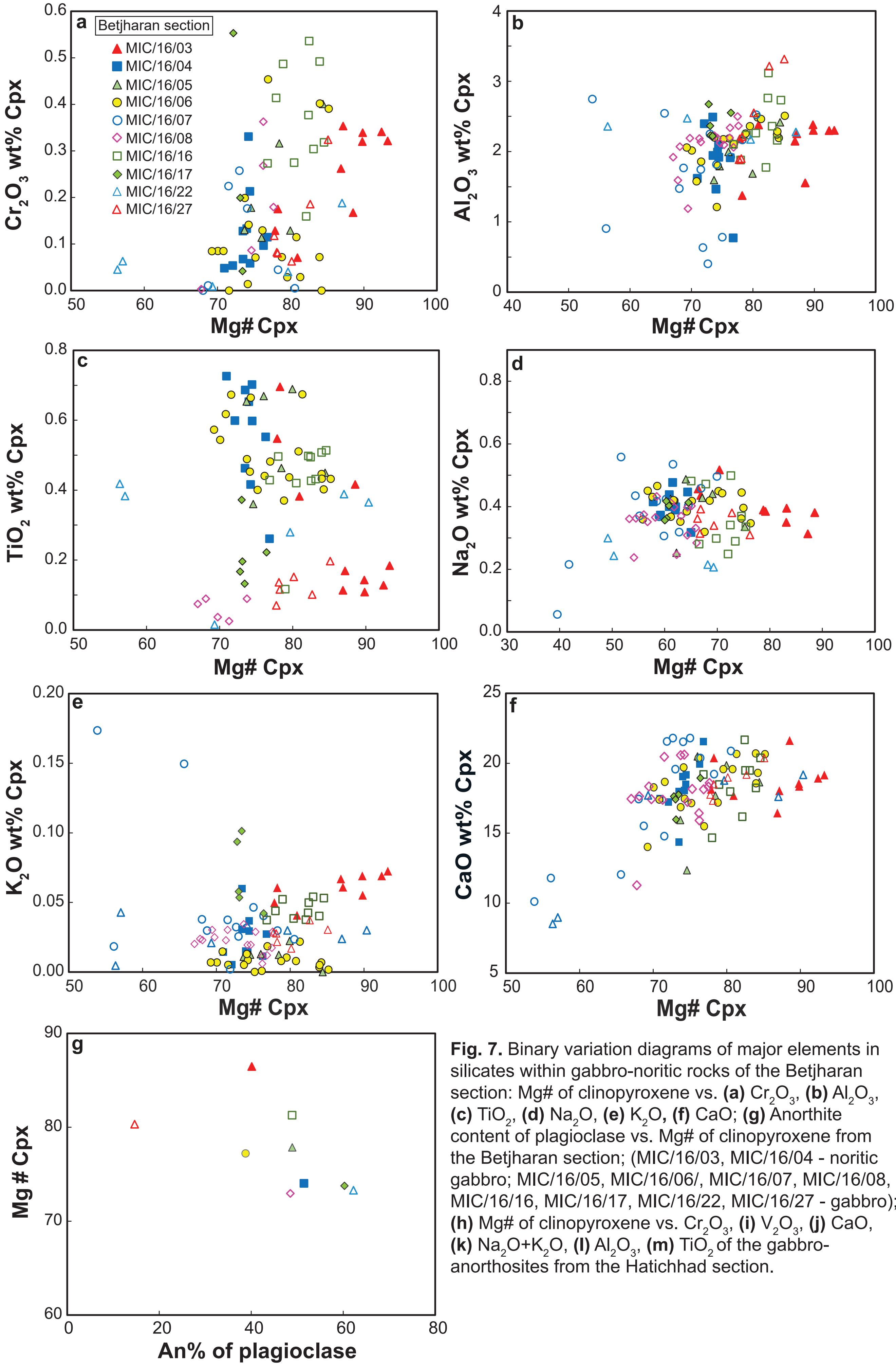

Fig. 7. Binary variation diagrams of major elements in silicates within gabbro-noritic rocks of the Betjharan section: Mg# of clinopyroxene vs. **(a)** Cr_2O_3, **(b)** Al_2O_3, **(c)** TiO_2, **(d)** Na_2O, **(e)** K_2O, **(f)** CaO; **(g)** Anorthite content of plagioclase vs. Mg# of clinopyroxene from the Betjharan section; (MIC/16/03, MIC/16/04 - noritic gabbro; MIC/16/05, MIC/16/06/, MIC/16/07, MIC/16/08, MIC/16/16, MIC/16/17, MIC/16/22, MIC/16/27 - gabbro); **(h)** Mg# of clinopyroxene vs. Cr_2O_3, **(i)** V_2O_3, **(j)** CaO, **(k)** Na_2O+K_2O, **(l)** Al_2O_3, **(m)** TiO_2 of the gabbro-anorthosites from the Hatichhad section.

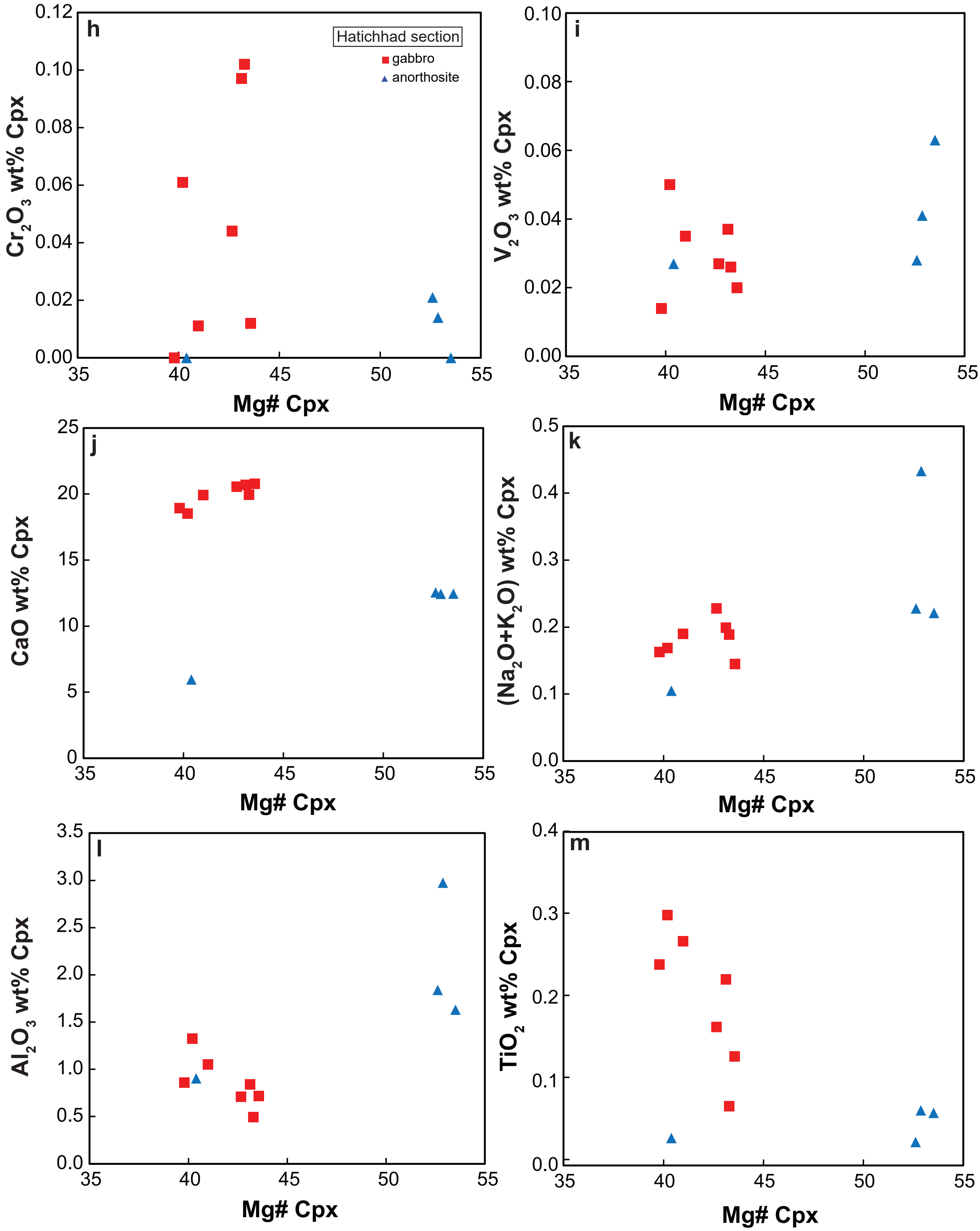

Fig. 7. continued.

The concentration of V_2O_3 and Cr_2O_3 is higher in the clinopyroxene grains than in the orthopyroxene grains. The TiO_2 and Cr_2O_3 content are higher in the clinopyroxene grains of the gabbro-anorthosite than in the clinopyroxene of the anorthosite. The Cr_2O_3, V_2O_3, CaO, and (Na_2O+K_2O) define poor positive trend with the Mg# (**Fig. 7h, i, j, k**), whereas Al_2O_3 and TiO_2 define an overall negative trend with the Mg# of the clinopyroxene (**Fig. 7l, m**).

The FeO-Fe_2O_3-TiO_2 plots show the compositional range of oxide minerals from the gabbro-norites, gabbroic-anorthosites and magnetitites (**Fig. 8a, f**). In the Betjharan section, the gabbro-norite and magnetitite ores have magnetite, titanomagnetite and ilmenite grains. Magnetites have Fe_2O_3 in the range of 17.59 - 67.66 wt. %, FeO = 23.7 - 50.46 wt. %, TiO_2 = 0.02 - 25.26 wt. % (**Table. 4**) and ilmenites have TiO_2 = 39.9 - 51.6 wt. %, FeO = 31.23 - 45.18 wt. %, Fe_2O_3 = 1.35 - 28.29 wt. % (**Table. 5**). Magnetite-titanomagnetite grains in magnetitite ores have higher MgO (1.07 - 2.73 wt. %) than those in the gabbro-norite (**Table. 4; Fig. 8b**). The accessory magnetite-titanomagnetite grains in the gabbro-noritic suite of rocks have Cr_2O_3 = 0.03 - 4.33 wt. % and Al_2O_3 = 0.01 - 7.07 wt. % (**Table. 4**). The Al_2O_3 contents of the magnetite-titanomagnetite grains within the magnetitite ores are considerably higher (~10 wt. %) than those of accessory grains in the gabbro-noritic rocks (**Table. 4**). The Cr_2O_3 content vs. TiO_2 (**Fig. 8c**) and Al_2O_3 plots (**Fig. 8d**) of both accessory and cumulus magnetite-titanomagnetites show negative correlations and a positive correlation with Fe_2O_3 content (**Fig. 8e**). In the Hatichhad section, the accessory magnetite of the gabbroic-anorthosites have Fe_2O_3 = 37.75 - 64.63 wt. %, FeO = 30.52 - 43.33 wt. %, TiO_2 = 1.17 - 14.78 wt. % whereas ilmenite grains have TiO_2 = 48.82 - 53.33 wt. %, FeO = 41.81 - 45.37 wt. % and Fe_2O_3 = 6.68 wt. % (**Table. 4** and **5**). In the magnetites of the magnetitite ores, Fe_2O_3 = 21.45 - 39.84 wt. %, FeO = 34.10 - 49.51 wt. %, TiO_2 = 17.02 - 21.64 wt. % and ilmenites have TiO_2 = 51.90 - 52.57 wt. %, FeO = 44.46 - 44.71 wt. % and Fe_2O_3 = 0.10 – 0.77

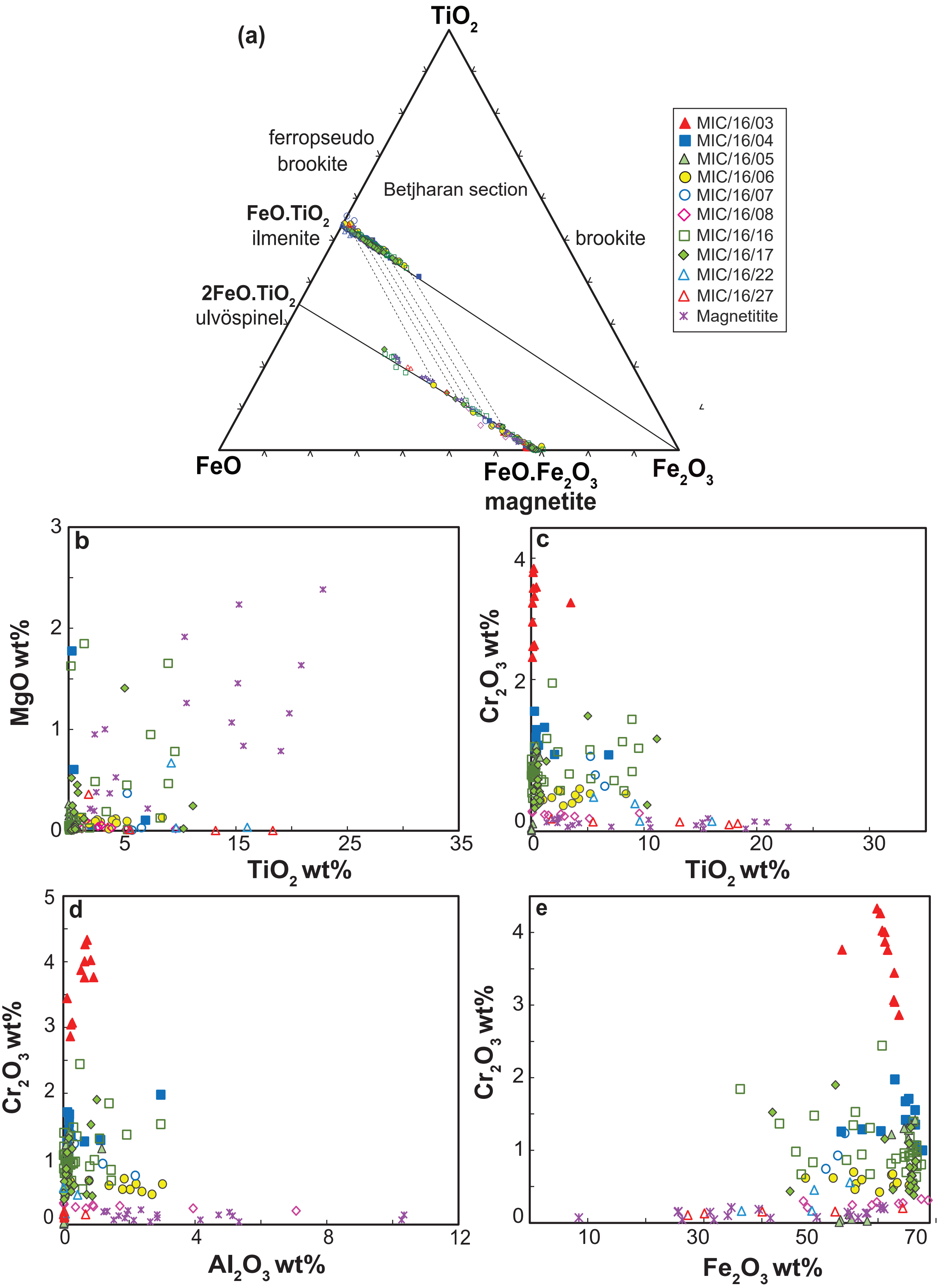

Fig. 8. **(a)** FeO-Fe_2O_3-TiO_2 ternary plot showing composition of Fe-Ti oxide of the Betjharan section (after Parat et al., 2005); (MIC/16/03, MIC/16/04 - noritic gabbro; MIC/16/05, MIC/16/06, MIC/16/07, MIC/16/08, MIC/16/16, MIC/16/17, MIC/16/22, MIC/16/27 - anorthositic gabbro);**(b)** TiO_2 vs MgO; **(c)** TiO_2 vs Cr_2O_3; **(d)** Al_2O_3 vs Cr_2O_3 and **(e)** Fe_2O_3 vs Cr_2O_3 plots of magnetite compositions from the Betjharan section; **(f)** FeO-Fe_2O_3-TiO_2 ternary plot showing composition of Fe-Ti oxide of the Hatichhad section; **(g)** Fe_2O_3 vs Cr_2O_3; **(h)** Fe_2O_3 vs V_2O_3; **(i)** Fe_2O_3 vs Al_2O_3; **(j)** Fe_2O_3 vs TiO_2 plots of magnetite compositions from the Hatichhad section; **(k)** Geothermometry and oxygen fugacity calculation for coexisting magnetite-ilmenite pairs from the Betjharan and **(l)** Hatichhad section.

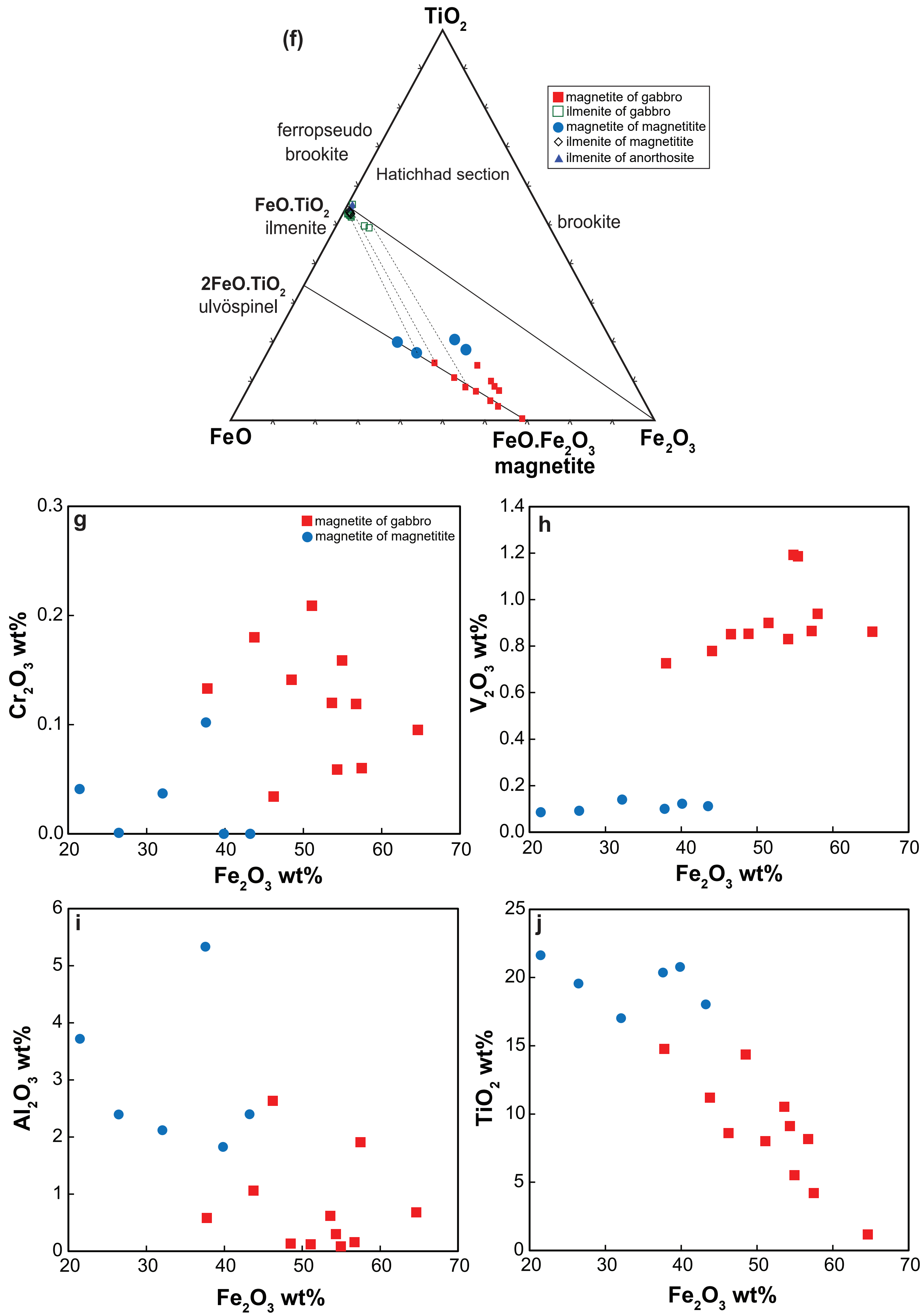

Fig. 8. continued.

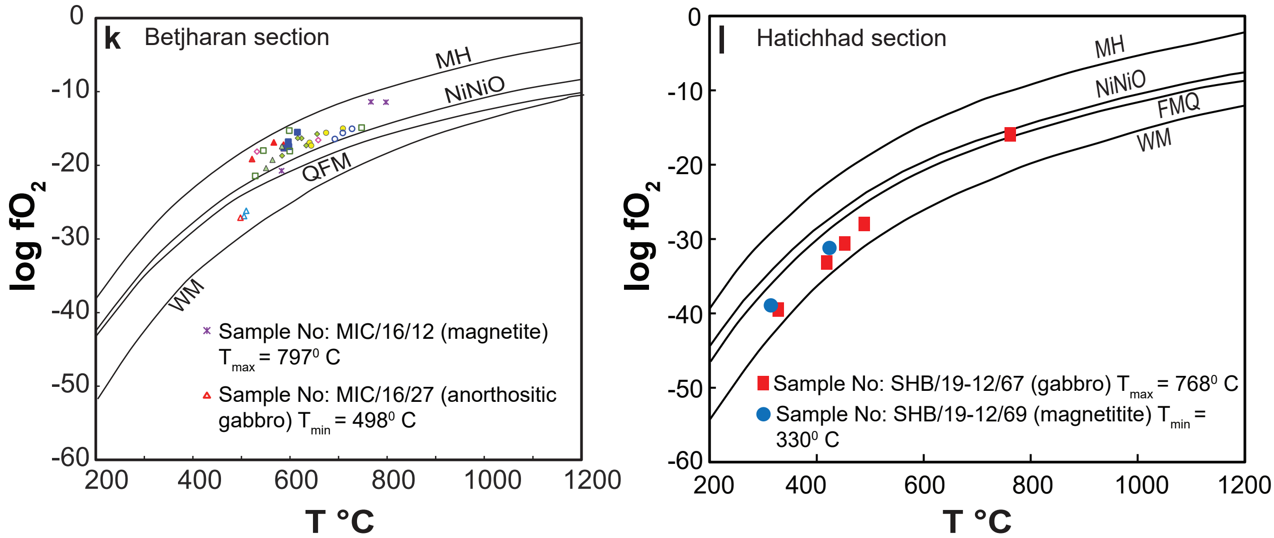

Fig. 8. continued.

wt. % (**Table. 4** and **5**). The accessory magnetite grains of the gabbroic-anorthosite have higher Cr_2O_3 (0.03 - 0.21 wt. %) and V_2O_3 (0.73 - 1.19 wt. %) and lower Al_2O_3 (0.09 - 2.64 wt. %) and TiO_2 (1.17 - 14.78 wt. %) than the cumulus magnetite of the magnetitites (**Table. 4**; **Fig. 8g, h, I, j**). The Fe_2O_3 vs. Cr_2O_3 and V_2O_3 show positive correlations (**Fig. 8g, h**) whereas Al_2O_3 and TiO_2 show negative correlation with Fe_2O_3 (**Fig. 8i, j**) for both accessory and cumulus magnetite of the gabbroic-anorthosite and magnetitite, respectively.

Among the sulfide minerals pyrite, chalcopyrite and pyrrhotite are the main sulfide phases along with minor pentlandite which are present in the gabbro-noritic rocks of the Betjharan section. The compositional data for the Fe-Ni-bearing sulfides are plotted in the Fe-Ni-S ternary diagram of Kullerud et al. (1969) (**Fig. 9a**). Pyrrhotite compositions show restricted variation whereas pyrite grains show a wider variation along the Fe-S join (**Fig. 9a**). Pyrites have Fe = 43.96 - 47.08 wt. % and S = 52.07 - 53.79 wt. % with Ni = 0.01 - 1.47 wt. % and Co = 0.01 - 1.98 wt. % (**Table. 6**). Pyrrhotites have Fe = 53.23 - 59.54 wt. % and S = 39.09 - 41.86 wt. % with Ni = 0.08 - 5.83 wt. %, Co = 0.01 - 0.29 wt. % (**Table. 6**). Pentlandite grains contain Fe = 24.60 - 31.12 wt. %, S = 32.44 - 33.06 wt. % and Ni = 35.23 - 42.04 wt. %. The compositional data for Cu-Fe-bearing sulfides are plotted in the Cu-Fe-S ternary diagram of Craig and Scott (1974) (**Fig. 9b**). Chalcopyrite grains have Fe = 29.89 - 36.46 wt. %, Cu = 19.13 - 35.7 wt. % and S = 33.55 - 44.42 wt. % (**Table. 6**). The gabbro-anorthositic rocks of the Hatichhad section have a negligible amount of sulfide minerals and the magnetitite ores are devoid of any sulfide mineralization.

4.3. Trace elements of Fe-Ti oxide and sulfide minerals:

In situ trace-element analysis of the Fe-Ti-oxide minerals from gabbro-norite and magnetitite of the Betjharan section show wide variation in trace element concentration (**Table. 7**). To compare the variation in trace elements in magnetite, titanomagnetite, and

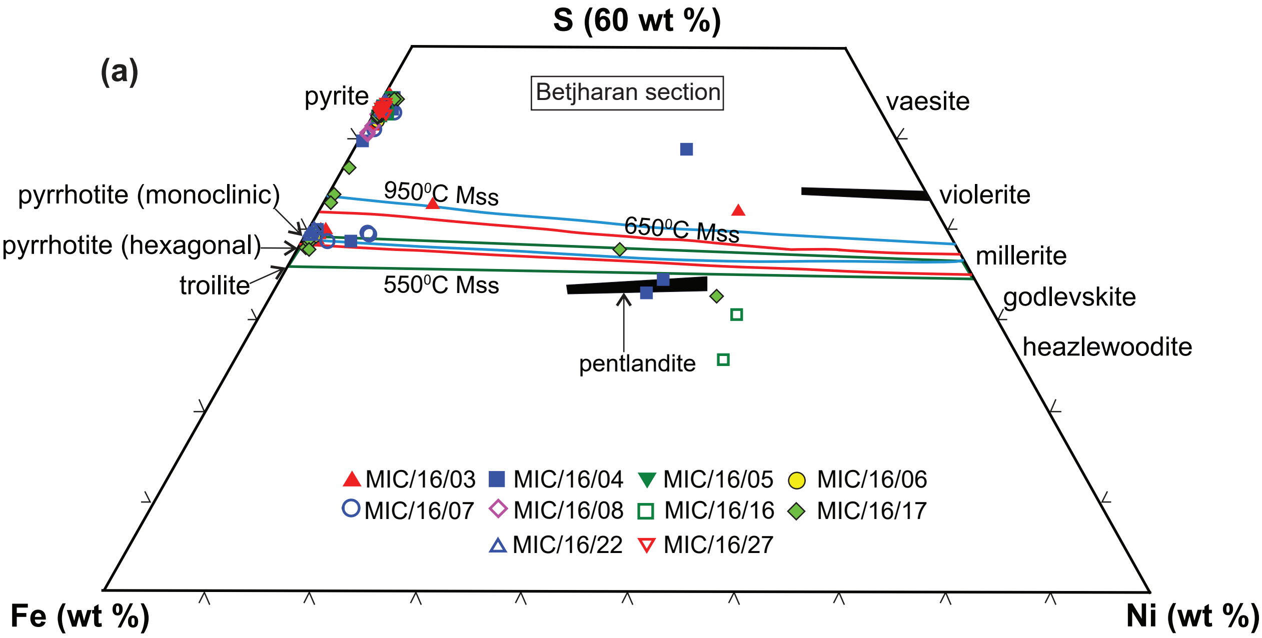

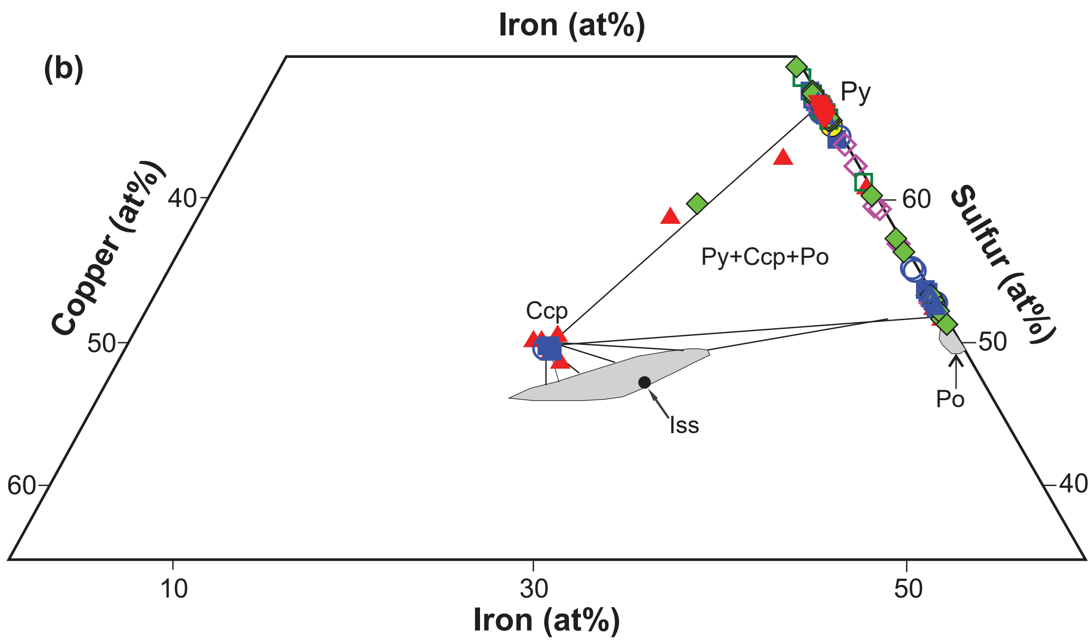

Fig.9. (a) Fe-Ni-S ternary plot showing the compositional field of pyrite, pyrrhotite, pentlandite, and monosulfide solid solution (Mss) from the gabbro-noritic rocks of the Betjharan section (after Kullerud et al., 1969); **(b)** Cu-Fe-S ternary plot showing the compositional field of chalcopyrite, pyrite, and pyrrhotite from the gabbro-noritic rocks of the Betjharan section (after Craig and Scott, 1974). Mss = monosulfide solid solution, Ccp = chalcopyrite, Py = pyrite, Po = pyrrhotite, Iss = intermediate solid solution. (MIC/16/03, MIC/16/04 - noritic gabbro; MIC/16/05, MIC/16/06/, MIC/16/07, MIC/16/08, MIC/16/16, MIC/16/17, MIC/16/22, MIC/16/27 - gabbro).

ilmenite from gabbro-noritic rocks and magnetitites elements that are commonly above the detection limit in Fe-oxides have been plotted on a multi-element variation diagram (**Fig. 10**). The order of the elements was chosen to reflect the order of the compatibility of each element in magnetite (e.g., Dare et al., 2012). The most compatible elements (Cr, Ti, V) are plotted on the right-hand side of the diagram. Normalization to MORB using values of Klein (2003) is preferred over primitive mantle because the parental magma responsible for the formation of the gabbro-noritic rock suite was iron-rich basalt. Magnetites from the gabbro-norites and magnetitites show wide variation in trace element concentration (**Fig. 10**). Ilmenites from the same assemblages are significantly enriched in Zr, Hf, Ta, Nb, Mn, Sc, and W and depleted in Zn, Co, Ni, Ga, and V relative to coexisting magnetites (**Fig. 10, Table. 7**). Magnetites from both gabbro-noritic rocks and magnetitite ores are relatively enriched in Ge, Ga, Ti, V, Cr, Ni, Co compared to the MORB whereas Zr, Hf, W, Ta, and Nb are relatively depleted (**Fig. 10, Table. 7**). Accessory magnetites of the gabbro-norites have higher concentrations of Pb (~2 - 11 ppm), Mo (~25 - 68 ppm), Sn (~8 - 33 ppm), Zn (~6773 - 8139 ppm), Ni (~896 - 3880 ppm), and Cr (~22301 - 67433 ppm), and lower Sc (~4 - 50 ppm), Co (~43 - 374 ppm) and V (~30211 - 34608 ppm) than the magnetites of the magnetitites (Pb = 0.3 - 1.3 ppm; Mo = 4.3 - 7.4 ppm; Sn = 6.1 - 10.9 ppm; Zn = 1431 - 1951 ppm; Ni = 664 - 854 ppm; Cr = 639 - 703 ppm; Sc = 47 - 81 ppm; Co = 1584 - 1895 ppm; V = 48534 - 64855 ppm). Trace elements such as Zr, Hf, Ge, Ga in magnetite display no such differences between the two different assemblages (**Fig. 10**, **Table. 7**). REE concentrations were also measured, but their concentrations are generally around or below 1 ppm or below the detection limit, which is expected for these minerals crystallized from a basaltic parental magma. Accessory Ilmenite grains from the gabbro-noritic rocks have lower concentrations of Co (~117 - 769 ppm), Ga (~10 - 53 ppm) and V (~5802 - 9063 ppm) and higher Pb (~0.9 - 7.9 ppm), Zr (~

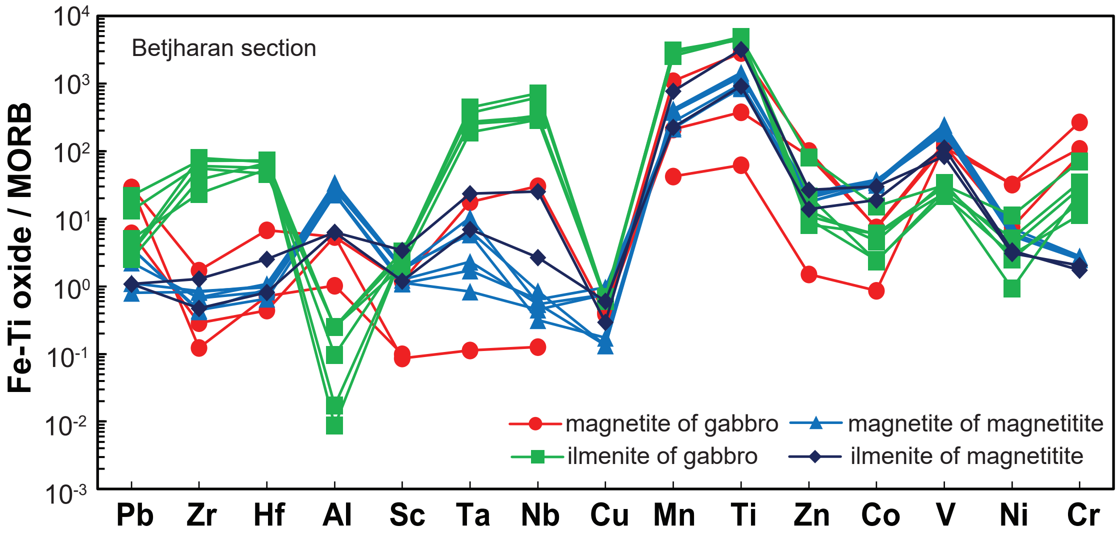

Fig. 10. Multi-element variation diagrams of lithophile and chalcophile element concentrations in Fe-oxides from the Betjharan section of the Mayurbhanj Complex. The analyses were done by LA-ICPMS. The normalization values are from Klein (2003).

2079 - 7029 ppm), Hf (~98 - 155 ppm), Ta (~38 - 90 ppm), Nb (~869 - 2153 ppm), Cu (~51 - 57 ppm), Mo (~14 - 37 ppm), Sn (~46 - 111 ppm) and Cr (~2874 - 17887 ppm) than the ilmenite of magnetitite ores (**Table. 7**). It is evident that the accessory Fe-Ti oxides (magnetite and ilmenite) in sulfide-bearing gabbro-noritic rocks have higher Ni, Cr, Pb, Mo, Sn, and Cu contents and lower V, Co, and Zn contents than the massive magnetitite ores having no sulfides. The binary diagrams have been prepared to examine the correlations of trace elements in different oxide phases from the gabbro-norite and magnetitite assemblages (**Fig. 11**). The Cr vs V plot shows a negative correlation in accessory magnetite of the gabbro-norite rocks (R^2 = 0.6724) but in case of ilmenite in gabbro Cr varies at a constant V content (**Fig. 11a**). The Cr vs Ge plot shows higher Ge concentrations in magnetites from both the assemblages than in ilmenite (**Fig. 11b**). The Cr vs Ti plot shows a positive trend in accessory magnetite of the gabbro-norite (R^2 = 1; **Fig. 11c**) and negative trend in cumulus magnetite of magnetitite (R^2 = 0.6451; **Fig. 11c**). The Hf vs Zr and Cr vs Ni plots show positive trends in Fe-Ti oxide minerals of both the assemblages (**Fig. 11d, e**). The V vs Ga plot reveals a negative trend in the ilmenite of the gabbro-noritic rocks (R^2 = 0.9623; **Fig. 11f**). The Sn vs Zn plot shows a negative correlation in magnetite of the magnetitite ore (R^2 = 0.685; **Fig. 11g**) but a positive correlation within accessory magnetite of the gabbro-norite (R^2 = 0.895; **Fig. 11g**). The accessory magnetite of gabbro-noritic rocks show negative correlations between Ni and Mo (R^2 = 0.9976; **Fig. 11h**). In contrast, in cumulus magnetite of magnetitite ore Mo varies at a constant Ni content. The Nb vs Zr plot reveals a negative correlation in the ilmenite of gabbro-noritic rocks (R^2 = 0.8107; **Fig. 11i**). The Ni vs Sn plot shows a lack of correlation in ilmenite but shows a positive trend in accessory magnetite of the gabbro-norite (R^2 = 0.9702; **Fig. 11j**).

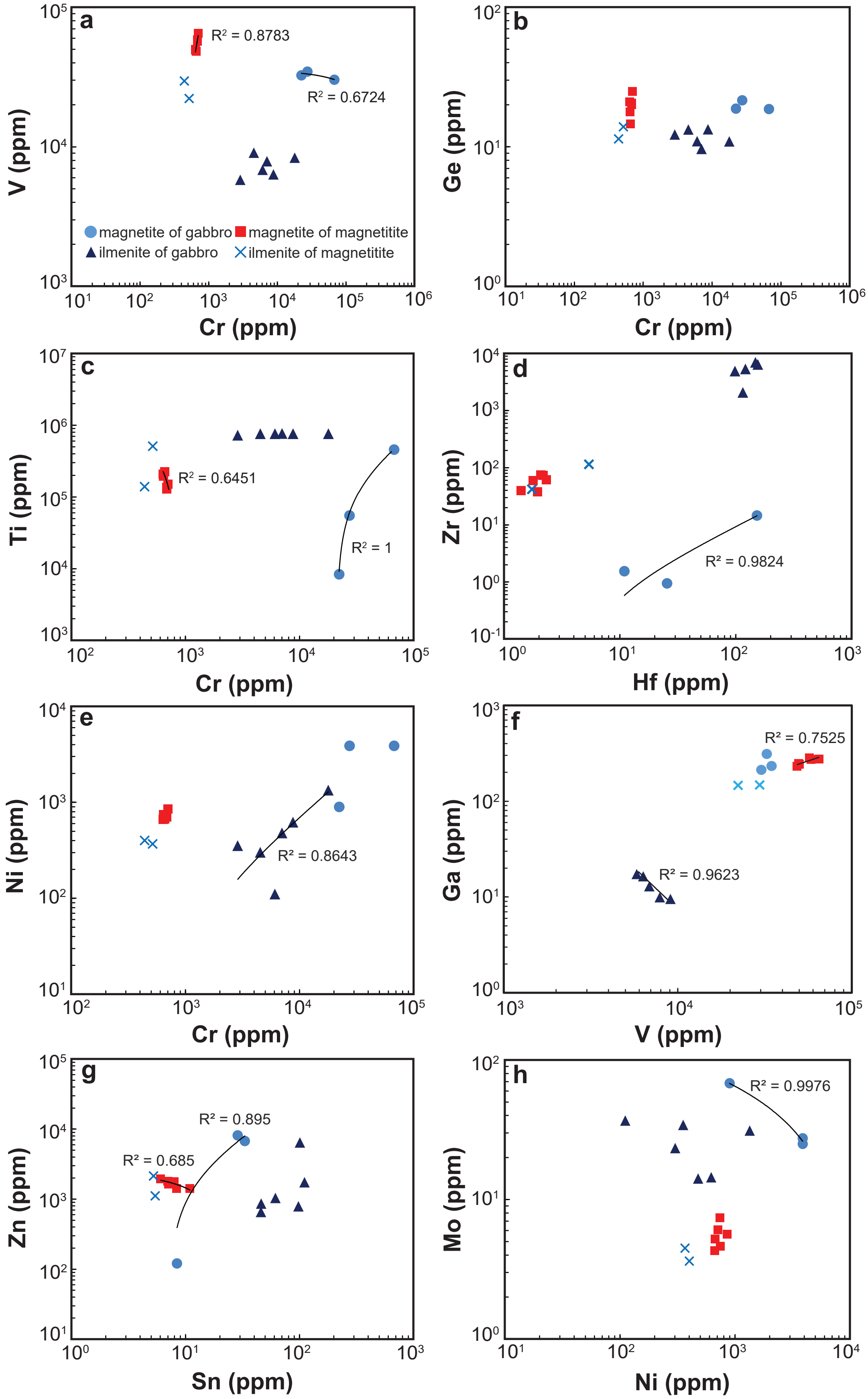

Fig. 11. Binary plots of lithophile and chalcophile elements in Fe-oxides from the Betjharan section of the Mayurbhanj Complex analyzed by LA-ICPMS: **(a)** Cr vs. V; **(b)** Cr vs. Ge; **(c)** Cr vs. Ti; **(d)** Hf vs. Zr; **(e)** Cr vs. Ni; **(f)** V vs. Ga; **(g)** Sn vs. Zn; **(h)** Ni vs. Mo; **(i)** Nb vs. Zr; **(j)** Ni vs. Sn.

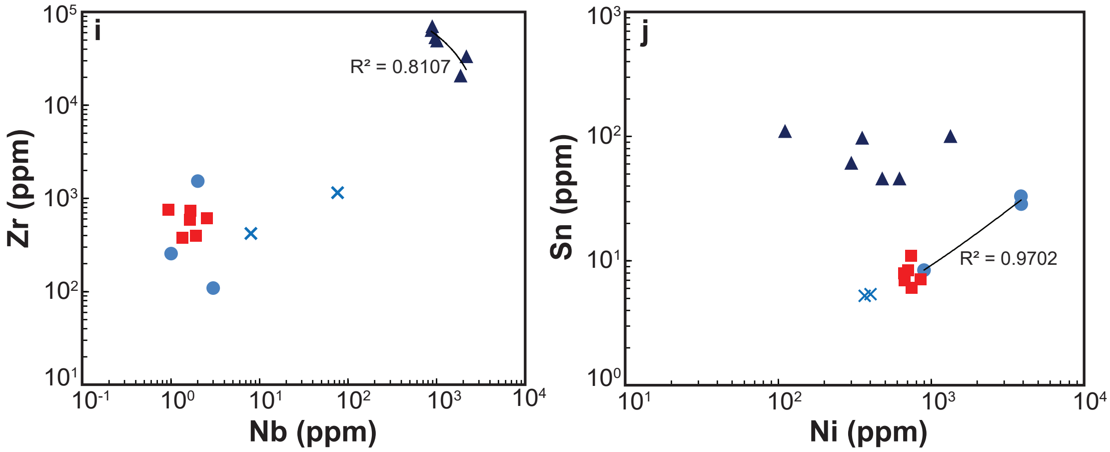

Fig. 11. continued.

Pyrite is the most abundant base metal sulfide mineral found in the gabbro-noritic rocks and exhibits a wide range of trace element compositions (**Fig. 12a**, **Table. 8**). Trace elements of pyrite are mostly heterogeneously distributed. The multi-element diagram (after Duran et al., 2015) shows pyrite trace element abundances normalized to primitive mantle values (**Fig. 12a**). Preferential enrichment of As, Pb, Au, Ag, and Co (**Fig. 12a**, **Table. 7**) is observed. Pyrite crystals have Pb = 27 - 3120 ppm, As = 48 - 6561 ppm, Ni = 81 - 20024 ppm, Co = 40 - 7234 ppm, Bi = 0.2 - 9 ppm, Sb = 0.4 - 18 ppm, Cu = 0.5 - 4610 ppm, Ag = 8 - 15 ppm. The concentrations of Pb, As, Ni, Co and Bi vary by several orders of magnitude between grains. The plots of Ag vs Bi (**Fig. 12b**) and Ag vs. Pb (**Fig. 12c**) of pyrite grains show weak positive correlations. In contrast, the plots of Bi vs Pb (**Fig. 12d**), As vs Pb (**Fig. 12e**), and Co vs Ni of pyrites show strong positive correlations (**Fig. 12f**).

4.4. Bulk-rock major and trace element geochemistry

The gabbroic suite of rocks of the Mayurbhanj Complex have LOI of 0.12 – 1.78 wt.% indicating minor alteration of these rocks due to secondary processes (**Table. 9**). The rocks from the Betjharan and the Hatichhad sections show significant compositional variations in major, minor and trace element concentrations (**Fig. 13 - 16**). All major and minor, and selected trace elements are plotted against MgO concentration of the rocks to understand the fractionation of the parental magma. The gabbro-norites of the Betjharan section have relatively higher MgO (5.88 - 11.55 wt. %) than the gabbro-anorthosites from the Hatichhad section (1.19 - 6.99 wt. %) (**Table. 9; Fig. 13**). The corresponding SiO_2 contents range from 49.14 to 53.07 wt. % in the Betjharan section and 48.49 to 68.28 wt. % in the Hatichhad section (**Table. 9; Fig. 13a**). The SiO_2 vs. MgO shows strong correlation with a negative trend for the Hatichhad gabbro-anorthositic rocks whereas Betjharan gabbro-noritic rocks show significant variation of MgO with limited change in the SiO_2 concentrations (**Fig. 13a**). The

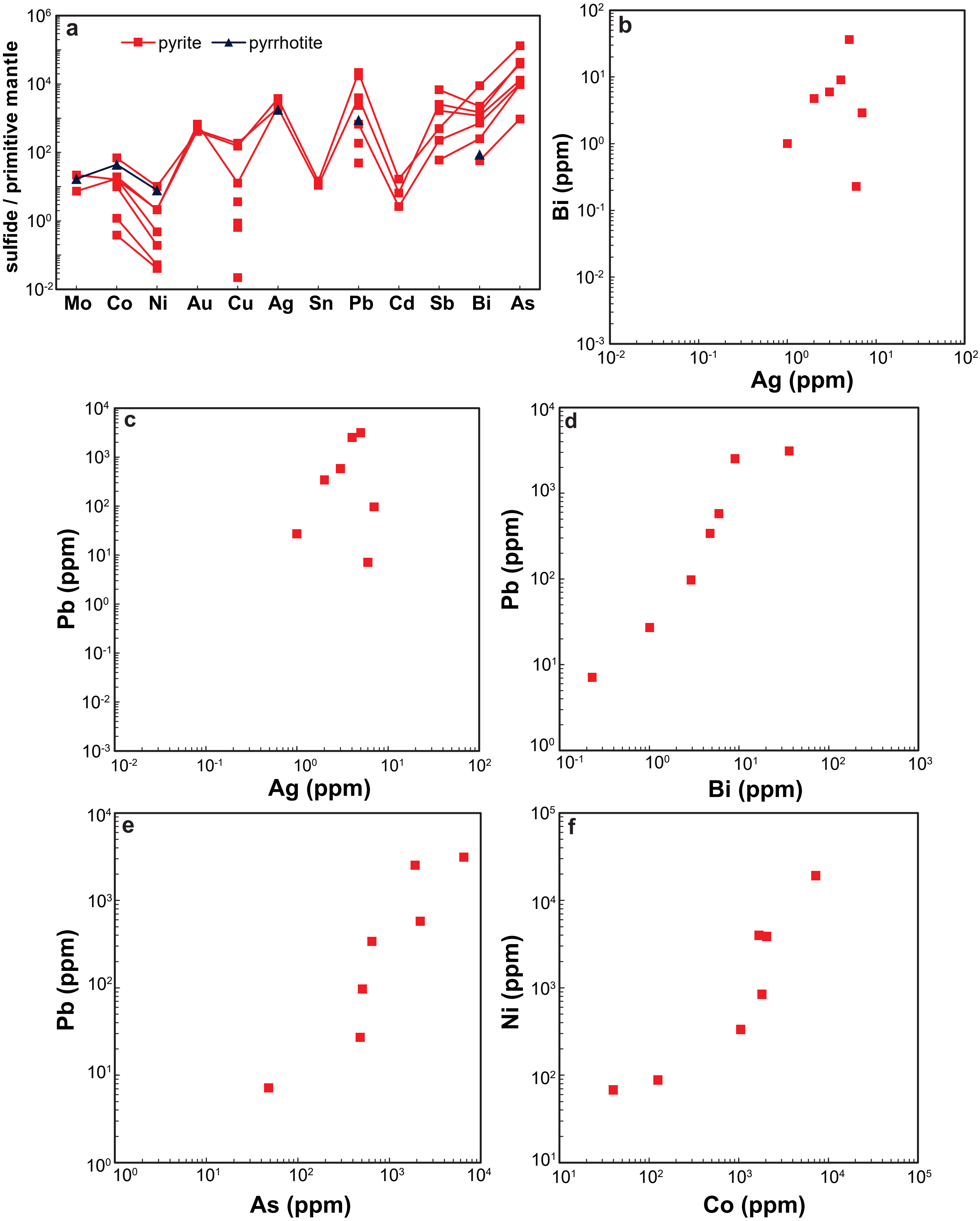

Fig. 12. (a) Primitive mantle normalized multi-element diagram of pyrite compared with pyrrhotite from the gabbro-norite of the Betjharan section (after Duran et al., 2015). The normalization values are from Lyubetskaya and Korenaga (2007); Binary variation diagrams of trace elements in pyrite of the gabbro-norite from the Betjharan section **(b)** Ag vs Bi; **(c)** Ag vs Pb; **(d)** Bi vs Pb; **(e)** As vs Pb; **(f)** Co vs Ni.

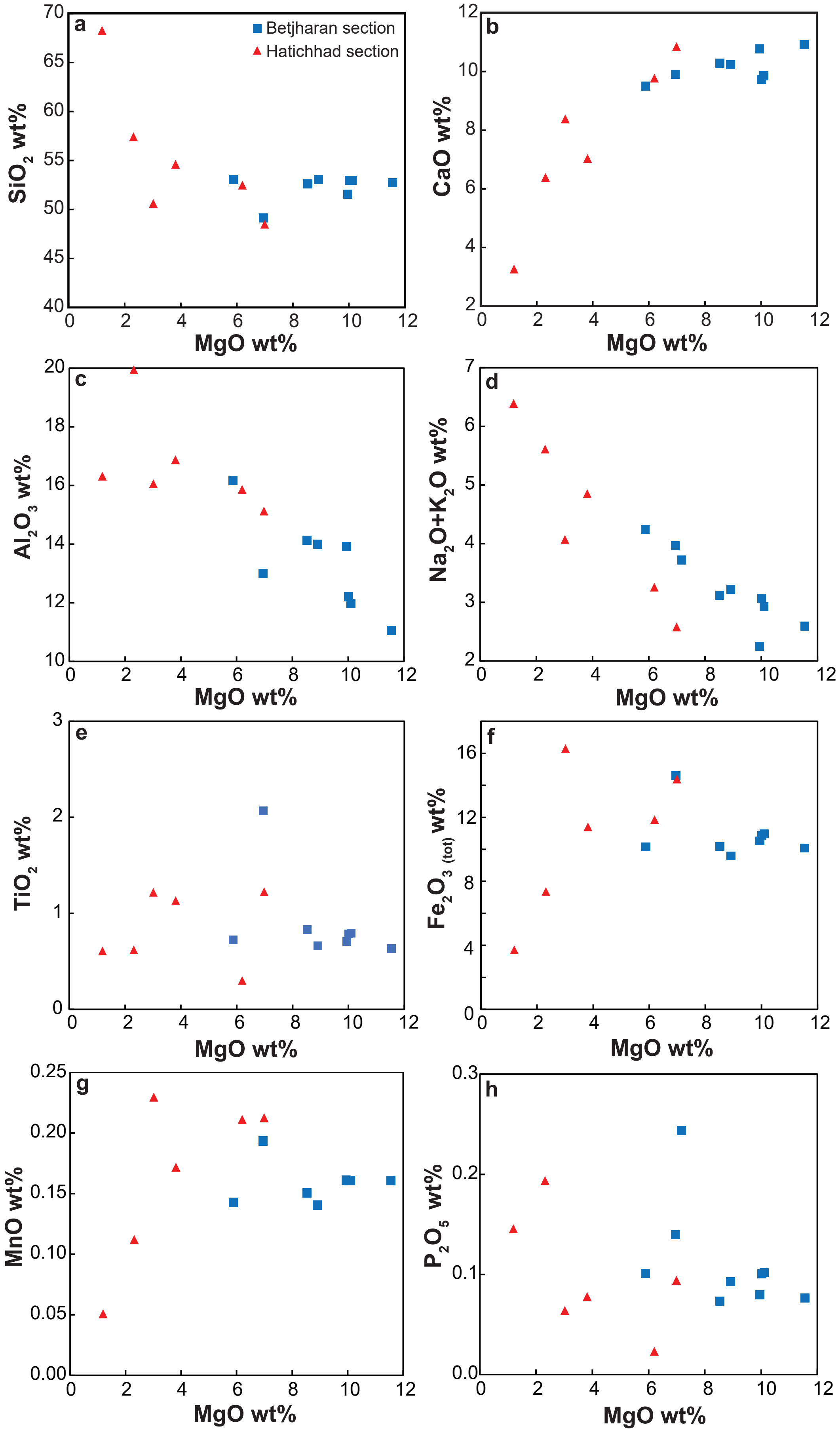

Fig. 13. Variation diagram of selected major elements (anhydrous basis) for the gabbroic rocks of the Mayurbhanj Complex: MgO vs **(a)** SiO_2; **(b)** CaO; **(c)** Al_2O_3; **(d)** Na_2O+K_2O; **(e)** TiO_2; **(f)** $Fe_2O_{3(tot)}$; **(g)** MnO; **(h)** P_2O_5.

CaO, Al_2O_3 and (Na_2O+K_2O) show strong correlations with MgO variations in both gabbro-noritic and gabbro-anorthositic rocks (**Fig. 13b-d**). The CaO concentration in the gabbro-noritic rocks of the Betjharan section ranges from 9.52 to 10.92 wt. % whereas in the gabbro-anorthositic rocks of the Hatichhad section the CaO varies from 3.27 to 10.85 wt. % and in both areas the CaO content shows a positive correlation with the MgO content (**Table. 9; Fig. 13b**). The Al_2O_3 content varies from 11.05 to 16.17 wt. % in the Betjharan gabbro-noritic rocks, and 15.13 to 19.14 wt. % in the Hatichhad gabbro-anorthositic rocks (**Table. 9; Fig. 13c**). The Al_2O_3 vs. MgO shows a correlation with negative trend for both gabbro-noritic and gabbro-anorthositic rocks (**Fig. 13c**). The total alkali content (K_2O+Na_2O) in the Betjharan gabbro-noritic rocks ranges from 2.25 to 4.25 wt. % whereas in the gabbro-anorthositic rocks of the Hatichhad the total alkali is 2.58-6.39 wt. % and it shows negative trend with MgO in both Betjharan and Hatichhad sections (**Table. 9; Fig. 13d**). The concentrations of TiO_2 and $Fe_2O_{3(total)}$ are higher in the Betjharan gabbro-norites (TiO_2 = 0.63 – 2.07 wt.%; $Fe_2O_{3(total)}$ = 9.57 – 14.61 wt.%) than the Hatichhad gabbro-anorthosites (TiO_2 = 0.30 – 1.23 wt.%; $Fe_2O_{3(total)}$ = 3.72 – 16.30 wt.%). The total iron concentrations show positive correlation with MgO for the Hatichhad gabbro-anorthosites whereas the Betjharan gabbro-norites show limited variations with a range of MgO (**Fig. 13f**). The concentrations of MnO are higher (0.14 – 0.19 wt.%) in the gabbro-norites relative to the gabbro-anorthosites (0.05 – 0.23 wt.%) and show a distinct correlation with MgO for the latter whereas the former shows limited variation of MnO with a range of MgO (**Table. 9**; **Fig. 13g**). The gabbroic rocks of the Mayurbhanj Complex spread from gabbro to gabbroic-diorite in the TAS diagram (**Fig. 14a**) and show tholeiitic trend in the AFM plot (**Fig. 14b**). Two samples fall in the diorite and granodiorite field due to high SiO_2 content for the high modal% of plagioclase.

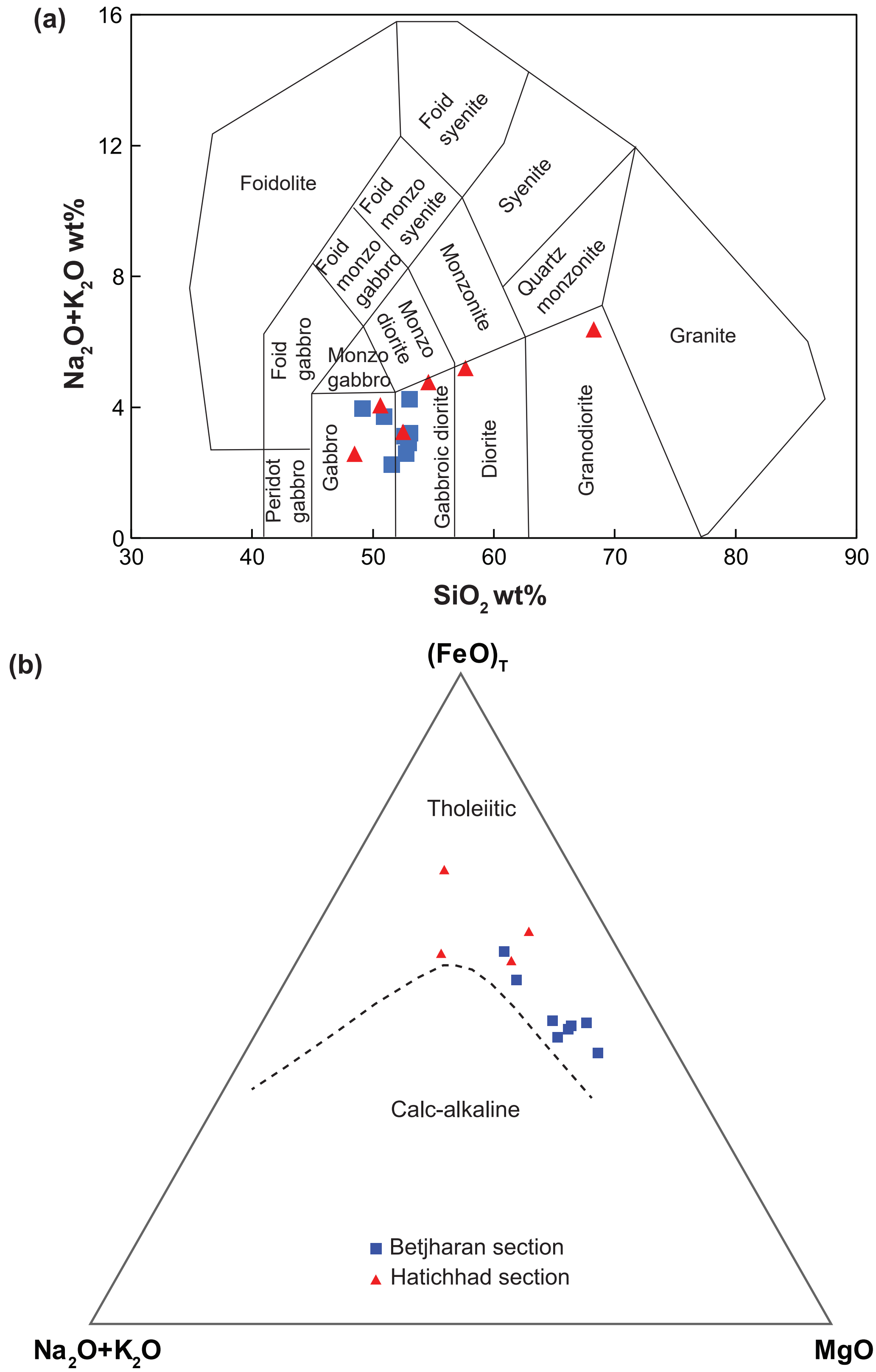

Fig. 14. (a) TAS and **(b)** AFM diagrams for the gabbro-anorthositic rocks of the Mayurbhanj Complex showing chemical classification and magmatic differentiation of the rocks.

The concentrations of Cr (~58 – 1250 ppm) and Ni (~109 – 469 ppm) are higher in the Betjharan gabbro-norites than the Hatichhad gabbro-anorthosites (Cr = up to 186 ppm; Ni = ~12 – 130 ppm) (**Table. 9**). The Cr vs. MgO show strong positive correlation for the gabbro-norites (R^2 = 0.9558) whereas the Ni vs. MgO plot shows strong positive correlations for the samples of the both Betjharan and Hatichhad section (Betjharan: R^2 = 0.8377, Hatichhad: R^2 = 0.9612) (**Fig. 15a, b**). The gabbro-norites have higher V concentrations (V = 149 – 540 ppm) than the gabbro-anorthosites (V = 37 – 372 ppm) (**Table. 9**). V shows a positive trend with the MgO variation of the gabbro-anorthosites whereas the gabbro-norites show a limited variation of V for a range of MgO (**Fig. 15c**). The Betjharan gabbro-norites and the Hatichar gabbro-anorthosites have Cu contents ranging from ~76 – 208 ppm and ~27 – 213 ppm respectively. The Cu vs. MgO shows a positive correlation for the gabbro-anorthosites (R^2 = 0.8212) whereas the gabbro-norites show a limited variation of Cu for a range of MgO (**Fig. 15d**). Nb, La and $REE_{(tot)}$ correlate negatively with MgO for the gabbro-anorthosites whereas the gabbro-norites show a limited variation for a range of MgO content (**Fig. 15e, f, g**). Sr has an overall negative correlation with MgO for the gabbro-norite-anorthosites of the igneous complex (**Fig. 15h**) whereas Ba and Rb define strong negative trend with MgO for the gabbro-anorthosite of the Hatichhad section (**Fig. 15i, j**).

The Betjharan gabbro-norites (LREE = 20-60 x chondrite) and the Hatichhad gabbro-anorthosites (LREE = 10-100 x chondrite) exhibit slight LREE enrichment relative to HREE (5-10 x chondrite) in chondrite normalized REE pattern plot (**Fig. 16a**). The gabbro-norites are relatively HREE enriched than the gabbro-anorthosites. Overall, the Hatichhad gabbro-anorthosites have more fractionated REE than the Betjharan gabbro-norites. The gabbro-anorthosites show strong positive Eu anomaly (Eu/Eu* = 1.2 – 21.62) in the chondrite normalized REE and multi-element plots (**Fig. 16a, b**). The chondrite normalized trace

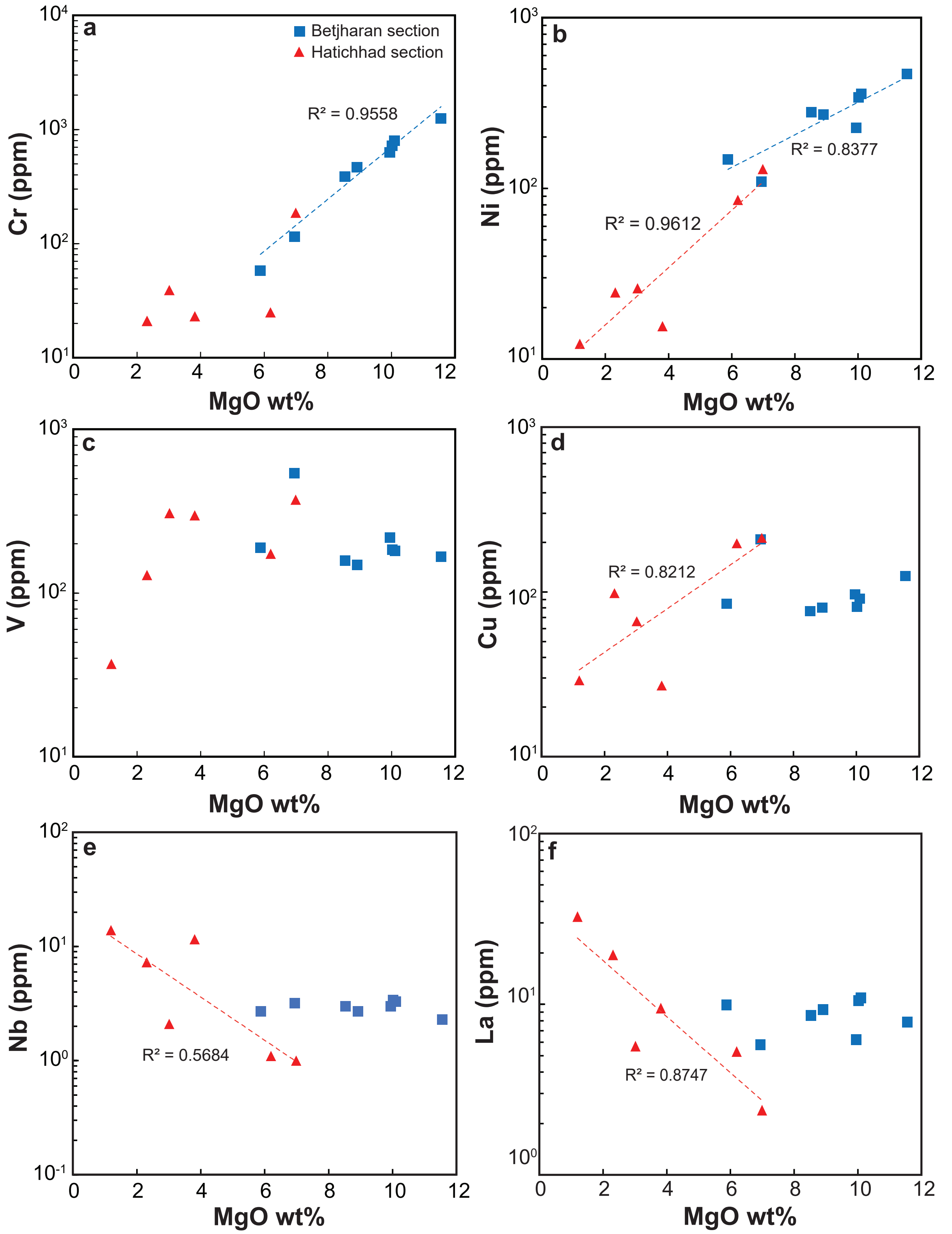

Fig. 15. Variation diagram of selected trace elements for the gabbro-anorthositic rocks of the Mayurbhanj Complex: MgO vs **(a)** Cr; **(b)** Ni; **(c)** V; **(d)** Cu; **(e)** Nb; **(f)** La; **(g)** $REE_{(tot)}$; **(h)** Sr; **(i)** Ba; **(j)** Rb.

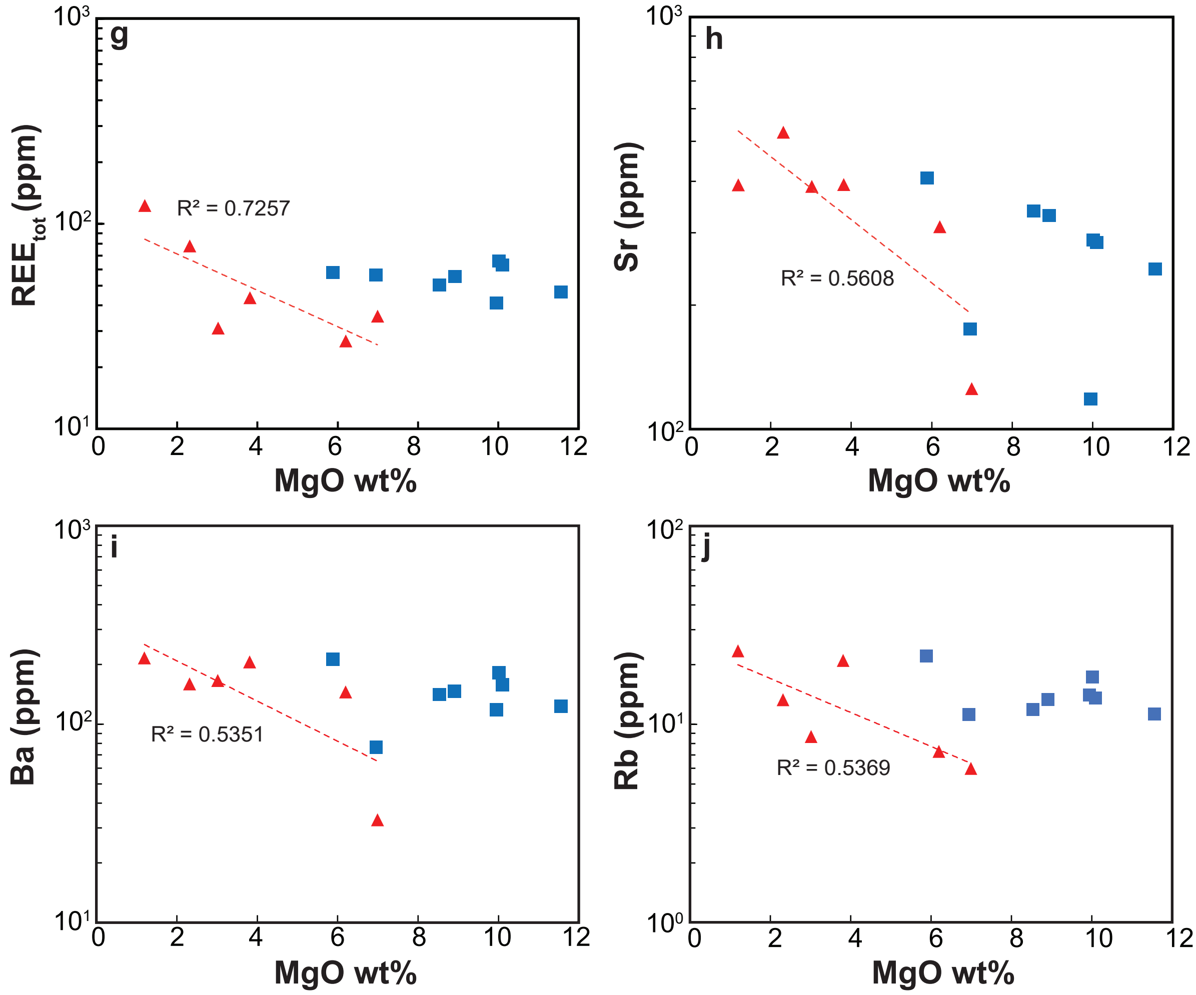

Fig. 15. continued.

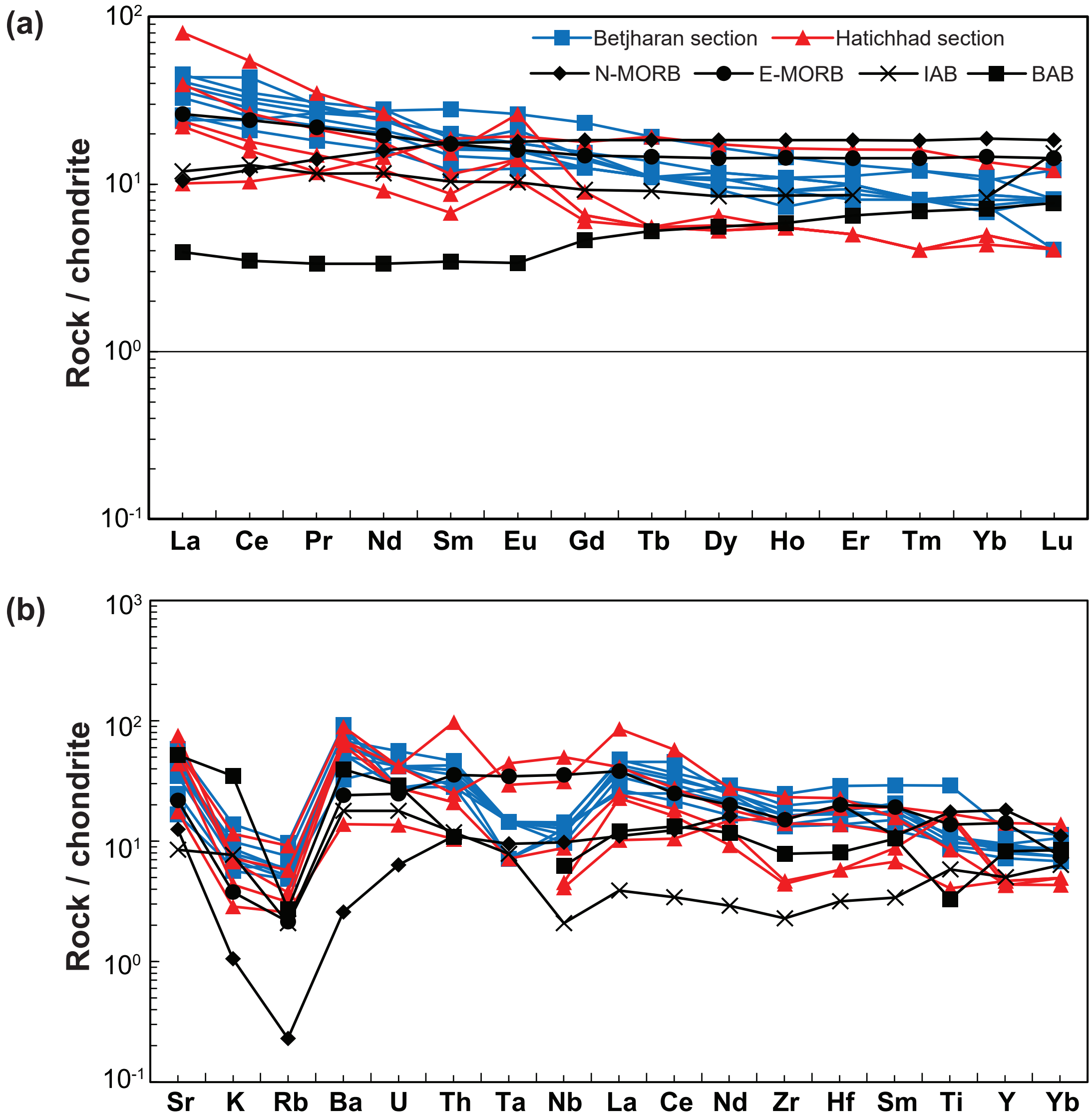

Figure 16: Chondrite-normalised **(a)** REE patterns; **(b)** trace element spidergrams for the gabbro-anorthositic rocks of the Mayurbhanj Complex. Normalizing values are from McDonough and Sun, 1995.

element pattern shows that all rocks are enriched in LILEs like Sr, Ba, U and Th (**Fig. 16b**). The Betjharan gabbro-norites are characterized by negative Nb and Ta anomaly (Nb_N/Ta_N = 0.65 – 1.7) with weak to positive Zr and Hf anomaly while the Hatichhad gabbro-anorthosites show negative Nb and Ta anomaly (Nb_N/Ta_N = 0.98 – 1.19) with variable Zr and Hf anomaly (**Fig. 16b**).

The chalcophile elements are plotted against bulk-rock S content of the rocks (**Fig. 17**). Since visible sulfide is negligible in the Hatichar gabbro-anorthosites the S content is below detection limit in these rocks. The Ni, Co and Ag contents of the gabbro-norites exhibit negative trends with S contents (**Fig. 17a, b, f**) whereas the Cu, $Fe_2O_{3(total)}$ and Pb contents are positively correlated with S contents (**Fig. 17c-e**).

4.5. Sm-Nd istope geochronology

The Sm-Nd isotopic analysis of whole rock gabbro-norite-anorthosite from the Mayurbhanj Complex was carried out to provide information on crystallization age of the igneous rocks and the mantle source of the parental magma. The Sm-Nd isotopic results for the gabbro-norites of the Betjharan section (n = 9) yielded an unrealistic errochron age of 3887 ± 810 Ma with Nd_i = 0.50786 ± 0.00079 (MSWD = 184). The gabbro-anorthisites of the Hatichhad section (n = 6) yielded an isochron age of 3022 ± 180 Ma with Nd_i = 0.50849 ± 0.00017 (MSWD = 72) (**Fig. 18a**) and $\varepsilon_{Nd(T)}$ = -4.4 ± 3.3. All samples from both sections when regressed they yielded an errochron age of 3169 ± 340 Ma with MSWD = 484. The correlation lines are calculated and plotted using the program ISOPLOT for excel by Ludwig (2008) (**Fig. 18a**). The gabbro-norite-anorthositic suite of rocks show variation in their present day $^{143}Nd/^{144}Nd$ ratios between 0.510419 to 0.512439 and $^{147}Sm/^{144}Sm$ ratios between 0.099 to 0.245. The high error in the isochron age was due to the low spread in the $^{147}Sm/^{144}Sm$ and $^{143}Nd/^{144}Nd$ ratios. When the samples of the gabbro-norites of the

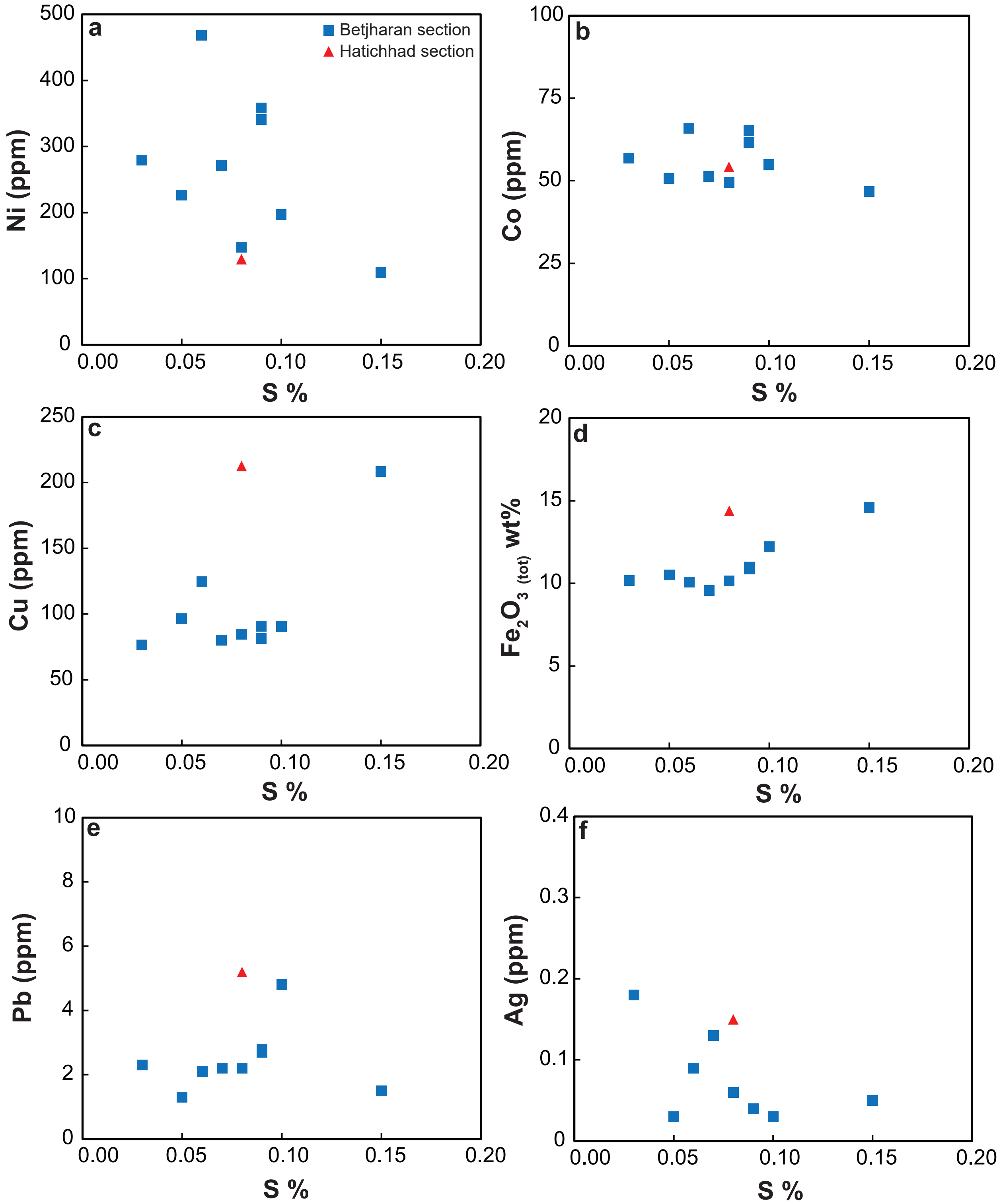

Fig. 17. (a) - (f) Plots of bulk rock S content versus trace elements of the gabbro-anorthositic rocks from of the Mayurbhanj Complex.

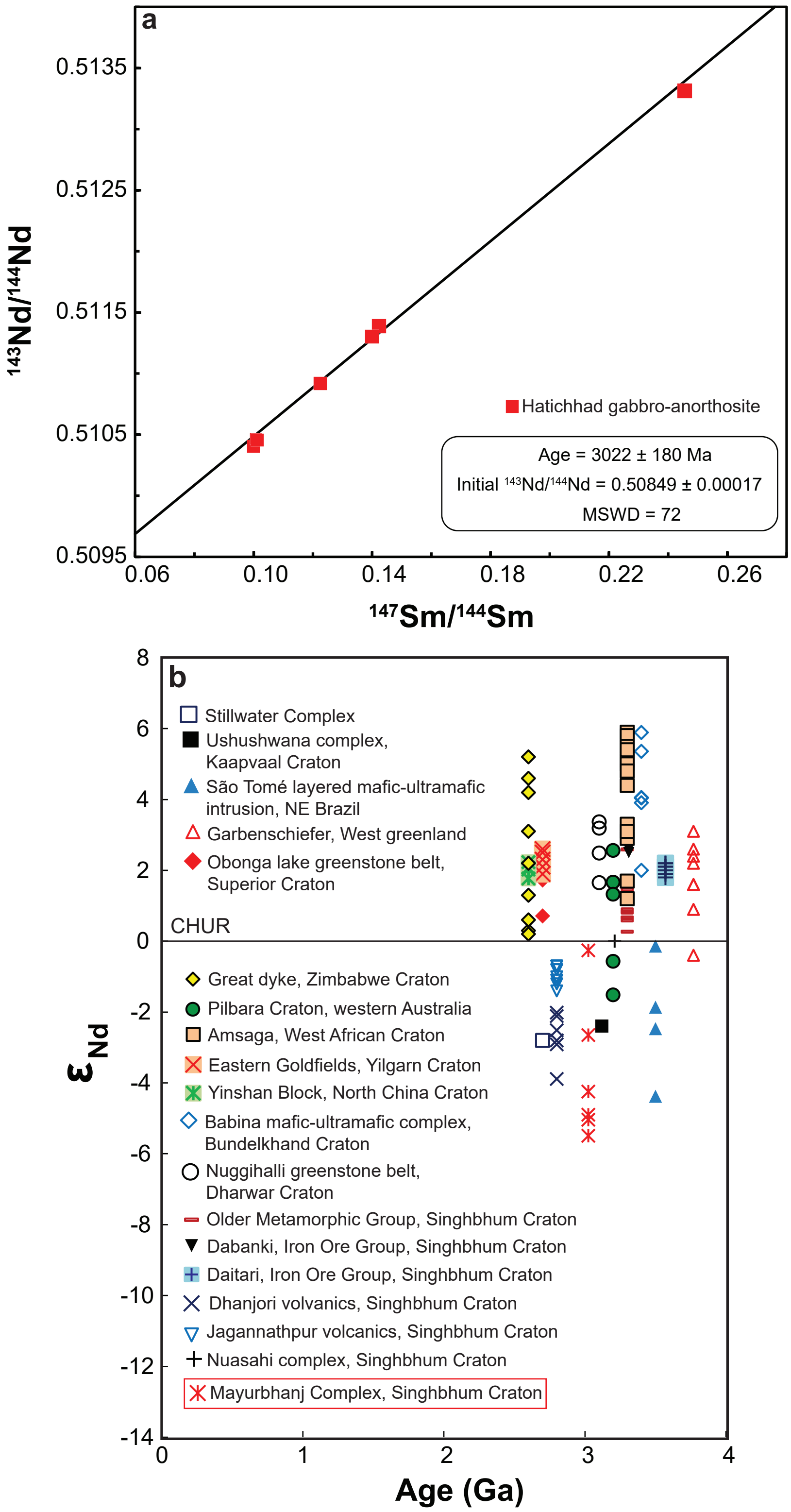

Fig. 18. (a) Whole-rock Sm-Nd isochron of gabbro-anorthosites from the Mayurbhanj Complex; **(b)** Plot of Age versus ε_{Nd} for ultramafic-mafic complex from different craton worldwide around ~3.0 Ga. The data of the Mayurbhanj Complex (from this study) along with data from other cratons and other litho-units from the Singhbhum Craton have been plotted for comparison. The other data from Paolo and wasserburg (1979); Hamilton et al. (1983); Hegner et al. (1984); Sharma et al. (1994); Bateman et al. (2001); Tomlinson et al. (2002); Obethur et al. (2002); Misra and Johnson (2004); Kranendonk et al. (2010); Mukherjee et al. (2012); Wang et al (2015); Ruiz et al. (2019); Singh et al. (2019); Wainwright et al. (2019); Adhikari et al. (2021).

Betjharan section are included with the gabbro-anorthosites of the Hatichhad section the correlation was degraded. Therefore, we have considered the isochron age of the Hatichhad section and other related data to constrains on the mantle source of the parental magma. The gabbro-anorthosites of the Hatichhad section yielded a depleted mantle model age (T_{DM}) that varies from 3.38 to 3.48 Ga which is not much earlier than the emplacement age of the magma considering the error (**Table. 10**). Our data are compared with the existing Sm-Nd data of the other litho-units of the Singhbhum craton i.e., OMG amphibolites and OMTG tonalitic rocks (Sharma et al., 1994), IOG rocks (Adhikari et al., 2021), Dhanjori volcanics (Roy et al., 2002), Jagannathpur volcanics (Adhikari et al., 2021), Nuasahi ultramafic-mafic complex (Augé et al., 2003) and are plotted in the Age vs. ε_{Nd} diagram (**Fig. 18b)** which show a range of crystallization age from 2.8 to 3.57 Ga for different litho-units of the Singhbhum craton.

Table. 2. EPMA major element (wt. %) compositions of plagioclases from the gabbro-norite-anorthosite of the Mayurbhanj Complex.

Sample	MIC-16-03	MIC-16-03	MIC-16-03	MIC-16-03	MIC-16-03	MIC-16-03	MIC-16-03	MIC-16-03	MIC-16-03	MIC-16-04	MIC-16-04	MIC-16-05	MIC-16-05	MIC-16-05	MIC-16-05	MIC-16-05	MIC-16-05	MIC-16-05	MIC-16-05
SiO_2	52.85	53.39	53.47	56.62	63.22	58.43	57.79	58.41	58.77	52.52	53.94	53.69	55.67	51.63	52.06	55.49	51.79	59.24	51.56
TiO_2	0.16	0.15	0.15	0.12	0.06	0.10	0.11	0.14	0.11	0.01	0.01	0.03	0.06	0.02	0.03	0.07	0.01	0.04	0.02
Al_2O_3	28.43	27.76	27.36	25.45	21.91	23.30	25.12	24.00	24.33	26.03	28.31	27.33	26.26	28.41	28.47	26.43	29.75	24.79	28.34
FeO	0.04	0.07	1.11	0.06	0.09	0.32	0.18	0.24	0.21	3.21	0.23	0.52	0.54	0.55	0.61	0.42	0.71	0.45	0.43
CaO	11.59	11.08	9.84	8.62	3.37	6.02	7.05	6.27	6.39	8.82	10.85	9.86	8.56	11.20	11.40	9.26	11.69	6.46	11.63
Na_2O	5.28	5.34	5.73	6.74	9.60	8.08	7.53	8.36	8.42	4.38	5.41	5.35	6.44	5.16	4.94	5.92	4.54	7.20	4.84
K_2O	0.24	0.29	0.23	0.35	0.61	0.40	0.49	0.23	0.05	1.09	0.27	0.47	0.43	0.36	0.33	0.35	0.52	0.47	0.32
Total	98.46	97.89	98.28	97.81	98.71	96.72	97.99	97.29	98.02	99.31	99.20	97.43	98.11	97.50	98.02	98.10	99.17	98.78	97.31
8 (O) basis																			
Si	9.72	9.85	9.91	10.39	9.72	10.81	10.54	10.70	10.69	10.00	9.72	9.98	10.24	9.65	9.67	10.20	9.72	10.71	9.65
Ti	0.02	0.02	0.02	0.02	0.02	0.01	0.02	0.02	0.02	0.00	0.02	0.00	0.01	0.00	0.00	0.01	0.02	0.01	0.00
Al	6.16	6.04	5.97	5.50	6.16	5.08	5.40	5.18	5.22	5.84	6.16	5.98	5.69	6.26	6.23	5.73	6.16	5.28	6.25
Fe	0.01	0.01	0.17	0.01	0.01	0.05	0.03	0.04	0.03	0.51	0.01	0.08	0.08	0.09	0.10	0.06	0.01	0.07	0.07
Ca	2.29	2.19	1.95	1.69	2.29	1.19	1.38	1.23	1.25	1.80	2.29	1.96	1.69	2.24	2.27	1.82	2.29	1.25	2.33
Na	1.88	1.91	2.06	2.40	1.88	2.90	2.66	2.97	2.97	1.61	1.88	1.93	2.30	1.87	1.78	2.11	1.88	2.53	1.76
K	0.06	0.07	0.05	0.08	0.06	0.09	0.11	0.05	0.01	0.26	0.06	0.11	0.10	0.09	0.08	0.08	0.06	0.11	0.08
An	54.07	52.55	48.03	40.57	54.07	28.50	33.14	28.92	29.46	48.89	54.07	49.04	41.28	53.41	54.96	45.43	54.07	32.21	56.00
Ab	44.58	45.83	50.62	57.46	44.58	69.24	64.12	69.79	70.26	43.90	44.58	48.18	56.25	44.56	43.13	52.54	44.58	65.01	42.16
Or	1.35	1.62	1.35	1.98	1.35	2.26	2.74	1.28	0.28	7.20	1.35	2.78	2.47	2.03	1.91	2.03	1.35	2.78	1.85

Sample	MIC-16-05	MIC-16-05	MIC-16-05	MIC-16-06	MIC-16-06	MIC-16-08	MIC-16-08	MIC-16-08	MIC-16-08	MIC-16-08	MIC-16-08	MIC-16-08	MIC-16-08	MIC-16-08	MIC-16-08	MIC-16-08	MIC-16-08	MIC-16-08	MIC-16-08
SiO_2	52.96	52.28	52.44	56.99	57.75	55.20	55.30	54.40	54.42	55.30	58.53	54.26	55.79	56.37	54.43	53.86	56.58	55.23	54.69
TiO_2	0.01	0.02	0.03	0.01	0.04	0.60	0.57	0.58	0.58	0.57	0.59	0.62	0.58	0.60	0.58	0.58	0.57	0.58	0.60
Al_2O_3	28.62	28.96	28.43	25.91	26.61	27.77	27.40	27.42	27.28	27.50	25.33	27.84	26.95	27.08	27.60	27.50	26.17	27.45	28.35
FeO	0.51	0.45	0.34	0.31	0.40	0.30	0.36	0.21	0.16	0.10	0.06	0.20	0.14	0.06	0.64	0.19	0.24	0.02	0.30
CaO	11.10	11.38	11.37	8.25	7.62	10.77	10.45	10.22	10.10	10.08	7.56	10.71	9.61	9.64	10.26	10.28	8.05	10.17	10.88

Na_2O	5.04	4.96	4.81	6.38	6.81	5.38	5.65	5.50	5.56	5.63	7.13	5.34	6.00	6.05	5.43	5.68	6.74	5.58	5.30
K_2O	0.20	0.33	0.31	0.50	0.52	0.32	0.25	0.32	0.32	0.24	0.36	0.31	0.31	0.22	0.75	0.24	0.32	0.23	0.29
Total	98.62	98.60	97.92	98.76	100.15	99.81	99.52	98.11	97.90	98.92	98.97	98.71	98.91	99.44	99.16	97.79	98.12	98.76	99.89
8 (O) basis																			
Si	9.75	9.65	9.72	10.40	10.38	9.95	10.00	9.96	9.72	10.02	10.52	9.88	10.11	10.14	9.72	9.90	10.30	10.02	9.85
Ti	0.00	0.00	0.02	0.00	0.00	0.08	0.08	0.08	0.02	0.08	0.08	0.08	0.08	0.08	0.02	0.08	0.08	0.08	0.08
Al	6.21	6.30	6.16	5.57	5.64	5.90	5.84	5.92	6.16	5.87	5.37	5.98	5.76	5.74	6.16	5.96	5.61	5.87	6.02
Fe	0.08	0.07	0.01	0.05	0.06	0.04	0.05	0.03	0.01	0.01	0.01	0.03	0.02	0.01	0.01	0.03	0.04	0.00	0.04
Ca	2.19	2.25	2.29	1.61	1.47	2.08	2.02	2.00	2.29	1.96	1.46	2.09	1.87	1.86	2.29	2.02	1.57	1.98	2.10
Na	1.80	1.78	1.88	2.25	2.37	1.88	1.98	1.95	1.88	1.98	2.49	1.88	2.11	2.11	1.88	2.02	2.38	1.96	1.85
K	0.05	0.08	0.06	0.12	0.12	0.07	0.06	0.07	0.06	0.06	0.08	0.07	0.07	0.05	0.06	0.06	0.07	0.05	0.07
An	54.23	54.82	54.07	40.48	37.07	51.55	49.80	49.71	54.07	49.06	36.19	51.66	46.13	46.24	54.07	49.33	39.04	49.52	52.30
Ab	44.59	43.27	44.58	56.58	59.90	46.61	48.76	48.43	44.58	49.54	61.78	46.58	52.11	52.50	44.58	49.30	59.12	49.15	46.07
Or	1.18	1.91	1.35	2.94	3.03	1.84	1.44	1.86	1.35	1.40	2.03	1.75	1.76	1.25	1.35	1.37	1.84	1.34	1.63

Sample	MIC-16-08	MIC-16-16	MIC-16-16	MIC-16-16	MIC-16-16	MIC-16-16	MIC-16-16	MIC-16-16	MIC-16-16	MIC-16-16	MIC-16-16	MIC-16-16	MIC-16-17	MIC-16-17	MIC-16-17	MIC-16-17	MIC-16-17	MIC-16-17	MIC-16-17
SiO_2	55.69	56.99	57.75	55.93	56.21	53.40	53.84	55.43	52.78	52.70	55.50	55.67	51.95	51.20	50.56	52.54	53.88	54.11	59.67
TiO_2	0.57	0.01	0.04	0.76	0.75	0.78	0.77	0.75	0.79	0.79	0.74	0.73	0.13	0.19	0.11	0.12	0.17	0.15	0.10
Al_2O_3	27.46	25.91	26.61	26.64	26.27	27.21	29.01	26.26	29.50	27.90	27.31	26.46	29.08	2.41	2.40	28.76	29.73	27.85	25.58
FeO	0.20	0.31	0.40	0.23	0.18	0.26	0.15	0.45	0.19	0.14	-0.03	0.46	0.22	10.43	8.47	0.40	0.12	0.00	0.16
CaO	10.11	8.25	7.62	8.96	9.11	11.29	11.20	9.51	11.61	11.66	9.79	9.22	12.61	18.19	20.11	12.32	11.74	11.15	7.36
Na_2O	5.64	6.38	6.81	6.17	6.14	4.90	5.22	5.86	4.93	4.83	5.80	5.97	4.64	0.40	0.34	4.48	4.57	5.01	7.15
K_2O	0.33	0.50	0.52	0.49	0.46	0.27	0.31	0.38	0.24	0.25	0.45	0.47	0.17	0.06	0.04	0.26	0.27	0.10	0.45
Total	99.55	98.76	100.15	98.88	98.85	97.61	100.11	98.29	99.70	97.62	99.09	98.62	98.84	99.03	98.04	98.89	100.40	98.41	100.50
8 (O) basis																			
Si	10.04	9.72	10.38	10.16	10.21	9.86	9.72	10.14	9.57	9.73	10.05	10.15	9.72	12.08	12.03	9.65	9.72	9.92	10.61
Ti	0.08	0.02	0.00	0.10	0.10	0.11	0.02	0.10	0.11	0.11	0.10	0.10	0.02	0.03	0.02	0.02	0.02	0.02	0.01
Al	5.84	6.16	5.64	5.70	5.63	5.92	6.16	5.66	6.31	6.07	5.83	5.68	6.16	0.67	0.67	6.23	6.16	6.02	5.36
Fe	0.03	0.01	0.06	0.04	0.03	0.04	0.01	0.07	0.03	0.02	0.00	0.07	0.01	2.06	1.68	0.06	0.01	0.00	0.02

Ca	1.95	2.29	1.47	1.74	1.77	2.23	2.29	1.86	2.26	2.31	1.90	1.80	2.29	4.60	5.13	2.42	2.29	2.19	1.40
Na	1.97	1.88	2.37	2.17	2.16	1.75	1.88	2.08	1.73	1.73	2.04	2.11	1.88	0.18	0.16	1.59	1.88	1.78	2.46
K	0.08	0.06	0.12	0.11	0.11	0.06	0.06	0.09	0.06	0.06	0.10	0.11	0.06	0.02	0.01	0.06	0.06	0.02	0.10
An	48.79	54.07	37.07	43.25	43.84	55.12	54.07	46.24	55.80	56.34	47.00	44.79	54.07	95.81	96.83	59.41	54.07	54.80	35.35
Ab	49.30	44.58	59.90	53.91	53.51	43.29	44.58	51.55	42.83	42.21	50.41	52.48	44.58	3.79	2.93	39.07	44.58	44.60	62.10
Or	1.91	1.35	3.03	2.84	2.65	1.59	1.35	2.21	1.37	1.45	2.59	2.73	1.35	0.40	0.23	1.52	1.35	0.60	2.55

Sample	MIC-16-17	MIC-16-22	MIC-16-22	MIC-16-22	MIC-16-22	MIC-16-22	MIC-16-22	MIC-16-22	MIC-16-27	MIC-16-27	MIC-16-27	SHB-19-12-62	SHB-19-12-62	SHB-19-12-62	SHB-19-12-62	SHB-19-12-62	SHB-19-12-62
SiO_2	58.62	53.86	52.69	49.96	49.48	49.29	51.98	49.88	67.70	65.98	68.24	65.67	59.37	66.99	66.91	68.36	59.53
TiO_2	0.10	0.59	0.60	0.63	0.59	0.61	0.62	0.58	0.65	0.65	0.65	0.00	0.00	0.00	0.00	0.00	0.00
Al_2O_3	24.60	28.33	28.51	30.37	30.13	30.82	28.89	30.62	19.65	18.64	19.75	20.55	24.39	19.91	20.64	18.89	25.45
FeO	0.19	0.70	0.57	0.84	0.59	0.59	0.27	0.40	0.10	2.07	0.24	0.46	0.60	0.10	0.08	0.09	0.06
CaO	7.52	11.37	12.35	14.17	14.08	14.39	12.38	14.11	0.25	1.59	0.15	1.88	6.85	1.44	1.89	0.29	7.30
Na_2O	7.06	5.13	4.51	3.61	3.45	3.13	4.49	3.74	11.70	8.87	10.79	9.77	7.27	10.33	10.24	10.94	6.97
K_2O	0.49	0.20	0.12	0.08	0.10	0.08	0.12	0.09	0.01	0.10	0.01	0.14	0.07	0.07	0.11	0.05	0.26
Total	98.67	99.79	98.95	99.15	98.01	98.52	98.26	99.09	99.38	98.01	98.92	99.00	98.99	98.86	99.91	98.81	99.81
8 (O) basis																	
Si	10.64	9.76	9.64	9.72	9.20	9.12	9.57	9.18	11.85	9.72	11.92	11.67	10.72	11.85	11.74	12.06	10.65
Ti	0.01	0.08	0.08	0.02	0.08	0.09	0.09	0.08	0.09	0.02	0.09	0.00	0.00	0.00	0.00	0.00	0.00
Al	5.26	6.05	6.15	6.16	6.60	6.72	6.27	6.64	4.05	6.16	4.06	4.30	5.19	4.15	4.27	3.93	5.37
Fe	0.03	0.11	0.09	0.01	0.09	0.09	0.04	0.06	0.01	0.01	0.03	0.07	0.09	0.01	0.01	0.01	0.01
Ca	1.46	2.21	2.42	2.29	2.80	2.85	2.44	2.78	0.05	2.29	0.03	0.36	1.33	0.27	0.35	0.06	1.40
Na	2.48	1.80	1.60	1.88	1.25	1.12	1.60	1.34	3.97	1.88	3.65	3.36	2.55	3.54	3.48	3.74	2.42
K	0.11	0.05	0.03	0.06	0.02	0.02	0.03	0.02	0.00	0.06	0.00	0.03	0.02	0.02	0.02	0.01	0.06
An	36.03	54.40	59.80	54.07	68.84	71.39	59.94	67.25	1.16	54.07	0.78	9.51	34.09	7.14	9.18	1.45	36.12
Ab	61.17	44.46	39.51	44.58	30.57	28.12	39.35	32.27	98.79	44.58	99.14	89.67	65.49	92.44	90.20	98.24	62.36
Or	2.80	1.14	0.69	1.35	0.59	0.49	0.71	0.48	0.04	1.35	0.09	0.82	0.42	0.42	0.62	0.31	1.52

Sample	SHB-19 -12-67	SHB-19 -12-67	SHB-19 -12-67	SHB-19 -12-67	SHB-19 -12-67	SHB-19 -12-67	SHB-19 -12-67
SiO_2	58.17	58.20	57.65	58.18	57.38	57.61	56.38
TiO_2	0.06	0.04	0.02	0.02	0.06	0.03	0.02
Al_2O_3	26.52	26.55	26.23	26.16	26.34	26.39	26.70
FeO	0.26	0.27	0.22	0.07	0.16	0.29	0.14
CaO	9.23	9.15	8.97	9.12	9.38	9.21	10.04
Na_2O	5.92	6.03	6.22	6.23	6.14	6.05	5.63
K_2O	0.57	0.45	0.38	0.41	0.45	0.42	0.40
Total	100.84	100.87	99.98	100.31	100.10	100.11	99.38
8 (O) basis							
Si	10.37	10.36	10.36	10.41	10.32	10.34	10.22
Ti	0.01	0.01	0.00	0.00	0.01	0.00	0.00
Al	5.57	5.57	5.56	5.52	5.58	5.58	5.70
Fe	0.04	0.04	0.03	0.01	0.02	0.04	0.02
Ca	1.76	1.75	1.73	1.75	1.81	1.77	1.95
Na	2.05	2.08	2.17	2.16	2.14	2.11	1.98
K	0.13	0.10	0.09	0.09	0.10	0.10	0.09
An	44.73	44.43	43.38	43.67	44.60	44.59	48.51
Ab	51.96	52.96	54.42	54.01	52.86	53.00	49.21
Or	3.30	2.61	2.20	2.32	2.54	2.41	2.27

Notes: Sample - Betjharan section (MIC/16/03, MIC/16/04 – noritic gabbro; MIC/16/05, MIC/16/06/, MIC/16/07, MIC/16/08, MIC/16/16, MIC/16/17, MIC/16/22, MIC/16/27 – gabbro); Hatichhad section (SHB/19-12/62 – anorthosite; SHB/19-12/67 – gabbro).

Table. 3. EPMA major element (wt. %) compositions of pyroxenes from the gabbro-norite-anorthosites of the Mayurbhanj Complex.

Sample	MIC-16-03	MIC-16-03	MIC-16-03	MIC-16-03	MIC-16-03	MIC-16-03	MIC-16-03	MIC-16-03	MIC-16-03	MIC-16-04	MIC-16-04	MIC-16-04	MIC-16-04	MIC-16-04	MIC-16-04	MIC-16-04	MIC-16-04	MIC-16-04	MIC-16-04
SiO_2	54.63	53.38	52.75	54.18	54.51	53.86	53.95	53.22	50.19	52.69	51.80	54.29	52.58	50.19	50.07	52.11	51.97	50.42	50.92
TiO_2	0.01	0.02	0.04	0.03	0.03	0.04	0.01	0.02	0.70	0.22	0.15	0.16	0.20	0.55	0.60	0.21	0.32	0.60	0.73
Al_2O_3	1.12	1.63	1.37	1.81	1.75	1.60	1.75	1.62	1.37	1.34	1.25	1.19	1.35	1.91	2.40	1.62	1.16	1.92	1.62
Cr_2O_3	0.12	0.01	0.20	0.32	0.29	0.05	0.30	0.29	0.18	0.14	0.16	0.15	0.09	0.10	0.05	0.15	0.07	0.06	0.05
Fe_2O_3	2.32	1.67	2.15	0.43	0.67	0.88	0.26	0.49	3.06	1.53	5.17	2.22	2.33	2.80	4.41	4.30	2.82	3.17	2.45
FeO	10.42	11.17	14.92	9.82	10.17	10.93	9.86	12.18	7.02	16.41	10.50	11.18	16.42	7.77	10.13	11.08	17.60	8.72	10.73
MnO	0.04	0.02	0.03	0.02	0.05	0.08	0.10	0.05	0.00	0.34	0.23	0.25	0.27	0.07	0.28	0.33	0.12	0.15	0.25
MgO	28.86	27.49	25.20	29.03	28.93	28.65	28.69	27.05	14.18	24.57	26.77	28.30	24.28	14.03	14.67	26.72	23.54	14.26	14.69
CaO	2.27	2.44	2.17	2.12	2.25	1.64	2.39	2.18	20.39	1.87	2.46	2.15	2.22	19.95	17.24	2.44	1.86	19.18	17.48
Na_2O	0.07	0.06	0.07	0.06	0.08	0.01	0.03	0.04	0.44	0.04	0.06	0.09	0.04	0.45	0.37	0.07	0.06	0.40	0.41
K_2O	0.07	0.07	0.05	0.08	0.05	0.07	0.07	0.08	0.06	0.03	0.06	0.01	0.01	0.01	0.01	0.00	0.02	0.04	0.01
V_2O_3	-	-	-	-	-	-	-	-	-	-	-	-	-	-	-	-	-	-	-
Total	99.92	97.98	98.95	97.89	98.79	97.80	97.41	97.23	97.59	99.18	98.63	100.00	99.78	97.83	100.22	99.04	99.55	98.91	99.35
6 (O) basis																			
Si	1.95	1.95	1.94	1.95	1.95	1.95	1.96	1.96	1.92	1.94	1.90	1.94	1.93	1.92	1.88	1.90	1.93	1.91	1.92
Ti	0.00	0.00	0.00	0.00	0.00	0.00	0.00	0.00	0.02	0.01	0.00	0.00	0.01	0.02	0.02	0.01	0.01	0.02	0.02
Al	0.05	0.07	0.06	0.08	0.07	0.07	0.07	0.07	0.06	0.06	0.05	0.05	0.06	0.09	0.11	0.07	0.05	0.09	0.07
Cr	0.00	0.00	0.01	0.01	0.01	0.00	0.01	0.01	0.01	0.00	0.00	0.00	0.00	0.00	0.00	0.00	0.00	0.00	0.00
Fe^{3+}	0.06	0.05	0.06	0.01	0.02	0.02	0.01	0.01	0.09	0.04	0.14	0.06	0.06	0.08	0.12	0.12	0.08	0.09	0.07
Fe^{2+}	0.31	0.34	0.46	0.30	0.30	0.33	0.30	0.37	0.22	0.51	0.32	0.33	0.51	0.25	0.32	0.34	0.55	0.28	0.34
Mn	0.00	0.00	0.00	0.00	0.00	0.00	0.00	0.00	0.00	0.01	0.01	0.01	0.01	0.00	0.01	0.01	0.00	0.00	0.01
Mg	1.53	1.49	1.38	1.56	1.55	1.55	1.55	1.48	0.81	1.35	1.46	1.51	1.33	0.80	0.82	1.45	1.30	0.81	0.83
Ca	0.09	0.10	0.09	0.08	0.09	0.06	0.09	0.09	0.84	0.07	0.10	0.08	0.09	0.82	0.69	0.10	0.07	0.78	0.71
Na	0.00	0.00	0.00	0.00	0.01	0.00	0.00	0.00	0.03	0.00	0.00	0.01	0.00	0.03	0.03	0.01	0.00	0.03	0.03
K	0.00	0.00	0.00	0.00	0.00	0.00	0.00	0.00	0.00	0.00	0.00	0.00	0.00	0.00	0.00	0.00	0.00	0.00	0.00
V	-	-	-	-	-	-	-	-	-	-	-	-	-	-	-	-	-	-	-

En	79.42	77.37	71.73	80.51	79.81	79.67	79.84	76.30	43.27	69.96	77.74	78.35	69.19	42.88	44.81	77.04	67.74	43.30	44.15
Fs	16.09	17.70	23.83	15.27	15.74	17.05	15.39	19.27	12.02	26.22	17.12	17.36	26.25	13.32	17.35	17.92	28.41	14.85	18.09
Wo	4.49	4.94	4.44	4.22	4.45	3.29	4.77	4.43	44.71	3.82	5.14	4.29	4.55	43.81	37.84	5.05	3.85	41.85	37.76
Mg#	83.16	81.44	75.06	84.06	83.53	82.37	83.84	79.83	78.25	72.74	81.96	81.86	72.49	76.30	72.09	81.13	70.45	74.46	70.93

Sample	MIC-16-04	MIC-16-04	MIC-16-04	MIC-16-04	MIC-16-04	MIC-16-04	MIC-16-04	MIC-16-05	MIC-16-05	MIC-16-05	MIC-16-05	MIC-16-05	MIC-16-05	MIC-16-05	MIC-16-05	MIC-16-05	MIC-16-05	MIC-16-05	MIC-16-05
SiO_2	53.16	51.35	52.16	51.63	50.35	51.44	50.77	51.59	51.10	52.63	50.96	52.42	53.54	51.35	50.71	50.07	51.23	50.67	52.45
TiO_2	0.11	0.32	0.21	0.18	0.69	0.26	0.65	0.20	0.36	0.16	0.34	0.17	0.19	0.46	0.45	0.67	0.36	0.46	0.21
Al_2O_3	1.24	1.06	1.57	1.10	1.94	0.77	1.47	1.16	1.14	1.06	1.04	1.09	1.13	1.04	2.41	1.99	1.79	2.25	1.49
Cr_2O_3	0.39	0.06	0.21	0.15	0.07	0.11	0.13	0.08	0.08	0.08	0.06	0.11	0.12	0.03	0.40	0.11	0.18	0.32	0.09
Fe_2O_3	1.74	3.40	3.04	2.55	2.91	3.75	3.90	3.29	4.41	1.52	3.00	4.64	1.74	2.35	3.76	4.00	2.39	3.74	3.15
FeO	12.26	18.38	16.11	19.80	9.42	7.51	8.93	17.67	18.57	18.12	20.03	12.92	14.54	18.85	5.53	7.59	11.27	7.77	11.85
MnO	0.17	0.34	0.24	0.45	0.14	0.21	0.30	0.26	0.43	0.29	0.57	0.28	0.18	0.46	0.11	0.27	0.20	0.25	0.22
MgO	26.96	22.62	24.09	21.87	14.65	13.95	14.25	22.98	22.00	23.32	21.12	26.02	25.85	22.28	16.81	13.50	18.56	15.88	26.70
CaO	2.20	1.53	2.26	1.84	17.97	21.55	19.05	2.12	2.17	2.15	1.97	2.25	2.35	1.92	18.64	20.49	12.35	17.69	2.37
Na_2O	0.07	0.08	0.07	0.06	0.44	0.32	0.48	0.05	0.08	0.07	0.08	0.08	0.08	0.05	0.34	0.49	0.25	0.43	0.04
K_2O	0.02	0.10	0.00	0.01	0.03	0.03	0.02	0.00	0.02	0.01	0.04	0.01	0.00	0.02	0.00	0.01	0.01	0.01	0.01
V_2O_3	-	-	-	-	-	-	-	-	-	-	-	-	-	-	-	-	-	-	-
Total	98.30	99.25	99.96	99.63	98.61	99.90	99.95	99.40	100.36	99.40	99.20	99.98	99.73	98.82	99.16	99.19	98.60	99.46	98.56
6 (O) basis																			
Si	1.94	1.92	1.92	1.93	1.91	1.93	1.91	1.92	1.90	1.95	1.93	1.91	1.95	1.93	1.89	1.90	1.92	1.90	1.92
Ti	0.00	0.01	0.01	0.01	0.02	0.01	0.02	0.01	0.01	0.00	0.01	0.00	0.01	0.01	0.01	0.02	0.01	0.01	0.01
Al	0.05	0.05	0.07	0.05	0.09	0.03	0.06	0.05	0.05	0.05	0.05	0.05	0.05	0.05	0.11	0.09	0.08	0.10	0.06
Cr	0.01	0.00	0.01	0.00	0.00	0.00	0.00	0.00	0.00	0.00	0.00	0.00	0.00	0.00	0.01	0.00	0.01	0.01	0.00
Fe^{3+}	0.05	0.10	0.08	0.07	0.08	0.11	0.11	0.09	0.12	0.04	0.09	0.13	0.05	0.07	0.11	0.11	0.07	0.11	0.09
Fe^{2+}	0.37	0.58	0.50	0.62	0.30	0.24	0.28	0.55	0.58	0.56	0.63	0.39	0.44	0.59	0.17	0.24	0.35	0.24	0.36
Mn	0.01	0.01	0.01	0.01	0.00	0.01	0.01	0.01	0.01	0.01	0.02	0.01	0.01	0.01	0.00	0.01	0.01	0.01	0.01
Mg	1.47	1.26	1.32	1.22	0.83	0.78	0.80	1.28	1.22	1.29	1.19	1.41	1.40	1.25	0.93	0.76	1.04	0.89	1.46
Ca	0.09	0.06	0.09	0.07	0.73	0.87	0.77	0.08	0.09	0.09	0.08	0.09	0.09	0.08	0.74	0.83	0.50	0.71	0.09

Na	0.00	0.01	0.01	0.00	0.03	0.02	0.03	0.00	0.01	0.00	0.01	0.01	0.01	0.00	0.02	0.04	0.02	0.03	0.00
K	0.00	0.00	0.00	0.00	0.00	0.00	0.00	0.00	0.00	0.00	0.00	0.00	0.00	0.00	0.00	0.00	0.00	0.00	0.00
V	-	-	-	-	-	-	-	-	-	-	-	-	-	-	-	-	-	-	-
En	76.13	66.48	69.32	63.76	44.59	41.45	43.25	66.78	64.75	66.57	62.54	74.58	72.42	65.09	50.46	41.55	54.97	48.18	76.18
Fs	19.41	30.30	26.00	32.39	16.09	12.52	15.20	28.80	30.66	29.01	33.27	20.78	22.85	30.89	9.32	13.10	18.72	13.24	18.97
Wo	4.46	3.22	4.67	3.85	39.32	46.03	41.55	4.42	4.59	4.41	4.19	4.63	4.73	4.02	40.23	45.34	26.30	38.58	4.86
Mg#	79.68	68.69	72.72	66.31	73.49	76.81	74.00	69.87	67.87	69.65	65.28	78.21	76.01	67.82	84.41	76.02	74.59	78.45	80.07

Sample	MIC-16-05	MIC-16-05	MIC-16-05	MIC-16-06	MIC-16-06	MIC-16-06	MIC-16-06	MIC-16-06	MIC-16-06	MIC-16-06	MIC-16-06	MIC-16-06	MIC-16-06	MIC-16-06	MIC-16-06	MIC-16-06	MIC-16-06	MIC-16-06
SiO_2	51.79	49.08	50.23	51.29	51.37	50.45	49.67	50.23	50.80	50.23	51.06	50.70	51.62	51.24	49.90	50.18	52.75	50.15
TiO_2	0.31	0.69	0.65	0.44	0.20	0.54	0.66	0.45	0.40	0.40	0.57	0.51	0.22	0.41	0.67	0.43	0.25	0.44
Al_2O_3	1.03	1.69	1.59	2.19	1.29	2.02	1.80	1.21	2.18	2.19	2.06	2.49	1.20	0.98	1.86	2.51	1.28	2.36
Cr_2O_3	0.06	0.13	0.13	0.13	0.15	0.09	0.14	0.01	0.07	0.00	0.08	0.11	0.12	0.01	0.00	0.39	0.07	0.03
Fe_2O_3	3.39	6.34	4.21	1.42	3.74	2.53	4.66	4.07	2.04	4.69	2.12	3.27	0.63	2.47	3.55	2.43	1.82	4.50
FeO	19.90	6.31	10.01	8.01	19.35	10.43	9.09	8.53	9.28	5.31	12.83	6.47	20.37	20.50	9.63	4.77	16.81	6.78
MnO	0.20	0.28	0.19	0.23	0.48	0.44	0.30	0.25	0.10	0.13	0.23	0.18	0.19	0.42	0.28	0.10	0.33	0.19
MgO	22.35	14.12	15.73	14.35	22.58	13.69	14.72	13.72	15.77	15.92	16.20	15.28	21.77	21.23	13.61	15.40	24.26	14.77
CaO	1.58	19.86	15.94	20.38	0.96	18.27	17.47	19.70	17.16	19.31	14.01	19.58	1.72	1.83	18.67	20.65	1.94	19.57
Na_2O	0.04	0.44	0.42	0.38	0.05	0.45	0.42	0.42	0.35	0.40	0.36	0.45	0.07	0.11	0.47	0.35	0.09	0.42
K_2O	0.01	0.02	0.01	0.00	0.01	0.01	0.01	0.01	0.00	0.01	0.01	0.01	0.01	0.01	0.01	0.00	0.01	0.01
V_2O_3	-	-	-	-	-	-	-	-	-	-	-	-	-	-	-	-	-	-
Total	100.66	98.96	99.12	98.82	100.19	98.92	98.94	98.61	98.15	98.59	99.53	99.05	97.93	99.21	98.63	97.21	99.61	99.22
6 (O) basis																		
Si	1.92	1.87	1.90	1.93	1.91	1.92	1.89	1.92	1.92	1.89	1.92	1.90	1.96	1.94	1.91	1.90	1.94	1.89
Ti	0.01	0.02	0.02	0.01	0.01	0.02	0.02	0.01	0.01	0.01	0.02	0.01	0.01	0.01	0.02	0.01	0.01	0.01
Al	0.05	0.08	0.07	0.10	0.06	0.09	0.08	0.05	0.10	0.10	0.09	0.11	0.05	0.04	0.08	0.11	0.06	0.10
Cr	0.00	0.00	0.00	0.00	0.00	0.00	0.00	0.00	0.00	0.00	0.00	0.00	0.00	0.00	0.00	0.01	0.00	0.00
Fe^{3+}	0.09	0.18	0.12	0.04	0.10	0.07	0.13	0.12	0.06	0.13	0.06	0.09	0.02	0.07	0.10	0.07	0.05	0.13
Fe^{2+}	0.62	0.20	0.32	0.25	0.60	0.33	0.29	0.27	0.29	0.17	0.40	0.20	0.65	0.65	0.31	0.15	0.52	0.21

Mn	0.01	0.01	0.01	0.01	0.02	0.01	0.01	0.01	0.00	0.00	0.01	0.01	0.01	0.01	0.01	0.00	0.01	0.01
Mg	1.24	0.80	0.89	0.81	1.25	0.78	0.83	0.78	0.89	0.89	0.91	0.85	1.23	1.20	0.77	0.87	1.33	0.83
Ca	0.06	0.81	0.65	0.82	0.04	0.74	0.71	0.81	0.70	0.78	0.56	0.79	0.07	0.07	0.76	0.84	0.08	0.79
Na	0.00	0.03	0.03	0.03	0.00	0.03	0.03	0.03	0.03	0.03	0.03	0.03	0.00	0.01	0.03	0.03	0.01	0.03
K	0.00	0.00	0.00	0.00	0.00	0.00	0.00	0.00	0.00	0.00	0.00	0.00	0.00	0.00	0.00	0.00	0.00	0.00
V	-	-	-	-	-	-	-	-	-	-	-	-	-	-	-	-	-	-
En	64.50	44.21	47.95	42.86	66.17	41.91	45.47	42.00	47.36	48.57	48.40	46.31	63.22	62.36	41.97	46.77	69.15	45.26
Fs	32.22	11.09	17.13	13.42	31.80	17.91	15.75	14.65	15.62	9.09	21.50	11.01	33.18	33.78	16.66	8.13	26.88	11.65
Wo	3.28	44.70	34.92	43.72	2.03	40.19	38.78	43.35	37.02	42.34	30.10	42.67	3.60	3.86	41.37	45.10	3.97	43.10
Mg#	66.69	79.95	73.68	76.15	67.54	70.06	74.27	74.14	75.19	84.23	69.24	80.79	65.58	64.86	71.59	85.20	72.01	79.53

Sample	MIC-16-06	MIC-16-06	MIC-16-07	MIC-16-07	MIC-16-07	MIC-16-07	MIC-16-07	MIC-16-07	MIC-16-07	MIC-16-07	MIC-16-07	MIC-16-07	MIC-16-07	MIC-16-07	MIC-16-07	MIC-16-07	MIC-16-08	MIC-16-08	MIC-16-08
SiO_2	50.58	51.93	51.60	51.75	51.00	51.39	51.77	50.83	50.38	50.94	52.18	52.17	52.32	51.73	51.93	51.94	51.49	50.15	50.90
TiO_2	0.37	0.18	0.34	0.45	0.07	0.08	0.07	0.10	0.09	0.55	0.26	0.29	0.31	0.24	0.25	0.33	0.02	0.11	0.09
Al_2O_3	2.26	1.21	0.78	0.63	2.25	1.47	1.82	1.77	1.92	0.40	1.05	1.37	1.26	1.05	1.02	1.06	2.14	2.19	1.19
Cr_2O_3	0.07	0.13	0.05	0.06	0.26	0.00	0.18	0.01	0.06	0.05	0.05	0.01	0.07	0.04	0.08	0.03	0.05	0.03	0.04
Fe_2O_3	3.05	3.01	2.44	1.35	1.97	2.65	1.41	2.26	4.11	2.24	1.24	0.92	0.63	2.15	1.35	0.34	2.82	4.77	3.39
FeO	7.89	13.81	8.06	9.23	9.12	11.81	8.22	12.16	7.58	8.68	20.07	17.62	17.35	20.43	20.93	20.94	9.45	8.15	10.82
MnO	0.10	0.13	0.20	0.14	0.13	0.11	0.09	0.30	0.09	0.20	0.30	0.21	0.11	0.36	0.32	0.49	0.09	0.11	0.24
MgO	16.44	25.51	13.57	13.22	13.84	14.10	13.17	14.99	13.77	12.94	22.10	23.26	23.33	21.54	21.57	21.32	13.32	13.17	13.78
CaO	17.19	1.90	21.81	21.57	19.58	17.44	21.54	15.52	20.37	21.81	2.00	2.38	2.68	1.95	1.86	2.05	20.46	20.61	18.33
Na_2O	0.32	0.08	0.32	0.37	0.42	0.44	0.54	0.37	0.40	0.31	0.04	0.04	0.07	0.07	0.05	0.05	0.43	0.40	0.37
K_2O	0.01	0.01	0.05	0.00	0.03	0.04	0.03	0.03	0.04	0.03	0.03	0.04	0.01	0.03	0.01	0.04	0.03	0.02	0.03
V_2O_3	-	-	-	-	-	-	-	-	-	-	-	-	-	-	-	-	-	-	-
Total	98.26	97.90	99.21	98.78	98.67	99.52	98.84	98.33	98.82	98.15	99.33	98.30	98.13	99.58	99.35	98.59	100.30	99.72	99.18
6 (O) basis																			
Si	1.91	1.93	1.95	1.97	1.93	1.94	1.96	1.94	1.91	1.95	1.95	1.95	1.96	1.94	1.95	1.96	1.93	1.89	1.94
Ti	0.01	0.01	0.01	0.01	0.00	0.00	0.00	0.00	0.00	0.02	0.01	0.01	0.01	0.01	0.01	0.01	0.00	0.00	0.00
Al	0.10	0.05	0.03	0.03	0.10	0.07	0.08	0.08	0.09	0.02	0.05	0.06	0.06	0.05	0.05	0.05	0.09	0.10	0.05

Cr	0.00	0.00	0.00	0.00	0.01	0.00	0.01	0.00	0.00	0.00	0.00	0.00	0.00	0.00	0.00	0.00	0.00	0.00	0.00
Fe^{3+}	0.09	0.08	0.07	0.04	0.06	0.08	0.04	0.06	0.12	0.06	0.03	0.03	0.02	0.06	0.04	0.01	0.08	0.14	0.10
Fe^{2+}	0.25	0.43	0.25	0.29	0.29	0.37	0.26	0.39	0.24	0.28	0.63	0.55	0.54	0.64	0.66	0.66	0.30	0.26	0.34
Mn	0.00	0.00	0.01	0.00	0.00	0.00	0.00	0.01	0.00	0.01	0.01	0.01	0.00	0.01	0.01	0.02	0.00	0.00	0.01
Mg	0.92	1.41	0.76	0.75	0.78	0.79	0.74	0.85	0.78	0.74	1.23	1.30	1.30	1.21	1.21	1.20	0.74	0.74	0.78
Ca	0.69	0.08	0.88	0.88	0.79	0.71	0.87	0.63	0.83	0.90	0.08	0.10	0.11	0.08	0.07	0.08	0.82	0.83	0.75
Na	0.02	0.01	0.02	0.03	0.03	0.03	0.04	0.03	0.03	0.02	0.00	0.00	0.01	0.00	0.00	0.00	0.03	0.03	0.03
K	0.00	0.00	0.00	0.00	0.00	0.00	0.00	0.00	0.00	0.00	0.00	0.00	0.00	0.00	0.00	0.00	0.00	0.00	0.00
V	-	-	-	-	-	-	-	-	-	-	-	-	-	-	-	-	-	-	-
En	49.49	73.67	40.19	39.01	41.90	42.39	39.59	45.46	42.15	38.65	63.52	66.74	66.67	62.62	62.26	61.72	39.95	40.46	41.72
Fs	13.32	22.38	13.39	15.27	15.49	19.92	13.86	20.69	13.02	14.54	32.36	28.36	27.82	33.31	33.89	34.01	15.91	14.05	18.38
Wo	37.19	3.95	46.43	45.72	42.61	37.70	46.55	33.84	44.82	46.81	4.13	4.90	5.51	4.07	3.86	4.27	44.13	45.49	39.90
Mg#	78.79	76.70	75.01	71.87	73.00	68.03	74.07	68.72	76.39	72.67	66.25	70.18	70.56	65.28	64.75	64.47	71.51	74.23	69.42

Sample	MIC-16-08	MIC-16-08	MIC-16-08	MIC-16-08	MIC-16-08	MIC-16-08	MIC-16-08	MIC-16-08	MIC-16-08	MIC-16-16	MIC-16-16	MIC-16-16	MIC-16-16	MIC-16-16	MIC-16-16	MIC-16-16	MIC-16-16	MIC-16-16
SiO_2	51.71	51.39	51.45	51.86	50.77	50.65	51.37	50.61	50.96	51.57	51.76	53.69	51.05	51.48	53.61	51.15	51.27	54.56
TiO_2	0.29	0.27	0.24	0.19	0.03	0.04	0.09	0.09	0.07	0.43	0.51	0.61	0.12	0.50	0.62	0.49	0.51	0.61
Al_2O_3	2.20	2.34	2.37	2.12	2.19	2.19	2.23	2.07	1.92	3.12	2.16	1.37	2.24	1.88	1.55	2.76	2.73	1.21
Cr_2O_3	0.27	0.36	0.18	0.09	0.04	0.03	0.07	0.09	0.08	0.54	0.49	0.28	0.49	0.41	0.31	0.38	0.32	0.18
Fe_2O_3	1.63	0.31	2.47	1.65	3.33	2.15	2.43	2.64	2.03	0.34	0.82	0.62	3.30	1.79	0.85	1.01	1.96	0.29
FeO	9.39	9.34	8.13	9.81	10.47	10.92	8.67	11.53	12.13	6.04	5.96	13.32	7.36	9.16	11.52	5.63	5.24	13.31
MnO	0.08	0.04	0.13	0.20	0.20	0.11	0.13	0.09	0.12	0.05	0.00	0.01	0.15	0.11	0.13	0.06	0.00	0.06
MgO	16.89	16.85	15.84	16.20	14.59	14.32	13.65	13.81	13.83	15.99	17.49	27.01	15.49	18.23	27.73	14.82	16.09	27.51
CaO	16.44	15.92	18.59	17.24	17.40	17.43	20.58	17.64	17.45	19.50	18.24	2.24	18.48	14.68	2.35	21.68	20.39	2.30
Na_2O	0.31	0.40	0.28	0.25	0.37	0.35	0.41	0.36	0.36	0.50	0.37	0.06	0.47	0.28	0.10	0.34	0.34	0.06
K_2O	0.01	0.01	0.03	0.02	0.02	0.03	0.03	0.02	0.02	0.05	0.04	0.05	0.05	0.04	0.05	0.04	0.05	0.05
V_2O_3	-	-	-	-	-	-	-	-	-	-	-	-	-	-	-	-	-	-
Total	99.21	97.23	99.71	99.62	99.39	98.22	99.66	98.96	98.98	98.13	97.84	99.25	99.20	98.57	98.81	98.37	98.90	100.14

6 (O) basis

Si	1.93	1.95	1.92	1.93	1.92	1.93	1.93	1.93	1.94	1.93	1.93	1.94	1.91	1.92	1.94	1.92	1.91	1.95
Ti	0.01	0.01	0.01	0.01	0.00	0.00	0.00	0.00	0.00	0.01	0.01	0.02	0.00	0.01	0.02	0.01	0.01	0.02
Al	0.10	0.10	0.10	0.09	0.10	0.10	0.10	0.09	0.09	0.14	0.10	0.06	0.10	0.08	0.07	0.12	0.12	0.05
Cr	0.01	0.01	0.01	0.00	0.00	0.00	0.00	0.00	0.00	0.02	0.01	0.01	0.01	0.01	0.01	0.01	0.01	0.01
Fe^{3+}	0.05	0.01	0.07	0.05	0.09	0.06	0.07	0.08	0.06	0.01	0.02	0.02	0.09	0.05	0.02	0.03	0.05	0.01
Fe^{2+}	0.29	0.30	0.25	0.31	0.33	0.35	0.27	0.37	0.39	0.19	0.19	0.40	0.23	0.29	0.35	0.18	0.16	0.40
Mn	0.00	0.00	0.00	0.01	0.01	0.00	0.00	0.00	0.00	0.00	0.00	0.00	0.00	0.00	0.00	0.00	0.00	0.00
Mg	0.94	0.95	0.88	0.90	0.82	0.81	0.76	0.78	0.78	0.89	0.97	1.46	0.86	1.02	1.49	0.83	0.89	1.47
Ca	0.66	0.65	0.74	0.69	0.70	0.71	0.83	0.72	0.71	0.78	0.73	0.09	0.74	0.59	0.09	0.87	0.81	0.09
Na	0.02	0.03	0.02	0.02	0.03	0.03	0.03	0.03	0.03	0.04	0.03	0.00	0.03	0.02	0.01	0.02	0.02	0.00
K	0.00	0.00	0.00	0.00	0.00	0.00	0.00	0.00	0.00	0.00	0.00	0.00	0.00	0.00	0.00	0.00	0.00	0.00
V	-	-	-	-	-	-	-	-	-	-	-	-	-	-	-	-	-	-
En	49.72	50.24	46.92	47.52	44.25	43.32	40.98	41.91	41.68	47.89	51.53	74.80	47.09	53.74	77.29	44.17	47.76	75.10
Fs	15.50	15.63	13.51	16.14	17.82	18.79	14.61	19.63	20.51	10.15	9.85	20.73	12.54	15.15	18.01	9.41	8.72	20.39
Wo	34.77	34.13	39.57	36.34	37.93	37.89	44.41	38.47	37.80	41.96	38.62	4.47	40.37	31.11	4.70	46.42	43.52	4.52
Mg#	76.23	76.27	77.64	74.65	71.29	70.04	73.72	68.11	67.02	82.52	83.95	78.33	78.96	78.01	81.10	82.43	84.56	78.65

Sample	MIC-16-16	MIC-16-16	MIC-16-16	MIC-16-16	MIC-16-16	MIC-16-16	MIC-16-16	MIC-16-16	MIC-16-16	MIC-16-16	MIC-16-16	MIC-16-17	MIC-16-17	MIC-16-17	MIC-16-17	MIC-16-17	MIC-16-17	MIC-16-17	MIC-16-17
SiO_2	54.50	52.37	52.46	51.28	52.22	53.36	53.39	53.73	53.26	53.46	53.87	52.03	51.50	51.45	53.23	53.27	50.73	51.15	54.67
TiO_2	0.60	0.42	0.43	0.43	0.50	0.66	0.60	0.62	0.64	0.60	0.63	0.20	0.13	0.17	0.12	0.07	0.37	0.22	0.01
Al_2O_3	1.11	2.26	2.36	2.10	1.77	1.30	1.30	0.88	1.26	1.25	1.75	2.23	2.22	2.67	1.37	1.30	2.37	2.55	1.23
Cr_2O_3	0.00	0.27	0.30	0.27	0.16	0.14	0.01	0.01	0.10	0.08	0.37	0.20	0.04	0.55	0.22	0.25	0.06	0.00	0.14
Fe_2O_3	0.38	0.12	1.44	1.60	0.54	1.91	1.41	0.02	1.48	0.67	0.61	0.10	1.98	1.68	0.44	1.26	1.73	1.19	0.85
FeO	12.74	7.51	6.15	8.03	7.30	11.46	10.95	12.76	13.11	13.78	12.34	10.74	9.75	10.08	16.66	15.71	9.81	8.21	12.79
MnO	0.11	0.03	0.22	0.11	0.06	0.18	0.09	0.06	0.16	0.01	0.25	0.16	0.06	0.08	0.03	0.10	0.20	0.23	0.04
MgO	27.69	17.35	16.98	14.93	18.81	27.70	28.07	27.45	26.80	26.39	27.41	16.37	15.12	15.14	24.57	24.91	14.90	14.92	27.54
CaO	2.32	17.98	19.49	19.20	16.18	2.23	2.27	2.14	2.16	2.30	2.31	15.97	17.75	17.63	2.19	2.37	17.42	18.95	2.26
Na_2O	0.08	0.30	0.29	0.48	0.25	0.08	0.05	0.03	0.06	0.11	0.08	0.36	0.40	0.36	0.04	0.05	0.42	0.41	0.07
K_2O	0.05	0.04	0.05	0.04	0.04	0.05	0.06	0.05	0.05	0.06	0.06	0.05	0.10	0.09	0.09	0.09	0.06	0.04	0.07

V_2O_3	-	-	-	-	-	-	-	-	-	-	-	-	-	-	-	-	-	-	-
Total	99.58	98.64	100.17	98.47	97.82	99.08	98.18	97.77	99.08	98.71	99.69	98.41	99.06	99.90	98.96	99.38	98.06	97.88	99.67
6 (O) basis																			
Si	1.96	1.94	1.92	1.93	1.95	1.93	1.94	1.97	1.94	1.95	1.94	1.96	1.94	1.92	1.96	1.95	1.93	1.94	1.96
Ti	0.02	0.01	0.01	0.01	0.01	0.02	0.02	0.02	0.02	0.02	0.02	0.01	0.00	0.00	0.00	0.00	0.01	0.01	0.00
Al	0.05	0.10	0.10	0.09	0.08	0.06	0.06	0.04	0.05	0.05	0.07	0.10	0.10	0.12	0.06	0.06	0.11	0.11	0.05
Cr	0.00	0.01	0.01	0.01	0.00	0.00	0.00	0.00	0.00	0.00	0.01	0.01	0.00	0.02	0.01	0.01	0.00	0.00	0.00
Fe^{3+}	0.01	0.00	0.04	0.05	0.02	0.05	0.04	0.00	0.04	0.02	0.02	0.00	0.06	0.05	0.01	0.03	0.05	0.03	0.02
Fe^{2+}	0.38	0.23	0.19	0.25	0.23	0.35	0.33	0.39	0.40	0.42	0.37	0.34	0.31	0.31	0.51	0.48	0.31	0.26	0.38
Mn	0.00	0.00	0.01	0.00	0.00	0.01	0.00	0.00	0.01	0.00	0.01	0.01	0.00	0.00	0.00	0.00	0.01	0.01	0.00
Mg	1.48	0.96	0.93	0.84	1.05	1.49	1.52	1.50	1.45	1.44	1.47	0.92	0.85	0.84	1.35	1.36	0.84	0.84	1.48
Ca	0.09	0.72	0.77	0.78	0.65	0.09	0.09	0.08	0.08	0.09	0.09	0.64	0.72	0.70	0.09	0.09	0.71	0.77	0.09
Na	0.01	0.02	0.02	0.04	0.02	0.01	0.00	0.00	0.00	0.01	0.01	0.03	0.03	0.03	0.00	0.00	0.03	0.03	0.01
K	0.00	0.00	0.00	0.00	0.00	0.00	0.00	0.00	0.00	0.00	0.00	0.00	0.00	0.00	0.00	0.00	0.00	0.00	0.00
V	-	-	-	-	-	-	-	-	-	-	-	-	-	-	-	-	-	-	-
En	75.86	50.32	49.32	44.92	54.47	77.52	78.32	75.94	75.06	73.77	76.15	48.33	45.34	45.24	69.23	70.32	45.25	45.01	75.78
Fs	19.58	12.21	10.01	13.55	11.86	17.99	17.14	19.81	20.60	21.61	19.23	17.78	16.40	16.90	26.33	24.88	16.71	13.89	19.75
Wo	4.57	37.47	40.67	41.53	33.67	4.49	4.54	4.26	4.34	4.61	4.62	33.89	38.26	37.86	4.44	4.80	38.04	41.10	4.48
Mg#	79.49	80.47	83.12	76.83	82.12	81.16	82.05	79.31	78.47	77.34	79.83	73.10	73.43	72.81	72.45	73.87	73.03	76.41	79.33

Sample	MIC-16-17	MIC-16-17	MIC-16-17	MIC-16-17	MIC-16-17	MIC-16-22	MIC-16-22	MIC-16-22	MIC-16-22	MIC-16-27	MIC-16-27	MIC-16-27	MIC-16-27	MIC-16-27	MIC-16-27	SHB-19-12-62	SHB-19-12-62	SHB-19-12-62	SHB-19-12-62
SiO_2	54.10	52.95	52.07	52.58	51.06	51.02	52.05	51.35	50.21	49.92	50.10	51.07	50.71	50.83	50.61	52.43	52.28	52.63	51.92
TiO_2	0.03	0.14	0.25	0.03	0.30	0.37	0.39	0.28	0.02	0.10	0.20	0.07	0.14	0.15	0.12	0.07	0.03	0.03	0.03
Al_2O_3	1.08	1.17	1.10	1.13	0.95	2.76	2.28	2.17	2.47	3.22	3.32	1.89	1.90	2.55	2.21	2.98	0.81	1.84	0.91
Cr_2O_3	0.00	0.28	0.26	0.22	0.24	1.14	0.19	0.04	0.01	0.19	0.32	0.12	0.08	0.06	0.08	0.01	0.07	0.02	0.00
Fe_2O_3	2.22	1.85	1.94	2.04	1.31	2.02	3.11	1.47	2.55	3.87	2.95	3.27	4.44	3.59	3.96	0.00	0.00	0.00	0.00
FeO	12.15	16.70	18.41	14.90	20.17	3.41	5.05	7.42	10.86	5.76	4.82	8.10	8.08	6.93	7.60	17.80	29.87	18.09	26.68
MnO	0.09	0.26	0.34	0.10	0.15	0.12	0.14	0.06	0.30	0.12	0.07	0.19	0.12	0.09	0.14	0.32	0.66	0.17	1.07
MgO	27.66	24.80	22.87	25.10	21.39	17.93	19.00	16.29	13.76	15.40	15.46	15.88	16.17	15.68	15.31	11.41	12.13	11.37	10.56

CaO	2.15	1.55	2.05	2.12	1.99	19.18	17.61	18.77	17.71	19.18	20.38	17.76	17.33	18.99	18.50	12.45	1.19	12.55	5.97
Na_2O	0.04	0.01	0.01	0.04	0.02	0.25	0.19	0.22	0.34	0.38	0.31	0.36	0.31	0.34	0.39	0.34	0.15	0.19	0.06
K_2O	0.07	0.08	0.09	0.08	0.08	0.03	0.02	0.03	0.02	0.04	0.03	0.03	0.03	0.02	0.02	0.10	0.01	0.04	0.04
V_2O_3	-	-	-	-	-	-	-	-	-	-	-	-	-	-	-	0.04	0.00	0.03	0.03
Total	99.59	99.79	99.39	98.33	97.67	98.22	100.04	98.09	98.26	98.17	97.96	98.74	99.31	99.22	98.94	98.15	97.32	97.00	97.28
6 (O) basis																			
Si	1.95	1.94	1.94	1.95	1.95	1.89	1.90	1.93	1.92	1.88	1.89	1.92	1.90	1.90	1.91	2.05	2.12	2.08	2.11
Ti	0.00	0.00	0.01	0.00	0.01	0.01	0.01	0.01	0.00	0.00	0.01	0.00	0.00	0.00	0.00	0.00	0.00	0.00	0.00
Al	0.05	0.05	0.05	0.05	0.04	0.12	0.10	0.10	0.11	0.14	0.15	0.08	0.08	0.11	0.10	0.14	0.04	0.09	0.04
Cr	0.00	0.01	0.01	0.01	0.01	0.03	0.01	0.00	0.00	0.01	0.01	0.00	0.00	0.00	0.00	0.00	0.00	0.00	0.00
Fe^{3+}	0.06	0.05	0.05	0.06	0.04	0.06	0.09	0.04	0.07	0.11	0.08	0.09	0.13	0.10	0.11	0.00	0.00	0.00	0.00
Fe^{2+}	0.37	0.51	0.57	0.46	0.64	0.11	0.15	0.23	0.35	0.18	0.15	0.25	0.25	0.22	0.24	0.58	1.01	0.60	0.91
Mn	0.00	0.01	0.01	0.00	0.00	0.00	0.00	0.00	0.01	0.00	0.00	0.01	0.00	0.00	0.00	0.01	0.02	0.01	0.04
Mg	1.49	1.36	1.27	1.39	1.22	0.99	1.03	0.91	0.78	0.87	0.87	0.89	0.90	0.87	0.86	0.66	0.73	0.67	0.64
Ca	0.08	0.06	0.08	0.08	0.08	0.76	0.69	0.76	0.73	0.78	0.82	0.72	0.70	0.76	0.75	0.52	0.05	0.53	0.26
Na	0.00	0.00	0.00	0.00	0.00	0.02	0.01	0.02	0.03	0.03	0.02	0.03	0.02	0.02	0.03	0.03	0.01	0.01	0.00
K	0.00	0.00	0.00	0.00	0.00	0.00	0.00	0.00	0.00	0.00	0.00	0.00	0.00	0.00	0.00	0.00	0.00	0.00	0.00
V	-	-	-	-	-	-	-	-	-	-	-	-	-	-	-	0.00	0.00	0.00	0.00
En	76.78	70.29	65.40	71.75	62.67	53.32	55.08	47.98	42.23	47.50	47.12	47.85	48.77	47.21	46.57	37.38	40.27	37.11	34.70
Fs	18.92	26.54	30.39	23.89	33.14	5.68	8.22	12.26	18.70	9.96	8.25	13.69	13.66	11.70	12.97	32.72	55.63	33.13	49.20
Wo	4.30	3.17	4.21	4.35	4.19	41.00	36.70	39.75	39.07	42.53	44.63	38.46	37.57	41.09	40.46	29.30	2.85	29.45	14.10
Mg#	80.23	72.59	68.89	75.02	65.41	90.37	87.01	79.64	69.31	82.66	85.11	77.75	78.11	80.14	78.22	52.87	41.45	52.61	40.39

Sample	SHB-19-12-62	SHB-19-12-62	SHB-19-12-62	SHB-19-12-67	SHB-19-12-67	SHB-19-12-67	SHB-19-12-67	SHB-19-12-67	SHB-19-12-67	SHB-19-12-67	SHB-19-12-67	SHB-19-12-67	SHB-19-12-67	SHB-19-12-67	SHB-19-12-67	SHB-19-12-67
SiO_2	52.48	53.06	51.77	49.70	51.00	49.55	49.86	49.49	51.40	50.71	49.64	50.65	49.52	49.93	50.88	48.97
TiO_2	0.03	0.06	0.02	0.09	0.17	0.17	0.30	0.12	0.22	0.27	0.16	0.24	0.10	0.12	0.13	0.08
Al_2O_3	0.33	1.63	0.90	0.33	0.71	0.38	1.32	0.43	0.84	1.05	0.54	0.86	0.35	0.33	0.72	0.25
Cr_2O_3	0.00	0.00	0.00	0.00	0.04	0.01	0.06	0.00	0.10	0.01	0.02	0.00	0.00	0.04	0.01	0.00
Fe_2O_3	0.00	0.00	0.00	0.00	0.25	0.00	0.22	0.00	0.00	0.85	0.00	1.25	0.00	0.00	0.00	0.00

FeO	29.87	18.39	29.62	38.27	18.68	38.64	20.45	38.42	18.73	19.62	36.20	20.79	37.31	34.91	18.79	36.39
MnO	0.92	0.17	1.00	0.68	0.52	0.67	0.64	0.88	0.35	0.38	0.62	0.34	0.83	0.77	0.23	0.97
MgO	12.28	11.99	11.87	9.69	8.11	9.83	8.03	9.37	8.12	8.10	9.47	8.26	9.36	9.47	8.24	9.27
CaO	1.08	12.46	1.09	1.56	20.57	0.98	18.53	1.56	20.69	19.91	2.60	18.92	2.40	4.76	20.78	2.30
Na_2O	0.04	0.21	0.11	0.00	0.21	0.05	0.15	0.00	0.20	0.19	0.03	0.16	0.07	0.05	0.13	0.07
K_2O	0.00	0.02	0.00	0.00	0.02	0.01	0.02	0.00	0.00	0.00	0.05	0.00	0.00	0.01	0.02	0.00
V_2O_3	0.03	0.06	0.01	0.02	0.03	0.00	0.05	0.01	0.04	0.04	0.01	0.01	0.01	0.00	0.02	0.01
Total	97.08	98.20	96.39	100.51	100.39	100.36	99.73	100.29	100.75	101.28	99.33	101.62	100.04	100.38	100.13	98.32
6 (O) basis																
Si	2.14	2.07	2.12	2.01	1.98	2.00	1.96	2.01	1.99	1.96	2.02	1.96	2.01	2.01	1.98	2.02
Ti	0.00	0.00	0.00	0.00	0.00	0.01	0.01	0.00	0.01	0.01	0.00	0.01	0.00	0.00	0.00	0.00
Al	0.02	0.08	0.04	0.02	0.03	0.02	0.06	0.02	0.04	0.05	0.03	0.04	0.02	0.02	0.03	0.01
Cr	0.00	0.00	0.00	0.00	0.00	0.00	0.00	0.00	0.00	0.00	0.00	0.00	0.00	0.00	0.00	0.00
Fe^{3+}	0.00	0.00	0.00	0.00	0.01	0.00	0.01	0.00	0.00	0.02	0.00	0.04	0.00	0.00	0.00	0.00
Fe^{2+}	1.02	0.60	1.02	1.29	0.61	1.31	0.67	1.30	0.61	0.63	1.23	0.67	1.27	1.17	0.61	1.25
Mn	0.03	0.01	0.03	0.02	0.02	0.02	0.02	0.03	0.01	0.01	0.02	0.01	0.03	0.03	0.01	0.03
Mg	0.74	0.70	0.73	0.58	0.47	0.59	0.47	0.57	0.47	0.47	0.57	0.48	0.57	0.57	0.48	0.57
Ca	0.05	0.52	0.05	0.07	0.86	0.04	0.78	0.07	0.86	0.82	0.11	0.78	0.10	0.20	0.87	0.10
Na	0.00	0.02	0.01	0.00	0.02	0.00	0.01	0.00	0.01	0.01	0.00	0.01	0.01	0.00	0.01	0.01
K	0.00	0.00	0.00	0.00	0.00	0.00	0.00	0.00	0.00	0.00	0.00	0.00	0.00	0.00	0.00	0.00
V	0.00	0.00	0.00	0.00	0.00	0.00	0.00	0.00	0.00	0.00	0.00	0.00	0.00	0.00	0.00	0.00
En	40.46	38.22	39.78	29.66	23.99	30.17	24.12	28.79	24.09	23.76	29.58	24.04	28.81	28.76	24.35	29.06
Fs	55.25	32.91	55.69	65.73	31.01	66.52	34.46	66.23	31.18	32.32	63.47	33.97	64.42	59.52	31.14	64.03
Wo	2.57	28.56	2.63	3.42	43.76	2.15	40.00	3.44	44.13	42.01	5.85	39.60	5.32	10.39	44.12	5.18
Mg#	41.52	53.51	40.85	30.71	42.66	30.83	40.20	29.81	43.12	40.98	31.41	39.79	30.42	32.10	43.57	30.65

Notes: Sample - Betjharan section (MIC/16/03, MIC/16/04 - noritic gabbro; MIC/16/05, MIC/16/06/, MIC/16/07, MIC/16/08, MIC/16/16, MIC/16/17, MIC/16/22, MIC/16/27 – gabbro); Hatichhad section (SHB/19-12/62 – anorthosite; SHB/19-12/67 – gabbro).

Table. 4. EPMA major element (wt. %) compositions of magnetite-titanomagnetite from the gabbro-norite-anorthosites and magnetitite ore of the Mayurbhanj Complex.

Sample	MIC-16-03	MIC-16-04	MIC-16-04	MIC-16-04	MIC-16-04	MIC-16-04	MIC-16-04	MIC-16-04	MIC-16-04	MIC-16-05	MIC-16-05	MIC-16-05	MIC-16-05	MIC-16-05	MIC-16-05	MIC-16-05	MIC-16-06	MIC-16-07
TiO_2	0.10	0.41	0.48	0.29	0.38	0.38	0.26	6.88	0.45	0.45	0.44	0.41	0.45	0.45	0.36	0.43	14.53	6.52
Al_2O_3	0.22	0.18	0.23	2.96	0.17	0.18	0.16	0.12	0.19	0.20	0.18	0.20	0.19	0.16	1.17	0.21	1.80	2.19
Cr_2O_3	2.87	1.55	1.36	1.98	1.07	1.37	1.00	1.26	1.68	1.36	1.28	1.31	1.42	1.09	1.16	0.99	0.54	0.75
V_2O_3	-	-	-	-	-	-	-	-	-	-	-	-	-	-	-	-	-	-
Fe_2O_3	63.63	66.43	66.45	62.90	66.37	65.39	67.66	53.68	64.74	65.70	65.27	65.10	66.41	65.77	65.23	66.54	36.64	51.01
FeO	30.20	31.11	31.41	28.54	30.93	30.61	31.24	36.73	30.55	30.94	30.65	30.54	31.11	30.85	31.31	31.12	42.92	36.12
MnO	0.06	0.16	0.04	0.13	0.07	0.07	0.14	0.29	0.12	0.06	0.09	0.05	0.19	0.01	0.03	0.02	0.63	0.40
NiO	0.00	0.00	0.00	0.00	0.00	0.00	0.00	0.00	0.00	0.00	0.00	0.00	0.00	0.00	0.00	0.00	0.48	0.00
MgO	0.03	0.12	0.06	1.78	0.10	0.11	0.07	0.10	0.11	0.09	0.08	0.11	0.10	0.10	0.02	0.11	0.07	0.03
ZnO	-	-	-	-	-	-	-	-	-	-	-	-	-	-	-	-	-	-
Total	97.11	99.97	100.03	98.57	99.09	98.11	100.53	99.06	97.84	98.81	97.99	97.73	99.86	98.43	99.27	99.42	97.62	97.02
32 (O) basis																		
Ti	0.02	0.10	0.11	0.07	0.09	0.09	0.06	1.60	0.11	0.11	0.10	0.10	0.10	0.11	0.08	0.10	3.36	1.53
Al	0.08	0.07	0.08	1.06	0.06	0.07	0.06	0.04	0.07	0.07	0.07	0.07	0.07	0.06	0.43	0.08	0.65	0.80
Cr	0.72	0.38	0.33	0.47	0.26	0.34	0.24	0.31	0.42	0.33	0.32	0.33	0.35	0.27	0.28	0.24	0.13	0.18
V	-	-	-	-	-	-	-	-	-	-	-	-	-	-	-	-	-	-
Fe^{3+}	15.15	15.37	15.37	14.34	15.50	15.41	15.58	12.46	15.30	15.38	15.41	15.40	15.38	15.46	15.13	15.48	8.49	11.96
Fe^{2+}	7.99	8.00	8.07	7.23	8.03	8.02	7.99	9.47	8.02	8.05	8.04	8.03	8.01	8.06	8.07	8.04	11.05	9.41
Mn	0.02	0.04	0.01	0.03	0.02	0.02	0.04	0.07	0.03	0.01	0.03	0.01	0.05	0.00	0.01	0.01	0.16	0.10
Ni	0.00	0.00	0.00	0.00	0.00	0.00	0.00	0.00	0.00	0.00	0.00	0.00	0.00	0.00	0.00	0.00	0.12	0.00
Mg	0.01	0.06	0.03	0.80	0.05	0.05	0.03	0.05	0.05	0.04	0.04	0.05	0.05	0.05	0.01	0.05	0.03	0.01
Zn	-	-	-	-	-	-	-	-	-	-	-	-	-	-	-	-	-	-

Sample	MIC-16-08	MIC-16-08	MIC-16-08	MIC-16-08	MIC-16-08	MIC-16-08	MIC-16-08	MIC-16-16	MIC-16-16	MIC-16-16	MIC-16-16	MIC-16-16	MIC-16-16	MIC-16-16	MIC-16-16	MIC-16-16	MIC-16-16	MIC-16-16
TiO_2	1.52	3.85	1.18	2.63	9.60	0.08	0.11	0.13	0.02	0.03	0.40	0.60	0.10	0.13	0.18	0.24	0.17	5.21

Al_2O_3	0.37	0.69	0.92	1.72	0.90	0.01	0.03	0.03	0.02	0.04	0.09	0.23	0.10	0.09	0.14	0.05	0.31	0.41
Cr_2O_3	0.27	0.25	0.28	0.29	0.30	0.33	0.31	0.78	1.19	1.07	1.03	0.91	0.90	1.00	0.81	0.98	0.93	1.35
V_2O_3	-	-	-	-	-	-	-	-	-	-	-	-	-	-	-	-	-	-
Fe_2O_3	63.59	58.96	64.31	59.81	47.17	67.48	68.65	66.69	65.51	66.66	66.63	64.63	66.73	66.02	67.46	66.65	65.36	55.74
FeO	31.49	33.96	31.74	32.77	38.86	30.50	31.09	30.35	29.76	30.14	30.51	30.31	30.37	30.40	30.51	30.83	29.77	33.67
MnO	0.07	0.05	0.06	0.15	0.36	0.06	0.10	0.05	0.06	0.04	0.11	0.07	0.01	0.00	0.04	0.02	0.13	0.18
NiO	0.00	0.00	0.00	0.00	0.00	0.00	0.00	0.21	0.26	0.36	0.56	0.21	0.31	0.00	0.57	0.00	0.15	0.75
MgO	0.10	0.03	0.02	0.04	0.02	0.06	0.03	0.02	0.01	0.03	0.04	0.10	0.01	0.04	0.03	0.04	0.18	0.45
ZnO	-	-	-	-	-	-										-	-	-
Total	97.41	97.78	98.50	97.40	97.21	98.51	100.32	98.27	96.83	98.38	99.38	97.06	98.52	97.68	99.74	98.81	97.01	97.77
32 (O) basis																		
Ti	0.36	0.91	0.28	0.62	2.25	0.02	0.03	0.03	0.01	0.01	0.09	0.14	0.02	0.03	0.04	0.06	0.04	1.22
Al	0.14	0.25	0.34	0.63	0.33	0.00	0.01	0.01	0.01	0.02	0.03	0.08	0.04	0.03	0.05	0.02	0.11	0.15
Cr	0.07	0.06	0.07	0.07	0.07	0.08	0.08	0.19	0.30	0.26	0.25	0.23	0.22	0.25	0.20	0.24	0.23	0.33
V	-	-	-	-	-	-	-	-	-	-	-	-	-	-	-	-	-	-
Fe^{3+}	15.07	13.87	15.04	14.06	11.09	15.88	15.86	15.73	15.68	15.70	15.53	15.40	15.70	15.66	15.67	15.63	15.57	13.07
Fe^{2+}	8.29	8.88	8.25	8.56	10.15	7.98	7.99	7.95	7.92	7.89	7.90	8.03	7.94	8.01	7.88	8.03	7.88	8.78
Mn	0.02	0.01	0.01	0.04	0.10	0.01	0.03	0.01	0.02	0.01	0.03	0.02	0.00	0.00	0.01	0.01	0.03	0.05
Ni	0.00	0.00	0.00	0.00	0.00	0.00	0.00	0.05	0.07	0.09	0.14	0.05	0.08	0.00	0.14	0.00	0.04	0.19
Mg	0.05	0.01	0.01	0.02	0.01	0.03	0.01	0.01	0.00	0.02	0.02	0.05	0.00	0.02	0.01	0.02	0.09	0.21
Zn	-	-	-	-	-	-	-	-	-	-	-	-	-	-	-	-	-	-

Sample	MIC-16-16	MIC-16-16	MIC-16-16	MIC-16-16	MIC-16-16	MIC-16-16	MIC-16-16	MIC-16-17	MIC-16-17	MIC-16-17	MIC-16-17	MIC-16-17	MIC-16-17	MIC-16-17	MIC-16-17	MIC-16-17	MIC-16-17	MIC-16-17
TiO_2	0.17	0.28	0.16	0.06	0.92	0.22	1.87	0.65	0.55	0.48	0.24	0.23	0.75	0.50	0.48	0.61	0.31	0.84
Al_2O_3	0.01	0.02	0.16	0.11	0.01	0.09	0.50	0.07	0.06	0.17	0.80	0.01	0.03	0.13	0.17	0.12	0.03	0.33
Cr_2O_3	1.06	1.40	1.01	0.63	0.85	0.79	2.44	0.44	0.56	0.65	0.67	0.48	0.66	0.76	1.32	1.10	0.38	0.60
V_2O_3	-	-	-	-	-	-	-	-	-	-	-	-	-	-	-	-	-	-
Fe_2O_3	66.02	66.16	65.97	66.61	65.71	66.71	60.72	65.38	66.12	65.91	65.73	66.49	65.87	66.14	65.66	65.39	66.17	65.54
FeO	30.16	30.81	29.85	29.91	31.47	30.59	31.81	30.76	30.86	30.06	29.70	29.99	31.23	30.81	30.85	30.92	30.34	30.58
MnO	0.10	0.04	0.06	0.07	0.02	0.07	0.14	0.05	0.04	0.08	0.12	0.09	0.01	0.09	0.02	0.12	0.12	0.17

NiO	0.21	0.05	0.62	0.46	0.10	0.10	0.21	0.00	0.05	0.51	0.15	0.52	0.05	0.16	0.26	0.05	0.05	0.10
MgO	0.04	0.03	0.02	0.01	0.03	0.04	0.03	0.02	0.06	0.18	0.52	0.00	0.02	0.04	0.01	0.02	0.01	0.38
ZnO	-	-	-	-	-	-	-	-	-	-	-	-	-	-	-	-	-	-
Total	97.76	98.79	97.85	97.88	99.12	98.62	97.71	97.37	98.30	98.03	97.93	97.81	98.62	98.62	98.77	98.32	97.40	98.55
32 (O) basis																		
Ti	0.04	0.07	0.04	0.01	0.22	0.05	0.44	0.15	0.13	0.11	0.06	0.05	0.18	0.12	0.11	0.14	0.07	0.20
Al	0.00	0.01	0.06	0.04	0.00	0.03	0.19	0.03	0.02	0.06	0.29	0.01	0.01	0.05	0.06	0.04	0.01	0.12
Cr	0.26	0.34	0.25	0.16	0.21	0.19	0.61	0.11	0.14	0.16	0.16	0.12	0.16	0.19	0.32	0.27	0.10	0.15
V	-	-	-	-	-	-	-	-	-	-	-	-	-	-	-	-	-	-
Fe^{3+}	15.65	15.52	15.62	15.77	15.36	15.67	14.33	15.55	15.58	15.55	15.43	15.77	15.47	15.53	15.39	15.40	15.75	15.34
Fe^{2+}	7.95	8.03	7.85	7.87	8.17	7.99	8.34	8.13	8.08	7.88	7.75	7.90	8.15	8.04	8.04	8.09	8.02	7.95
Mn	0.03	0.01	0.02	0.02	0.01	0.02	0.04	0.01	0.01	0.02	0.03	0.02	0.00	0.02	0.01	0.03	0.03	0.04
Ni	0.05	0.01	0.16	0.12	0.03	0.03	0.05	0.00	0.01	0.13	0.04	0.13	0.01	0.04	0.06	0.01	0.01	0.03
Mg	0.02	0.01	0.01	0.01	0.01	0.02	0.01	0.01	0.03	0.09	0.24	0.00	0.01	0.02	0.01	0.01	0.01	0.17
Zn	-	-	-	-	-	-	-	-	-	-	-	-	-	-	-	-	-	-

Sample	MIC-16-17	MIC-16-17	MIC-16-17	MIC-16-22	MIC-16-22	MIC-16-22	MIC-16-27	MIC-16-12	MIC-16-12	MIC-16-14	MIC-16-14	MIC-16-14	MIC-16-14	MIC-16-14	SHB-19-12-67	SHB-19-12-67	SHB-19-12-67	SHB-19-12-67
TiO_2	0.77	0.57	0.58	9.20	16.03	9.63	1.78	20.87	4.23	3.25	2.48	2.34	1.37	15.68	4.20	8.17	8.61	10.55
Al_2O_3	0.24	0.08	0.09	0.44	0.06	0.01	0.03	2.85	1.68	4.16	2.36	5.14	10.35	1.97	1.91	0.16	2.64	0.62
Cr_2O_3	0.51	0.77	0.85	0.46	0.17	0.17	0.20	0.15	0.14	0.07	0.23	0.14	0.15	0.21	0.06	0.12	0.03	0.12
V_2O_3	-	-	-	-	-	-	-	-	-	-	-	-	-	-	0.94	0.87	0.85	0.83
Fe_2O_3	65.62	65.47	66.49	49.04	36.50	48.63	64.26	25.56	57.95	56.58	60.81	58.15	54.81	34.75	57.47	56.72	46.21	53.61
FeO	30.25	30.72	31.03	37.67	45.03	39.03	32.22	47.26	33.82	31.97	32.58	31.98	29.38	43.19	34.54	32.78	38.20	33.40
MnO	0.05	0.13	0.02	0.28	0.30	0.21	0.02	0.67	0.12	0.13	0.03	0.09	0.15	0.36	0.07	0.29	0.14	0.19
NiO	0.20	0.00	0.36	0.00	0.00	0.00	0.00	0.28	0.05	0.40	0.30	0.30	0.10	0.29	0.02	0.00	0.00	0.00
MgO	0.45	0.03	0.01	0.67	0.03	0.03	0.00	1.63	0.53	1.00	0.38	0.95	2.73	0.84	0.04	0.02	0.09	0.03
ZnO	-	-	-	-	-	-	-	-	-	-	-	-	-	-	0.73	0.03	0.32	0.40
Total	98.09	97.78	99.44	97.74	98.12	97.71	98.52	99.29	98.50	97.56	99.17	99.08	99.04	97.29	100.01	99.16	97.19	99.79
32 (O) basis																		

Ti	0.18	0.14	0.13	2.14	3.73	2.26	0.42	4.64	0.98	0.75	0.57	0.53	0.30	3.61	0.96	1.00	2.00	1.30
Al	0.09	0.03	0.03	0.16	0.02	0.00	0.01	0.99	0.61	1.50	0.85	1.81	3.51	0.71	0.68	0.02	0.96	0.08
Cr	0.13	0.19	0.21	0.11	0.04	0.04	0.05	0.04	0.03	0.02	0.05	0.03	0.03	0.05	0.01	0.01	0.01	0.01
V	-	-	-	-	-	-	-	-	-	-	-	-	-	-	0.23	0.11	0.21	0.11
Fe^{3+}	15.43	15.51	15.49	11.44	8.49	11.43	15.10	5.69	13.40	12.99	13.96	13.10	11.86	8.01	13.13	13.86	10.76	13.20
Fe^{2+}	7.90	8.09	8.03	9.76	11.63	10.20	8.41	11.69	8.69	8.16	8.31	8.01	7.07	11.06	8.77	8.90	9.88	9.14
Mn	0.01	0.03	0.01	0.07	0.08	0.06	0.00	0.17	0.03	0.03	0.01	0.02	0.04	0.09	0.02	0.08	0.04	0.05
Ni	0.05	0.00	0.09	0.00	0.00	0.00	0.00	0.07	0.01	0.10	0.07	0.07	0.02	0.07	0.00	0.00	0.00	0.00
Mg	0.21	0.02	0.01	0.31	0.01	0.01	0.00	0.72	0.24	0.46	0.17	0.42	1.17	0.38	0.02	0.01	0.04	0.02
Zn	-	-	-	-	-	-	-	-	-	-	-	-	-	-	0.16	0.01	0.07	0.10

Sample	SHB-19-12-67	SHB-19-12-67	SHB-19-12-67	SHB-19-12-67	SHB-19-12-67	SHB-19-12-67	SHB-19-12-67	SHB-19-12-69	SHB-19-12-69	SHB-19-12-69	SHB-19-12-69
TiO_2	11.20	9.11	8.01	14.36	14.78	1.17	5.52	20.77	19.56	18.03	17.02
Al_2O_3	1.06	0.30	0.13	0.14	0.59	0.68	0.09	1.83	2.40	2.40	2.12
Cr_2O_3	0.18	0.06	0.21	0.14	0.13	0.10	0.16	0.00	0.00	0.00	0.04
V_2O_3	0.78	1.19	0.90	0.85	0.73	0.86	1.19	0.12	0.09	0.11	0.14
Fe_2O_3	43.75	54.33	51.08	48.51	37.75	64.63	54.93	39.84	26.44	43.23	32.05
FeO	40.57	32.78	37.86	34.58	43.33	30.52	35.39	36.38	48.09	34.69	45.53
MnO	0.33	0.23	0.14	0.39	0.43	0.05	0.02	0.15	0.41	0.46	0.27
NiO	0.08	0.00	0.08	0.00	0.23	0.00	0.00	0.00	0.01	0.00	0.12
MgO	0.05	0.02	0.13	0.04	0.04	0.03	0.00	0.29	0.25	0.44	0.43
ZnO	0.06	0.00	0.00	0.00	0.54	0.00	0.05	0.00	0.00	0.37	0.00
Total	98.11	98.06	98.65	99.05	98.61	98.11	97.39	99.40	97.32	99.74	97.76
32 (O) basis											
Ti	2.60	1.13	1.86	1.81	3.41	0.14	1.30	2.69	4.49	2.30	3.90
Al	0.39	0.04	0.05	0.02	0.21	0.09	0.03	0.25	0.86	0.32	0.76
Cr	0.04	0.01	0.05	0.01	0.03	0.01	0.04	0.00	0.00	0.00	0.01
V	0.19	0.16	0.22	0.11	0.18	0.11	0.30	0.02	0.02	0.02	0.03
Fe^{3+}	10.16	13.52	11.88	12.23	8.72	15.49	12.99	10.35	6.08	11.05	7.36

Fe^{2+}	10.47	9.07	9.79	9.69	11.12	8.13	9.30	10.50	12.29	9.86	11.62
Mn	0.09	0.06	0.04	0.11	0.11	0.01	0.01	0.05	0.11	0.13	0.07
Ni	0.02	0.00	0.02	0.00	0.06	0.00	0.00	0.00	0.00	0.00	0.03
Mg	0.02	0.01	0.06	0.02	0.02	0.01	0.00	0.15	0.11	0.22	0.19
Zn	0.01	0.00	0.00	0.00	0.12	0.00	0.01	0.00	0.00	0.09	0.00

Notes: Sample - Betjharan section (MIC/16/03, MIC/16/04 - noritic gabbro; MIC/16/05, MIC/16/06/, MIC/16/07, MIC/16/08, MIC/16/16, MIC/16/17, MIC/16/22, MIC/16/27 – gabbro; MIC/16/12, MIC/16/14 – magnetitite); Hatichhad section (SHB/19-12/62 – anorthosite; SHB/19-12/67 – gabbro; SHB/19-12/69 - magnetitite).

Table. 5. EPMA major element (wt. %) compositions of ilmenite from the gabbro-norite-anorthosites and magnetitite ore of the Mayurbhanj Complex.

Sample	MIC-16-03	MIC-16-03	MIC-16-03	MIC-16-03	MIC-16-03	MIC-16-03	MIC-16-03	MIC-16-03	MIC-16-03	MIC-16-03	MIC-16-03	MIC-16-04	MIC-16-04	MIC-16-04	MIC-16-04	MIC-16-04	MIC-16-04	MIC-16-04
TiO_2	47.61	47.52	45.93	46.65	48.89	47.22	45.94	45.52	46.61	41.36	47.92	47.63	47.27	47.43	46.12	47.84	46.63	48.67
Al_2O_3	0.02	0.02	0.28	0.00	0.04	0.00	0.11	0.18	0.03	0.10	0.05	0.03	0.18	0.03	1.03	0.05	0.03	0.05
Cr_2O_3	0.27	0.20	0.49	0.31	0.32	0.24	0.36	0.53	0.35	1.07	0.36	0.30	0.42	0.43	0.27	0.36	0.45	0.44
V_2O_3	-	-	-	-	-	-	-	-	-	-	-	-	-	-	-	-	-	-
Fe_2O_3	7.99	7.37	11.17	7.87	3.93	7.62	10.32	10.62	9.65	17.65	5.22	9.55	8.31	10.39	7.78	7.97	11.04	7.26
FeO	41.81	41.33	39.73	40.73	42.41	41.26	40.26	39.79	40.48	35.73	41.57	41.62	41.30	40.96	38.38	41.85	40.48	42.26
MnO	0.83	1.17	1.36	1.08	1.31	0.95	0.83	0.86	1.25	1.19	1.43	1.14	1.04	1.61	1.27	1.06	1.35	1.39
NiO	-	-	-	-	-	-	-	-	-	-	-	-	-	-	-	-	-	-
MgO	0.08	0.13	0.10	0.07	0.13	0.13	0.12	0.15	0.10	0.14	0.18	0.01	0.06	0.02	2.02	0.03	0.03	0.01
ZnO	-	-	-	-	-	-	-	-	-	-	-	-	-	-	-	-	-	-
Total	98.63	97.78	99.08	96.72	97.07	97.43	97.93	97.67	98.50	97.26	97.00	100.32	98.61	100.90	98.60	99.20	100.04	100.16
6 (O) basis																		
Ti	1.84	1.85	1.77	1.84	1.91	1.85	1.79	1.78	1.80	1.63	1.88	1.81	1.83	1.79	1.74	1.84	1.78	1.85
Al	0.00	0.00	0.02	0.00	0.00	0.00	0.01	0.01	0.00	0.01	0.00	0.00	0.01	0.00	0.06	0.00	0.00	0.00
Cr	0.01	0.01	0.02	0.01	0.01	0.01	0.01	0.02	0.01	0.04	0.01	0.01	0.02	0.02	0.01	0.01	0.02	0.02
V	-	-	-	-	-	-	-	-	-	-	-	-	-	-	-	-	-	-
Fe^{+3}	0.31	0.29	0.43	0.31	0.15	0.30	0.40	0.41	0.37	0.69	0.20	0.36	0.32	0.39	0.29	0.31	0.42	0.28
Fe^{+2}	1.80	1.79	1.70	1.78	1.85	1.79	1.74	1.73	1.74	1.56	1.81	1.76	1.77	1.72	1.61	1.79	1.72	1.79
Mn	0.04	0.05	0.06	0.05	0.06	0.04	0.04	0.04	0.05	0.05	0.06	0.05	0.05	0.07	0.05	0.05	0.06	0.06
Ni	-	-	-	-	-	-	-	-	-	-	-	-	-	-	-	-	-	-
Mg	0.01	0.01	0.01	0.01	0.01	0.01	0.01	0.01	0.01	0.01	0.01	0.00	0.00	0.00	0.15	0.00	0.00	0.00
Zn	-	-	-	-	-	-	-	-	-	-	-	-	-	-	-	-	-	-

Sample	MIC-16-04	MIC-16-04	MIC-16-04	MIC-16-04	MIC-16-04	MIC-16-04	MIC-16-04	MIC-16-04	MIC-16-04	MIC-16-04	MIC-16-04	MIC-16-04	MIC-16-04	MIC-16-04	MIC-16-04	MIC-16-04
TiO_2	49.89	47.61	51.07	47.86	49.18	41.28	44.88	48.51	47.97	49.49	51.01	47.34	48.10	49.54	47.57	47.43

Al_2O_3	0.04	2.11	0.16	0.05	0.17	0.06	0.02	0.03	0.05	0.04	0.41	0.04	0.03	0.26	0.02	0.02
Cr_2O_3	0.37	1.14	0.35	0.33	0.33	0.34	0.31	0.26	0.33	0.31	0.31	0.34	0.57	0.43	0.42	0.43
V_2O_3	-	-	-	-	-	-	-	-	-	-	-	-	-	-	-	-
Fe_2O_3	6.17	6.39	2.90	11.63	5.66	22.98	14.27	8.45	8.85	6.08	2.74	10.20	9.01	5.33	9.03	9.43
FeO	43.25	41.07	44.23	41.71	42.93	35.82	39.14	41.99	41.45	43.01	44.19	41.06	41.63	42.88	41.49	41.17
MnO	1.55	1.61	1.73	1.23	1.17	1.05	0.97	1.56	1.56	1.42	1.58	1.43	1.54	1.42	1.25	1.42
NiO	-	-	-	-	-	-	-	-	-	-	-	-	-	-	-	-
MgO	0.00	0.05	0.22	0.03	0.04	0.11	0.11	0.00	0.03	0.02	0.02	0.00	0.00	0.06	0.00	0.00
ZnO	-	-	-	-	-	-	-	-	-	-	-	-	-	-	-	-
Total	101.31	100.12	101.16	102.87	99.51	101.69	99.74	100.85	100.30	100.39	100.31	100.47	100.93	100.03	99.80	99.95
6 (O) basis																
Ti	1.88	1.79	1.91	1.78	1.88	1.56	1.72	1.83	1.82	1.88	1.93	1.80	1.82	1.88	1.82	1.81
Al	0.00	0.12	0.01	0.00	0.01	0.00	0.00	0.00	0.00	0.00	0.02	0.00	0.00	0.02	0.00	0.00
Cr	0.01	0.05	0.01	0.01	0.01	0.01	0.01	0.01	0.01	0.01	0.01	0.01	0.02	0.02	0.02	0.02
V	-	-	-	-	-	-	-	-	-	-	-	-	-	-	-	-
Fe^{+3}	0.23	0.24	0.11	0.43	0.22	0.87	0.55	0.32	0.34	0.23	0.10	0.39	0.34	0.20	0.35	0.36
Fe^{+2}	1.81	1.72	1.84	1.72	1.82	1.50	1.67	1.76	1.75	1.81	1.86	1.73	1.75	1.81	1.76	1.75
Mn	0.07	0.07	0.07	0.05	0.05	0.04	0.04	0.07	0.07	0.06	0.07	0.06	0.07	0.06	0.05	0.06
Ni	-	-	-	-	-	-	-	-	-	-	-	-	-	-	-	-
Mg	0.00	0.00	0.02	0.00	0.00	0.01	0.01	0.00	0.00	0.00	0.00	0.00	0.00	0.00	0.00	0.00
Zn	-	-	-	-	-	-	-	-	-	-	-	-	-	-	-	-

Sample	MIC-16-05	MIC-16-05	MIC-16-05	MIC-16-05	MIC-16-05	MIC-16-05	MIC-16-05	MIC-16-05	MIC-16-05	MIC-16-06	MIC-16-06	MIC-16-06	MIC-16-06	MIC-16-06	MIC-16-06	MIC-16-06	MIC-16-06
TiO_2	49.27	49.72	49.12	49.43	47.78	51.66	49.07	48.33	51.84	49.18	51.47	47.36	47.28	47.72	47.06	45.47	47.52
Al_2O_3	0.61	1.17	0.12	0.13	0.40	0.05	0.04	0.05	0.05	0.05	0.09	0.06	0.06	0.06	0.08	0.21	0.08
Cr_2O_3	0.45	0.13	1.09	0.37	0.48	0.27	0.30	0.38	0.26	0.14	0.13	0.08	0.06	0.14	0.08	0.14	0.11
V_2O_3	-	-	-	-	-	-	-	-	-	-	-	-	-	-	-	-	-
Fe_2O_3	4.18	2.82	6.47	5.72	8.84	1.50	6.72	6.50	1.32	4.09	0.31	7.40	8.48	9.11	10.19	2.40	6.23
FeO	42.86	43.42	42.69	42.95	41.23	45.05	42.45	42.11	44.73	41.30	43.67	40.17	40.34	40.60	40.51	39.04	40.60

MnO	0.97	0.88	1.42	1.37	1.57	1.33	1.59	1.25	1.76	2.52	2.40	2.10	1.80	1.90	1.47	2.44	1.90
NiO	-	-	-	-	-	-	-	-	-	-	-	-	-	-	-	-	-
MgO	0.24	0.18	0.00	0.05	0.05	0.01	0.01	0.03	0.00	0.05	0.05	0.05	0.05	0.06	0.03	0.32	0.05
ZnO	-	-	-	-	-	-	-	-	-	-	-	-	-	-	-	-	-
Total	98.63	98.38	100.96	100.04	100.40	99.91	100.22	98.67	100.06	97.56	98.26	97.39	98.28	99.81	99.62	91.52	96.60
6 (O) basis																	
Ti	1.89	1.91	1.85	1.88	1.81	1.96	1.87	1.87	1.97	1.92	1.99	1.85	1.83	1.82	1.80	1.87	1.87
Al	0.04	0.07	0.01	0.01	0.02	0.00	0.00	0.00	0.00	0.00	0.01	0.00	0.00	0.00	0.00	0.01	0.00
Cr	0.02	0.01	0.04	0.01	0.02	0.01	0.01	0.02	0.01	0.01	0.01	0.00	0.00	0.01	0.00	0.01	0.00
V	-	-	-	-	-	-	-	-	-	-	-	-	-	-	-	-	-
Fe^{+3}	0.16	0.11	0.24	0.22	0.34	0.06	0.26	0.25	0.05	0.16	0.01	0.29	0.33	0.35	0.39	0.10	0.25
Fe^{+2}	1.83	1.85	1.79	1.82	1.74	1.90	1.79	1.81	1.89	1.79	1.87	1.75	1.74	1.72	1.72	1.79	1.78
Mn	0.04	0.04	0.06	0.06	0.07	0.06	0.07	0.05	0.08	0.11	0.10	0.09	0.08	0.08	0.06	0.11	0.08
Ni	-	-	-	-	-	-	-	-	-	-	-	-	-	-	-	-	-
Mg	0.02	0.01	0.00	0.00	0.00	0.00	0.00	0.00	0.00	0.00	0.00	0.00	0.00	0.00	0.00	0.03	0.00
Zn	-	-	-	-	-	-	-	-	-	-	-	-	-	-	-	-	-

Sample	MIC-16-06	MIC-16-06	MIC-16-06	MIC-16-06	MIC-16-06	MIC-16-06	MIC-16-06	MIC-16-06	MIC-16-06	MIC-16-06	MIC-16-06	MIC-16-06	MIC-16-06	MIC-16-06	MIC-16-06	MIC-16-06	MIC-16-06	MIC-16-7
TiO_2	51.33	47.30	45.31	46.23	47.23	47.50	41.19	47.29	42.87	46.06	48.38	47.41	46.54	43.40	44.17	46.64	48.34	48.09
Al_2O_3	0.05	0.50	0.09	0.20	0.19	0.06	0.19	0.09	0.07	0.05	0.09	0.07	0.04	0.05	0.09	0.11	0.04	0.01
Cr_2O_3	0.12	0.10	0.13	0.00	0.04	0.11	0.19	0.19	0.11	0.13	0.14	0.22	0.06	0.19	0.15	0.24	0.04	0.19
V_2O_3	-	-	-	-	-	-	-	-	-	-	-	-	-	-	-	-	-	-
Fe_2O_3	1.59	7.94	11.97	10.44	8.80	8.70	14.87	8.13	18.05	11.70	7.26	8.30	10.36	15.30	16.48	10.99	8.44	6.97
FeO	42.41	39.84	38.33	39.64	40.08	40.84	35.92	40.09	36.54	38.81	41.57	40.61	39.94	37.18	37.60	39.76	41.55	40.90
MnO	3.38	2.32	2.09	1.47	1.93	1.46	1.66	2.01	1.62	2.20	1.62	1.60	1.45	1.47	1.65	1.76	1.55	2.25
NiO	-	-	-	-	-	-	-	-	-	-	-	-	-	-	-	-	-	-
MgO	0.05	0.04	0.02	0.08	0.07	0.06	0.11	0.06	0.05	0.04	0.01	0.05	0.07	0.03	0.09	0.08	0.04	0.02
ZnO	-	-	-	-	-	-	-	-	-	-	-	-	-	-	-	-	-	-
Total	99.12	98.27	98.15	98.30	98.60	98.97	95.03	98.10	99.55	99.24	99.30	98.52	98.72	97.86	100.47	99.80	100.21	98.46

6 (O) basis																		
Ti	1.97	1.83	1.76	1.79	1.82	1.83	1.65	1.84	1.65	1.77	1.86	1.83	1.80	1.70	1.68	1.78	1.84	1.86
Al	0.00	0.03	0.01	0.01	0.01	0.00	0.01	0.01	0.00	0.00	0.01	0.00	0.00	0.00	0.01	0.01	0.00	0.00
Cr	0.00	0.00	0.01	0.00	0.00	0.00	0.01	0.01	0.00	0.01	0.01	0.01	0.00	0.01	0.01	0.01	0.00	0.01
V	-	-	-	-	-	-	-	-	-	-	-	-	-	-	-	-	-	-
Fe^{+3}	0.06	0.31	0.47	0.40	0.34	0.34	0.60	0.32	0.69	0.45	0.28	0.32	0.40	0.60	0.63	0.42	0.32	0.27
Fe^{+2}	1.81	1.71	1.66	1.71	1.72	1.75	1.60	1.73	1.56	1.66	1.77	1.75	1.71	1.61	1.59	1.69	1.76	1.76
Mn	0.15	0.10	0.09	0.06	0.08	0.06	0.07	0.09	0.07	0.10	0.07	0.07	0.06	0.06	0.07	0.08	0.07	0.10
Ni	-	-	-	-	-	-	-	-	-	-	-	-	-	-	-	-	-	-
Mg	0.00	0.00	0.00	0.01	0.01	0.00	0.01	0.00	0.00	0.00	0.00	0.00	0.01	0.00	0.01	0.01	0.00	0.00
Zn	-	-	-	-	-	-	-	-	-	-	-	-	-	-	-	-	-	-

Sample	MIC-16-7	MIC-16-7	MIC-16-7	MIC-16-7	MIC-16-7	MIC-16-7	MIC-16-7	MIC-16-7	MIC-16-7	MIC-16-7	MIC-16-7	MIC-16-7	MIC-16-7	MIC-16-7	MIC-16-7	MIC-16-7	MIC-16-7	MIC-16-7
TiO_2	47.41	46.44	47.54	46.26	47.81	46.91	47.95	47.58	49.89	48.19	46.71	46.96	48.62	48.17	47.45	47.44	51.23	49.89
Al_2O_3	0.03	0.00	0.02	0.09	0.03	0.11	0.04	0.05	0.13	0.03	0.01	0.00	0.01	0.03	0.02	0.01	0.06	0.02
Cr_2O_3	0.13	0.23	0.19	0.24	0.14	0.13	0.15	0.16	0.11	0.17	0.15	0.24	0.16	0.15	0.19	0.14	0.07	0.11
V_2O_3	-	-	-	-	-	-	-	-	-	-	-	-	-	-	-	-	-	-
Fe_2O_3	7.65	10.74	7.80	12.38	6.44	8.93	9.49	6.56	1.90	7.58	8.81	9.12	5.04	7.69	9.88	8.46	-3.97	3.35
FeO	40.31	39.80	40.42	39.15	40.76	39.71	40.95	40.29	39.65	41.05	39.84	40.14	41.37	41.29	40.43	40.63	44.27	42.51
MnO	2.24	1.87	2.25	2.39	2.20	2.33	2.03	2.43	2.10	2.21	2.08	1.98	2.24	1.85	2.16	1.96	2.49	2.29
NiO	-	-	-	-	-	-	-	-	-	-	-	-	-	-	-	-	-	-
MgO	0.02	0.04	0.03	0.01	0.00	0.06	0.05	0.01	0.05	0.02	0.02	0.05	0.04	0.07	0.01	0.02	0.04	0.03
ZnO	-	-	-	-	-	-	-	-	-	-	-	-	-	-	-	-	-	-
Total	97.81	99.13	98.27	100.54	97.41	98.21	100.69	97.09	101.82	99.27	97.65	98.48	97.49	99.29	100.16	98.68	100.58	98.22
6 (O) basis																		
Ti	1.85	1.79	1.84	1.76	1.87	1.82	1.82	1.87	1.82	1.85	1.82	1.82	1.90	1.85	1.81	1.83	1.89	1.93
Al	0.00	0.00	0.00	0.01	0.00	0.01	0.00	0.00	0.01	0.00	0.00	0.00	0.00	0.00	0.00	0.00	0.00	0.00
Cr	0.01	0.01	0.01	0.01	0.01	0.01	0.01	0.01	0.00	0.01	0.01	0.01	0.01	0.01	0.01	0.01	0.00	0.00
V	-	-	-	-	-	-	-	-	-	-	-	-	-	-	-	-	-	-

Fe^{+3}	0.30	0.41	0.30	0.47	0.25	0.35	0.36	0.26	0.07	0.29	0.34	0.35	0.20	0.30	0.38	0.33	-0.15	0.13
Fe^{+2}	1.75	1.70	1.74	1.65	1.77	1.71	1.72	1.76	1.61	1.75	1.73	1.73	1.80	1.76	1.71	1.75	1.82	1.83
Mn	0.10	0.08	0.10	0.10	0.10	0.10	0.09	0.11	0.09	0.10	0.09	0.09	0.10	0.08	0.09	0.09	0.10	0.10
Ni	-	-	-	-	-	-	-	-	-	-	-	-	-	-	-	-	-	-
Mg	0.00	0.00	0.00	0.00	0.00	0.00	0.00	0.00	0.00	0.00	0.00	0.00	0.00	0.01	0.00	0.00	0.00	0.00
Zn	-	-	-	-	-	-	-	-	-	-	-	-	-	-	-	-	-	-

Sample	MIC-16-7	MIC-16-7	MIC-16-8	MIC-16-8	MIC-16-8	MIC-16-8	MIC-16-8	MIC-16-8	MIC-16-8	MIC-16-16	MIC-16-16	MIC-16-16	MIC-16-16	MIC-16-16	MIC-16-16	MIC-16-16	MIC-16-16	MIC-16-16
TiO_2	47.32	48.22	48.09	49.82	49.45	48.00	48.00	47.09	47.08	46.81	44.36	46.69	45.42	45.31	49.07	45.80	46.86	43.12
Al_2O_3	0.05	0.03	0.04	0.03	0.03	0.04	0.02	0.04	0.03	0.03	0.07	0.03	0.04	0.04	0.05	1.04	0.12	0.06
Cr_2O_3	0.13	0.12	0.10	0.09	0.11	0.13	0.06	0.09	0.09	0.10	0.05	0.15	0.00	0.21	0.13	0.22	0.11	0.11
V_2O_3	-	-	-	-	-	-	-	-	-	-	-	-	-	-	-	-	-	-
Fe_2O_3	9.05	6.08	7.75	4.00	6.27	8.70	6.92	10.18	8.16	9.57	12.85	9.24	12.86	10.83	4.42	8.94	7.91	16.48
FeO	40.42	41.35	42.09	43.49	43.23	41.67	41.79	41.04	40.90	40.65	38.46	40.34	39.37	39.03	41.94	39.03	39.86	36.89
MnO	2.08	1.93	1.09	1.27	1.21	1.43	1.35	1.21	1.35	1.36	1.38	1.53	1.35	1.57	1.93	1.88	2.07	1.74
NiO	-	-	-	-	-	-	-	-	-	-	-	-	-	-	-	-	-	-
MgO	0.02	0.02	0.02	0.02	0.00	0.01	0.00	0.03	0.03	0.03	0.03	0.06	0.05	0.07	0.11	0.14	0.09	0.07
ZnO	-	-	-	-	-	-	-	-	-	-	-	-	-	-	-	-	-	-
Total	99.07	97.78	99.21	98.73	100.32	100.00	98.17	99.70	97.66	98.61	97.22	98.08	99.12	97.10	97.67	97.06	97.04	98.49
6 (O) basis																		
Ti	1.82	1.88	1.85	1.92	1.88	1.83	1.86	1.80	1.84	1.81	1.74	1.81	1.75	1.78	1.91	1.79	1.84	1.68
Al	0.00	0.00	0.00	0.00	0.00	0.00	0.00	0.00	0.00	0.00	0.00	0.00	0.00	0.00	0.00	0.06	0.01	0.00
Cr	0.01	0.00	0.00	0.00	0.00	0.01	0.00	0.00	0.00	0.00	0.00	0.01	0.00	0.01	0.01	0.01	0.00	0.00
V	-	-	-	-	-	-	-	-	-	-	-	-	-	-	-	-	-	-
Fe^{+3}	0.35	0.24	0.30	0.15	0.24	0.33	0.27	0.39	0.32	0.37	0.51	0.36	0.50	0.43	0.17	0.35	0.31	0.64
Fe^{+2}	1.73	1.79	1.80	1.86	1.83	1.77	1.80	1.75	1.78	1.75	1.68	1.74	1.69	1.71	1.82	1.69	1.74	1.59
Mn	0.09	0.08	0.05	0.05	0.05	0.06	0.06	0.05	0.06	0.06	0.06	0.07	0.06	0.07	0.08	0.08	0.09	0.08
Ni	-	-	-	-	-	-	-	-	-	-	-	-	-	-	-	-	-	-
Mg	0.00	0.00	0.00	0.00	0.00	0.00	0.00	0.00	0.00	0.00	0.00	0.00	0.00	0.01	0.01	0.01	0.01	0.01

Zn	-	-	-	-	-	-	-	-	-	-	-	-	-	-	-	-	-	-

Sample	MIC-16-16	MIC-16-16	MIC-16-16	MIC-16-16	MIC-16-16	MIC-16-16	MIC-16-16	MIC-16-16	MIC-16-16	MIC-16-16	MIC-16-16	MIC-16-16	MIC-16-16	MIC-16-16	MIC-16-16	MIC-16-16	MIC-16-16	MIC-16-16
TiO_2	41.90	46.00	47.51	47.36	46.58	50.05	45.93	45.08	46.99	46.05	47.36	44.51	44.61	45.93	47.36	46.58	50.05	45.93
Al_2O_3	0.06	0.03	0.08	0.16	0.06	0.04	0.04	0.59	0.01	0.05	0.23	0.02	0.07	0.02	0.16	0.06	0.04	0.04
Cr_2O_3	0.19	0.14	0.00	0.04	0.08	0.04	0.14	1.81	0.11	0.01	0.25	0.16	0.37	0.11	0.04	0.08	0.04	0.14
V_2O_3	-	-	-	-	-	-	-	-	-	-	-	-	-	-	-	-	-	-
Fe_2O_3	18.45	10.54	7.34	6.42	9.80	1.84	11.32	10.51	7.70	10.73	6.96	14.64	12.67	10.36	6.42	9.80	1.84	11.32
FeO	36.33	39.51	40.92	40.62	40.05	42.89	39.60	38.71	40.51	39.40	40.68	37.88	38.46	39.58	40.62	40.05	42.89	39.60
MnO	1.28	1.68	1.63	1.73	1.61	1.92	1.54	1.69	1.63	1.87	1.66	1.97	1.53	1.60	1.73	1.61	1.92	1.54
NiO	-	-	-	-	-	-	-	-	-	-	-	-	-	-	-	-	-	-
MgO	0.02	0.08	0.09	0.27	0.09	0.15	0.08	0.05	0.05	0.07	0.12	0.09	0.03	0.06	0.27	0.09	0.15	0.08
ZnO	-	-	-	-	-	-	-	-	-	-	-	-	-	-	-	-	-	-
Total	98.24	98.00	97.57	97.01	98.31	97.07	98.67	98.48	97.02	98.21	97.28	99.27	97.80	97.66	97.01	98.31	97.07	98.67
6 (O) basis																		
Ti	1.63	1.79	1.85	1.85	1.81	1.96	1.78	1.74	1.85	1.79	1.85	1.71	1.74	1.79	1.85	1.81	1.96	1.78
Al	0.00	0.00	0.01	0.01	0.00	0.00	0.00	0.04	0.00	0.00	0.01	0.00	0.00	0.00	0.01	0.00	0.00	0.00
Cr	0.01	0.01	0.00	0.00	0.00	0.00	0.01	0.07	0.00	0.00	0.01	0.01	0.02	0.00	0.00	0.00	0.00	0.01
V	-	-	-	-	-	-	-	-	-	-	-	-	-	-	-	-	-	-
Fe^{+3}	0.72	0.41	0.29	0.25	0.38	0.07	0.44	0.41	0.30	0.42	0.27	0.56	0.50	0.40	0.25	0.38	0.07	0.44
Fe^{+2}	1.58	1.71	1.78	1.77	1.73	1.86	1.70	1.66	1.77	1.70	1.77	1.62	1.67	1.72	1.77	1.73	1.86	1.70
Mn	0.06	0.07	0.07	0.08	0.07	0.08	0.07	0.07	0.07	0.08	0.07	0.09	0.07	0.07	0.08	0.07	0.08	0.07
Ni	-	-	-	-	-	-	-	-	-	-	-	-	-	-	-	-	-	-
Mg	0.00	0.01	0.01	0.02	0.01	0.01	0.01	0.00	0.00	0.01	0.01	0.01	0.00	0.00	0.02	0.01	0.01	0.01
Zn	-	-	-	-	-	-	-	-	-	-	-	-	-	-	-	-	-	-

Sample	MIC-16-16	MIC-16-16	MIC-16-16	MIC-16-16	MIC-16-16	MIC-16-16	MIC-16-16	MIC-16-17	MIC-16-17	MIC-16-17	MIC-16-17	MIC-16-17	MIC-16-17	MIC-16-17	MIC-16-17	MIC-16-17	MIC-16-17	MIC-16-17
TiO_2	45.08	46.99	46.05	47.36	44.51	44.61	45.93	44.44	46.18	47.39	45.74	46.53	45.78	45.61	44.13	46.78	48.25	46.11

Al_2O_3	0.59	0.01	0.05	0.23	0.02	0.07	0.02	1.28	0.01	0.04	0.01	0.03	0.02	0.01	0.00	0.02	0.00	0.05
Cr_2O_3	1.81	0.11	0.01	0.25	0.16	0.37	0.11	0.52	0.13	0.14	0.00	0.00	0.00	0.00	0.00	0.01	0.00	0.20
V_2O_3	-	-	-	-	-	-	-	-	-	-	-	-	-	-	-	-	-	-
Fe_2O_3	10.51	7.70	10.73	6.96	14.64	12.67	10.36	8.24	10.59	7.29	11.49	10.15	10.98	11.34	15.55	7.20	6.70	10.72
FeO	38.71	40.51	39.40	40.68	37.88	38.46	39.58	38.70	39.78	41.22	39.64	40.53	39.91	39.24	38.27	40.88	41.80	40.11
MnO	1.69	1.63	1.87	1.66	1.97	1.53	1.60	1.50	1.59	1.27	1.37	1.19	1.16	1.70	1.34	1.14	1.48	1.25
NiO	-	-	-	-	-	-	-	-	-	-	-	-	-	-	-	-	-	-
MgO	0.05	0.05	0.07	0.12	0.09	0.03	0.06	0.73	0.06	0.08	0.05	0.09	0.07	0.06	0.03	0.13	0.06	0.08
ZnO	-	-	-	-	-	-	-	-	-	-	-	-	-	-	-	-	-	-
Total	98.48	97.02	98.21	97.28	99.27	97.80	97.66	97.07	98.37	97.49	98.35	98.54	97.95	98.03	99.38	96.42	98.32	98.58
6 (O) basis																		
Ti	1.74	1.85	1.79	1.85	1.71	1.74	1.79	1.72	1.79	1.85	1.78	1.80	1.78	1.78	1.70	1.85	1.87	1.78
Al	0.04	0.00	0.00	0.01	0.00	0.00	0.00	0.08	0.00	0.00	0.00	0.00	0.00	0.00	0.00	0.00	0.00	0.00
Cr	0.07	0.00	0.00	0.01	0.01	0.02	0.00	0.02	0.01	0.01	0.00	0.00	0.00	0.00	0.00	0.00	0.00	0.01
V	-	-	-	-	-	-	-	-	-	-	-	-	-	-	-	-	-	-
Fe^{+3}	0.41	0.30	0.42	0.27	0.56	0.50	0.40	0.32	0.41	0.28	0.45	0.39	0.43	0.44	0.60	0.28	0.26	0.42
Fe^{+2}	1.66	1.77	1.70	1.77	1.62	1.67	1.72	1.66	1.72	1.79	1.71	1.74	1.73	1.70	1.64	1.79	1.80	1.73
Mn	0.07	0.07	0.08	0.07	0.09	0.07	0.07	0.07	0.07	0.06	0.06	0.05	0.05	0.07	0.06	0.05	0.06	0.05
Ni	-	-	-	-	-	-	-	-	-	-	-	-	-	-	-	-	-	-
Mg	0.00	0.00	0.01	0.01	0.01	0.00	0.00	0.06	0.00	0.01	0.00	0.01	0.01	0.00	0.00	0.01	0.00	0.01
Zn	-	-	-	-	-	-	-	-	-	-	-	-	-	-	-	-	-	-

Sample	MIC-16-17	MIC-16-17	MIC-16-17	MIC-16-17	MIC-16-17	MIC-16-17	MIC-16-17	MIC-16-17	MIC-16-17	MIC-16-17	MIC-16-17	MIC-16-17	MIC-16-17	MIC-16-17	MIC-16-17	MIC-16-17	MIC-16-17	MIC-16-17
TiO_2	46.68	49.05	46.49	46.79	47.66	44.08	46.75	49.41	50.17	46.75	46.48	46.46	46.70	49.61	48.29	45.28	46.68	47.73
Al_2O_3	0.01	0.26	0.09	0.00	0.01	0.02	0.01	0.00	0.00	0.02	0.01	0.00	0.01	0.03	0.02	0.01	0.01	0.01
Cr_2O_3	0.00	0.00	0.00	0.00	0.16	0.06	0.01	0.00	0.00	0.00	0.00	0.00	0.04	0.10	0.15	0.00	0.00	0.11
V_2O_3	-	-	-	-	-	-	-	-	-	-	-	-	-	-	-	-	-	-
Fe_2O_3	8.38	4.48	9.35	10.02	7.54	14.26	10.39	3.53	1.82	9.06	10.49	9.65	8.53	2.68	6.08	11.72	8.94	6.49
FeO	40.49	42.44	40.24	40.37	41.27	38.01	40.25	42.96	43.43	40.81	40.61	40.30	40.61	42.97	41.72	39.12	40.50	41.44

MnO	1.46	1.55	1.44	1.61	1.50	1.44	1.58	1.35	1.52	1.11	1.04	1.35	1.25	1.56	1.58	1.36	1.39	1.26
NiO	-	-	-	-	-	-	-	-	-	-	-	-	-	-	-	-	-	-
MgO	0.01	0.05	0.06	0.04	0.05	0.09	0.10	0.08	0.10	0.06	0.09	0.06	0.10	0.06	0.07	0.11	0.05	0.05
ZnO	-	-	-	-	-	-	-	-	-	-	-	-	-	-	-	-	-	-
Total	97.09	97.88	97.71	98.89	98.23	97.98	99.12	97.35	97.16	97.87	98.74	97.83	97.28	97.05	97.91	97.64	97.61	97.29
6 (O) basis																		
Ti	1.83	1.90	1.81	1.81	1.85	1.72	1.80	1.93	1.96	1.82	1.80	1.81	1.83	1.94	1.88	1.77	1.82	1.87
Al	0.00	0.02	0.01	0.00	0.00	0.00	0.00	0.00	0.00	0.00	0.00	0.00	0.00	0.00	0.00	0.00	0.00	0.00
Cr	0.00	0.00	0.00	0.00	0.01	0.00	0.00	0.00	0.00	0.00	0.00	0.00	0.00	0.00	0.01	0.00	0.00	0.00
V	-	-	-	-	-	-	-	-	-	-	-	-	-	-	-	-	-	-
Fe^{+3}	0.33	0.17	0.36	0.39	0.29	0.56	0.40	0.14	0.07	0.35	0.41	0.38	0.33	0.10	0.24	0.46	0.35	0.25
Fe^{+2}	1.77	1.83	1.75	1.73	1.78	1.65	1.72	1.87	1.89	1.77	1.74	1.75	1.77	1.87	1.80	1.70	1.76	1.80
Mn	0.06	0.07	0.06	0.07	0.07	0.06	0.07	0.06	0.07	0.05	0.05	0.06	0.06	0.07	0.07	0.06	0.06	0.06
Ni	-	-	-	-	-	-	-	-	-	-	-	-	-	-	-	-	-	-
Mg	0.00	0.00	0.00	0.00	0.00	0.01	0.01	0.01	0.01	0.00	0.01	0.00	0.01	0.00	0.01	0.01	0.00	0.00
Zn	-	-	-	-	-	-	-	-	-	-	-	-	-	-	-	-	-	-

Sample	MIC-16-17	MIC-16-17	MIC-16-22	MIC-16-22	MIC-16-22	MIC-16-22	MIC-16-22	MIC-16-22	MIC-16-22	MIC-16-27	MIC-16-27	SHB-19-12-62	SHB-19-12-62	SHB-19-12-62	SHB-19-12-62	SHB-19-12-62	SHB-19-12-62	SHB-19-12-62
TiO_2	48.04	47.62	36.82	51.13	51.01	51.33	50.11	49.10	50.13	50.88	50.85	52.36	52.17	52.86	52.36	52.32	52.46	52.67
Al_2O_3	0.01	0.01	0.01	0.03	0.01	0.00	0.15	0.05	0.04	0.00	0.04	0.15	0.23	0.12	0.18	0.17	0.17	0.18
Cr_2O_3	0.00	0.00	0.00	0.03	0.05	0.16	0.08	0.10	0.13	0.14	0.06	0.00	0.00	0.00	0.00	0.03	0.03	0.00
V_2O_3	-	-	-	-	-	-	-	-	-	-	-	0.18	0.36	0.20	0.29	0.54	0.24	0.16
Fe_2O_3	5.93	8.21	27.48	1.84	1.05	-1.19	1.34	3.82	3.23	1.19	1.56	0.00	0.00	0.00	0.00	0.00	0.00	0.00
FeO	41.80	41.42	32.60	44.84	44.68	45.66	45.09	43.28	44.23	42.23	42.66	42.82	42.89	42.69	41.81	42.68	43.15	43.94
MnO	1.24	1.32	0.66	1.04	1.10	1.10	0.60	0.77	0.81	2.95	2.65	3.05	2.77	2.75	2.86	3.28	3.09	2.91
NiO	-	-	-	-	-	-	-	-	-	-	-	0.00	0.00	0.07	0.00	0.00	0.00	0.03
MgO	0.09	0.04	0.06	0.00	0.01	0.10	0.16	0.01	0.03	0.02	0.01	0.09	0.14	0.12	0.08	0.09	0.06	0.10
ZnO	-	-	-	-	-	-	-	-	-	-	-	0.16	0.26	0.00	0.14	0.00	0.04	0.00

Total	97.18	98.62	98.00	99.02	98.01	99.06	98.66	97.22	98.66	98.05	98.81	98.83	98.82	98.82	97.73	99.09	99.24	99.99
6 (O) basis																		
Ti	1.88	1.84	1.44	1.96	1.98	1.95	1.92	1.92	1.93	1.97	1.95	2.01	2.00	2.03	2.03	2.00	2.01	2.00
Al	0.00	0.00	0.00	0.00	0.00	0.00	0.01	0.00	0.00	0.00	0.00	0.01	0.01	0.01	0.01	0.01	0.01	0.01
Cr	0.00	0.00	0.00	0.00	0.00	0.01	0.00	0.00	0.01	0.01	0.00	0.00	0.00	0.00	0.00	0.00	0.00	0.00
V	-	-	-	-	-	-	-	-	-	-	-	0.01	0.01	0.01	0.01	0.02	0.01	0.01
Fe^{+3}	0.23	0.32	1.08	0.07	0.04	-0.05	0.05	0.15	0.12	0.05	0.06	0.00	0.00	0.00	0.00	0.00	0.00	0.00
Fe^{+2}	1.82	1.78	1.42	1.91	1.93	1.93	1.92	1.88	1.90	1.82	1.82	1.83	1.83	1.82	1.81	1.82	1.83	1.85
Mn	0.05	0.06	0.03	0.05	0.05	0.05	0.03	0.03	0.04	0.13	0.11	0.13	0.12	0.12	0.12	0.14	0.13	0.12
Ni	-	-	-	-	-	-	-	-	-	-	-	0.00	0.00	0.00	0.00	0.00	0.00	0.00
Mg	0.01	0.00	0.00	0.00	0.00	0.01	0.01	0.00	0.00	0.00	0.00	0.01	0.01	0.01	0.01	0.01	0.00	0.01
Zn	-	-	-	-	-	-	-	-	-	-	-	0.01	0.01	0.00	0.01	0.00	0.00	0.00

Sample	SHB-19-12-62	SHB-19-12-67	SHB-19-12-67	SHB-19-12-67	SHB-19-12-67	SHB-19-12-67	SHB-19-12-67	SHB-19-12-67	SHB-19-12-67	SHB-19-12-67	SHB-19-12-69	SHB-19-12-69	SHB-19-12-69
TiO_2	53.33	51.99	51.49	51.75	52.00	48.82	51.48	51.25	49.11	52.60	51.90	52.57	51.92
Al_2O_3	0.11	0.16	0.12	0.12	0.21	0.14	0.17	0.17	0.19	0.18	0.21	0.21	0.20
Cr_2O_3	0.10	0.00	0.00	0.03	0.00	0.10	0.00	0.00	0.09	0.08	0.00	0.00	0.00
V_2O_3	0.22	0.00	0.00	0.00	0.01	0.10	0.00	0.00	0.00	0.00	0.13	0.21	0.08
Fe_2O_3	0.00	0.00	0.96	0.57	0.11	5.30	1.33	0.22	6.68	0.00	0.77	0.10	0.42
FeO	42.29	45.26	45.02	45.21	45.36	42.98	45.11	44.69	42.68	41.80	44.51	44.71	44.46
MnO	3.15	1.05	1.24	1.31	1.20	0.88	1.14	1.30	1.42	1.22	0.79	0.81	0.65
NiO	0.06	0.00	0.00	0.00	0.20	0.00	0.00	0.03	0.00	0.05	0.09	0.08	0.15
MgO	0.07	0.01	0.02	0.00	0.00	0.02	0.02	0.04	0.04	0.00	0.73	0.94	0.77
ZnO	0.00	0.00	0.00	0.00	0.00	0.00	0.00	0.00	0.00	0.19	0.00	0.00	0.09
Total	99.34	98.49	98.83	98.99	99.09	98.34	99.25	97.70	100.20	96.11	99.11	99.62	98.72
6 (O) basis													
Ti	2.04	2.00	1.98	1.98	1.99	1.89	1.97	1.99	1.87	2.08	1.98	1.99	1.98
Al	0.01	0.01	0.01	0.01	0.01	0.01	0.01	0.01	0.01	0.01	0.01	0.01	0.01

Cr	0.00	0.00	0.00	0.00	0.00	0.00	0.00	0.00	0.00	0.00	0.00	0.00	0.00
V	0.01	0.00	0.00	0.00	0.00	0.00	0.00	0.00	0.00	0.00	0.01	0.01	0.00
Fe^{+3}	0.00	0.00	0.04	0.02	0.00	0.21	0.05	0.01	0.25	0.00	0.03	0.00	0.02
Fe^{+2}	1.80	1.94	1.92	1.93	1.93	1.85	1.92	1.93	1.80	1.84	1.88	1.88	1.89
Mn	0.14	0.05	0.05	0.06	0.05	0.04	0.05	0.06	0.06	0.05	0.03	0.03	0.03
Ni	0.00	0.00	0.00	0.00	0.01	0.00	0.00	0.00	0.00	0.00	0.00	0.00	0.01
Mg	0.01	0.00	0.00	0.00	0.00	0.00	0.00	0.00	0.00	0.00	0.05	0.07	0.06
Zn	0.00	0.00	0.00	0.00	0.00	0.00	0.00	0.00	0.00	0.01	0.00	0.00	0.00

Notes: Sample - Betjharan section (MIC/16/03, MIC/16/04 – noritic gabbro; MIC/16/05, MIC/16/06/, MIC/16/07, MIC/16/08, MIC/16/16, MIC/16/17, MIC/16/22, MIC/16/27 – gabbro; MIC/16/12, MIC/16/14 – magnetitite); Hatichhad section (SHB/19-12/62 – anorthosite; SHB/19-12/67 – gabbro; SHB/19-12/69 - magnetitite).

Table. 6. EPMA major element (wt. %) compositions of sulfides from the gabbro-norites of the Betjharan section of the Mayurbhanj Complex.

Sample	MIC-16-03/Py	MIC-16-03/Py	MIC-16-03/Py	MIC-16-03/Ccp	MIC-16-03/Ccp	MIC-16-03/Ccp	MIC-16-03/Ccp	MIC-16-03/Ccp	MIC-16-03/Ccp	MIC-16-03/Po	MIC-16-03/Po	MIC-16-03/Po	MIC-16-03/Po	MIC-16-03/Po	MIC-16-03/Po	MIC-16-03/Mss	MIC-16-03/Mss
S	50.59	53.98	53.28	35.29	44.42	34.91	34.61	34.46	33.93	39.09	39.13	37.72	38.00	39.31	39.31	42.01	38.06
Fe	44.79	46.48	46.23	30.54	36.46	29.30	28.40	30.56	29.66	57.62	58.73	58.14	58.83	57.49	59.05	46.17	16.38
Cu	0.01	0.00	0.00	32.37	19.14	33.71	34.24	34.09	32.92	0.00	0.05	0.00	0.00	0.00	0.00	0.00	0.07
Ni	0.09	0.08	0.29	0.08	0.17	0.06	0.00	0.08	0.00	0.81	0.99	1.03	0.77	1.30	1.03	10.17	36.17
Co	0.39	0.20	0.24	0.04	0.46	0.02	0.09	0.03	0.06	0.11	0.21	0.04	0.20	0.16	0.00	0.40	3.81
Mn	0.07	0.05	0.05	0.05	0.05	0.04	0.02	0.02	0.01	0.05	0.07	0.11	0.03	0.03	0.05	0.05	0.08
As	0.09	0.08	0.06	0.06	0.08	0.05	0.05	0.01	0.06	0.05	0.13	0.09	0.07	0.12	0.05	0.04	0.00
Ag	0.04	0.05	0.11	0.15	0.07	0.03	0.10	0.04	0.11	0.14	0.11	0.12	0.18	0.12	0.14	0.05	0.01
Total	96.07	100.91	100.25	98.58	100.86	98.13	97.50	99.29	96.75	97.87	99.42	97.26	98.07	98.53	99.63	98.89	94.57

Sample	MIC-16-04/Py	MIC-16-04/Py	MIC-16-04/Py	MIC-16-04/Py	MIC-16-04/Py	MIC-16-04/Py	MIC-16-04/Py	MIC-16-04/Ccp	MIC-16-04/Ccp	MIC-16-04/Ccp	MIC-16-04/Po	MIC-16-04/Po	MIC-16-04/Po	MIC-16-04/Pn	MIC-16-05/Py	MIC-16-05/Py	MIC-16-05/Py
S	52.97	50.38	52.75	53.55	53.31	53.27	53.58	34.07	34.61	34.17	38.61	37.47	38.94	32.72	53.29	52.98	53.05
Fe	45.31	43.56	44.18	44.92	46.05	46.23	43.96	30.18	30.00	29.53	56.50	57.94	57.57	31.12	45.61	46.17	46.89
Cu	0.00	2.95	0.41	0.00	0.00	0.00	0.00	33.18	33.45	33.25	0.00	0.21	0.00	0.00	0.00	0.33	0.00
Ni	1.12	0.92	0.34	0.51	0.05	0.70	0.61	0.00	0.16	0.02	4.32	0.49	0.60	35.23	0.10	0.03	0.57
Co	0.00	0.59	1.99	0.15	0.59	0.17	0.19	0.03	0.19	0.19	0.11	0.19	0.01	0.00	0.00	0.23	0.00
Mn	0.02	0.01	0.04	0.04	0.05	0.10	0.08	0.02	0.14	0.06	0.11	0.05	0.04	0.05	0.04	0.05	0.11
As	0.06	0.02	0.08	0.03	0.05	0.03	0.06	0.02	0.01	0.01	0.03	0.03	0.07	0.04	0.05	0.05	0.08
Ag	0.02	0.04	0.03	0.00	0.03	0.02	0.04	0.01	0.07	0.03	0.01	0.01	0.07	0.03	0.04	0.03	0.02
Total	99.50	98.48	99.82	99.20	100.14	100.52	98.52	97.51	98.62	97.27	99.68	96.41	97.30	99.19	99.13	99.87	100.72

Sample	MIC-16-06/Py	MIC-16-06/Py	MIC-16-06/Py	MIC-16-06/Py	MIC-16-06/Po	MIC-16-7/Py	MIC-16-7/Ccp	MIC-16-7/Po	MIC-16-7/Po	MIC-16-8/Py	MIC-16-8/Py	MIC-16-8/Py	MIC-16-8/Py	MIC-16-8/Py	MIC-16-8/Py	MIC-16-8/Py	MIC-16-8/Ccp
S	53.21	53.31	50.41	52.13	38.78	51.75	33.96	39.57	39.24	53.46	53.76	53.27	53.79	47.26	52.38	53.32	31.94
Fe	46.63	45.90	46.18	46.17	59.20	45.18	29.47	54.46	54.49	45.71	45.43	45.93	46.08	44.54	45.31	46.42	31.15
Cu	0.00	0.05	0.00	0.00	0.08	0.00	33.53	0.00	0.00	0.00	0.00	0.00	0.00	0.26	0.00	0.00	32.10
Ni	0.06	0.36	0.37	0.22	0.60	0.44	0.00	5.52	5.83	0.00	0.13	0.14	0.16	0.15	0.01	0.08	0.06
Co	0.01	0.29	0.33	0.14	0.10	0.81	0.01	0.12	0.26	0.09	0.34	0.01	0.01	0.01	0.08	0.10	0.06
Mn	0.08	0.16	0.06	0.00	0.11	0.14	0.02	0.05	0.12	0.09	0.10	0.07	0.10	0.04	0.16	0.07	0.00
As	0.02	0.04	0.04	0.01	0.05	0.06	0.05	0.09	0.06	0.07	0.06	0.04	0.05	0.05	0.06	0.05	0.05
Ag	0.09	0.07	0.04	0.04	0.16	0.00	0.02	0.09	0.13	0.05	0.04	0.07	0.01	0.01	0.03	0.15	0.04
Total	100.10	100.17	97.43	98.72	99.08	98.39	97.05	99.90	100.14	99.46	99.85	99.54	100.19	92.31	98.02	100.19	95.41

Sample	MIC-16-8/Ccp	MIC-16-16/Py	MIC-16-16/Py	MIC-16-16/Py	MIC-16-16/Py	MIC-16-16/Py	MIC-16-16/Py	MIC-16-16/Py	MIC-16-16/Py	MIC-16-16/Py	MIC-16-16/Py	MIC-16-16/Py	MIC-16-16/Py	MIC-16-16/Pn	MIC-16-16/Pn	MIC-16-17/Py	MIC-16-17/Py
S	34.34	52.07	52.68	52.42	52.88	52.43	52.74	52.53	52.60	52.54	53.02	52.76	52.46	23.53	33.06	52.94	52.75
Fe	29.51	45.11	47.02	46.11	45.69	43.40	45.24	45.47	46.09	46.92	45.64	45.06	47.09	25.41	25.86	43.41	45.24
Cu	34.83	0.00	0.00	0.00	0.00	0.00	0.00	0.00	0.00	0.06	0.04	0.04	0.00	0.13	0.14	0.00	0.02
Ni	0.01	0.39	0.17	0.97	0.44	0.33	0.44	0.39	0.08	0.36	0.39	0.33	0.11	42.57	49.15	1.03	0.06
Co	0.09	0.01	0.05	0.06	0.53	1.92	0.05	0.14	0.02	0.08	0.02	0.02	0.01	0.60	1.57	0.09	0.29
Mn	0.02	0.06	0.00	0.01	0.07	0.07	0.07	0.06	0.04	0.04	0.06	0.05	0.02	0.08	0.02	0.03	0.01
As	0.09	0.06	0.05	0.06	0.03	0.08	0.08	0.05	0.03	0.10	0.06	0.04	0.08	0.01	0.08	0.27	0.12
Ag	0.04	0.02	0.09	0.14	0.12	0.00	0.04	0.10	0.15	0.09	0.11	0.06	0.10	0.00	0.12	0.04	0.03
Total	98.93	97.71	100.07	99.77	99.77	98.23	98.67	98.73	99.00	100.17	99.32	98.35	99.86	92.33	110.00	97.82	98.51

Sample	MIC-16-17/Py	MIC-16-17/Py	MIC-16-17/Py	MIC-16-17/Py	MIC-16-17/Py	MIC-16-17/Py	MIC-16-17/Py	MIC-16-17/Py	MIC-16-17/Py	MIC-16-17/Py	MIC-16-17/Py	MIC-16-17/Po	MIC-16-17/Po	MIC-16-17/Po	MIC-16-17/Po	MIC-16-17/Po	MIC-16-22/Py
S	52.90	50.88	52.56	52.91	52.82	52.94	52.36	52.60	52.10	52.10	52.06	38.45	38.94	38.22	38.29	41.86	52.70
Fe	45.65	46.00	46.08	45.44	45.48	46.39	45.39	46.07	46.87	46.93	42.88	58.17	57.99	59.02	59.65	55.18	45.32

Cu	0.00	0.00	0.07	0.00	0.07	0.01	0.01	0.04	0.00	0.01	0.07	0.00	0.00	0.00	0.08	0.12	0.17
Ni	0.06	0.08	0.00	0.17	0.19	0.14	0.20	0.25	0.17	0.14	0.71	0.51	0.29	0.38	0.42	0.34	0.10
Co	0.25	0.20	0.16	0.23	0.30	0.24	0.65	0.34	0.23	0.15	0.77	0.04	0.05	0.03	0.30	0.13	0.18
Mn	0.04	0.04	0.01	0.02	0.06	0.04	0.14	0.04	0.02	0.06	0.05	0.08	0.04	0.12	0.07	0.04	0.17
As	0.11	0.01	0.08	0.04	0.02	0.12	0.05	0.05	0.00	0.07	0.71	0.08	0.04	0.09	0.07	0.08	0.05
Ag	0.05	0.02	0.02	0.02	0.05	0.07	0.06	0.01	0.02	0.04	0.09	0.01	0.05	0.10	0.02	0.01	0.05
Total	99.05	97.24	98.99	98.83	98.98	99.95	98.86	99.40	99.42	99.51	97.32	97.34	97.40	97.97	98.89	97.78	98.76

Sample	MIC-16-22/Py	MIC-16-22/Py	MIC-16-22/Py	MIC-16-22/Po	MIC-16-22/Po	MIC-16-22/Po	MIC-16-22/Po	MIC-16-27/Py	MIC-16-27/Py	MIC-16-27/Py	MIC-16-27/Py	MIC-16-27/Py	MIC-16-27/Py	MIC-16-27/Py	MIC-16-27/Py
S	53.38	52.71	52.76	39.09	39.08	39.31	38.65	53.41	52.62	52.41	53.35	53.11	53.65	51.46	51.83
Fe	45.11	45.99	46.42	59.54	58.97	58.70	59.26	46.51	45.84	45.14	46.26	46.73	45.46	45.33	45.53
Cu	0.10	0.10	0.00	0.00	0.00	0.01	0.00	0.00	0.00	0.09	0.19	0.16	0.19	0.00	0.12
Ni	0.06	0.14	0.14	0.09	0.28	0.42	0.45	0.09	0.01	0.07	0.06	0.01	0.14	0.70	0.31
Co	0.16	0.05	0.08	0.24	0.03	0.12	0.03	0.06	0.05	0.01	0.05	0.09	0.11	0.27	0.12
Mn	0.07	0.07	0.10	0.06	0.13	0.00	0.06	0.14	0.09	0.02	0.10	0.18	0.17	0.10	0.04
As	0.06	0.10	0.02	0.01	0.05	0.04	0.08	0.04	0.11	0.11	0.09	0.02	0.09	0.07	0.08
Ag	0.02	0.04	0.05	0.10	0.04	0.05	0.18	0.07	0.02	0.08	0.06	0.03	0.01	0.01	0.01
Total	98.97	99.20	99.58	99.12	98.58	98.66	98.71	100.32	98.74	97.92	100.15	100.33	99.83	97.93	98.05

Notes: Sample: MIC/16/03, MIC/16/04 – noritic gabbro; MIC/16/05, MIC/16/06/, MIC/16/07, MIC/16/08, MIC/16/16, MIC/16/17, MIC/16/22, MIC/16/27 – gabbro (Py = pyrite, Ccp = chalcopyrite, Po = pyrrhotite, Mss = monosulfide solid solution, Pn = pentlandite).

Table. 7. LA-ICPMS *in-situ* trace element compositions of magnetite and ilmenite from the gabbro-norites and magnetitite ores of the Betjharan section of the Mayurbhanj Complex.

Sample	MIC-16-17 Mag	MIC-16-17 Mag	MIC-16-17 Mag	MIC-16-14 Ti-Mag	MIC-16-14 Ti-Mag	MIC-16-14 Mag	MIC-16-14 Mag	MIC-16-14 Mag	MIC-16-14 Ti-Mag
Rock	gb	gb	gb	mt	mt	mt	mt	mt	mt
Al	17010.00	16740.00	3186.00	92035.56	85181.04	72877.00	71020.62	73333.97	106165.88
Sc	3.63	49.82	4.18	74.26	75.79	47.75	46.65	53.18	80.74
V	32480.75	30210.87	34608.20	50015.11	48533.76	57188.87	58479.75	64855.07	49408.77
Cr	22301.28	67432.64	27453.78	638.68	657.94	684.40	684.85	702.91	641.79
Mn	961.77	24443.93	4770.69	8600.34	9469.10	4916.53	5193.00	6181.44	8658.36
Co	43.34	366.80	373.83	1781.52	1739.64	1583.76	1732.73	1818.92	1894.95
Ni	895.55	3880.13	3868.37	663.91	670.62	705.94	736.32	854.20	742.25
Cu	BDL	31.90	34.37	10.97	10.96	62.68	79.83	62.61	14.36
Zn	120.96	8139.49	6773.24	1771.54	1804.22	1431.28	1415.91	1641.53	1951.24
Ga	311.16	212.59	232.55	242.38	230.43	282.00	274.04	275.73	247.18
Ge	18.79	18.64	21.58	21.08	14.61	20.57	20.12	25.03	17.80
Rb	2.33	2.74	5.09	BDL	BDL	BDL	BDL	BDL	0.09
Sr	13.97	9.68	5.89	0.11	0.33	0.97	0.40	0.49	0.04
Y	7.93	14.58	0.51	BDL	0.39	0.18	BDL	BDL	0.04
Zr	25.56	152.54	10.92	61.11	73.09	38.00	39.68	59.17	75.11
Nb	0.38	91.24	BDL	2.55	1.66	1.35	1.92	1.64	0.94
Mo	68.02	24.99	27.45	4.30	5.19	6.06	7.40	5.63	4.61
Sn	8.43	28.64	33.09	7.95	6.94	8.38	10.94	7.11	6.06
La	0.90	9.71	0.58	0.04	0.21	0.05	0.19	0.13	0.17
Ce	3.03	20.03	0.69	BDL	0.63	0.13	0.27	0.14	0.11
Pr	0.51	2.54	0.05	BDL	0.09	BDL	0.04	0.04	0.01
Nd	2.65	12.88	0.50	0.08	0.15	BDL	BDL	BDL	BDL
Sm	0.96	3.92	BDL	BDL	0.09	BDL	BDL	BDL	BDL
Eu	0.28	0.62	0.06	BDL	0.02	0.05	BDL	BDL	BDL
Gd	0.58	3.19	0.11	BDL	BDL	BDL	BDL	BDL	BDL
Tb	0.25	0.55	BDL	BDL	0.01	BDL	BDL	0.02	0.01
Dy	1.52	3.39	0.33	0.06	0.10	0.13	BDL	0.09	BDL
Ho	0.30	0.71	0.03	BDL	BDL	BDL	0.02	BDL	BDL
Er	0.61	1.61	0.09	0.04	0.04	BDL	BDL	BDL	BDL
Tm	0.23	0.28	0.02	BDL	0.01	BDL	BDL	BDL	BDL
Yb	0.73	1.50	BDL	BDL	0.26	BDL	BDL	BDL	0.06
Lu	0.13	0.24	0.05	BDL	0.01	BDL	BDL	0.02	BDL
Hf	0.94	14.54	1.54	2.31	2.17	1.95	1.41	1.79	2.08
Ta	0.02	3.61	BDL	1.34	2.11	0.17	0.35	0.47	1.19
Pb	2.19	10.50	10.40	BDL	0.29	1.31	1.31	0.81	0.40
Th	0.01	3.28	0.01	0.04	0.04	0.05	0.10	0.05	0.10
U	0.03	0.09	BDL	BDL78	BDL72	0.04	0.01	0.02	BDL

Sample	MIC-16-17 Ilm	MIC-16-17 Ilm	MIC-16-17 Ilm	MIC-16-17 Ilm	MIC-16-17 Ilm	MIC-16-17 Ilm	MIC-16-17 Ilm	MIC-16-14 Ilm	MIC-16-14 Ilm
Rock	gb	gb	gb	gb	gb	gb	gb	mt	mt
Al	421.69	1859.61	625.93	1778.26	25395.36	9569.64	270.98	52126.39	90220.59
Sc	123.42	125.79	58.37	140.02	118.51	83.20	122.69	50.74	143.19
V	5801.68	6851.98	9051.01	7877.06	6334.48	8348.18	9063.37	29608.57	22192.12
Cr	2874.26	6091.27	5455.18	7037.21	8766.33	17886.61	4535.13	439.13	516.68
Mn	70044.42	66454.10	81730.83	66908.64	69597.58	58409.86	63964.37	5100.30	17382.47
Co	122.85	117.20	53.42	304.25	293.93	769.56	235.38	946.52	1497.94
Ni	353.46	110.68	39.09	477.73	620.03	1337.73	300.93	400.63	367.58
Cu	54.27	53.25	64.36	57.43	50.61	52.25	54.52	49.88	24.30
Zn	792.84	1740.25	568.40	654.93	865.43	6476.70	1042.12	1116.32	2146.44
Ga	17.33	12.93	5.34	9.93	16.43	52.59	9.56	147.52	146.57
Ge	12.28	10.97	BDL	9.68	13.38	10.94	13.31	11.42	13.92
Rb	0.78	BDL	1.28	0.13	0.92	0.49	BDL	0.19	BDL
Sr	0.58	1.45	20.78	3.15	95.23	2.57	0.45	0.18	0.25
Y	1.78	2.05	4.25	2.72	3.68	3.70	4.71	0.24	0.20
Zr	3337.46	2079.06	642.43	4926.29	5369.46	6402.15	7028.73	41.84	114.56
Nb	2152.62	1851.41	1966.18	1005.06	963.00	868.73	890.33	7.97	75.73
Mo	34.16	36.82	60.94	14.14	14.44	31.17	23.32	3.62	4.48
Sn	97.75	110.64	151.06	45.91	46.03	100.94	61.29	5.41	5.23
La	0.13	0.71	26.56	5.85	5.20	5.92	0.42	0.04	0.12
Ce	0.41	1.56	59.33	5.34	6.79	7.06	1.06	0.24	0.28
Pr	0.02	0.17	6.71	0.30	0.44	0.67	0.07	0.01	0.07
Nd	BDL	0.66	29.11	1.02	1.23	2.48	BDL	BDL	BDL
Sm	BDL	BDL	5.49	BDL	0.64	0.71	0.11	0.08	BDL
Eu	0.06	0.02	0.91	0.04	0.41	0.17	0.08	0.02	BDL
Gd	BDL	0.27	4.39	0.14	0.12	0.45	0.11	BDL	BDL
Tb	0.02	0.04	0.51	0.04	BDL	0.08	0.11	BDL	BDL
Dy	0.07	0.45	1.40	0.51	0.65	0.69	0.45	0.10	0.04
Ho	0.10	0.23	0.37	0.21	0.24	0.24	0.25	BDL	BDL9
Er	1.06	1.15	0.81	0.60	0.84	1.03	1.24	BDL	BDL
Tm	0.44	0.27	0.09	0.14	0.09	0.35	0.31	BDL	BDL
Yb	5.38	3.24	1.84	2.44	2.38	3.69	2.74	0.05	0.04
Lu	1.16	0.78	0.30	0.39	0.58	1.11	0.65	0.01	BDL
Hf	143.16	115.10	34.48	98.22	121.05	155.11	147.52	1.74	5.40
Ta	90.29	74.64	92.38	50.54	54.96	38.35	51.19	1.41	4.76
Pb	0.92	1.80	31.92	1.14	4.78	7.86	1.18	0.39	0.39
Th	2.69	0.25	2.86	0.17	2.37	3.60	3.02	BDL	BDL
U	0.66	0.18	3.92	3.98	3.70	5.06	10.88	BDL69	0.02

Notes: Sample – Mag = magnetite, Ti-Mag = titanomagnetite, Ilm = ilmenite; Rock – gb = gabbro, mt = magnetitite.

Table. 8. LA-ICPMS *in-situ* trace element compositions of sulfides of the gabbro-noritic rocks from the Betjharan section of the Mayurbhanj Complex.

Sample	MIC-16-17	MIC-16-17	MIC-16-17	MIC-16-17	MIC-16-17	MIC-16-17	MIC-16-17	MIC-16-17
Mineral	Py	Py	Py	Py	Po	Py	Py	Py
Co	124.93	1812.11	1691.15	2043.81	4683.26	7234.45	39.81	1047.7
Ni	103.83	938.53	4316.29	4161.37	15574.74	20023.96	80.58	379.82
Cu	15.84	91.13	4609.67	322.54	BDL	3874.92	0.54	21.6
Zn	BDL	BDL	16.35	21.7	6.81	17.37	BDL	BDL
As	482.54	647.9	2174.68	1917.35	BDL	6560.98	47.72	509.12
Ag	BDL	BDL	8.15	9	7.17	15.26	BDL	BDL
Sb	0.42	11.7	18.02	47.9	BDL	3.54	BDL	1.61
Ba	BDL	104.68	145.31	20.46	0.2	10.21	BDL	BDL
Au	BDL	BDL	0.4	0.59	BDL	0.36	BDL	BDL
Pb	27.17	340.48	578.62	2525.83	128.53	3120	7.16	97.05
Bi	1.01	4.73	5.98	8.99	0.35	36.14	0.23	2.91

Notes: Py = pyrite, Po= pyrrhotite

Table. 9. Bulk-rock major and trace element data of the gabbro-norite-anorthosites from the Mayurbhanj Complex.

Sample	MIC/ 16/03	MIC/ 16/04	MIC/ 16/05	MIC/ 16/08	MIC/ 16/16	MIC/ 16/17	MIC/ 16/22	MIC/ 16/27	SHB/19 -12/62	SHB/19 -12/63	SHB/19 -12/64	SHB/19- 12/65	SHB/19- 12/67	SHB/19- 12/70
Rock	nt-gb	nt-gb	gb	gb	gb	gb	gb	gb	an	an	an-gb	an-gb	gb	gb
Major oxides (wt%)														
SiO_2	52.52	52.83	52.38	51.98	52.66	52.72	51.15	48.23	56.36	67.09	54.00	52.19	50.69	47.89
TiO_2	0.63	0.66	0.83	0.71	0.79	0.78	0.70	2.03	0.61	0.60	1.12	0.30	1.22	1.21
Al_2O_3	11.00	13.93	14.07	15.84	11.90	12.14	13.81	12.76	19.57	16.03	16.69	15.77	16.08	14.94
$Fe_2O_{3\,(tot)}$	10.03	9.53	10.12	9.95	10.92	10.81	10.43	14.34	7.23	3.65	11.27	11.79	16.32	14.21
MnO	0.16	0.14	0.15	0.14	0.16	0.16	0.16	0.19	0.11	0.05	0.17	0.21	0.23	0.21
MgO	11.50	8.87	8.49	5.76	10.04	9.97	9.87	6.82	2.27	1.17	3.77	6.16	3.02	6.90
CaO	10.87	10.19	10.25	9.31	9.80	9.68	10.68	9.73	6.27	3.21	6.96	9.72	8.40	10.72
Na_2O	2.12	2.64	2.61	3.27	2.39	2.40	1.83	3.52	5.04	5.42	4.05	2.95	3.63	2.36
K_2O	0.46	0.57	0.50	0.89	0.52	0.65	0.40	0.37	0.47	0.86	0.75	0.29	0.45	0.19
P_2O_5	0.08	0.09	0.07	0.10	0.10	0.10	0.08	0.14	0.19	0.14	0.08	0.02	0.06	0.09
Total	99.57	99.54	99.56	97.99	99.42	99.55	99.22	98.16	98.14	98.25	98.88	99.42	100.14	98.76
LOI	0.62	0.55	0.36	1.78	0.57	0.53	0.89	1.54	1.45	1.04	1.00	0.54	0.12	1.20
S	0.06	0.07	0.03	0.08	0.09	0.09	0.05	0.15	X	X	X	X	X	0.08
Trace element (ppm)														
Sc	32	26	26	24	28	28	34	29	10	X	27	36	46	33
V	167	149	158	189	181	184	218	540	129	37	298	174	308	372
Cr	1250	466	384	58	795	718	630	115	21	X	23	25	39	186
Co	65.80	51.30	56.80	49.50	65.10	61.50	50.70	46.70	24.00	8.30	62.40	77.20	77.40	54.20
Ni	468.50	271.40	279.60	147.90	358.70	341.00	226.70	109.40	24.60	12.30	15.60	85.60	26	129.80
Cu	124.60	80.20	76.30	84.60	90.80	81.30	96.30	208.30	98.30	29.10	27	197.50	66.40	212.60
Ag	0.09	0.13	0.18	0.06	0.04	0.04	0.03	0.05	0.07	0.02	0.02	0.11	0.03	0.15
Zn	63	58	68	69	74	73	70	97	79	66	96	78	83	109
Ga	12.70	13.90	14.40	17.90	13.20	13.70	12.00	24.70	24.00	18.90	19.30	17.70	20.20	21
Rb	11.30	13.30	11.90	22.20	13.60	17.30	14.10	11.20	13.30	23.50	21	7.30	8.70	6
Sr	245.20	330.60	338.80	407.40	284.30	287.60	118.60	175.20	525.90	392.10	393	310.20	388.80	125.60

Y	11.30	12.90	12.50	13.60	14.80	14.00	14.70	19.30	6.90	10.70	6.80	7.40	7.40	22
Zr	50	61	62	52	74	68	50	92	87	199	53	17	18	59
Nb	2.30	2.70	3.00	2.70	3.30	3.40	3	3.20	7.30	13.90	11.60	1.10	2.10	1
Mo	0.20	0.30	0.20	0.20	0.40	0.30	0.20	0.20	0.30	0.30	0.20	0.10	0.30	0.10
Cs	0.70	0.70	0.70	0.70	0.80	0.60	0.60	0.50	0.50	0.30	0.80	0.30	0.50	1.10
Ba	122.80	146.40	141.50	211.90	158.50	181.50	118.60	76.50	159.60	215.70	205.70	145.20	165.90	33
La	7.90	9.30	8.60	9.90	10.90	10.50	6.20	5.80	19.50	32.70	9.50	5.30	5.70	2.40
Ce	15.80	19.30	17.70	20.40	22.00	27.00	13.00	15.00	34.00	53.80	16.50	9.80	11.10	6.40
Pr	2.10	2.50	2.30	2.70	2.90	2.80	1.70	2.50	3.30	5.50	2.00	1.10	1.40	1.10
Nd	9.30	11.50	9.70	11.10	13.00	11.20	7.40	12.70	12.30	18.40	8.20	4.20	5.60	6.70
Sm	2.20	2.40	2.50	2.60	2.80	3.00	1.80	4.20	2.30	3.40	1.70	1.00	1.30	2.80
Eu	0.80	0.90	0.90	1.20	1.00	1.00	0.70	1.50	1.50	1.10	0.80	0.60	0.80	1.10
Gd	2.50	2.80	2.50	2.90	3.10	3.10	2.50	4.70	1.80	2.60	1.30	1.20	1.30	3.60
Tb	0.40	0.40	0.40	0.40	0.50	0.40	0.40	0.70	0.20	0.40	0.20	0.20	0.20	0.70
Dy	2.30	2.70	2.40	2.70	2.90	2.90	2.60	4.10	1.30	2.20	1.30	1.40	1.60	4.30
Ho	0.40	0.50	0.50	0.50	0.60	0.60	0.60	0.80	0.30	0.40	0.30	0.30	0.30	0.90
Er	1.40	1.50	1.30	1.60	1.60	1.60	1.80	2.10	0.80	1.10	0.80	0.80	0.80	2.60
Tm	0.20	0.20	0.20	0.20	0.20	0.20	0.30	0.30	0.10	0.20	0.10	0.10	0.10	0.40
Yb	1.10	1.20	1.20	1.40	1.30	1.40	1.70	1.80	0.70	1.10	0.80	0.80	0.80	2.20
Lu	0.20	0.20	0.10	0.20	0.20	0.20	0.30	0.20	0.10	0.20	0.10	0.10	0.10	0.30
Hf	1.40	1.80	1.70	1.60	2.20	1.80	1.40	2.90	2.30	4.60	1.40	0.60	0.60	1.90
Ta	0.20	0.20	0.10	0.10	0.20	0.20	0.20	0.20	0.40	0.80	0.60	X	0.10	X
Pb	2.10	2.20	2.30	2.20	2.80	2.70	1.30	1.50	5.90	12.50	4.50	1.20	1.30	5.20
Th	0.90	1.10	1.10	0.80	1.30	1.20	1.00	0.80	2.70	3.60	0.70	0.60	0.60	0.30
U	0.20	0.30	0.30	0.20	0.40	0.30	0.30	0.30	0.30	0.90	0.30	0.20	0.20	0.10

Notes: nt-gb - noritic gabbro, gb - gabbro; an – anorthosite; an-gb = anorthositic gabbro.

Table. 10. Bulk rock Sm–Nd isotopic data of the gabbro-anorthosites from the Mayurbhanj Complex.

Sample	Rock	Sm (ppm)	Nd (ppm)	$^{147}Sm/^{144}Nd$	$^{143}Nd/^{144}Nd$	±2σ	$(^{143}Nd/^{144}Nd)_i$ 3022 Ma	T_{DM}	ε_{Nd} (3022 Ma)
SHB/19-12/62	an	1.98	12.00	0.09934	0.51042	0.000014	0.508702	3.45	-0.20
SHB/19-12/63	an	3.00	18.00	0.10069	0.51047	0.000012	0.508436	3.42	-5.42
SHB/19-12/64	an-gb	1.47	7.27	0.12184	0.51093	0.000013	0.508466	3.45	-4.83
SHB/19-12/65	an-gb	0.96	4.10	0.14163	0.51141	0.000013	0.508459	3.38	-4.97
SHB/19-12/67	gb	1.27	5.49	0.13925	0.51132	0.000013	0.508499	3.47	-4.18
SHB/19-12/70	gb	2.56	6.32	0.24474	0.51333	0.000015	0.508580	2.20	-2.59

Notes: an - anorthosite; an-gb - anorthositic gabbro; gb - gabbro.

CHAPTER 5

DISCUSSION

5.1. Magmatic crystallization and sub-solidus re-equilibration of the mineral assemblages

Presence of a gabbro-noritic suite of rocks with accessory magnetite-titanomagnetite phases in the lower part and anorthosites with magnetitite bodies in the upper part of the Mayurbhanj Complex suggest probable origin of these plutonic rock suite from a relatively Fe-Ti-rich tholeiitic basaltic magma. The phase assemblages and the compositions of the minerals (**Table. 2-5**) resemble those of the Skaergaard layered mafic igneous complex (Greenland) and magnetitite bearing Upper Zone of the Bushveld Complex (South Africa). Therefore, it can be speculated that the parental magma of the Mayurbhanj Complex was similar to the parental magma of the Skaergaard intrusion (e.g., Wager and Mitchell, 1951; Jakobsen et al., 2005, 2010) or the magnetitite bearing Upper Zone of the Bushveld Complex (e.g., Barnes et al., 2010; Cawthorn, 2015).

The mineral assemblage of the gabbro-noritic and the gabbro-anorthositic rocks of the Mayurbhanj Complex is equivalent to that of the middle zone of the Skaergaard intrusion as characterized by the presence of plagioclase + orthopyroxene + clinopyroxene + Fe-Ti oxides + quartz and absence of olivine, which suggest that this assemblage was formed from the fractionation of a silica saturated Fe-Ti rich tholeiitic basaltic magma (e.g., Morse, 1980). The fractional crystallization sequence of the gabbroic rocks of the Mayurbhanj Complex was plagioclase - pyroxene (both clinopyroxene and orthopyroxene) – magnetite (accessory phase) which can be rationalized by using both petrographic features along with the three-phase experimental system forsterite-diopside-anorthite (Fo-Di-An) at 1 atmospheric pressure (e.g., Osborn and Tait, 1952; Morse, 1980). Since the Mayurbhanj Complex consists of plagioclase dominated (~50 modal %) gabbro-noritic rocks in the lower part, we infer that the liquid composition at the beginning of crystallization was in the plagioclase field of the Fo-Di-An system and relatively Ca-rich plagioclase was the first solid phase crystallized from the magma (An ~ 52.55 – 54.07 for the gabbro-norite of the Betjharan section). Upon the formation of plagioclase, the liquid moved towards the plagioclase-pyroxene cotectic when both plagioclase and pyroxene started crystallizing as cumulus crystals. Crystallization of plagioclase and clinopyroxene as early crystallizing phases resulted in the Fe_2O_3 and TiO_2 enrichment of the residual magma which is responsible for the formation of accessory magnetite-titanomagnetite within the gabbro-noritic rock (e.g., Reynolds, 1985b). Magnetite-titanomagnetite crystallized from the interstitial Fe-rich melt at the magma chamber floor where plagioclase and pyroxene crystals settled down as cumulus phases. The enrichment of the silica is attributed to the crystallization of magnetite from the magma leading to the formation of minor amounts of interstitial quartz (e.g., Morse, 1980; Hunter and Sparks, 1990). The early formed plagioclase crystals occur as large cumulus phases while the later formed plagioclase simultaneously crystallized with the clinopyroxene resulting in ophitic textures (e.g., Wager et al., 1960; Phillpotts and Ague, 2009). The occurrence of pigeonite in a few gabbros instead of orthopyroxene suggests a sub-solidus reaction between enstatite and diopside (e.g., Kushiro, 1972; Morse, 1980). Intercumulus Cr-rich magnetite/-titanomagnetite in the gabbro-norites of the Betjharan section is commonly enclosed within clinopyroxene and plagioclase indicating that it was crystallised concurrently with pyroxene and plagioclase, and it is an early crystallising phase of the magma (**Fig. 3c, d, e; 4d, e, f**). Chromium is strongly compatible in magnetite (D_{Cr} magnetite/melt = 100-600; Irving, 1978), moderately compatible in clinopyroxene (D_{Cr} clinopyroxene/melt = 2.7; Hart and Dunn, 1993) and incompatible in plagioclase (D_{Cr} plagioclase/melt = 0.03; Phinney and Morrison, 1990). Therefore, relatively low Cr content in the magnetite-titanomagnetite from the upper part of the igneous complex can be attributed to the depletion of Cr in the fractionated magma due to early crystallization of Cr-rich magnetite-titanomagnetite and clinopyroxene that formed the lower part of the plutonic complex.

The two-pyroxene thermometer of Brey and Kohler (1990) has been utilized for the gabbro-norites and gabbro-anorthosites to determine the liquidus and sub-solidus re-equilibration temperatures of the igneous assemblages. The computation has been done using the spreadsheet of Putrika (2008). The calculation reveals a range of temperatures that vary between 1199° and 956°C for the gabbro-norites and 1096° - 839°C for the gabbro-anorthosites (**Table. 11**). The gabbro-norites of the Luhasila area **(Fig. 6e)** of the Betjharan section have calculated temperatures ranging from 1199° to 1055°C that are close to the primary liquidus temperature of pyroxene in a fractionating basaltic magma (e.g., Lindsley, 1983) (**Fig. 6e**).

5.2. Formation of Fe-Ti oxides and the magnetitite layer

The compositions of Fe-Ti oxide minerals in the gabbro-norites, gabbro-anorthosites and magnetitite ore bodies of the Mayurbhanj Complex are shown in the FeO-TiO_2-Fe_2O_3 triangular diagrams (**Fig. 8a, f**). The oxide minerals from the gabbro-norite and magnetitite of the Betjharan section fall along the magnetite-ulvöspinel and ilmenite-hematite solid solution series whereas the oxide minerals of the gabbro-anorthosite and the magnetitites of the Hatichhad section show a systematic deviation along the magnetite-ulvöspinel and ilmenite-hematite solid solution series, which can be attributed to the presence of ilmenite as exsolved phases within the host magnetite grains.

The cumulus magnetites of the magnetitite ore bodies of the Betjharan section show enrichment of TiO_2, Al_2O_3 and depletion of Cr_2O_3 relative to the accessory magnetite grains of the gabbro-norites (**Fig. 8b, c, d**). The accessory magnetites of the gabbro-anorthosites have higher Cr_2O_3 and V_2O_3 than the cumulus magnetites of the magnetitites from the

Table. 11: Parameters used for two-pyroxene thermometry and calculated temperatures from gabbro-norite-anorthosites from the Mayurbhanj Complex.

Sample	Thermometer after Putrika, 2008							Range of temp (T °C)
	Parameters							
	X_{EnFs}^{Cpx}	X_{EnFs}^{Opx}	X_{CaO}^{Cpx}	X_{MnO}^{Opx}	X_{Na2O}^{Opx}	X_{En}^{Opx}	X_{Di}^{Opx}	
MIC/16/03 Opx-Cpx = 9 pairs	0.0805 - 0.2808	0.8514 - 0.9279	0.7303 - 0.9358	0.0003 - 0.0032	0.0006 - 0.0048	0.6316 - 0.7781	0.0438 - 0.0774	956.21 - 1182.44
MIC/16/04 Opx-Cpx = 10 pairs	0.1423 - 0.3905	0.9134 - 0.9493	0.5906 - 0.8753	0.0052 - 0.0144	0.0026 - 0.0063	0.5922 - 0.7270	0.0470 - 0.0740	1011.47 - 1175.70
MIC/16/05 Opx-Cpx = 6 pairs	0.1660 - 0.5019	0.9063 - 0.9392	0.6522 - 0.8394	0.0055 - 0.0184	0.0039 - 0.0057	0.5741 - 0.6831	0.0496 - 0.0679	1042.63 - 1192.10
MIC/16/06 Opx-Cpx = 7 pairs	0.1568 - 0.3136	0.8891 - 0.9792	0.6974 - 0.8248	0.0040 - 0.0154	0.0036 – 0.0081	0.5771 – 0.6846	0.0246 – 0.0567	1009.30 – 1161.66
MIC/16/07 Opx-Cpx = 6 pairs	0.1091 – 0.5276	0.8716 – 0.9246	0.4265 – 0.8884	0.0035 – 0.0157	0.0029 – 0.0052	0.5693 – 0.6099	0.0474 – 0.0750	956.37 – 1194.15
MIC/16/16 Opx-Cpx = 9 pairs	0.1757 – 0.3375	0.8661 – 0.9055	0.5905 – 0.8165	0.0004 – 0.0055	0.0029 – 0.0067	0.6679 – 0.7213	0.0677 – 0.0740	1055.17 – 1199.21
MIC/16/17 Opx-Cpx = 5 pairs	0.2050 – 0.3267	0.8675 – 0.9186	0.6433 – 0.7708	0.0008 – 0.0051	0.0017 – 0.0051	0.6383 – 0.7129	0.0623 – 0.0684	1054.67 – 1175.55
MIC/16/22 Opx-Cpx = 1 pair	0.1977	0.7092	0.7667	0.0157	0.0122	0.3537	0.0739	1162.21
SHB/19-12/62 Opx-Cpx = 2 pair	0.4190 – 0.4320	0.7906 – 0.8028	0.5125 – 0.5133	0.0223 – 0.0311	0.0030 – 0.0119	0.3278 – 0.3334	0.0192 – 0.0210	1073.29 – 1081.60
SHB/19-12/67 Opx-Cpx = 7 pair	0.1148 – 0.2096	0.7711 – 0.9288	0.7818 – 0.8684	0.0213 – 0.0338	0.0000 – 0.0052	0.2475 – 0.2864	0.0130 – 0.0655	839.20 – 1096.14

Notes: Betjharan section (MIC/16/03, MIC/16/04 = noritic gabbro; MIC/16/04, MIC/16/06, MIC/16/07, MIC/16/16, MIC/16/17, MIC/16/22 = gabbro); Hatichhad section (SHB/19-12/62 = anorthosite; SHB/19-12/67 = gabbro).

Hatichhad section (**Fig. 8g, h**). Since Cr and V are concentrated within the early formed spinel, it can be inferred that the Ti, Al and Fe^{3+} are concentrated in late-stage magnetite crystals that formed the magnetitite ore bodies. Accessory Fe-Ti oxides in the gabbro-norites from the Betjharan section have a relatively higher Cr_2O_3 content and lower TiO_2 and Al_2O_3 content than the gabbro-anorthosites of the Hatichhad section of the igneous complex which is due to the fractionation of the parental Fe-rich basaltic magma.

The magnetitite ores primarily show cumulus texture represented by the relatively coarser grains of magnetite-titanomagnetite (**Fig. 5a-e**)with a minor amount of interstitial silicate minerals altered to chlorite (**Fig. 5e**). Many re-equilibrium textures are present in the Fe-Ti-oxide minerals of the gabbroic rocks and magnetitites which indicate a change in the degree of oxidation and rate of diffusion e.g., (i) single-phase homogeneous spinel formation, (ii) trellis intergrowths of thin ilmenite lamellae within the host, (iii) sandwich intergrowths of thick ilmenite lamellae, (iv) granules or occasional lamellae of ilmenite on the external borders of the magnetite (e.g., Buddington and Lindsley, 1964). In the spinel (magnetite) Fe_2TiO_4 component transforms to ilmenite exsolution by sub-solidus oxidation, and in most of the cases exsolution-oxidation plays the key role (e.g., Buddington and Lindsley, 1964; Tan et al., 2016). In the samples of the Mayurbhanj Complex two distinctive types of ilmenite lamellae are present within the magnetite-titanomagnetite grains (**Fig. 3c, 3e, 4d, 4f**) representing two stages of ilmenite formation. The coarse ilmenite lamellae within titanomagnetite-magnetite grains (**Figs. 3c, 3e**) suggest formation by direct exsolution at high temperature and the thin ilmenite lamellae within host magnetite grains (**Figs. 3e, 4d**) may have resulted from inter-oxide re-equilibration (e.g., Haggerty, 1991; Tan et al., 2016).

The compositions of co-existing magnetite-ilmenite pairs in gabbro-norite and magnetitite ores have been used to calculate the equilibrium temperature and oxygen fugacity of the different textural assemblages mentioned above. This geothermometer is based on the observation that the TiO_2 concentration in magnetite is a function of temperature of magnetite crystallization (Buddington and Lindsley, 1964). The authors showed that at a constant temperature, higher fO_2 leads to decrease in TiO_2 content of the magnetite and an increase in Fe_2O_3 content of the ilmenite. The method of Spencer and Lindsley (1981) was used to determine the ulvöspinel component in magnetite and the ilmenite component in the ilmenite. These parameters were used to calculate the temperature and fO_2 of the oxide assemblages. The calculation was done using the computation of Lepage (2003), following Carmichael (1967). The calculated temperature of the accessory magnetite in the Betjharan gabbro-norite was 748°C to 498°C and oxygen fugacity was 14.90 to 27.12 whereas the cumulus magnetite of the magnetitite yielded T = 798°C to 583°C and fO_2 = 11.38 – 20.73 (**Table. 12; Fig. 8k**). The Hatichhad section has T = 768°C to 336°C and fO_2 = 15.42 – 38.89 for the accessory magnetite of the gabbro-anorthosites whereas the temperature and oxygen fugacity of the cumulus magnetite of the magnetitites ranges from 431°C – 330°C and 30.65 – 38.35 respectively (**Table. 12; Fig. 8l**). The large variation in temperature and oxygen fugacity indicates various stages of cooling history with sub-solidus re-equilibration of the co-existing oxide phases. The large variation in temperature and fO_2 indicates re-equilibration during hydrothermal alteration of the igneous complex. The lowest temperature and corresponding fO_2 reflect the last stage of re-equilibration. For this final stage, the accessory oxide phases in gabbro-anorthositic rocks reveal an equilibration temperature of 336°C with log fO_2 = 38.89 (Sample SHB/19-12/67 **Fig. 8l; Table. 12**) whereas in magnetitite the temperature is 330°C with log fO_2 = 38.35 (Sample

Table. 12. Parameters used for oxide thermometry, calculated temperature and oxygen fugacity from the gabbro-norite-anorthosites and magnetitites of the Mayurbhanj Complex.

Sample	Thermometer after Carmichael, 1967; Lepage, 2003				Temp(^{o}C)	*f*O_2
	Parameters					
	Recalculated FeO(T) of magnetite	**Recalculated FeO(T) of ilmenite**	**Mol% of ulvöspinel in magnetite**	**Mol% of ilmenite**		
MIC/16/03 Mag-Ilm = 3 pairs	95.53 - 97.17	98.51 – 99.14	0.0038 – 0.0131	0.8830 – 0.9202	521.64 - 586.69 ,	-16.88 to - 19.15
MIC/16/04 Mag-Ilm = 4 pairs	98.35 – 100.22	98.79 – 100.46	0.0139 – 0.0208	0.8613 – 0.9139	587.24 - 615.36	-15.53 to - 17.67
MIC/16/05 Mag-Ilm = 3 pairs	98.48 – 99.07	98.73 – 100.55	0.0131 – 0.0175	0.9067 – 0.9472	550.61 - 583.47	-17.42 to - 20.37
MIC/16/06 Mag-Ilm = 4 pairs	98.17 – 100.10	99.27 – 100.26	0.0569 – 0.1263	0.8961 – 0.9260	643.82 - 709.27	-15.00 to - 17.33
MIC/16/07 Mag-Ilm = 3 pairs	96.25 – 97.09	99.10 - 100.25	0.1710 - 0.1912	0.9037 - 0.9242	692.46 - 727.66	-15.04 to - 16.44
MIC/16/08 Mag-Ilm = 2 pairs	97.36 - 100.38	99.75 - 99.94	0.0035 - 0.0782	0.9016 - 0.9150	531.89 - 658.06	-16.57 to - 18.13
MIC/16/12 MIC/16/14 Mag – Ilm = 3 pairs	98.27 - 98.41	98.63 – 102.84	0.0628 – 0.1160	0.6252 – 0.9575	582.72 - 797.63	-11.38 to - 20.73
MIC/16/16 Mag-Ilm = 5 pairs	96.85 – 99.66	96.80 – 98.96	0.0051 – 0.2559	0.8358 – 0.9543	545.23 - 747.66	-14.90 to - 21.45
MIC/16/17 Mag-Ilm = 5 pairs	98.86 – 99.52	97.25 – 99.13	0.0204 – 0.0556	0.8901 – 0.9321	615.99 - 655.81	-15.74 to - 18.69
MIC/16/22 Mag-Ilm = 2 pairs	97.45 - 98.20	98.70 - 99.05	0.1854 - 0.4674	0.9813 - 0.9838	505.41 - 509.72	-26.18 to - 26.90
MIC/16/27 Mag-Ilm = 1 pair	96.92	98.84	0.3101	0.9837	498.05	-27.12
SHB/19-12/67 Mag-Ilm = 5 pair	97.19 – 98.66	97.70 – 100.21	0.2376 – 0.4291	0.9328 – 0.9953	335.97 – 768.33	-15.42 to - 38.89
SHB/19-12/69 Mag-Ilm = 2 pair	97.70 – 97.79	99.14 – 99.62	0.5729 – 0.6133	0.9884 – 0.9942	329.85 – 431.44	-30.65 to - 38.35

Notes: Betjharan section (MIC/16/03, MIC/16/04 - noritic gabbro; MIC/16/04, MIC/16/06, MIC/16/07, MIC/16/16, MIC/16/17, MIC/16/22, MIC/16/27 - gabbro; MIC/16/12, MIC/16/14 - magnetitite); Hatichhad section (SHB/19-2/67 – gabbro; SHB/19-12/69 - magnetitite).

SHB/19-12/69 **Fig. 8l; Table. 12**). These low temperatures and the associated oxygen fugacities indicate hydrothermal alteration of the primary magmatic assemblages corresponding to chlorite formation. In the fO_2 - T profile, these data indicate that the igneous assemblages have re-equilibrated in oxygen fugacity conditions equivalent to QFM±2 (**Fig. 8k, l**).

A variety of mechanisms have been proposed to explain the concentration of Fe-Ti oxides from magmas (e.g., Lister, 1966; Duchesne, 1999). The critical question arises that whether Fe-Ti oxides are precipitated directly from magmas or alternatively from an immiscible Fe-Ti oxide liquid separation from the magmas. The formation of Fe-Ti-V magnetitite can be attributed to several processes. Wager (1960) proposed extensive fractionation responsible for the formation of Fe-rich melts which eventually become FeO saturated and as a result form Fe-Ti-V rich oxide layer in the upper part of layered mafic intrusions. Alternatively, formation of an immiscible oxide melt from silicate magma and settling of the oxide minerals can also form Fe-Ti oxide layer of mafic intrusions (Zhou et al., 2005). Earlier studies on the Mayurbhanj magnetitites suggest late magmatic crystallization of oxide minerals from the tholeiitic magma followed by residual liquid injection is the process responsible for the formation of the oxide layer in the igneous complex (Das, 2014). Based on the textural relationship and geochemistry it can be assumed that the increased concentration of Fe and Ti by fractional crystallization of tholeiitic magma followed by separation into silicate magma and a Fe-rich oxide melt might be responsible for the formation of the magnetitite layers at the upper part of the igneous complex. With the continuous fractionation process the basaltic magma became rich in Fe and Ti and reached to the silicate immiscibility (e.g., Charlier and Grove, 2012) with the formation of a Si-rich liquid and a Fe-Ti rich liquid (e.g., Namur et al., 2012; Wang and Zhou, 2013). The mineral assemblage of the magnetitite layer (Cr-poor magnetite-titanomagnetite + ilmenite) accumulated from the Fe-Ti rich melts. The co-existing Si-rich melts may form plagioclase rich gabbroic-anorthosite and anorthosite in the upper part of the igneous complex. This model is similar to the formation of the magnetitites in the Sept Iles layered intrusion (e.g., Namur et al., 2012) and magnetitites of the Panzhihua gabbro intrusion of the Emeishan Large Igneous Province, PR China (e.g., Wang and Zhou, 2013). The Fe-Ti rich melt had low viscosity and relatively high density with volatiles and had settled downward. The percolating Fe-Ti rich immiscible melt were collected as stagnant layers at the bottom of the magma chamber and solidified later than silicate minerals. Alternatively, the massive magnetitite layer might have produced by infiltration of Fe-Ti rich melts through an unconsolidated pyroxene-plagioclase cumulate similar to the model proposed for Fe-Ti oxide rich layer in the Upper Zone of the Bushveld Complex (Reynolds, 1985; Gruenewaldt, 1993) and due to the filter pressing mechanism the crystals of magnetites moved upward in the Mayurbhanj Complex. A lower ultramafic cumulate sequence is missing in the Mayurbhanj Complex which is unlike the Panzhihua mafic intrusion of the Emeishan Large Igneous Province. The probable reasons for the missing of a lower ultramafic unit maybe early crystallization in a deep crustal chamber before the emplacement of the parental magma into a shallow crustal chamber now occupied by the plutonic complex. Alternatively, ultramafic rocks which contain adequate Cr-rich magnetite-titanomagnetite may simply not be exposed in this intrusion.

5.3. Trace element fingerprint of oxide minerals

Accessory magnetite-titanomagnetite in the gabbro-noritic rocks of the Betjharan section of the Mayurbhanj Complex crystallized from the basaltic melt along with the common rock-forming silicate minerals (e.g., plagioclase and pyroxene), whereas cumulus magnetite crystals in magnetitite layers crystallized from a relatively evolved basaltic magma. Magnetite crystals may also crystallize from a magmatic sulfide liquid as well as from sulfides that formed from a late-stage hydrothermal solution (e.g., Dare et al., 2012). Magnetite crystals from different sources accommodate a range of trace elements from divalent metals e.g., Mn, Zn, Co, and Ni through trivalent metals Cr, V, Ga to high field strength elements (Ti, Hf, Zn, Ta, Nb) and Ge (Dare et al., 2014; 2015; Nadoll et al., 2014; Liu et al., 2015; Augé et al., 2017; Broughm et al., 2017). In situ trace element analyses by LA-ICPMS of accessory magnetites (**Table. 7**) in the gabbro-norites show relatively higher Cr (~22301 - 67433 ppm) than the cumulus magnetite crystals in the magnetitite ores (~664 - 854 ppm) which is due to early fractionation of the accessory magnetite during the formation of the gabbroic rocks (**Fig. 11a, b**). Fractionation of accessory magnetite-titanomagnetite from the basaltic magmas would have depleted the residual magma in Cr. This is also supported by the relatively higher Ni concentrations (~896 - 3880 ppm) in the accessory magnetite of gabbro-noritic rocks than in the cumulus magnetite of magnetitite ores (≈ 664 - 884 ppm) (**Fig. 11e, h**).

The composition of Fe-rich tholeiitic basalt has been used to calculate the partitioning behavior of Cr and Ni in gabbro-norite during the crystallization of magnetite. Iron-rich tholeiitic basalt has been proposed as the parental magma composition of the Upper Zone of the Bushveld Complex, which is similar to the parental magma of the Skaergaard intrusion (Barnes et al., 2010). The composition of diorite (Smithies and Champion, 2000) has been used to calculate the partition co-efficient of trace elements within the magnetitite bodies because when the magnetite crystallizes to form the magnetitite layer the magma has evolved to a diorite or granodiorite composition. Cr^{3+} within the magnetite crystals mainly entered the octahedral site, substituting for Fe^{3+}. The calculated partition coefficient for Cr in accessory magnetite is $D_{Cr}^{Mt\ of\ gabbro/Fe\ tholeiite}$ = 110.95 - 335.49 from the gabbro-norites whereas in cumulus magnetite from the magnetitite is $D_{Cr}^{Mt\ of\ magnetitite/diorite}$ = 4.78 - 5.27 and for Ni $D_{Ni}^{Mt\ of\ gabbro/Fe\ tholeiite}$ = 8.45 - 36.61 and $D_{Ni}^{Mt\ of\ magnetitite/diorite}$ =10.93 - 14.06. Vanadium shows an inverse relation (**Fig. 11a**), that is, the accessory magnetites of the gabbro-norites have a lower V concentration (~30211 - 34608 ppm) than the magnetite of the magnetitite ores (~48534 - 64855 ppm). This is due to the fractionation of clinopyroxene before accessory magnetite within the gabbroic rocks. The partition coefficient of vanadium for both clinopyroxene and magnetite is a strong function of oxygen fugacity and $D_V^{Mt/liquid}$ is always higher than $D_V^{Cpx/liquid}$ under the same experimental conditions (e.g., Toplis and Corgne, 2002). In the gabbro-norites, the value of the partition coefficient of vanadium in magnetite is $D_V^{Mt\ of\ gabbro/Fe\ tholeiite}$ = 126.41 – 144.80. The partitioning behavior of HFSE (Zr, Hf, Nb, Ta) in magnetite is strongly dependent on the major element composition of the magnetite in general, and are particularly dependent on D_{Ti}, Ti, and Al content of the magnetite, temperature and pressure (e.g., Nielsen, 2000). The partition coefficient for the HFSE in the accessory magnetite of gabbro and cumulus magnetite of the magnetitite has been calculated. The $D_{Zr}^{Mt\ of\ gabbro/Fe\ tholeiite}$ = 0.2-2.81 and $D_{Zr}^{Mt\ of\ magnetitite/diorite}$ =0.24 – 0.48; $D_{Hf}^{Mt\ of\ gabbro/Fe\ tholeiite}$ = 0.71-10.93; $D_{Nb}^{Mt\ of\ gabbro/Fe\ tholeiite}$ = 0.10-23.58 and $D_{Nb}^{Mt\ of\ magnetitite/diorite}$ =0.14 – 0.37; $D_{Ta}^{Mt\ of\ gabbro/Fe\ tholeiite}$ = 0.07-10.71 and $D_{Ta}^{Mt\ of\ magnetitite/diorite}$ = 0.27 – 3.38. The partition coefficient for Ga has also been calculated in magnetite but there was no difference observed between two rock units ($D_{Ga}^{Mt\ of\ gabbro/Fe\ tholeiite}$ = 14.97-21.91; $D_{Ga}^{Mt\ of\ magnetitite/diorite}$ =12.80 – 15.67). The calculated partition coefficient values are compared with the experimental partitioning behaviors of these elements in magnetite in equilibrium with synthetic CaO–FeO–SiO_2 (CFS) melts as determined by Sievwright et al. (2020) where all experiments were conducted at 1 bar, 1150°C with fO_2 varied from FMQ-1 to FMQ+4.89 (**Table. 13**). The experimentally determined D values for these trace elements are D_{Ni} = 3.01-18.41, D_{Ga} = 0.32-2.79, D_{Cr} = 0.11-197, D_{Nb} = 0.0024-0.52, D_{Hf} = 0.007-0.50, D_{Ta} = 0.0024-0.33, D_{Zr} = 0.006-0.30. The differences in the experimental values and our observed values from the Mayurbhanj Complex may be the result of different fO_2 conditions and sub-solidus re-equilibration of the oxides up to 330°C, which would in this case not represent the primary magmatic condition (**Table. 12**). Relatively higher concentrations of Zn (~6773 - 8139 ppm), Ni (~896 - 3880 ppm), Pb (~2 - 11 ppm), and Mo (~25 - 68 ppm) in the accessory magnetite of the gabbro-norites than the cumulus magnetites of the magnetitite are due to equilibration of the accessory magnetite with the co-existing base metal sulfide minerals (**Table. 7**; **Fig. 11e, g, h**) (e.g., Dare et al., 2014), and this should depend on the trace element content of the sulfides prior to equilibration. The Cu content in the magnetites of both assemblages does not show any systematic variation because the concentration of Cu in magnetite is controlled by the co-existing ilmenite (**Fig. 10**) (e.g., Ward et al., 2018). Relatively lower Co content in the accessory magnetite (~43 - 374 ppm) of the gabbro-norites than the cumulus magnetite of the magnetitites (~1584 - 1895 ppm) may be the result of cobalt fractionation in the co-existing sulfide (**Table. 7**).

Nb, Ta, Zr, Hf, Sn, and Sc (**Fig. 10**) are preferentially partitioned into ilmenite suggesting a more compatible nature of these elements in ilmenite than the co-existing magnetite. Relatively higher Zr^{4+} (~2079 - 7029 ppm) and Hf^{4+} (98 - 155 ppm) in ilmenite compared to the co-existing magnetite (Zr^{4+} = 11 - 153 ppm; Hf^{4+} = 0.9 - 15 ppm; **Table. 7**) of the gabbro-norites (**Fig. 11d**) are attributed to the fact that these elements replace Ti^{4+} because of their chemical similarity (e.g., Bowles et al., 2011). Relatively higher concentrations of Nb^{5+} (~869 - 2153 ppm) and Ta^{5+} (~38 - 90 ppm) in ilmenite than magnetite (Nb^{5+} up to 91 ppm; Ta^{5+} up

Table. 13. Comparison of partition co-efficients of trace elements of magnetite measured by from the gabbro-norite and magnetitite ores of the Betjharan section from the Mayurbhanj Complex.

Partition co-efficient	Accessory magnetite in gabbro	Cumulus magnetite in magnetitite	Experimental value Sievwright et al. (2020)
D_{Cr}	110.95 - 335.49	4.78 - 5.27	0.11-197
D_{Ni}	8.45 - 36.61	10.93 - 14.06	3.01-18.41
D_{V}	126.41-144.81	546.86 – 730.76	--
D_{Zr}	0.20-2.81	0.24 – 0.48	0.006-0.30
D_{Hf}	0.71-10.93	--	0.007-0.50
D_{Nb}	0.10-23.58	0.14 – 0.37	0.0024-0.52
D_{Ta}	0.07-10.71	0.27 – 3.38	0.0024-0.33

to 3.6 ppm; **Table. 7**) of the gabbro-norites are the result of coupled substitution with Ti^{4+} (e.g., Bowles et al., 2011). Since the Ti^{4+} content of ilmenite in the magnetitite is much lower than that of the ilmenite of the gabbro-norites, the concentrations of Nb, Ta, Zr, and Hf are less in the ilmenite of the magnetitite bodies than in those of the gabbro-norites from the Mayurbhanj Complex.

5.4. Sulfide saturation of the parental magma and formation of sulfide minerals

The sulfide assemblages in the gabbro-norites occur as disseminated grains in the interstitial spaces of the common rock-forming silicate minerals along with magnetite. There is no trace of sulfide mineralization in the gabbro-anorthosite rocks of the Hatichhad section and in the magnetitite layers of both sections. It is likely that the parental Fe-Ti-rich basaltic magma experienced sulfide saturation at the time of gabbro-norite formation. The most probable mechanism is perhaps that crystallization of accessory magnetite within the gabbro-norite caused depletion of the parental magma in Fe. The decreasing FeO activity would then have favored sulfide saturation of the magma, resulting in the formation of an immiscible sulfide liquid and segregation of minor amounts of sulfides along with magnetite as disseminated phases in the gabbro-norites. It is likely that deuteric alteration of the entire igneous complex was responsible for the minor modification of the primary magmatic sulfide assemblage along with the formation of some late-stage sulfide minerals in the altered part of the gabbro-norites of the Mayurbhanj Complex. Since the magnetitite layer and gabbro-anorthositic rocks are the late crystallizing products of the fractionated basaltic magma (after the sulfide saturation and crystallization of sulfides as disseminated phases) so the presence of sulfide minerals are negligible in these rocks. The large compositional variations of plagioclase (presence of Na-rich plagioclase) in the gabbro-norites are probably linked to this post-magmatic hydrothermal alteration of the assemblage (**Fig. 6a & c, 7g**). In addition, Fe-Ti oxides from gabbro-norites and magnetitite ores show wide variation in trace element concentration, suggesting that these minerals are also variably altered due to late hydrothermal activities (**Fig. 10**).

In the gabbro-norites, pyrite is the most abundant sulfide mineral. In magmatic systems pyrite may form due to several processes: (i) exsolution from S-rich monosulfide solid solution (***mss***) on cooling (e.g., Naldrett et al., 1967; Dare et al., 2011; Piña et al., 2013; Duran et al., 2015); (ii) S addition to the ***mss*** components i.e., pyrrhotite and pentlandite during post-cumulus re-equilibration (e.g., Duran et al., 2015); (iii) Fe loss from the ***mss*** components during post-cumulus re-equilibration (e.g., Djon and Barnes, 2012; Duran et al., 2015) and (iv) direct precipitation from hydrothermal fluids (Naldrett et al., 1999; Dare et al., 2011; Djon and Barnes, 2012; Piña et al., 2013; Duran et al., 2015). The petrographic study of gabbro-norites shows that sulfide minerals are present as droplets within silicate minerals indicating their later origin relative to the common rock-forming silicates (**Fig. 3h, i, j, k, l**). Chalcopyrite is present in a few samples as a minor phase and is absent in most of the samples. In the Fe-Ni-S plot, some of the sulfide compositions from the Mayurbhanj Complex occupy the field of ***mss*** indicating a high-temperature magmatic origin (**Fig. 9a**). This suggests that irrespective of hydrothermal alteration of the gabbro-norites, the primary compositions of sulfide minerals are present at some places. From the Cu-Fe-S plot, it is observed that the chalcopyrite grains plot in the expected field which means that this mineral has not been altered (**Fig. 9b**). This is also true for pyrrhotite grains (**Fig. 9a, b**). However, the composition of pyrites shows a wide variation that indicates a primary magmatic origin from a segregated sulfide liquid, but also suggests that these phases might have been altered during a low-temperature alteration event. From the petrographic study, we have observed that in some places within the gabbro-norite sulfide mineral assemblages are rimmed by thin Fe-oxide minerals which formed due to secondary alteration of the primary magmatic sulfide assemblages (**Fig. 3k).** Pyrrhotite was converted to pyrite due to this process and the iron released formed the oxide minerals surrounding the sulfide mineral assemblages.

The trace element analysis of pyrite grains (**Table. 8**) shows a similar pattern with the co-existing pyrrhotite from the gabbro-norite in the multi-element variation diagram with a few exceptions where the pyrites show negative Ni anomalies (**Fig. 12a**). This implies that the pyrite grains were formed after the early crystallized pyrrhotite where Ni has been preferentially lost from the system along with Fe (e.g., Boudreau et al., 2014). Enrichment of Ag, Bi, As, Sb (**Fig. 12a, b, c, d, e**) within a few pyrite grains suggests hydrothermal alteration. Since these elements do not fit well in the pyrite structure (e.g., Duran et al., 2015) and are incompatible in ***mss*** (e.g., Barnes and Lightfoot, 2005; Brenan, 2008; Duran et al., 2015; Liu and Brenan, 2015) it is more likely that elevated Ag, Bi, As, Sb were not inherited from the primary sulfides (like ***mss***), and were incorporated into the pyrite structure by some later fluid activity (e.g., Duran et al., 2015). High Pb content in a few pyrite grains (**Fig. 12c, d, e**) is attributed to the presence of small-scale inclusions of Pb-bearing minerals e.g., galena (Huston et al., 1995; Abraitis et al., 2004). The trace element analysis of some pyrite grains show a relatively high concentration of Co along with As and Sb which suggests the involvement of Co-rich hydrothermal fluids (e.g., Dare et al., 2011). The major element and trace element data indicate that major pyrites of the gabbro-norites from the Mayurbhanj Complex are primarily magmatic in origin, though some are of secondary origin and genetically linked with later hydrothermal activity.

5.5. Magma genesis in an active continental margin setting in the Mesoarchean

Layered mafic intrusions are formed by fractional crystallization, gravitative settling and solidification of the accumulated crystals at the magma chamber floor (e.g., Wager and Brown, 1968; Cawthorn, 1996; Zhou et al., 2005; Tegner et al., 2006; Charlier et al., 2006; 2009; 2015; Namur et al., 2010; 2012). In a few scenarios it is a closed system crystallization process of a single influx of a magma with little or no recharge (e.g., Skaergaard intrusion; Hunter and Sparks, 1987; McBirney, 1979; 1996) and in some other cases there is an open system crystallization process with repetitive intrusions of similar magmas (e.g., Muskox and Rum layered intrusion; Brown, 1956; Irvine and Smith, 1967; Irvine, 1977; Bedard et al., 1988). The occurrences of more fractionated rocks at the upper part of the Mayurbhanj Complex exhibit the obvious magma evolutionary trend that suggests differentiation of the parental magma by fractional crystallization process. The gabbroic rocks of the Mayurbhanj Complex have low LOI (0.12 – 1.78 wt. %; **Table. 9**) indicating minor post-magmatic alteration of the rocks due to secondary hydrothermal process. The major and trace element geochemical trends clearly indicate that the Betjharan gabbro-norites are geochemically more primitive than the Hatichhad gabbro-anorthosites (**Figs. 13-15**). Relatively higher SiO_2 content of the gabbro-anorthosites than the gabbro-norites is due to the higher modes of plagioclase in the former (**Fig. 13a**). The positive trend of CaO vs. MgO (**Fig. 13b**) and negative trend of Al_2O_3 vs. MgO (**Fig. 13c**) and (Na_2O+K_2O) vs. MgO (**Fig. 13d**) suggest both pyroxene (Opx and Cpx) and plagioclase were controlling the magma fractionation during the formation of the gabbro-noritic rocks of the Betjharan section, whereas, plagioclase was the early crystallizing phase in the gabbro-anorthositic rocks of the Hatichhad section. The higher $Fe_2O_{3\ (total)}$ content of the gabbro-norites is due to higher modes of magnetite-titanomagnetite than the gabbro-anorthosites (**Fig. 13f**). The positive correlation between Cr, Ni and MgO is due to crystallization of clinopyroxene from a fractionating basaltic magma (**Fig. 15a, b**). The higher MnO content in the gabbro-norites is due to higher modal abundance of ilmenite relative to the gabbro-anorthosite (**Fig. 13g**). The V and Cu content are also higher in the gabbro-norites relative to the gabbro-anorthosites (**Fig. 15c, d**) which are due to higher modes of magnetite and chalcopyrite within the Betjharan gabbro-norites. The incompatible trace elements e.g., Nb, La vs MgO plots (**Fig. 15e, f**) also show evolved nature of the gabbro-anorthositic rocks of the Hatichhad section than the gabbro-norites of the Betjharan section. The Hatichhad gabbro-anorthosites show strong positive Eu anomaly in the chondrite normalized REE plots, which is due to early fractionation of plagioclase from the magma that were accumulated to form these rocks (**Fig. 16a, b**). In the chondrite normalized REE plot (**Fig. 16a**) gabbroic suite of rocks from both the sections shows REE enrichment (LREE = 10-70 × chondrite, HREE = 10-30 × chondrite) with LREE fractionated trends. However, the Hatichhad gabbro-anorthositic samples have relatively lower enrichment of HREE than the Betjharan gabbro-norites due to lower modes of clinopyroxene grains in the former. The Betjharan gabbro-norites show negative relations in Ni, Co vs bulk rock S plots (**Fig. 17**) suggesting their variations are not controlled by sulfide minerals only. Ni and Co are also incorporated in magnetite and pyroxene minerals; therefore, the negative correlation is due to fractional crystallization of these minerals from the magma. The sample which has high mode of pyroxene and magnetite has high Ni content and the lowest Ni concentration can be found in the plagioclase dominated gabbro of the Betjharan section (**Fig. 17a**). The Cu and Fe (as total iron) vs S plots show positive trends suggesting the concentration of Cu (and a part of Fe) is controlled by the modal abundance of chalcopyrite and pyrite (**Fig. 17c, d**). Other than a few samples, the bulk rock Pb concentration shows overall positive correlation with S contents of the rocks (**Fig. 17e**). The LA-ICPMS data of pyrite shows higher Pb concentration (Pb = 7.16 – 2525.83 ppm; **Table. 7**) and the positive correlation between bulk rock Pb and S might be related to the modal abundance of the pyrite grains in the gabbro-noritic rocks (**Fig. 12a, c, d, e)**. In contrast, the Ag content have a negative relation with the bulk rock S concentration suggesting a different source of Ag than the primary sulfides (**Fig. 17f**).

Assimilation with the crustal rocks and fractional crystallization is an effective mechanism for magma differentiation (e.g., DePaolo, 1981; Zhao and Zhou, 2007; Dong et al., 2011; Banerjee and Mondal, 2021). In the AFM plot the Mayurbhanj gabbro-anorthositic suite of rocks show a Fe-rich tholeiitic trend (**Fig. 14b**). The Sm-Nd isochron of this study yields an age of 3022 ± 180 Ma for these rocks (**Fig. 18a**) suggesting contemporaneous magmatic activities with other ultramafic-mafic (e.g., Nuasahi and Sukinda Complexes) and granitic intrusions (e.g., Mayurbhanj-Nilgiri-Bonai grantite intrusions) in the craton (e.g., Mondal, 2009 and references therein). Therefore, it might be possible that the parental magma of the Mayurbhanj gabbroic complex interacted with the still older crustal components of the craton e.g., rocks of the OMTG, OMG, IOG and the Singhbhum Granite I and II. The plots of most incompatible elements vs. immobile elements are prepared to trace the probable crustal contaminants if there was any (**Fig. 19**). The Archean continental crustal materials are rich in LILE (Sr, K, Rb, Ba, Th, U) and K_2O, and depleted in TiO_2 and P_2O_5 (Zhou et al., 2004; Zhao and Zhou, 2007; Bi et al., 2015). Therefore, assimilation with the continental crustal materials would have increased K_2O and LILE, and decreased TiO_2 and P_2O_5 in the mantle-derived ultramafic-mafic magmas (e.g., Zhao and Zhou, 2007 and references therein). The gabbroic rocks of the Mayurbhanj Complex show enrichment of LILE ($Sr_{(N)}$ = 16.36 – 72.54; $K_{(N)}$ = 2.90- 13.71; $Rb_{(N)}$ = 2.61 – 10.22; $Ba_{(N)}$ = 13.69 – 89.50; $Th_{(N)}$ = 10.34 – 124.14; $U_{(N)}$ = 13.51 – 121.62), a little negative Nb, Ta and Ti anomaly with weak

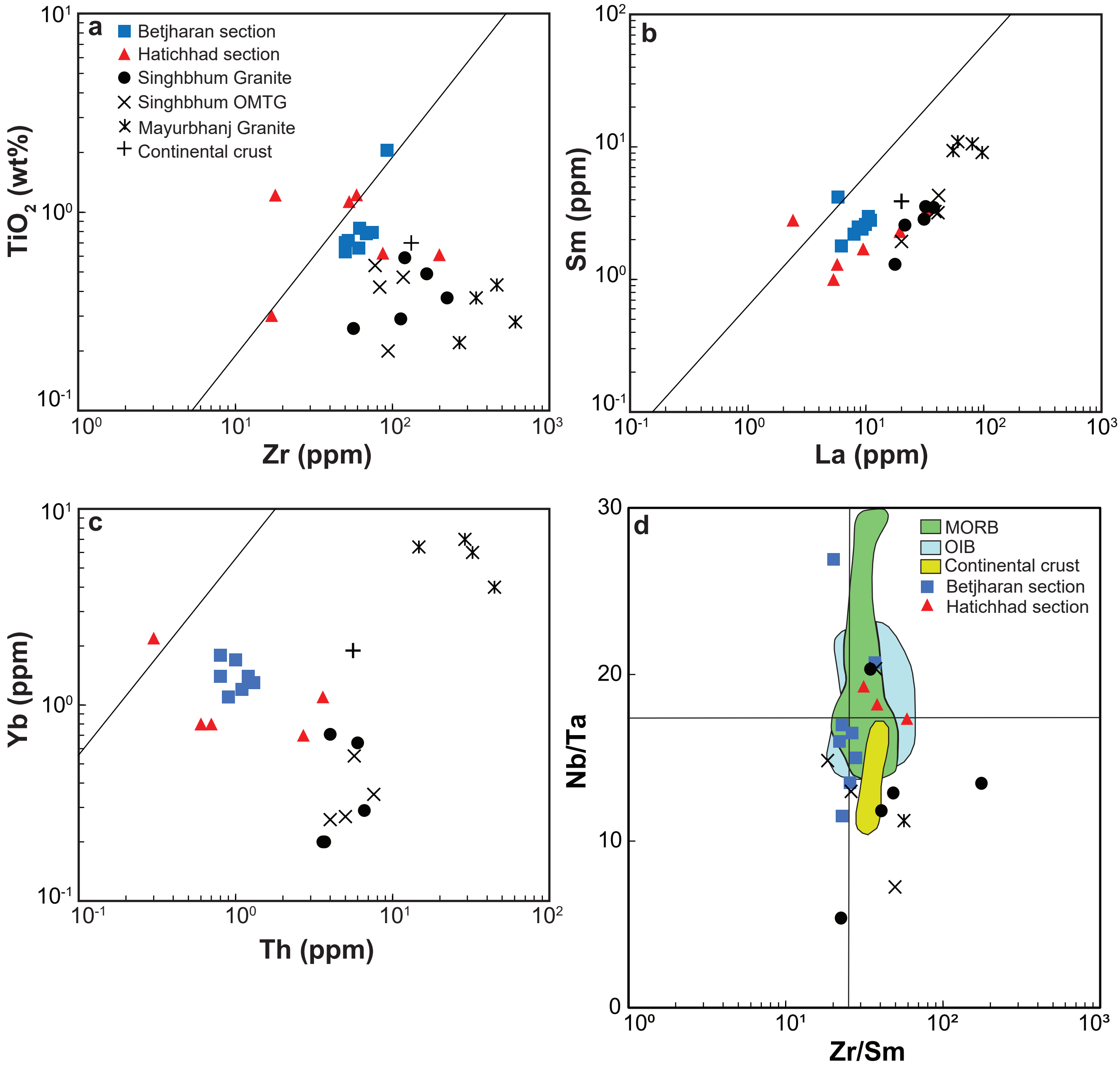

Fig. 19. Plots of **(a)** Zr vs. TiO_2; **(b)** La vs Sm; **(c)** Th vs Yb for the gabbro-anorthositic rocks of the Mayurbhanj Complex and Early to Mesoarchean TTG rocks of the Singhbhum craton to show whether crustal contamination has affected the gabbroic rocks. The line illustrates the primitive mantle ratio (after McDonough and Sun, 1995). The composition of average continental crust is after Rudnick and Gao (2003); **(d)** Zr/Sm vs. Nb/Ta contents of the gabbroic rocks from the Mayurbhanj Complex (after Foley et al., 2002). The lines indicate primitive mantle ratio.

positive Zr and Hf anomaly indicating a small degree of crustal contamination (**Fig. 16b**). In the plots of various incompatible elements e.g., Zr vs. TiO_2 (**Fig. 19a**), La vs. Sm (**Fig. 19b**), Th vs. Yb (**Fig. 19c**) the gabbroic rocks from both sections show a little deflection towards the field occupied by the OMTG and SG I, II indicating incorporation of minor crustal materials. The gabbroic suite of rocks has an average Nb/Ta ratio ~20 (gabbro-norites: Nb/Ta = 11.5 - 30 and gabbro-anorthosite: Nb/Ta = 17.4 - 21) and Zr/Sm ratio ~27 (gabbro-norite: Zr/Sm = 20 - 36.8 and gabbro-anorthosite: Zr/Sm = 13.9 to 58.5) which are close to the primitive mantle ratios (Nb/Ta_{PM} = 17.4; Zr/Sm_{PM} = 25.86) (**Table. 9**) indicates minimal incorporation of crustal component (**Fig. 19d**).

In various tectonic discrimination plots such as Nb/Th vs La/Nb (**Fig. 20a**), Ba/Nb vs La/Nb (**Fig. 20b**), Zr/Nb vs Nb/Th (**Fig. 20c**) the Mayurbhanj gabbroic suite of rocks show an affinity towards arc related magmatic activities. The gabbroic rocks of the plutonic complex have Zr/Nb = 4.57 – 22.6, Nb/La = 0.21 – 0.55, La/Nb = 0.82 - 4.82, Ba/Nb = 15.52 - 132, Zr/Nb = 4.57 – 22.6 and Nb/Th = 1.83 – 4 (**Table. 9**). These values are distinct from the magmas that generated in the intraplate tectonic settings but similar to the arc related magmas (e.g., Foley and Wheller, 1990; Pearce and Peate, 1995; Condie, 2005; Bi et al., 2015). In the Ta/Yb vs Th/Yb tectonic discrimination plot (**Fig. 20d**; after Pearce, 1983) the compositions of the gabbroic rocks occupy the field of active continental margin setting suggesting an ocean-continent convergence in the Mesoarchean era. The normalizing factor Yb was used by Pearce (1983) because it is effective in largely eliminating variation due to partial melting and fractional crystallization by not participating in various enrichment processes. The intra-plate enrichment events enrich Ta and Th equally in the magmas whereas, the subduction component affects Th but not Ta (Pearce, 1983). The change in Ta

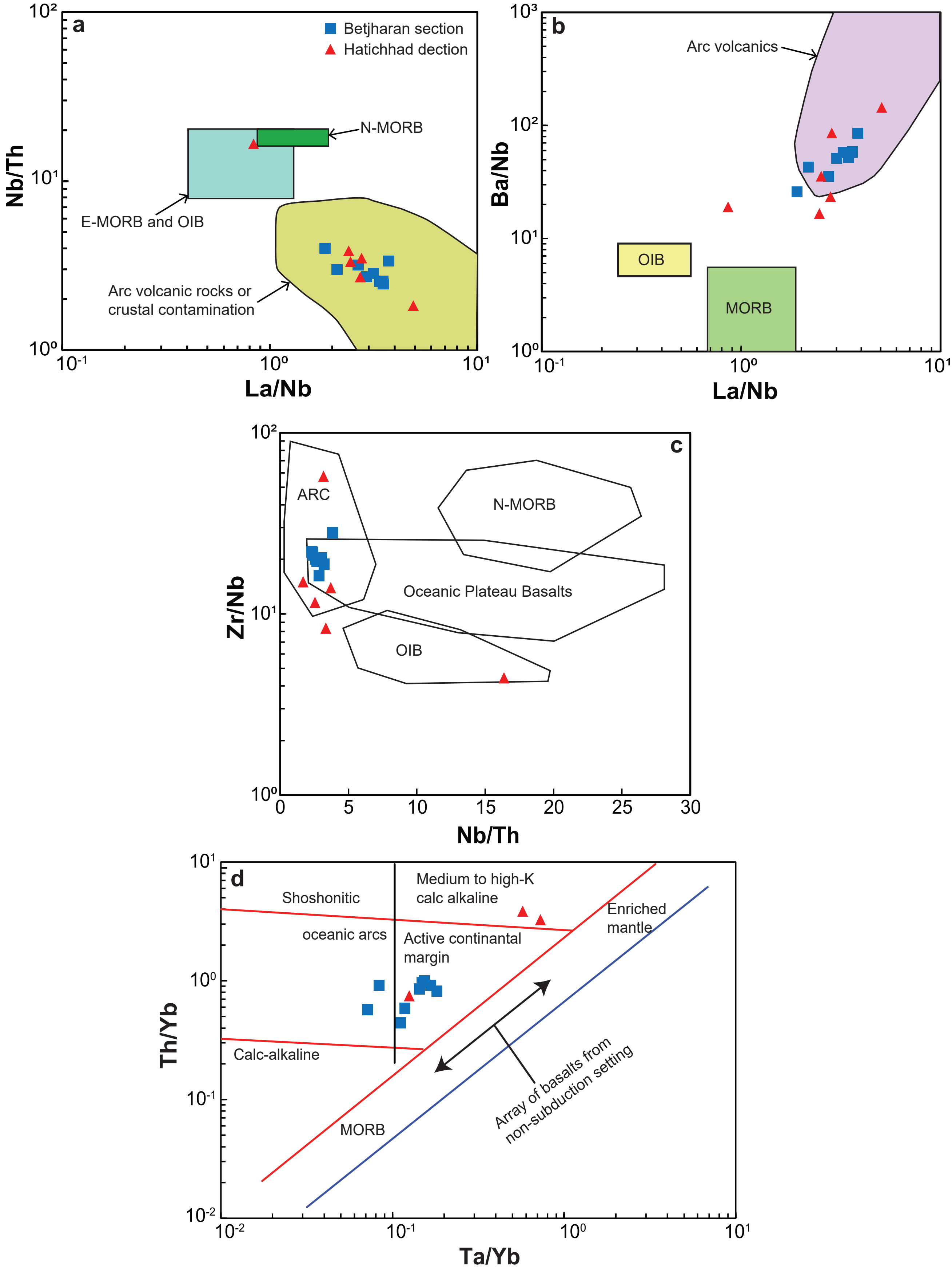

Fig. 20. La/Nb vs. **(a)** Nb/Th; **(b)** Ba/Nb (after Bi et al., 2015); **(c)** Nb/Th vs. Zr/Nb (after Condie, 2005) diagrams for the gabbro-anorthositic rocks of the Mayurbhanj Complex; **(d)** Plot of Ta/Nb vs. Th/Yb (after Pearce, 1983) for the gabbro-anorthositic rocks of the Mayurbhanj Complex.

and Th content in few gabbroic samples is due to hydrothermal alteration of the rocks (**Fig. 20d**).

Ultramafic-mafic magmatism in a tectonic setting in the Mesoarchean era similar to the modern active continental margin setting bears significant implications in terms of mechanisms of crustal evolution and stabilization of the craton (e.g., Mondal et al., 2006; Mukherjee et al., 2012). In a continental arc setting basaltic magmas are generated from different mantle sources e.g., melting of (i) partial melting of continental lithospheric mantle wedge above the subducting oceanic plate, (ii) subducted oceanic lithospheric plate including the oceanic crust and sediments, or (iii) mixing of any of the above sources (e.g., Winter, 2013; Bi et al., 2015). The bulk-rock geochemistry and mineral assemblage of the Mayurbhanj gabbroic rocks suggest a Fe-Ti-rich basaltic magma to be parental to the plutonic complex. The trace element geochemistry suggests the gabbroic rocks of the Betjharan and Hatichhad section have lower Nb/Th (1.83 – 3.86), Nb/La (0.21 – 0.55), Zr/Nb (4.57 – 28.75), Zr/Hf (28.33 – 37.86) and higher Th/U (3 – 4.5) and La/Nb (1.81 – 4.82) ratios than the primitive mantle ratios, and are similar to the ratios of the basaltic magmas derived from the lithospheric mantle wedge (e.g., Yan et al., 2008; Bi et al., 2015). In addition, incorporation of minor continental crustal material in the parental basaltic magma during emplacement indicates that the source of the magma was the continental lithospheric mantle wedge above the subducting oceanic plate which suffered a lower degree of partial melting (**Fig. 21**) (e.g., Zhao and Zhou, 2007; Winter 2013; Bi et al., 2015). However, in this setting the melting should occur under the H_2O saturated condition i.e., accompanied by dehydration of the hydrous phases (e.g., pargasite or phlogopite) in a metasomatized continental lithospheric mantle wedge (Zhao and Zhou, 2007; Winter, 2013; Bi et al., 2015 and reference therein). The continental lithospheric mantle wedge of the convergence

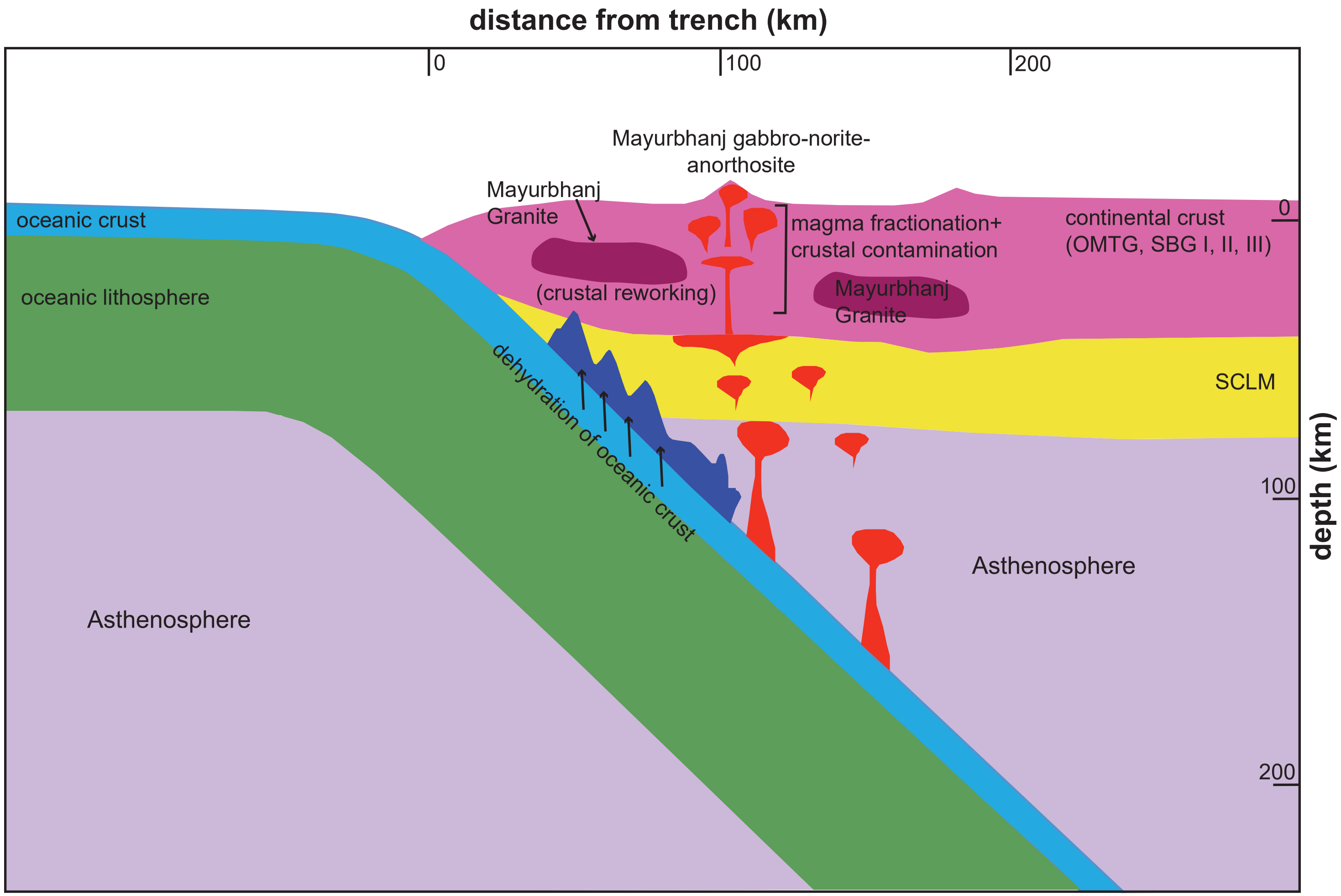

Fig. 21. Model showing the probable geodynamic setting of the Mayurbhanj Complex. The model illustrates the gabbro-anorthositic rocks of the Mayurbhanj Complex is generated by partial melting of metasomatized continental lithospheric mantle wedge and the contemporaneous Mayurbhanj Granite is generated by crustal reworking of the older TTG rocks.

setting can be modified by (i) fluxing of fluids during dehydration of the subducting oceanic crust (e.g., Winter, 2013) or, (ii) addition of melts generated from the subducted slab (e.g., Bi et al., 2015). Slab dehydration occurs at shallower depths than the slab melting (e.g., Rollinson and Tarney, 2005), and in comparison with LILE, both HFSE and HREE remain immobile during the slab fluxing processes, therefore, high Ba/Th (59.1 – 293.9) and U/Th (0.11 – 0.43) ratios in the Mayurbhanj gabbroic rocks suggest that the parental basaltic magma derived from a mantle source that was metasomatized by slab-derived fluids rather than a slab-derived melts (e.g., Bi et al., 2015).

5.6. Petrogenetic evolution: Mesoarchean Large Igneous Province in the Singhbhum Craton and major magmatic activities in a subduction setting

The Sm-Nd isotope analysis of the gabbroic suite of rocks from the Mayurbhanj Complex yields an isochron age of 3022 ± 180 Ma for the samples of the Hatichhad section (**Fig. 18a**). If the samples of the Betjharan gabbro-norites are included with the gabbroic rocks of the Hatichhad section they yield an errochron age of 3169 Ma with a large error (± 340). The large error and degradation in correlation suggests that the Sm-Nd systematics of the Betjharan gabbro-norites have been perturbed due to hydrothermal alteration. For the gabbroic rocks of the Hatichhad section the Nd model ages were calculated after DePaolo (1988) and the calculated values of 3.48 - 3.38 Ga are interpreted as average crustal residence times of the parental magmas (**Table. 10**). The ε_{Nd} values of the gabbro-anorthositic rocks from the Hatichhad section are plotted against the isochron age along with other data of globally occurring Archean ultramafic-mafic plutonic and volcanic rocks from different cratons (**Fig. 18b**). Similar data of the other major ultramafic-mafic litho-units of the Singhbhum Craton such as the OMG amphibolite, IOG-komatiites, Dhanjori-Jagannathpur-Malangtoli mafic volcanics are also included in the diagram. A large range of the ε_{Nd} value (-4.4±3.3) of the Mayurbhanj gabbroic rocks suggest few possibilities (e.g., Faure and Mensing, 2005): (i) contamination of the parental basaltic magma with the continental crust, (ii) late hydrothermal disturbances of the Sm-Nd isotopic systematics, or (iii) combination of both.

Since the Hatichhad gabbro-anorthosites bear the signature of a very negligible crustal contamination and also suffered a minor post-magmatic hydrothermal alteration, therefore, the overprinting of secondary alteration upon the crustal contamination was perhaps responsible for the large negative ε_{Nd} value of the rocks. The Mayurbhanj gabbroic rocks are surrounded by the tonalite-trondhjemite-granodioritic (TTG) rocks of the Singhbhum Granite Batholithic Complex and the OMTG rocks that were emplaced at early to Mesoarchean era (~3.4-3.3Ga; Upadhyay et al., 2014). In addition, nearest country rocks are the Iron Ore Group metavolcano-sedimentary supracrustal which are also early Archean in age (Adhikari et al., 2021). The Mayurbhanj granitic intrusion along with the Niligiri-Bonai granitic intrusions represent the younger pulse of the felsic plutons in the craton that has a crystallization age of ~3.1 Ga (Sengupta et al., 1991; Mishra et al., 1999). The bulk rock trace element data suggest origin of the parental basaltic magma of the Mayurbhanj gabbroic rocks in an active continental margin setting (**Fig. 20d**). The resulted 3022 ± 180 Ma Sm-Nd isochron age of the Mayurbhanj gabbroic rocks suggest a possible geodynamic model that invokes partial melting of a continental lithospheric mantle wedge in a subduction zone setting in the Mesoarchean era (**Fig. 21**). In this setting the basaltic magma emplaced at the shallow magma chamber within the continental crust and fractionated to form the gabbro-anorthositic suite of rocks and the magnetitite bodies (Mayurbhanj Complex). The contemporaneous granitic plutons (3.1 Ga Mayurbhanj-Niligiri-Bonai granitic intrusions) formed by widespread reworking of the older TTG dominated continental crust at relatively shallower depth (**Fig. 21**). The older TTG dominated continental crust was formed from the partial melting of the ultramafic-mafic rich primordial crust (Moyen and Martin, 2012). The older continental crustal component was made up of the rocks of the OMG, OMTG, Singhbhum Granite Phase I and Phase II. These early Archean to Mesoarchean crustal components were relatively mafic rich and incompatible element depleted, and perhaps, that is the reason that the rocks of the Mayurbhanj gabbroic complex show minimal crustal contamination.

Figure 18b shows that the ε_{Nd} value of the Mayurbhanj Complex is similar to the range shown by the ultramafic-mafic rocks of the Pilbara Craton (Western Australia), São Tomé layered mafic-ultramafic intrusion (NE Brazil), Stillwater Complex (Montana, USA), Ushushwana Complex (Kaapvaal Craton, Southern Africa), Isua supracrustal belt (West Greenland) and the Nuasahi ultramafic-mafic complex (Singhbhum Craton, India). The wide range of ε_{Nd} values shown by the ultramafic-mafic rocks of the Archean age from different cratons indicate disturbances in the Sm-Nd system because the Archean ultramafic-mafic complexes have a very complex deformation history, suffered metamorphism and late-stage hydrothermal alteration that might have affected the isotope system. **Figure 18b** also shows an increased abundances in the occurrence of the ultramafic-mafic complexes from Early Archean to Late Archean (i.e., 3800 Ma - 2600 Ma) indicating major ultramafic-mafic magmatism was concentrated during this period, and the magmatic event spanned ~1200 Ma. This specific and concentrated occurrence of ultramafic-mafic complexes may be associated with a supercontinent cycle (e.g., Mukherjee et al., 2012). The term supercontinent cycle refers to repetitive assembly and break-up of the Earth's large continental blocks periodically, which plays a major role in constraining the evolution of planet's surface (Rodger and Santosh, 2003; Nance et al., 2014; Mitchell et al., 2021). In the

Archean there were hypothesized supercratons like Vaalbaara (3.5 Ga event; break up ~2.7 Ga), Superia (2.7 Ga event; break up ~2.45 Ga) and Sclavia (2.6 Ga event; break up ~2.2 Ga) from which the Kaapvaal, Superior and Slave Cratons were originated with distinct amalgamation and break-up histories (Bleeker, 2003). The rifting and breakup of cratons are a major reason for the formation of the Large Igneous Provinces (LIP) (e.g., Ernst, 2014). The LIPs represent emplacement of high pulses of ultramafic-mafic magmas in a short duration that have punctuated the Earth's history as often as 10-30 million years (Ernst et al., 2008). The main LIPs in the Archean era are represented by continental flood basalts and komatiitic suite of magmas in greenstone belts (Ernst et al., 2005). In addition, with the komatiitic-tholeiitic association within the greenstone belt, Ivanic et al (2010) considered that the ultramafic-mafic plutonic rocks associated with the greenstone belts are part of the LIP (e.g., Ernst, 2014).

Broadly, the Indian Shield comprises twelve LIP events during Precambrian (e.g., Ernst and Srivastava, 2008; Srivastava et al., 2020). According to Srivastava et al. (2020) and Samal et al. (2021), in the Archean, two major LIP events were observed - (i) the Sargur LIP (3.35 - 3.34 Ga), which includes 3.35 Ga komatiite associated with the Sargur Group greenstone belt of the western Dharwar Craton (Jayananda et al., 2008), 3.34 Ga Badampahar komatiite associated with the Gorumahisani-Badampahar greenstone belt of the Singhbhum Craton (Chaudhuri et al., 2017; Bachhar et al., 2021), 3.4 Ga Babina ultramafic-mafic rocks of the Bundelkhand Craton (Singh et al., 2019), and (ii) the Ghatgaon LIP (2.80 – 2.75 Ga), which includes 2.80 Ga Keshargaria and 2.76 – 2.75 Ga Ghatgaon dyke swarm of the Singhbhum Craton (Kumar et al., 2017). The gabbroic rocks of the Mayurbhanj Complex (Sm-Nd age of 3022 ± 180 Ma from this study), the ultramafic-mafic volcanic rocks of the Dhanjori Complex (~2.8 Ga; Misra and Johnson, 2005), Jagannathpur-Malangtoli ultramafic-mafic volcanics (~2.8 Ga; Adhikari et al., 2021), Keshargaria mafic dyke swarm (~2.8 Ga; Kumar et al., 2017), Nuasahi-Sukinda ultramafic-mafic Complex (~3.1 Ga; Augé et al., 2003) of the Singhbhum Craton and the ultramafic-mafic rocks of the Sargur-Nuggihalli-Holenarsipur greenstone belt of the western Dharwar Craton (~3.1 Ga; Mukherjee et al., 2012) may represent a major component of the Ghatgaon LIP of 2.80 – 2.75 Ga (within the error limits of ages of all the ultramafic-mafic complexes). This particular LIP event is also a part of the large scale global ultramafic-mafic event in the above-mentioned time period (e.g., Ernst, 2014).

The ultramafic-mafic complexes are not only important for the crust-mantle evolution of the Earth but also for their resource endowment (e.g., Barley and Groves, 1992; Arndt et al., 2005; Begg et al., 2010). The ultramafic-mafic plutonic components of the LIPs are prime hosts of chromite, magnetite-titanomagnetite-ilmenite and Ni-Cu-(PGE) sulfide deposits (e.g., Ripley and Li, 2018). The Archean ultramafic-mafic layered complexes of the Singhbhum and the Dharwar Cratons of the Indian Shield are important source of Cr, Fe-Ti-V and Ni-Cu-PGE (Mondal and Baidya, 1997; Mondal et al., 2001; Mondal and Zhou, 2010; Mukherjee et al., 2012, 2015; Khatun et al., 2014; Prichard et al., 2018; Bhattacharjee and Mondal, 2021 and references therein). In the Singhbhum Craton the rocks of the Mayurbhanj - Nuasahi - Sukinda Complexes are major hosts of chromite and magnetite deposits (Mondal et al., 2006; Bhattacharjee and Mondal, 2021). In the western Dharwar Craton the gabbro-anorthosite units of the Nuggihalli greenstone belt associated with the 3.35-3.34 Ga Sargur LIP host Ti-V rich magnetite deposits (Mukherjee et al., 2012). The magnetite deposits related to ultramafic-mafic igneous complexes are reported worldwide, i.e., Bushveld Complex of South Africa (Von Gruenewaldt, 1973), Skaergaard intrusion of Greenland (Jang et al., 2001), Emeishan Large Igneous Province of China (Pang et al., 2010), Panzhihua layered gabbroic intrusion of SW China (Zhou et al., 2005; Pang et al., 2008; 2009), Kachkanar intrusion of Russia (Augé et al., 2005), Sept Iles intrusion of Quebec (Namur et al., 2010; 2012), Duluth Complex of Minnesota (Ripley et al., 1998; Miller et al., 2002). Along with the Ti-V rich oxide deposits the ultramafic-mafic plutonic complexes also host world's major Ni-Cu-PGE deposits (Begg et al., 2010; Naldrett, 2011; Ernst and Jowitt, 2013; Ripley and Li, 2018). The Ni-Cu-PGE sulfide deposits are mainly concentrated in the Late Archean period and are related to craton rifting processes (Begg et al., 2010; Maier and Groves, 2011). The magma plumes impacting on the base of sub-continental lithospheric mantle (SCLM) was responsible for forming large volume of ultramafic-mafic magmas that host the Ni-sulfide deposits (Begg et al., 2010) or, in case of smaller deposits ultramafic-mafic magmatism is an outcome of melting of metasomatized mantle lithosphere by asthenospheric upwelling induced by lithospheric delamination (Begg et al., 2010). The PGE deposits occur in association with magmatic Ni-Cu sulfide, chromitite and magnetitite mineralization (e.g., Prichard et al., 2018). In terms of tectonic settings, the Ni-Cu-PGE deposits have been classified into three major groups: (a) komatiite associated Ni-Cu deposit (e.g., Abitibi greenstone belt of Superior Province, Canada), (b) world-class PGE deposits in giant layered intrusion (e.g., Bushveld and Stillwater Complexes), and (c) Ni-Cu-PGE deposits form in magma conduits in smaller ultramafic-mafic intrusions (e.g., Ripley and Li, 2008). The breccia hosted Ni-Cu-sulfides with PGE, and PGE-rich magnetities have been reported from the 3.1 Ga Nuasahi Complex, (Mondal and Baidya, 1997; Mondal et al., 2001; Mondal and Zhou; Prichard et al., 2018) and the Co-pyrites have been reported from the 1.77 Ga Satkoshia dolerite dyke in the Singhbhum Craton (Dey and Mondal, 2021). In the Archean era the Ni-Cu-PGE deposits are also present in the West Pilbara Craton of western Australia (Munni Munni layered ultramafic-mafic intrusion, ~2.9 Ga, Hoatson and Sun, 2002), Superior Province, Manitoba (several anorthosite intrusions and associated ultramafic-mafic rocks, Peck et al., 1999), Superior Province, Canada (Percival, 2007); Great Dyke of Zimbabwe Craton (~2.6 Ga, Stribrny et al., 2000). The global predominance of chromite, Ti-V bearing magnetite and Ni-Cu-PGE sulfide deposits within the layered mafic complexes of the Archean era signifies a large scale ultramafic-mafic magmatism which is connected to the supercontinent cycle. Mukherjee et al. (2012) hypothesized two supercontinents at 3.7 Ga and 2.7 Ga with an overlap between the breakup of older supercontinent and formation of the younger one like the Rodinia supercontinent (Ernst et al., 2008). The active continental margin setting for the ~3.1 Ga Mayurbhanj Complex hosting Ti-V bearing magnetitite deposits suggest that the plutonic complex was related to the amalgamation phase of a supercontinent named ‘Ur’ (Rogers and Santosh, 2003). ‘Ur’ is the earth’s oldest continental assembly (~3000 Ma) which is based on the cratons that became stable at ~3000 Ma (Western Dharwar and Singhbhum cratons of India, Kaapvaal craton of southern Africa and Pilbara craton of western Australia) (Rogers and Santosh, 2003) and was culminated at ~2.5 Ga.

CHAPTER 6

CONCLUSION

6. Conclusions

1) The gabbro-norite-anorthositic rocks and the magnetitite ore bodies of the Masoarchean Mayurbhanj Complex formed from iron (Fe) - titanium (Ti) - rich basaltic magma by fractional crystallization process within a crustal magma chamber in an active continental margin setting. The magnetitite layers were formed due to increase of Fe and Ti during fractionation of the basaltic magma followed by separation of a Fe-rich oxide melt from the silicate melt and subsequent crystallization of magnetite and accumulation of these grains. The host gabbro-anorthositic rocks of the magnetitite layers were formed from the co-existing Si-rich melt. The two-pyroxene thermometry yields a primary magmatic crystallization temperature ranging from 1199° and 956°C for the gabbro-norites and 1096° - 839°C for the gabbro-anorthosites. The large variation in temperature and fO_2 calculated from the oxide assemblage of the mafic plutonic complex indicates various stages of cooling history with sub-solidus re-equilibration.
2) The high concentration of Ni, Pb, Mo, Zn in the accessory magnetite of the gabbro-norite is due to the equilibration of the accessory magnetite with the co-existing base metal sulfide minerals and it was dependent on the trace element content of the sulfide minerals prior to equilibration. Crystallization of accessory magnetite decreased the FeO activity of the fractionated basaltic magma resulting the sulfide saturation and subsequent minor amounts of sulfide segregation expressed as a disseminated assemblage in the gabbro-noritic rocks of the plutonic complex. The *in-situ* major and trace element data of sulfide minerals from the gabbro-norites suggest some sulfides are primary magmatic in origin and some are secondary which are genetically linked with later hydrothermal activity.

3) Early crystallization of plagioclase in the gabbro-anorthosite and simultaneous crystallization of pyroxene and plagioclase in the gabbro-norites are responsible for different patterns of the chondrite normalized REE and multi-elements spidergrams. The gabbro-anorthositic rocks indicate a small degree of crustal contamination by means of incorporation of OMTG, SBG I and II in the parental basaltic magma. The parental basaltic magma of the mafic complex was generated due to partial melting of a metasomatized continental lithospheric mantle wedge in an ocean-continent convergence setting.
4) The gabbro-anorthositic rocks of the Mayurbhanj Complex yield a bulk-rock Sm-Nd isochron age of 3022± 180 Ma. The negative ε_{Nd} value is due to combined effect of minor crustal contamination of the parental basaltic magma and post-magmatic hydrothermal alteration of the igneous complex. The ~3.1 Ga gabbro-anorthositic suite of rocks were formed from the basaltic magma within the older continental crust, and the contemporaneous granite plutons of the craton were formed due to widespread reworking of the older TTG dominated continental crust.
5) The Mayurbhanj Mafic Complex along with the time-equivalent Mesoarchean to Late Archean other ultramafic-mafic intrusive and extrusive rocks of the Singhbhum Craton as well as from the Dharwar Craton represent a major component of the Ghatgaon Large Igneous Province which was a part of the large scale ultramafic-mafic event related to the amalgamation stage of a supercontinent cycle of the 'Ur'.

References

Abraitis, P., Pattrick, R., Vaughan, D., 2004. Variations in the compositional, textural and electrical properties of natural pyrite: a review. International Journal of Mineral Processing, 74(1-4), 41-59.

Acharyya, S.K., Gupta, A., Orihashi, Y., 2010. New U-Pb zircon ages from Paleo-Mesoarchean TTG gneisses of the Singhbhum Craton, eastern India. Geochemical Journal, 44(2), 81-88.

Adhikari, A., Mukherjee, S., Vadlamani, R., 2021. A plume-mantle interaction model for the petrogenesis of komatiite-komatiitic basalt-basalt-basaltic andesite volcanism from the Paleoarchean (3.57–3.31 Ga) Iron Ore Group greenstone belts, Singhbhum craton, India: Constraints from trace element geochemistry and SmNd geochronology. Lithos, 398, 106315.

Arif, M., Dey, S., Gond, A.K., Zong, K., Liu, Y., Mitra, A., Mitra, A., Sarangi, S., 2021. Mesoarchean continental intraplate volcanism and sedimentation: The case of the Simlipal basin, Singhbhum Craton, eastern India. Precambrian Research, 361, 106245.

Arndt, N., Lesher, C., Czamanske, G., 2005. Mantle-derived magmas and magmatic Ni-Cu-(PGE) deposits.

Ashwal, L.D., 1993. Proterozoic Massif-Type Anorthosites, Anorthosites. Springer, pp. 82-218.

Ashwal, L.D., Bybee, G.M., 2017. Crustal evolution and the temporality of anorthosites. Earth-Science Reviews, 173, 307-330.

Augé, T., Bailly, L., Roig, J.-Y., 2017. A double Fe-Ti oxide and Fe-sulphide liquid immiscibility in the Itsindro Gabbro Complex, Madagascar. Journal of African Earth Sciences, 135, 152-172.

Augé, T., Cocherie, A., Genna, A., Armstrong, R., Guerrot, C., Mukherjee, M.M., Patra, R.N., 2003. Age of the Baula PGE mineralization (Orissa, India) and its implications concerning the Singhbhum Archaean nucleus. Precambrian Research, 121(1-2), 85-101.

Bachhar, P., Saha, D., Santosh, M., Liu, H.-D., Kwon, S., Banerjee, A., Patranabis-Deb, S., Deb, G.K., 2021. Mantle heterogeneity and crust-mantle interaction in the Singhbhum craton, India: New evidence from 3340 Ma komatiites. Lithos, 382, 105931.

Bai, Z.-J., Zhong, H., Hu, R.-Z., Zhu, W.-G., Hu, W.-J., 2019. Composition of the chilled marginal rocks of the Panzhihua layered intrusion, Emeishan Large Igneous Province, SW China:

Implications for parental magma compositions, sulfide saturation history and Fe–Ti oxide mineralization. Journal of Petrology, 60(3), 619-648.

Bai, Z.-J., Zhong, H., Li, C., Zhu, W.-G., Xu, G.-W., 2012. Platinum-group elements in the oxide layers of the Hongge mafic–ultramafic intrusion, Emeishan Large Igneous Province, SW China. Ore Geology Reviews, 46, 149-161.

Banerjee, R., Mondal, S.K., 2021. Petrology and geochemistry of the Deccan basalts from the KBH-7 borehole, Koyna Seismic Zone (Western Ghats, India): Implications for nature of crustal contamination and sulfide saturation of magma. Lithos, 380, 105864.

Banerji, P., 1984. On some geochemical features of the vanadiferous magnetite deposits of Kumhardubi and Betjharan, Mayurbhanj district, Orissa, India. Chemical geology, 43(3-4), 257-269.

Barley, M., Groves, D., 1992. Supercontinent cycles and the distribution of metal deposits through time. Geology, 20(4), 291-294.

Barnes, S.-J., Lightfoot, P.C., 2005. Formation of magmatic nickel sulfide deposits and processes affecting their copper and platinum group element contents.

Barnes, S.-J., Maier, W.D., Curl, E.A., 2010. Composition of the marginal rocks and sills of the Rustenburg Layered Suite, Bushveld Complex, South Africa: implications for the formation of the platinum-group element deposits. Economic Geology, 105(8), 1491-1511.

Barnes, S.-J., Maier, W.D., Curl, E.A., 2010. Composition of the marginal rocks and sills of the Rustenburg Layered Suite, Bushveld Complex, South Africa: implications for the formation of the platinum-group element deposits. Economic Geology, 105(8), 1491-1511.

Bateman, R., Costa, S., Swe, T., Lambert, D., 2001. Archaean mafic magmatism in the Kalgoorlie area of the Yilgarn Craton, Western Australia: a geochemical and Nd isotopic study of the petrogenetic and tectonic evolution of a greenstone belt. Precambrian Research, 108(1-2), 75-112.

Bédard, J., Sparks, R., Renner, R., Cheadle, M., Hallworth, M., 1988. Peridotite sills and metasomatic gabbros in the Eastern Layered Series of the Rhum complex. Journal of the Geological Society, 145(2), 207-224.

Begg, G.C., Hronsky, J.A., Arndt, N.T., Griffin, W.L., O'Reilly, S.Y., Hayward, N., 2010. Lithospheric, cratonic, and geodynamic setting of Ni-Cu-PGE sulfide deposits. Economic geology, 105(6), 1057-1070.

Bhattacharjee, C., Mondal, S.K., 2021. Geochemistry of Fe-Ti oxide and sulfide minerals in gabbroic rocks and magnetitite of the Archean Mayurbhanj mafic complex (eastern India): Magma fractionation, thermometry and oxygen fugacity of re-equilibration, and implications for Ni-Cu mineralization. Ore Geology Reviews, 131, 104005.

Bhattacharjee, S., Mulder, J.A., Roy, S., Chowdhury, P., Cawood, P.A., Nebel, O., 2021. Unravelling depositional setting, age and provenance of the Simlipal volcano-sedimentary complex, Singhbhum craton: Evidence for Hadean crust and Mesoarchean marginal marine sedimentation. Precambrian Research, 354, 106038.

Bi, J.-H., Ge, W.-C., Yang, H., Zhao, G.-C., Xu, W.-L., Wang, Z.-H., 2015. Geochronology, geochemistry and zircon Hf isotopes of the Dongfanghong gabbroic complex at the eastern margin of the Jiamusi Massif, NE China: Petrogensis and tectonic implications. Lithos, 234, 27-46.

Bleeker, W., 2003. The late Archean record: a puzzle in ca. 35 pieces. Lithos, 71(2-4), 99-134.

Boudreau, A., Djon, L., Tchalikian, A., Corkery, J., 2014. The Lac Des Iles Palladium deposit, Ontario, Canada part I. The effect of variable alteration on the offset zone. Mineralium Deposita, 49(5), 625-654.

Boutroy, E., Dare, S.A., Beaudoin, G., Barnes, S.-J., Lightfoot, P.C., 2014. Magnetite composition in Ni-Cu-PGE deposits worldwide: application to mineral exploration. Journal of Geochemical Exploration, 145, 64-81.

Bowles, J., Howie, R., Vaughan, D., Zussman, J., 2011. Non-silicates: volume 5A. Rock-Forming Minerals; Deer, WA, Howie, RA, Zussman, J., Eds, 920.

Brenan, J.M., 2008. Re–Os fractionation by sulfide melt–silicate melt partitioning: a new spin. Chemical Geology, 248(3-4), 140-165.

Broughm, S.G., Hanchar, J.M., Tornos, F., Westhues, A., Attersley, S., 2017. Mineral chemistry of magnetite from magnetite-apatite mineralization and their host rocks: examples from Kiruna, Sweden, and El Laco, Chile. Mineralium Deposita, 52(8), 1223-1244.

Brown, G.M., 1956. The layered ultrabasic rocks of Rhum, Inner Hebrides. Philosophical

Transactions of the Royal Society of London. Series B, Biological Sciences, 1-53.
Buddington, A.F., Lindsley, D., 1964. Iron-titanium oxide minerals and synthetic equivalents. Journal of petrology, 5(2), 310-357.
Cameron, E., 1979. Titanium-bearing oxide minerals of the Critical Zone of the Eastern Bushveld Complex. American Mineralogist, 64(1-2), 140-150.
Carmichael, I., Nicholls, J., 1967. Iron-titanium oxides and oxygen fugacities in volcanic rocks. Journal of Geophysical Research, 72(18), 4665-4687.
Cawthorn, R., 2005. Pressure fluctuations and the formation of the PGE-rich Merensky and chromitite reefs, Bushveld Complex. Mineralium Deposita, 40(2), 231-235.
Cawthorn, R.G., 1996. Layered intrusions. Elsevier.
Cawthorn, R.G., 2015. The Bushveld Complex, South Africa, Layered intrusions. Springer, pp. 517-587.
Chakraborti, T.M., Ray, A., Deb, G.K., Upadhyay, D., Chakrabarti, R., 2019. Evidence of crustal reworking in the Mesoarchean: Insights from geochemical, U-Pb zircon and Nd isotopic study of a 3.08–3.12 Ga ferro-potassic granite-gneiss from north-eastern margin of Singhbhum Craton, India. Lithos, 330, 16-34.
Chakraborty, K., 1959. Mineragraphic study of the vanadium-bearing titaniferous magnetites associated with the gabbro-anorthosites of Nuasahi, Keonjhar district, Orissa, India—their textural relations and paragenesis, Proc Nat Inst Sci India A, pp. 262-272.
Chalokwu, C.I., Armitage, A.E., Seney, P.J., Wurie, C.A., Bersch, M., 1995. Petrology of the Freetown Layered Complex, Sierra Leone: Part I. Stratigraphy and mineral-chemical evidence for multiple magma injection. International Geology Review, 37(3), 230-253.
Charlier, B., Duchesne, J.-C., Vander Auwera, J., 2006. Magma chamber processes in the Tellnes ilmenite deposit (Rogaland Anorthosite Province, SW Norway) and the formation of Fe–Ti ores in massif-type anorthosites. Chemical Geology, 234(3-4), 264-290.
Charlier, B., Grove, T.L., 2012. Experiments on liquid immiscibility along tholeiitic liquid lines of descent. Contributions to Mineralogy and Petrology, 164(1), 27-44.
Charlier, B., Namur, O., Bolle, O., Latypov, R., Duchesne, J.-C., 2015. Fe–Ti–V–P ore deposits associated with Proterozoic massif-type anorthosites and related rocks. Earth-Science

Reviews, 141, 56-81.

Charlier, B., Namur, O., Duchesne, J.C., Wiszniewska, J., Parecki, A., Auwera, J.V., 2009. Cumulate origin and polybaric crystallization of Fe-Ti oxide ores in the suwalki anorthosite, northeastern Poland. Economic Geology, 104(2), 205-221.

Charlier, B., Namur, O., Latypov, R., Tegner, C., 2015. Layered intrusions. Springer.

Charlier, B., Sakoma, E., Sauvé, M., Stanaway, K., Vander Auwera, J., Duchesne, J.-C., 2008. The Grader layered intrusion (Havre-Saint-Pierre Anorthosite, Quebec) and genesis of nelsonite and other Fe–Ti–P ores. Lithos, 101(3-4), 359-378.

Charlier, B., Skår, Ø., Korneliussen, A., Duchesne, J.-C., Vander Auwera, J., 2007. Ilmenite composition in the Tellnes Fe–Ti deposit, SW Norway: fractional crystallization, postcumulus evolution and ilmenite–zircon relation. Contributions to Mineralogy and Petrology, 154(2), 119-134.

Chaudhuri, T., Satish-Kumar, M., Mazumder, R., Biswas, S., 2017. Geochemistry and Sm-Nd isotopic characteristics of the Paleoarchean Komatiites from Singhbhum Craton, Eastern India and their implications. Precambrian Research, 298, 385-402.

Chaudhuri, T., Wan, Y., Mazumder, R., Ma, M., Liu, D., 2018. Evidence of enriched, Hadean mantle reservoir from 4.2-4.0 Ga zircon xenocrysts from Paleoarchean TTGs of the Singhbhum Craton, Eastern India. Scientific reports, 8(1), 1-12.

Chen, W.T., Zhou, M.-F., Zhao, T.-P., 2013. Differentiation of nelsonitic magmas in the formation of the~ 1.74 Ga Damiao Fe–Ti–P ore deposit, North China. Contributions to Mineralogy and Petrology, 165(6), 1341-1362.

Condie, K.C., 2005. High field strength element ratios in Archean basalts: a window to evolving sources of mantle plumes? Lithos, 79(3-4), 491-504.

Craig, J., 1974. Sulfide phase equilibria. Sulfide Mineralogy. Mineralogical Society of America. 1.

Dare, S.A., Barnes, S.-J., Beaudoin, G., 2012. Variation in trace element content of magnetite crystallized from a fractionating sulfide liquid, Sudbury, Canada: Implications for provenance discrimination. Geochimica et Cosmochimica Acta, 88, 27-50.

Dare, S.A., Barnes, S.-J., Beaudoin, G., 2015. Did the massive magnetite "lava flows" of El Laco (Chile) form by magmatic or hydrothermal processes? New constraints from magnetite composition by LA-ICP-MS. Mineralium Deposita, 50(5), 607-617.

Dare, S.A., Barnes, S.-J., Beaudoin, G., Méric, J., Boutroy, E., Potvin-Doucet, C., 2014. Trace elements in magnetite as petrogenetic indicators. Mineralium Deposita, 49(7), 785-796.

Dare, S.A., Barnes, S.-J., Prichard, H.M., Fisher, P.C., 2011. Chalcophile and platinum-group element (PGE) concentrations in the sulfide minerals from the McCreedy East deposit, Sudbury, Canada, and the origin of PGE in pyrite. Mineralium Deposita, 46(4), 381-407.

Das, S., 2014. Mineralogy and Ore Petrography of Vanadiferous Titaniferous Magnetite Ores of Mayurbhanj Basic Igneous Complex, Odisha, Conference GSI, pp. 127-137.

Das, S., Mukherji, S., 2001. Mineralogy and geochemistry of V-Ti magnetite deposits of Mayurbhanj basic igneous complex, Orissa. Indian Mineralogist, 35(1), 134-150.

DePaolo, D., Wasserburg, G., 1979. Sm-Nd age of the Stillwater Complex and the mantle evolution curve for neodymium. Geochimica et Cosmochimica Acta, 43(7), 999-1008.

DePaolo, D.J., 1981. Trace element and isotopic effects of combined wallrock assimilation and fractional crystallization. Earth and planetary science letters, 53(2), 189-202.

DePaolo, D.J., 1988. Age dependence of the composition of continental crust: evidence from Nd isotopic variations in granitic rocks. Earth and Planetary Science Letters, 90(3), 263-271.

Dey, A., Mondal, S.K., 2022. Origin of Fe–Ni–Cu (Co) sulfide and Fe–Ti oxide minerals in the c. 1.77 Ga dolerite dyke, Singhbhum Craton (eastern India). Geological Society, London, Special Publications, 518(1), 553-574.

Dick, H.J., Ozawa, K., Meyer, P.S., Niu, Y., Robinson, P.T., Constantin, M., Hebert, R., Maeda, J., Natland, J.H., Hirth, G., 2002. 10. Primary silicate mineral chemistry of a 1.5-km section of very slow spreading lower ocean crust: ODP hole 735B, Southwest Indian ridge. Proceedings of Ocean Drilling Program, Scientific Results, 000. College Station, TX: Ocean Drilling Program, 1-60.

Dick, H.J., Lissenberg, C.J., Warren, J.M., 2010. Mantle melting, melt transport, and delivery beneath a slow-spreading ridge: The paleo-MAR from 23 15′ N to 23 45′ N. Journal of Petrology 51, 425-467.

Djon, M.L.N., Barnes, S.-J., 2012. Changes in sulfides and platinum-group minerals with the degree of alteration in the Roby, Twilight, and High Grade Zones of the Lac des Iles Complex, Ontario, Canada. Mineralium Deposita, 47(8), 875-896.

Dong, Y., Liu, X., Santosh, M., Zhang, X., Chen, Q., Yang, C., Yang, Z., 2011. Neoproterozoic subduction tectonics of the northwestern Yangtze Block in South China: constrains from zircon U–Pb geochronology and geochemistry of mafic intrusions in the Hannan Massif. Precambrian Research, 189(1-2), 66-90.

Duchesne, J.-C., 1996. Liquid ilmenite or liquidus ilmenite: a comment on the nature of ilmenite vein deposits. ---.

Duchesne, J.-C., 1999. Fe-Ti deposits in Rogaland anorthosites (South Norway): geochemical characteristics and problems of interpretation. Mineralium Deposita, 34(2), 182-198.

Duchesne, J.-C., Charlier, B., 2005. Geochemistry of cumulates from the Bjerkreim–Sokndal layered intrusion (S. Norway). Part I: Constraints from major elements on the mechanism of cumulate formation and on the jotunite liquid line of descent. Lithos, 83(3-4), 229-254.

Duran, C.J., Barnes, S.-J., Corkery, J.T., 2015. Chalcophile and platinum-group element distribution in pyrites from the sulfide-rich pods of the Lac des Iles Pd deposits, Western Ontario, Canada: Implications for post-cumulus re-equilibration of the ore and the use of pyrite compositions in exploration. Journal of Geochemical Exploration, 158, 223-242.

Ernst, R., Wingate, M., Buchan, K., Li, Z.-X., 2008. Global record of 1600–700 Ma Large Igneous Provinces (LIPs): implications for the reconstruction of the proposed Nuna (Columbia) and Rodinia supercontinents. Precambrian Research, 160(1-2), 159-178.

Ernst, R.E., 2014. Large igneous provinces. Cambridge University Press.

Ernst, R.E., Buchan, K.L., Campbell, I.H., 2005. Frontiers in large igneous province research. Lithos, 79(3-4), 271-297.

Ernst, R.E., Jowitt, S.M., 2013. Large igneous provinces (LIPs) and metallogeny. Society of Economic Geologists Special Publication, 17, 17-51.

Ernst, R.E., Srivastava, R.K., 2008. India's place in the Proterozoic world: constraints from the Large Igneous Province (LIP) record. Indian dykes. Edited by RK Srivastava, Ch. Sivaji, and NV Chalapathi Rao. Geochemistry, Geophysics, and Geochronology, Narosa Publishing House Pvt. Ltd, New Delhi, India, 41-56.

Faure, G., Mensing, T.M., 2005. Isotopes: Principles and applications. John Wiley & Sons, Inc.

Foley, S., Tiepolo, M., Vannucci, R., 2002. Growth of early continental crust controlled by melting of amphibolite in subduction zones. Nature, 417(6891), 837-840.

Foley, S.F., Wheller, G.E., 1990. Parallels in the origin of the geochemical signatures of island arc volcanics and continental potassic igneous rocks: the role of residual titanates. Chemical Geology, 85(1-2), 1-18.

Gao, W., Ciobanu, C.L., Cook, N.J., Huang, F., Meng, L., Gao, S., 2017. Petrography and trace element signatures in silicates and Fe–Ti-oxides from the Lanjiahuoshan deposit, Panzhihua layered intrusion, Southwest China. Lithos, 294, 164-183.

Ghosh, D., Sarkar, S., Saha, A., Ray, S., 1996. New insights on the early Archaean crustal evolution in eastern India: Re-evaluation of lead-lead, samarium-neodymium and rubidium-strontium geochronology. Indian Minerals, 50.

Goswami, J., Mishra, S., Wiedenbeck, M., Ray, S., Saha, A., 1995. 3.55 ga old zircon from Singhbhum–Orissa iron ore craton, eastern India. Current Science, 1008-1012.

Haggerty, S.E., 1976. Opaque mineral oxides in terrestrial igneous rocks, Oxide minerals. De Gruyter, pp. 303-502.

Haggerty, S.E., 1991. Oxide textures-a mini-atlas, Oxide minerals. De Gruyter, pp. 129-220.

Hamilton, P., O'nions, R., Bridgwater, D., Nutman, A., 1983. Sm-Nd studies of Archaean metasediments and metavolcanics from West Greenland and their implications for the Earth's early history. Earth and Planetary Science Letters, 62(2), 263-272.

Hart, S.R., Dunn, T., 1993. Experimental cpx/melt partitioning of 24 trace elements. Contributions to Mineralogy and Petrology, 113(1), 1-8.

Hegner, E., Kröner, A., Hofmann, A., 1984. Age and isotope geochemistry of the Archaean Pongola and Usushwana suites in Swaziland, southern Africa: a case for crustal contamination of mantle-derived magma. Earth and Planetary Science Letters, 70(2), 267-279.

Hoatson, D.M., Sun, S.-S., 2002. Archean layered mafic-ultramafic intrusions in the West Pilbara Craton, Western Australia: A synthesis of some of the oldest orthomagmatic mineralizing systems in the world. Economic Geology, 97(4), 847-872.

Holwell, D.A., Keays, R.R., McDonald, I., Williams, M.R., 2015. Extreme enrichment of Se, Te, PGE and Au in Cu sulfide microdroplets: evidence from LA-ICP-MS analysis of sulfides in the

Skaergaard Intrusion, east Greenland. Contributions to Mineralogy and Petrology, 170(5), 1-26.

Hou, T., Zhang, Z., Encarnacion, J., Santosh, M., 2012. Petrogenesis and metallogenesis of the Taihe gabbroic intrusion associated with Fe–Ti-oxide ores in the Panxi district, Emeishan Large Igneous Province, southwest China. Ore Geology Reviews, 49, 109-127.

Howarth, G.H., Prevec, S.A., 2013. Trace element, PGE, and Sr–Nd isotope geochemistry of the Panzhihua mafic layered intrusion, SW China: Constraints on ore-forming processes and evolution of parent magma at depth in a plumbing-system. Geochimica et Cosmochimica Acta, 120, 459-478.

Hunter, R., Sparks, R., 1987. The differentiation of the Skaergaard intrusion. Contributions to Mineralogy and Petrology, 95(4), 451-461.

Hunter, R., SPARKS, R.J., 1990. The differentiation of the Skargaard Intrusion. Reply to AR McBirney and HR Naslund. Contributions to Mineralogy and Petrology, 104(2), 248-251.

Huston, D.L., Sie, S.H., Suter, G.F., Cooke, D.R., Both, R.A., 1995. Trace elements in sulfide minerals from eastern Australian volcanic-hosted massive sulfide deposits; Part I, Proton microprobe analyses of pyrite, chalcopyrite, and sphalerite, and Part II, Selenium levels in pyrite; comparison with delta 34 S values and implications for the source of sulfur in volcanogenic hydrothermal systems. Economic Geology, 90(5), 1167-1196.

Irvine, T., 1967. The ultramafic rocks of the Muskox intrusion, Nothern Territories, Canada. Ultramafic and related rocks, 38-49.

Irvine, T., 1976. Crystallization sequences in the Muskox intrusion and other layered intrusions—II. Origin of chromitite layers and similar deposits of other magmatic ores, Chromium: its Physicochemical Behavior and Petrologic Significance. Elsevier, pp. 991-1020.

Irvine, T., 1977. Origin of chromitite layers in the Muskox intrusion and other stratiform intrusions: A new interpretation. Geology, 5(5), 273-277.

Irving, A.J., 1978. A review of experimental studies of crystal/liquid trace element partitioning. Geochimica et Cosmochimica Acta, 42(6), 743-770.

Ivanic, T., Wingate, M., Kirkland, C., Van Kranendonk, M., Wyche, S., 2010. Age and significance of voluminous mafic–ultramafic magmatic events in the Murchison Domain, Yilgarn Craton.

Australian Journal of Earth Sciences, 57(5), 597-614.
Jakobsen, J., Veksler, I., Tegner, C., Brooks, C., 2005. Immiscible iron-and silica-rich melts in basalt petrogenesis documented in the Skaergaard intrusion. Geology, 33(11), 885-888.
Jakobsen, J.K., Tegner, C., Brooks, C.K., Kent, A.J., Lesher, C.E., Nielsen, T.F., Wiedenbeck, M., 2010. Parental magma of the Skaergaard intrusion: constraints from melt inclusions in primitive troctolite blocks and FG-1 dykes. Contributions to Mineralogy and Petrology, 159(1), 61-79.
Jang, Y.D., Naslund, H., McBirney, A., 2001. The differentiation trend of the Skaergaard intrusion and the timing of magnetite crystallization: iron enrichment revisited. Earth and Planetary Science Letters, 189(3-4), 189-196.
Jayananda, M., Kano, T., Peucat, J.-J., Channabasappa, S., 2008. 3.35 Ga komatiite volcanism in the western Dharwar craton, southern India: constraints from Nd isotopes and whole-rock geochemistry. Precambrian Research, 162(1-2), 160-179.
Keays, R.R., 1995. The role of komatiitic and picritic magmatism and S-saturation in the formation of ore deposits. Lithos, 34(1-3), 1-18.
Khatun, S., Mondal, S.K., Zhou, M.-F., Balaram, V., Prichard, H.M., 2014. Platinum-group element (PGE) geochemistry of Mesoarchean ultramafic–mafic cumulate rocks and chromitites from the Nuasahi Massif, Singhbhum Craton (India). Lithos, 205, 322-340.
Klein, E., 2003. Geochemistry of the igneous oceanic crust. Treatise on geochemistry, 3, 659.
Kullerud, G., 1969. Phase relations in the Cu-Fe-S, Cu-Ni-S, and Fe-Ni-S systems. Economic Geology Monograph 4, 323-343.
Kumar, A., Parashuramulu, V., Shankar, R., Besse, J., 2017. Evidence for a Neoarchean LIP in the Singhbhum craton, eastern India: Implications to Vaalbara supercontinent. Precambrian Research, 292, 163-174.
Kushiro, I., 1972. Determination of liquidus relations in synthetic silicate systems with electron probe analysis: the system forsterite-diopside-silica at 1 atmosphere. American Mineralogist: Journal of Earth and Planetary Materials, 57(7-8), 1260-1271.
Lepage, L.D., 2003. ILMAT: an Excel worksheet for ilmenite-magnetite geothermometry and geobarometry. Computers & Geosciences, 29(5), 673-678.
Li, H., Li, L., Zhang, Z., Santosh, M., Liu, M., Cui, Y., Yang, X., Chen, J., Yao, T., 2014. Alteration of the

Damiao anorthosite complex in the northern North China Craton: Implications for high-grade iron mineralization. Ore Geology Reviews, 57, 574-588.

Lindsley, D., Duchesne, J., Korneliussen, A., 2003. Do Fe–Ti oxide magmas exist? Geology: yes, experiments: no. NGU Special Publication, 9, 34-35.

Lindsley, D.H., 1983. Pyroxene thermometry. American mineralogist, 68(5-6), 477-493.

Lister, G.F., 1966. The composition and origin of selected iron-titanium deposits. Economic Geology, 61(2), 275-310.

Liu, P.-P., Zhou, M.-F., Chen, W.T., Gao, J.-F., Huang, X.-W., 2015. In-situ LA-ICP-MS trace elemental analyses of magnetite: Fe–Ti–(V) oxide-bearing mafic–ultramafic layered intrusions of the Emeishan Large Igneous Province, SW China. Ore Geology Reviews, 65, 853-871.

Liu, Y., Brenan, J., 2015. Partitioning of platinum-group elements (PGE) and chalcogens (Se, Te, As, Sb, Bi) between monosulfide-solid solution (MSS), intermediate solid solution (ISS) and sulfide liquid at controlled fO2–fS2 conditions. Geochimica et Cosmochimica Acta, 159, 139-161.

Ludwig, K., 2011. User's manual for Isoplot 4.15: A geochronological toolkit for Microsoft Excel. Berkeley Geochronology Center, Berkeley, California, USA concentrations: Loess and the upper continental crust. Geochemistry, Geophysics, and Geosystems, 2.

Lyubetskaya, T., Korenaga, J., 2007. Chemical composition of Earth's primitive mantle and its variance: 1. Method and results. Journal of Geophysical Research: Solid Earth, 112(B3).

Maier, W.D., Groves, D.I., 2011. Temporal and spatial controls on the formation of magmatic PGE and Ni–Cu deposits. Mineralium Deposita, 46(8), 841-857.

McBirney, A., 1996. The Skaergaard intrusion, Developments in Petrology. Elsevier, pp. 147-180.

McBIRNEY, A.R., Noyes, R.M., 1979. Crystallization and layering of the Skaergaard intrusion. Journal of Petrology, 20(3), 487-554.

McDonough, W.F., Sun, S.-S., 1995. The composition of the Earth. Chemical geology, 120(3-4), 223-253.

Miller Jr, J.D., Green, J.C., Severson, M.J., Chandler, V.W., Hauck, S.A., Peterson, D.M., Wahl, T.E., 2002. RI-58 Geology and mineral potential of the Duluth Complex and related rocks of northeastern Minnesota.

Mishra, S., Deomurari, M., Wiedenbeck, M., Goswami, J., Ray, S., Saha, A., 1999. 207Pb/206Pb zircon ages and the evolution of the Singhbhum Craton, eastern India: an ion microprobe study. Precambrian Research, 93(2-3), 139-151.

Misra, S., Johnson, P.T., 2005. Geochronological constraints on evolution of Singhbhum mobile belt and associated basic volcanics of eastern Indian shield. Gondwana Research, 8(2), 129-142.

Misra, S., Sarkar, S.S., Ghosh, S., 2002. Evolution of Mayurbhanj Granite Pluton, eastern Singhbhum, India: a case study of petrogenesis of an A-type granite in bimodal association. Journal of Asian Earth Sciences, 20(8), 965-989.

Mitchell, R.N., Zhang, N., Salminen, J., Liu, Y., Spencer, C.J., Steinberger, B., Murphy, J.B., Li, Z.-X., 2021. The supercontinent cycle. Nature Reviews Earth & Environment, 2(5), 358-374.

Mohanty, J., Paul, A., 2008. Fe-Ti-oxide Ore of the Mesorchaean Nuasahi Ultramafic-Mafic Complex, Orissa and its Utilization Potential.

Mondal, S.K., 2009. Chromite and PGE deposits of Mesoarchaean ultramafic-mafic suites within the greenstone belts of the Singhbhum craton, India: implications for mantle heterogeneity and tectonic setting. Journal of the Geological Society of India, 73(1), 36-51.

Mondal, S.K., Baidya, T.K., 1997. Platinum-group minerals from the Nuasahi ultramafic-mafic complex, Orissa, India. Mineralogical Magazine, 61(409), 902-906.

Mondal, S.K., Baidya, T.K., Rao, K.N.G., Glascock, M.D., 2001. PGE and Ag mineralization in a breccia zone of the Precambrian Nuasahi ultramafic-mafic complex, Orissa, India. The Canadian Mineralogist, 39(4), 979-996.

Mondal, S.K., Bhattacharjee, C., Reisberg, L., 2021. 3.2-3.0 Ga Sm-Nd age of gabbro-anorthositic rocks from the Nuasahi and Mayurbhanj Complexes (eastern India): Major mafic magmatic event in the Singhbhum Craton and associated Ni-Cu-(PGE) sulphide mineralization. Goldschmidt2021• Virtual• 4-9 July.

Mondal, S.K., Khatun, S., Prichard, H.M., Satyanarayanan, M., Kumar, G.R., 2019. Platinum-group element geochemistry of boninite-derived Mesoarchean chromitites and ultramafic-mafic cumulate rocks from the Sukinda Massif (Orissa, India). Ore Geology Reviews, 104, 722-744.

Mondal, S.K., Ripley, E.M., Li, C., Frei, R., 2006. The genesis of Archaean chromitites from the Nuasahi and Sukinda massifs in the Singhbhum Craton, India. Precambrian Research, 148(1-2), 45-66.

Mondal, S.K., Zhou, M.-F., 2010. Enrichment of PGE through interaction of evolved boninitic magmas with early formed cumulates in a gabbro–breccia zone of the Mesoarchean Nuasahi massif (eastern India). Mineralium Deposita, 45(1), 69-91.

Morisset, C.-E., Scoates, J.S., Weis, D., Sauvé, M., Stanaway, K.J., 2010. Rutile-bearing ilmenite deposits associated with the Proterozoic Saint-Urbain and Lac Allard anorthosite massifs, Grenville Province, Quebec. The Canadian Mineralogist, 48(4), 821-849.

Morse, S.A., 1980. Basalts and phase diagrams: an introduction to the quantitative use of phase diagrams in igneous petrology. Springer.

Moyen, J.-F., Martin, H., 2012. Forty years of TTG research. Lithos, 148, 312-336.

Mukherjee, R., Mondal, S.K., Frei, R., Rosing, M.T., Waight, T.E., Zhong, H., Kumar, G.R., 2012. The 3.1 Ga Nuggihalli chromite deposits, Western Dharwar craton (India): Geochemical and isotopic constraints on mantle sources, crustal evolution and implications for supercontinent formation and ore mineralization. Lithos, 155, 392-409.

Mukherjee, R., Mondal, S.K., González-Jiménez, J.M., Griffin, W.L., Pearson, N.J., O'Reilly, S.Y., 2015. Trace-element fingerprints of chromite, magnetite and sulfides from the 3.1 Ga ultramafic–mafic rocks of the Nuggihalli greenstone belt, Western Dharwar craton (India). Contributions to Mineralogy and Petrology, 169(6), 1-23.

Mukhopadhyay, D., 2001. The Archaean nucleus of Singhbhum: the present state of knowledge. Gondwana Research, 4(3), 307-318.

Mukhopadhyay, J., Beukes, N., Armstrong, R., Zimmermann, U., Ghosh, G., Medda, R., 2008. Dating the oldest greenstone in India: a 3.51-Ga precise U-Pb SHRIMP zircon age for dacitic lava of the southern Iron Ore Group, Singhbhum craton. The Journal of Geology, 116(5), 449-461.

Nadoll, P., Angerer, T., Mauk, J.L., French, D., Walshe, J., 2014. The chemistry of hydrothermal magnetite: A review. Ore Geology Reviews, 61, 1-32.

Naldrett, A., 2011. Fundamentals of magmatic sulfide deposits.

Naldrett, A., Asif, M., Scandl, E., Searcy, T., Morrison, G., Binney, W., Moore, C., 1999. Platinum-group elements in the Sudbury ores; significance with respect to the origin of different ore zones and to the exploration for footwall orebodies. Economic Geology, 94(2), 185-210.

Namur, O., Charlier, B., Holness, M.B., 2012. Dual origin of Fe–Ti–P gabbros by immiscibility and fractional crystallization of evolved tholeiitic basalts in the Sept Iles layered intrusion. Lithos, 154, 100-114.

Namur, O., Charlier, B., Toplis, M.J., Higgins, M.D., Liégeois, J.-P., Vander Auwera, J., 2010. Crystallization sequence and magma chamber processes in the ferrobasaltic Sept Iles layered intrusion, Canada. Journal of Petrology, 51(6), 1203-1236.

Nance, R.D., Murphy, J.B., Santosh, M., 2014. The supercontinent cycle: a retrospective essay. Gondwana Research, 25(1), 4-29.

Oberthür, T., Davis, D.W., Blenkinsop, T.G., Höhndorf, A., 2002. Precise U–Pb mineral ages, Rb–Sr and Sm–Nd systematics for the Great Dyke, Zimbabwe—constraints on late Archean events in the Zimbabwe craton and Limpopo belt. Precambrian Research, 113(3-4), 293-305.

Osborn, E., Tait, D., 1952. The system diopside-forsterite-anorthite. American Journal of Science, 250, 413-433.

Pandey, O.P., Mezger, K., Ranjan, S., Upadhyay, D., Villa, I.M., Nägler, T.F., Vollstaedt, H., 2019. Genesis of the Singhbhum Craton, eastern India; implications for Archean crust-mantle evolution of the Earth. Chemical Geology, 512, 85-106.

Pang, K.-N., Li, C., Zhou, M.-F., Ripley, E.M., 2009. Mineral compositional constraints on petrogenesis and oxide ore genesis of the late Permian Panzhihua layered gabbroic intrusion, SW China. Lithos, 110(1-4), 199-214.

Pang, K.-N., Shellnutt, J.G., 2018. Magmatic sulfide and Fe-Ti oxide deposits associated with mafic-ultramafic intrusions in China, Processes and Ore Deposits of Ultramafic-Mafic Magmas through Space and Time. Elsevier, pp. 239-267.

Pang, K.-N., Zhou, M.-F., Lindsley, D., Zhao, D., Malpas, J., 2008. Origin of Fe–Ti oxide ores in mafic intrusions: evidence from the Panzhihua intrusion, SW China. Journal of Petrology, 49(2), 295-313.

Pang, K.-N., Zhou, M.-F., Qi, L., Shellnutt, G., Wang, C.Y., Zhao, D., 2010. Flood basalt-related Fe–Ti oxide deposits in the Emeishan large igneous province, SW China. Lithos, 119(1-2), 123-136.

Pearce, J.A., 1983. Role of the sub-continental lithosphere in magma genesis at active continental margins.

Pearce, J.A., Peate, D.W., 1995. Tectonic implications of the composition of volcanic arc magmas. Annual review of Earth and planetary sciences, 23, 251-286.

Peck, D., Halden, N., Jobin-Bevans, S., Cameron, H., Theyer, P., 1999. Summary of metallogenetic and petrogenetic features of Archean anorthosites and associated mafic and ultramafic rocks in the Superior Province, Manitoba (parts of NTS 63I, 63J, 63P and 64A). Report of Activities, 94-96.

Percival, J.A., 2007. Geology and metallogeny of the Superior Province, Canada. Mineral deposits of Canada: A synthesis of major deposit-types, district metallogeny, the evolution of geological provinces, and exploration methods: Geological Association of Canada, Mineral Deposits Division, Special Publication, 5, 903-928.

Philpotts, A., 1982. Compositions of immiscible liquids in volcanic rocks. Contributions to Mineralogy and Petrology, 80(3), 201-218.

Philpotts, A.R., Ague, J.J., 2022. Principles of igneous and metamorphic petrology. Cambridge University Press.

Phinney, W., Morrison, D., 1990. Partition coefficients for calcic plagioclase: Implications for Archean anorthosites. Geochimica et Cosmochimica Acta, 54(6), 1639-1654.

Piña, R., Gervilla, F., Barnes, S.-J., Ortega, L., Lunar, R., 2013. Platinum-group elements-bearing pyrite from the Aguablanca Ni-Cu sulphide deposit (SW Spain): a LA-ICP-MS study. European Journal of Mineralogy, 25(2), 241-252.

Prabhakar, N., Bhattacharya, A., 2013. Paleoarchean partial convective overturn in the Singhbhum Craton, Eastern India. Precambrian Research, 231, 106-121.

Prichard, H.M., Mondal, S.K., Mukherjee, R., Fisher, P.C., Giles, N., 2018. Geochemistry and mineralogy of Pd in the magnetitite layer within the upper gabbro of the Mesoarchean Nuasahi Massif (Orissa, India). Mineralium Deposita, 53(4), 547-564.

Reynolds, I.M., 1985. Contrasted mineralogy and textural relationships in the uppermost titaniferous magnetite layers of the Bushveld Complex in the Bierkraal area north of Rustenburg. Economic Geology, 80(4), 1027-1048.

Reynolds, I.M., 1985. The nature and origin of titaniferous magnetite-rich layers in the upper zone of the Bushveld Complex; a review and synthesis. Economic Geology, 80(4), 1089-1108.

Ripley, E.M., Li, C., 2018. Metallic ore deposits associated with mafic to ultramafic igneous rocks, Processes and Ore Deposits of Ultramafic-Mafic Magmas through Space and Time. Elsevier, pp. 79-111.

Ripley, E.M., Severson, M.J., Hauck, S.A., 1998. Evidence for sulfide and Fe-Ti-P-rich liquid immiscibility in the Duluth Complex, Minnesota. Economic Geology, 93(7), 1052-1062.

Rogers, J.J., Santosh, M., 2003. Supercontinents in Earth history. Gondwana Research, 6(3), 357-368.

Rollinson, H.R., Tarney, J., 2005. Adakites—the key to understanding LILE depletion in granulites. Lithos, 79(1-2), 61-81.

Rose, E.R., 1969. Geology of titanium and titaniferous deposits of Canada. Department of Energy, Mines and Resources.

Roy, A., Sarkar, A., Jeyakumar, S., Ebihara, M., 2002. Sm-Nd age and mantle source characteristics of the Dhanjori volcanic rocks, eastern India. Geochemical Journal, 36(5), 503-518.

Roy, S., 1955. Thermal experiments with the vanadium bearing titaniferous magnetites of Mayurbhanj. Proc. Nat. Insti. Sci. India, 21(5), 222.

Roy, S., 1956. Origin of the vanadium bearing titaniferous magnetite ores of Mayurbhanj, India, Proc. Nat. Inst. Sci. India, pp. 285-292.

Rudnick, R., Gao, S., Holland, H., Turekian, K., 2003. Composition of the continental crust. The crust, 3, 1-64.

Ruiz, F.V., Della Giustina, M.E.S., de Oliveira, C.G., Dantas, E.L., Hollanda, M.H.B., 2019. The 3.5 Ga São Tomé layered mafic-ultramafic intrusion, NE Brazil: insights into a Paleoarchean Fe-Ti-V oxide mineralization and its reworking during West Gondwana assembly. Precambrian Research, 326, 462-478.

Saha, A.K., 1994. Crustal evolution of Singhbhum north Orissa eastern India. Mem. Geolog. Soc. India.

Samal, A.K., Srivastava, R.K., Ernst, R.E., 2021. An appraisal of mineral systems associated with Precambrian Large Igneous Provinces of the Indian Shield. Ore Geology Reviews, 131, 104009.

Sarkar, S., Ghosh, D., Lambert, R.S., 1985. Rb–Sr and Pb isotopic studies on the Soda granites from Mosabani, Singhbhum copper belt, eastern India. Indian Journal of Earth Sciences, 13, 101-116.

Sengupta, S., Paul, D., Bishui, P., Gupta, S., Chakrabarti, R., Purnendu, S., 1994. Geochemical and Rb-Sr isotopic study of Kuilapal granite and Arkasani granophyre from the eastern Indian craton. Indian Minerals, 48.

Sengupta, S., Paul, D., De Laeter, J., McNaughton, N., Bandopadhyay, P., De Smeth, J., 1991. Mid-Archaean evolution of the eastern Indian craton: geochemical and isotopic evidence from the Bonai pluton. Precambrian Research, 49(1-2), 23-37.

Shankar, R., Vijayagopal, B., Kumar, A., 2014. Precise Pb–Pb baddeleyite ages of 1765 Ma for a Singhbhum 'newer dolerite'dyke swarm. Current Science, 106, 1306-1310.

Sharma, M., Basu, A.R., Ray, S.L., 1994. Sm-Nd isotopic and geochemical study of the Archean tonalite-amphibolite association from the eastern Indian Craton. Contributions to Mineralogy and Petrology, 117(1), 45-55.

She, Y.-W., Song, X.-Y., Yu, S.-Y., He, H.-L., 2015. Variations of trace element concentration of magnetite and ilmenite from the Taihe layered intrusion, Emeishan large igneous province, SW China: Implications for magmatic fractionation and origin of Fe–Ti–V oxide ore deposits. Journal of Asian Earth Sciences, 113, 1117-1131.

Sievwright, R., O'Neill, H.S.C., Tolley, J., Wilkinson, J., Berry, A., 2020. Diffusion and partition coefficients of minor and trace elements in magnetite as a function of oxygen fugacity at 1150 ºC. Contributions to Mineralogy and Petrology, 175(5), 1-21.

Singh, P.K., Verma, S.K., Moreno, J.A., Singh, V.K., Malviya, V.P., Oliveira, E.P., Mishra, S., Arima, M., 2019. Geochemistry and SmNd isotope systematics of mafic-ultramafic rocks from the Babina and Mauranipur greenstone belts, Bundelkhand Craton, India: Implications for tectonic setting and Paleoarchean mantle evolution. Lithos, 330, 90-107.

Smithies, R., Champion, D., 2000. The Archaean high-Mg diorite suite: links to tonalite–

trondhjemite–granodiorite magmatism and implications for early Archaean crustal growth. Journal of Petrology, 41(12), 1653-1671.

Srivastava, R.K., Samal, A.K., Ernst, R.E., Söderlund, U., Shankar, R., 2020. Spatial and temporal distribution of Large Igneous Provinces in the Indian Shield–highlights of recent investigations. Proceedings of Indian National Science Academy, 86, 313-330.

Srivastava, R.K., Söderlund, U., Ernst, R.E., Mondal, S.K., Samal, A.K., 2019. Precambrian mafic dyke swarms in the Singhbhum craton (eastern India) and their links with dyke swarms of the eastern Dharwar craton (southern India). Precambrian Research, 329, 5-17.

Stribrny, B., Wellmer, F.-W., Burgath, K.-P., Oberthür, T., Tarkian, M., Pfeiffer, T., 2000. Unconventional PGE occurrences and PGE mineralization in the Great Dyke: metallogenic and economic aspects. Mineralium Deposita, 35(2), 260-280.

Tan, W., Liu, P., He, H., Wang, C.Y., Liang, X., 2016. Mineralogy and origin of exsolution in Ti-rich magnetite from different magmatic Fe-Ti oxide-bearing intrusions. The Canadian Mineralogist, 54(3), 539-553.

Tegner, C., Cawthorn, R.G., Kruger, F.J., 2006. Cyclicity in the Main and Upper Zones of the Bushveld Complex, South Africa: crystallization from a zoned magma sheet. Journal of Petrology, 47(11), 2257-2279.

Tegner, C., Wilson, J.R., Brooks, C.K., 1993. Intraplutonic quench zones in the Kap Edvard Holm layered gabbro complex, East Greenland. Journal of Petrology, 34(4), 681-710.

Toplis, M., Carroll, M., 1995. An experimental study of the influence of oxygen fugacity on Fe-Ti oxide stability, phase relations, and mineral—melt equilibria in ferro-basaltic systems. Journal of Petrology, 36(5), 1137-1170.

Upadhyay, D., Chattopadhyay, S., Kooijman, E., Mezger, K., Berndt, J., 2014. Magmatic and metamorphic history of Paleoarchean tonalite–trondhjemite–granodiorite (TTG) suite from the Singhbhum craton, eastern India. Precambrian research, 252, 180-190.

Valdiya, K.S., 2015. The making of India: geodynamic evolution. Springer.

Van Kranendonk, M.J., Smithies, R.H., Hickman, A.H., Wingate, M.T., Bodorkos, S., 2010. Evidence for Mesoarchean (~ 3.2 Ga) rifting of the Pilbara Craton: The missing link in an early Precambrian Wilson cycle. Precambrian Research, 177(1-2), 145-161.

Von Gruenewaldt, G., 1973. The main and upper zones of the Bushveld Complex in the Roossenekal area, eastern Transvaal. Transactions of the Geological Society of South Africa, 76, 207-227.
Von Gruenewaldt, G., 1973. The main and upper zones of the Bushveld Complex in the Roossenekal area, eastern Transvaal. Transactions of the Geological Society of South Africa, 76, 207-227.
Von Gruenewaldt, G., 1993. Ilmenite-apatite enrichments in the Upper Zone of the Bushveld Complex: a major titanium-rock phosphate resource. International Geology Review, 35(11), 987-1000.

Wager, L., Brown, G., 1968. Layered Igneous Rocks: London (Oliver and Boyd). Plate, 3, 26-28.

Wager, L., Brown, G., Wadsworth, W., 1960. Types of igneous cumulates. Journal of Petrology, 1(1), 73-85.

Wager, L.R., 1960. The major element variation of the layered series of the Skaergaard intrusion and a re-estimation of the average composition of the hidden layered series and of the successive residual magmas. Journal of Petrology, 1(1), 364-398.

Wager, L.R., Mitchell, R., 1951. The distribution of trace elements during strong fractionation of basic magma—a further study of the Skaergaard intrusion, East Greenland. Geochimica et Cosmochimica Acta, 1(3), 129-208.

Wainwright, A.N., El Atrassi, F., Debaille, V., Mattielli, N., 2019. Geochemistry and petrogenesis of Archean mafic rocks from the Amsaga area, West African craton, Mauritania. Precambrian Research, 324, 208-219.

Wang, C.Y., Zhou, M.-F., 2013. New textural and mineralogical constraints on the origin of the Hongge Fe-Ti-V oxide deposit, SW China. Mineralium Deposita, 48(6), 787-798.

Wang, C.Y., Zhou, M.-F., Zhao, D., 2008. Fe–Ti–Cr oxides from the Permian Xinjie mafic–ultramafic layered intrusion in the Emeishan large igneous province, SW China: crystallization from Fe- and Ti-rich basaltic magmas. Lithos, 102(1-2), 198-217.

Wang, D., Guo, J., Huang, G., Scheltens, M., 2015. The Neoarchean ultramafic–mafic complex in the Yinshan Block, North China Craton: Magmatic monitor of development of Archean lithospheric mantle. Precambrian Research, 270, 80-99.

Wang, K., Wang, C.Y., Ren, Z.-Y., 2018. Apatite-hosted melt inclusions from the Panzhihua gabbroic-layered intrusion associated with a giant Fe–Ti oxide deposit in SW China: insights for magma unmixing within a crystal mush. Contributions to Mineralogy and Petrology, 173(7), 1-14.

Ward, L.A., Holwell, D.A., Barry, T.L., Blanks, D.E., Graham, S.D., 2018. The use of magnetite as a geochemical indicator in the exploration for magmatic Ni-Cu-PGE sulfide deposits: A case study from Munali, Zambia. Journal of Geochemical Exploration, 188, 172-184.

Whitney, D.L., Evans, B.W., 2010. Abbreviations for names of rock-forming minerals. American mineralogist 95, 185.

Winter, J.D., 2013. Principles of igneous and metamorphic petrology. Pearson education.

Yan, J., Chen, J.-F., Xu, X.-S., 2008. Geochemistry of Cretaceous mafic rocks from the Lower Yangtze region, eastern China: Characteristics and evolution of the lithospheric mantle. Journal of Asian Earth Sciences, 33(3-4), 177-193.

Zhang, D., Zhang, Z., Huang, H., Cheng, Z., Charlier, B., 2018. Petrogenesis and metallogenesis of the Wajilitag and Puchang Fe-Ti oxide-rich intrusive complexes, northwestern Tarim Large Igneous Province. Lithos, 304, 412-435.

Zhao, J.-H., Zhou, M.-F., 2007. Geochemistry of Neoproterozoic mafic intrusions in the Panzhihua district (Sichuan Province, SW China): Implications for subduction-related metasomatism in the upper mantle. Precambrian research, 152(1-2), 27-47.

Zhong, H., Zhu, W.-G., Hu, R.-Z., Xie, L.-W., He, D.-F., Liu, F., Chu, Z.-Y., 2009. Zircon U–Pb age and Sr–Nd–Hf isotope geochemistry of the Panzhihua A-type syenitic intrusion in the Emeishan large igneous province, southwest China and implications for growth of juvenile crust. Lithos, 110(1-4), 109-128.

Zhou, M.-F., Chen, W.T., Wang, C.Y., Prevec, S.A., Liu, P., Howarth, G.H., 2013. Two stages of immiscible liquid separation in the formation of Panzhihua-type Fe-Ti-V oxide deposits, SW China. Geoscience Frontiers, 4(5), 481-502.

Zhou, M.-F., Lesher, C.M., Yang, Z., Li, J., Sun, M., 2004. Geochemistry and petrogenesis of 270 Ma Ni–Cu–(PGE) sulfide-bearing mafic intrusions in the Huangshan district, Eastern Xinjiang, Northwest China: implications for the tectonic evolution of the Central Asian orogenic belt.

Chemical Geology, 209(3-4), 233-257.

Zhou, M.-f., Robinson, P.T., Lesher, C.M., Keays, R.R., Zhang, C.-J., Malpas, J., 2005. Geochemistry, petrogenesis and metallogenesis of the Panzhihua gabbroic layered intrusion and associated Fe–Ti–V oxide deposits, Sichuan Province, SW China. Journal of Petrology, 46(11), 2253-2280.